Computer simulation of two-dimensional condensed matter systems

Peter D. Duncan, MChemPhys

A thesis submitted in fulfilment of requirements for the degree of

Doctor of Philosophy

to

School of Chemistry

University of Edinburgh

July 2006

Declaration

I hereby declare that this thesis is of my own composition, and that it contains no material previously submitted for the award of any other degree. The work reported in this thesis has been executed by myself, except where due acknowledgement is made in the text.

Abstract

There are many experimental situations in which the system under study can be reasonably described as two dimensional. Examples include molecules adsorbed on a solid surface, colloidal thin films, surfactant molecules at a water-air interface, biological membranes, many magnetic materials with strong exchange interactions within two dimensional layers but weak interactions between layers. In addition, qualitatively different physics can emerge in two dimensions as compared to three dimensions. Motivated by this large diversity of two dimensional condensed matter systems, various two dimensional systems were investigated using computer simulation.

The structure and dynamics in a monolayer of dipolar soft spheres were studied using Molecular Dynamics simulation. This is a model for colloidal ferrofluids. The particles form into chains on account of the favourable nose-to-tail configuration of the dipole-dipole interaction. The effect of this chaining on the structure and dynamics has been invesigated. The fact that particles are confined within chains has a pronounced effect on the dynamics. Various time autocorrelation functions reveal processes occurring over two different timescales – the slow motion of chains and rings as a whole and the fast oscillatory motion of particles within those chains.

Langevin Dynamics simulations have been employed to study the aggregation kinetics of the dipolar chains and rings starting from a 'random' configuration. Clusters were identified using an energy criterion, and classified as chains, rings or defect clusters. The mechanisms by which these clusters form are discussed. At high density, there is a network structure at intermediate times with a high concentration of defects. This suggests that the phase transition proposed by Tlusty and Safran [Tlusty, Safran, Science **290**, 1328 (2000)] could be recovered as a metastable phase transition if the system could be kinetically trapped in the transient network structure.

The dynamics of antiferromagnetically coupled Heisenberg spins on a kagomé lattice has been studied using numerical simulation. This system is highly frustrated - the lattice places competing constraints on the spins. We investigate the effect of breaking bonds in the lattice, which relieves the frustration to a certain extent. The excitations in the system are found to be local, consisting of motions of small groups of spins. As bonds are broken, certain spins are able to align antiferromagnetically and undergo motions characteristic of unfrustrated antiferromagnets.

The phase diagram of a two dimensional system of hard disk trimers has been explored by Monte Carlo simulation. This might serve as a coarse grained model for the aggregation of proteins in a biological membrane. Many proteins are roughly triangular in shape or form trimeric units. The model consists of three hard disks fused together in a triangular arrangement. One of the disks interacts with the corresponding disk on other trimers via a square-well potential, representing specific interactions between the protein molecules. In the fluid phase at low density the trimers form aggregates containing typically four to six trimers. In the solid phase, the trimers pack such that individual disks are on a triangular lattice. There are different possible packings of the trimers consistent with this

packing of individual disks. At low temperature, the solid exhibits an orientationally ordered structure built up of repeating motifs, dependent upon which packing is adopted by the trimers.

Acknowledgements

Many thanks go to my supervisor, Dr. Philip Camp for all his help and guidance during course of my PhD.

I would also like to thank my colleagues Dr. Alastair Dewar, Leonardo Lenoci, Alexandros Chremos and Georg Ganzenmueller.

I acknowledge funding from the Engineering and Physical Sciences Research Council.

Contents

CHAPTER 1

Introduction

In this thesis we report the results of computer simulations of various two-dimensional condensed matter systems. This may seem rather strange, given that we live in a three dimensional world, but there are in fact many experimental situations in which the system under study can reasonably be described as two dimensional. One example is a system of molecules adsorbed onto the surface of a solid. The molecules can be thought of as constituting a two dimensional fluid on the surface (although, note that a system of molecules grafted to a surface in fixed positions cannot be considered to be two dimensional in this way). Another example is what is known as a 'Langmuir-Blodgett' film. Amphiphilic molecules in water will arrange themselves at the surface with the hydrophilic head groups in the water and the hydrophobic tails pointing out of the water. Again the molecules are confined to a two dimensional plane. Soft condensed matter systems are often studied experimentally as thin films. This is necessary for example to perform light scattering in otherwise opaque materials. Direct imaging by microscope also requires a thin film or at least an exposed surface. Often the film thickness is comparable to the size of the particles which comprise the material and hence the particles are confined in the plane of the film.

Two-dimensional systems are very prominent in magnetism. There are many magnetic materials with strong magnetic exchange interactions within two dimensional layers, but very weak interactions between the layers.

Qualitatively different physics can emerge in lower dimensions. A well known example of this can be seen in the comparison of the phase behaviour of hard spheres in three dimensions with its two dimensional analogue, hard disks. In the hard sphere system, there is a first-order phase transition between fluid and solid with an associated fluid-solid phase coexistence when the system is at the transition pressure or chemical potential. In the two-dimensional hard disk system on the other hand, Kosterlitz, Thouless, Halperin, Nelson and Young [1–4] proposed that the first order phase transition is replaced by two continuous phase transitions - from the fluid to a 'hexatic' phase and then from the hexatic to solid phase. An order parameter is constructed which measures the extent of the sixfold bond ordering around a given particle as would be seen on a perfect triangular lattice. The solid phase has long-range bond orientational order, whereas in the fluid phase the bond orientational correlations die away exponentially with distance. In the intermediate hexatic phase the sixfold bond orientation correlations die off much more slowly, as a power-law. Another example of the different physics than can emerge in lower dimensions is provided by the Heisenberg model of magnetism. In three dimensions, a system of Heisenberg spins can show long range order below a critical temperature. In one or two dimensions, it was shown by Mermin and Wagner [5] that there can be no long range order at any finite temperature (but note that the Mermin-Wagner theorem only applies to short-range forces. In particular, it does not apply to the long-range dipole-dipole interaction).

Motivated by the wide variety of two-dimensional condensed matter systems, we have studied some model two-dimensional systems by computer simulation.

In Chapters 3 and 4 we study a system of soft spheres with central point dipoles confined to a plane. This model is of particular interest because of the tendency of the dipole moments on neighbouring particles to align 'nose-to-tail', causing the formation of chains. In chapter 3, we perform molecular dynamics simulations which shows the profound effect this chaining has on the particle dynamics. In Chapter 4, we study the aggregation kinetics as the system comes to equilibrium starting from a configuration generated by a soft sphere simulation with the dipole moments 'switched off'. Our results have impact on the possibility of observing the defect-mediated phase transition proposed by Tlusty and Safran [6] (see Section 1.1).

Chapter 5 reports simulations of the dynamics of antiferromagnetically coupled Heisenberg spins on the sites of a kagomé lattice. This system is highly frustrated - the lattice places competing constraints on the spins. Motivated by experimental observations, we investigate the effect of breaking a fraction of the bonds on the lattice which will relieve some of the frustration.

Finally, in chapter 6, we study the phase behaviour of a two dimensional system of hard disk trimers with an attractive interaction between one of the disks and corresponding disks on other trimers. This represents a crude model for protein molecules in a biological membrane, which can be thought of as a two-dimensional system. As explained in Section 1.3, the use of such simple coarse grained models has been successful in the past in the study of the phase behaviour of systems containing a large number of protein molecules.

In the remainder of this chapter, we give an introduction to the real physical systems we aim to simulate, and describe the models that are used to represent them.

1.1 Dipolar fluids

The closest physical realisation of the dipolar soft sphere model studied in Chapters 3 and 4 is the colloidal ferrofluid. A ferrofluid is a colloidal suspension of roughly spherical ferromagnetic particles (e.g. Fe, Co, magnetite (Fe_3O_4)) dispersed in a solvent. The particles are typically around 10nm in diameter and are usually coated with a layer of surfactant or polymer to stabilise them against irreversible agglomeration. The steric repulsion of the surfactant or polymer counteracts the short range attractive van der Waals interaction when the particles come into contact. The particles are small enough that they contain a single magnetic domain. Ferrofluids are therefore often modelled as consisting of spherical particles with a central point magnetic dipole moment. Reviews of experimental and simulation work on dipolar fluids can be found in Refs. [7–9].

Dipolar fluids are often described by the pair potential

$$U(r) = u_{sr}(r) + \frac{\boldsymbol{\mu}_1 \cdot \boldsymbol{\mu}_2}{r^3} - \frac{3(\boldsymbol{\mu}_1 \cdot \boldsymbol{r})(\boldsymbol{\mu}_2 \cdot \boldsymbol{r})}{r^5} . \tag{1.1}$$

$\boldsymbol{r}$ is the vector between particles 1 and 2 with dipole moments $\boldsymbol{\mu}_1$ and $\boldsymbol{\mu}_2$. The first term is a short-range potential, often a hard sphere or soft sphere, which prevents the particles interpenetrating. In the case that a Lennard-Jones form is used, the overall potential is called a Stockmayer potential. The dipole-dipole interaction is highly anisotropic. The minimum energy, $-2\mu^2/r^3$, comes when the dipole moments, $\boldsymbol{\mu}_1$ and $\boldsymbol{\mu}_2$, point in the same direction and along the inter-particle vector, i.e. they are aligned 'nose-to-tail'. There is a secondary minimum for 'side-by-side' dipoles pointing in opposite directions ($-\mu^2/r^3$).

The preference for nose-to-tail alignment causes the particles, at low density and temperature, to self-assemble into chains, as first pointed out by de Gennes and Pincus [10]. With an externally applied magnetic field, these chains line up with

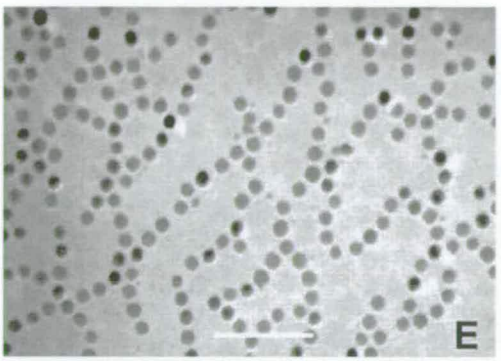

Figure 1.1: Monolayer of cobalt ferrofluid containing particles of 16 nm diameter, imaged by transmission electron microscopy [21].

the field direction, but the chains also exist in the absence of a field, oriented randomly. Such chains have been observed in numerous computer simulations [11–19].

Experimentally, it has proved harder to image the chains. The particles in the most common magnetite dispersions have rather low dipole moments (see for example Ref. [20], where no chaining was observed at all). The dipole moment needs to be large enough that the dipole-dipole interaction dominates over thermal fluctuations. Imaging is usually carried out in thin films, where the thickness of the film is comparable to the particle diameter. This is because ferrofluids tend to be very opaque. For this reason, light scattering studies must also be performed in thin films.

Chaining has been observed in cobalt [21] and iron [22–24] dispersions. These have a much larger dipole moment than magnetite. Puntes *et al.* [21] prepared cobalt ferrofluids and observed the self-assembled structures in a thin film using transmission electron microscopy (TEM). Fig. 1.1 shows a network of chains in a dispersion with particles of diameter 16 nm.

Butter and co-workers [22–24] have obtained images of thin films of iron ferrofluids using cryogenic transmission electron microscopy (cryo-TEM). In this tech-

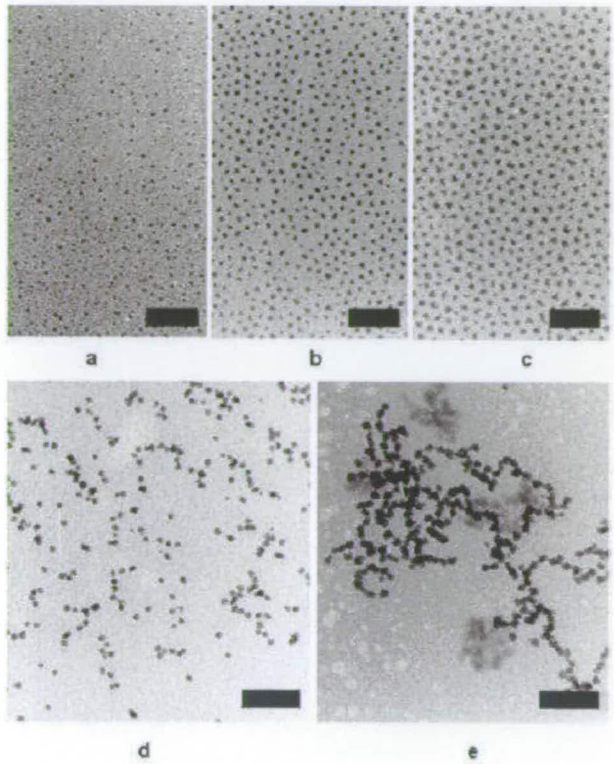

Figure 1.2: Cryogenic electron micrographs of iron ferrofluids with particles of various radii: (a)2.1 nm; (b) 6.0 nm; (c) 6.6 nm; (d) 6.9 nm; (e) 8.2 nm.

nique, the film in liquid form is rapidly frozen. The solvent molecules become trapped in a glassy state, rather than in their positions on a crystal lattice. Fig. 1.2 shows images obtained for dispersion of particles of increasing size. Since the dipole moment of a particle is proportional to its volume, the larger particles have stronger dipoles. For the weakest dipoles (smallest particles) in Fig. 1.2(A-C), the isotropic steric repulsion due to the polymer coatings is dominant, and no aggregation of the particles is seen. For the larger particles in Fig. 1.2(D), the dipole-dipole interaction is now strong enough relative to the thermal energy that chaining can occur, although there are still many free particles. With the largest particles (E), almost all the particles are included in a chain.

More recently, magnetite ferrofluids have been synthesised containing larger particles than was previously possible. The larger particles have larger dipole

moments, and chaining can be observed in these dispersions [25, 26].

Wen *et al.* [27] have studied the aggregation process in a system of magnetic microspheres. Glass spheres of size 47 μm were coated with a thin layer of nickel (2.5-4 μm). The particles were dispersed into a small volume of alcohol or oil. This system can also be described by the dipolar fluid model. Pictures taken using a charge-coupled device (CCD) camera showed that the particles formed chains and rings.

It should be noted that as well as chains, closed rings can also be formed. For a cluster containing more than three particles, this is in fact the ground state structure [28]. The rings can be seen in simulations of quasi-two-dimensional dipolar fluids, but are rarely seen in three dimensions. This is because of the larger entropy cost associated with connecting the two dangling ends of a chain in three dimensions.

The magnetic susceptibility spectrum for a ferrofluid has been measured experimentally by Butter *et al.* over a large frequency range (1-10^5 Hz) [23]. They prepared suspensions of magnetite (Fe_3O_4) in toluene with different particle diameters (and hence different dipole moments). For the particles with the smallest diameters (6.0 nm and 6.6 nm) there is a high frequency peak in the spectrum. The system is not aggregated here and the peak corresponds to the rotation of single dipoles. There are two mechanisms by which the dipoles may rotate: the dipole moments of the atoms within the particle may rotate (Néel relaxation), or the particles themselves may rotate (Brownian relaxation). For the 6.0 nm diameter particles, the maximum is at very much higher frequency than the equipment can measure, probably indicating Néel relaxation is dominant here. For the 6.6 nm particles, the maximum is at approximately 4000 Hz and is probably due to Brownian relaxation. In the usual models employed in simulations of dipolar fluids, the dipole moment of the particle is represented as a single point dipole, and

no account is taken of the individual atoms of which the particle consists. This model of particles with a single point dipole and a fixed value of the moment of inertia cannot make a distinction between the two relaxation mechanisms. The model particles have a single, fixed moment of inertia For the largest diameters (6.9 nm and 8.2 nm), where chaining does occur, there is a low frequency peak (respectively at approximately 150 Hz and at less than 1 Hz) associated with the rotation of entire chains.

In Chapter 3, we study the effect of chaining on the structure and dynamics of the quasi-two-dimensional dipolar fluid by molecular dynamics simulation. The structure has been extensively studied by computer simulation, but so far there has been very little work on the dynamics, at least in the strongly dipolar regime where chaining occurs. In our simulations, we see a separation of timescales between the motions of chains and rings and the motion of individual particles within those chains, similar to the separation of timescales observed by Butter as mentioned above.

In Chapter 4, we use Brownian dynamics simulations to examine the processes occurring as the particles aggregate into their chains and rings starting from a 'random' configuration. Our most significant observation is that there is a high transient concentration of 'Y' defects associated with the branching of two chains. This has relevance to the possibility of observing the defect-driven phase transition proposed by Tlusty and Safran [6]. The issue of phase transitions in dipolar fluids will be discussed more fully in Section 3.1.

1.2 Frustrated magnets

In Chapter 5, we investigate the dynamics of spins in a geometrically frustrated antiferromagnet. Before explaining the concept of frustration, we must intro-

duce the Heisenberg model which is a very widely used model for the so-called 'exchange interactions' between spins on a lattice.

It is possible for the energy to depend on the spin state despite the absence of spin-dependent terms in the Hamiltonian. To see why, let us consider first the hydrogen molecule which has two electrons. The possible spin states are given by

$$\chi_S = \frac{1}{\sqrt{2}}(|\uparrow\downarrow\rangle - |\downarrow\uparrow\rangle) \tag{1.2}$$

$$\chi_{T1} = |\uparrow\uparrow\rangle \tag{1.3}$$

$$\chi_{T2} = \frac{1}{\sqrt{2}}(|\uparrow\downarrow\rangle + |\downarrow\uparrow\rangle) \tag{1.4}$$

$$\chi_{T3} = |\downarrow\downarrow\rangle \tag{1.5}$$

The singlet state, χ_S is antisymmetric and has $S = 0$. The triplet states are symmetric and have $S = 1$. The overall wavefunction will be the product of the spatial and spin parts, and must be antisymmetric with respect to exchange of both spin and spatial variables. If the spin part is the singlet state, the spatial part must therefore be symmetric and if the spin part is in a triplet state, the spatial part must be antisymmetric. Whether the system is in the singlet or triplet state depends on which of the corresponding spatial states are lowest in energy. Ignoring any higher energy excited states, we can use an effective Hamiltonian,

$$\mathcal{H} = \frac{1}{4}(E_S + 3E_T) - (E_S - E_T)\boldsymbol{S}_1 \cdot \boldsymbol{S}_2 \,, \tag{1.6}$$

which has eigenvalues E_S for the singlet ($S = 0$) state and E_T for the triplet ($S = 1$) state. The first term can be removed by redefining the zero of energy, giving

$$\mathcal{H} = -J\boldsymbol{S}_1 \cdot \boldsymbol{S}_2 \,, \tag{1.7}$$

where J is the exchange constant, giving the splitting between the singlet and triplet states.

The Hamiltonian can be generalised to the case where there are more than two ions situated at sites on a lattice, giving the 'Heisenberg Hamiltonian',

$$\mathcal{H} = -J \sum_{[ij]} \boldsymbol{S}_i \cdot \boldsymbol{S}_j \,, \tag{1.8}$$

where $\boldsymbol{S}_i$ and $\boldsymbol{S}_j$ are the spin angular momenta on sites i and j. Usually only interactions between spins on neighbouring sites are considered. The spins are also often approximated as classical vectors which may point in any direction. For materials in which $J = E_S - E_T > 0$, the triplet energy is lower than the singlet energy, and the energy is minimised when spins on neighbouring sites are parallel. These are called ferromagnets. In 'antiferromagnets' on the other hand, $J < 0$, and energy is minimised when neighbouring spins are antiparallel.

The phenomenon of frustration arises in antiferromagnets when competing constraints are placed upon the spins. For example, consider the triangular plaquette in Fig. 1.3(a). The first two spins can be oriented antiparallel, as expected from the exchange interaction. The third spin, however, cannot be antiparallel to both. The system is said to be 'frustrated'. A compromise can be found by orienting the spins at 120° to one another (Fig. 1.3(b)). Any lattice built up from these triangular plaquettes will exhibit frustration. Examples are the triangular lattice, formed by edge-sharing triangles, or the kagomé lattice (Fig. 1.4), formed by corner-sharing triangles. The frustration prevents the system from finding a unique ground state. The ground state will be highly degenerate. This confers many unusual properties on these materials.

The frustration described above is known as 'geometric frustration'. For reviews, see Refs. [29–31]. In general, geometrically frustrated magnets exhibit a phase

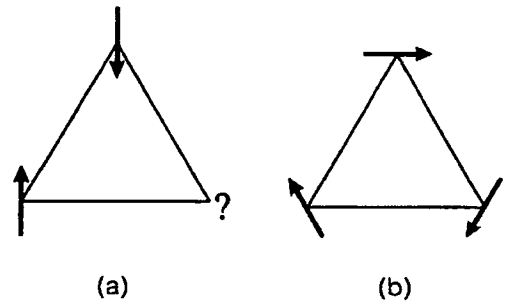

Figure 1.3: (a) Frustrated triangular plaquette (b) compromise 120° configuration.

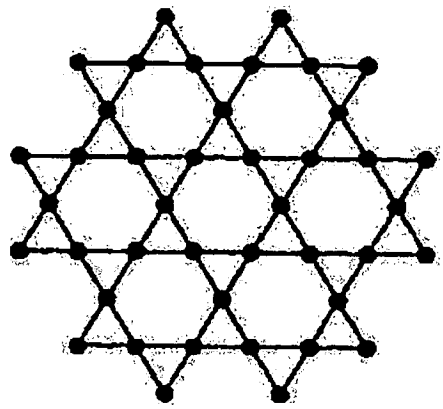

Figure 1.4: Kagomé lattice

transition at a particular temperature, which can be identified for example by a cusp in the susceptibility or heat capacity. Below this temperature, the behaviour varies from material to material. Sometimes a long range ordered state may be established. Another possibility is a 'spin glass' in which the spins become frozen in a random state. In a 'spin liquid', in contrast to the spin glass, some spins remain dynamic down to $T = 0$. The 'spin ice' is a special case of the spin liquid, which applies to Ising spins on the pyrochlore lattice.

Frustration can also occur as a result of disorder in materials known as 'spin glasses' [32]. An example is an alloy of copper with a low concentration of manganese. The magnetic manganese is distributed randomly throughout the non-magnetic copper host. The type of exchange interaction in this materials is

strongly dependent on distance and may fluctuate between ferromagnetic and antiferromagnetic as a function of distance. Again, this places competing constraints on the spins, giving rise to frustration. Below a transition temperature, T_f the spins freeze into a random configuration, corresponding to a local minimum in the free energy. In this glassy state, there are many nearly equivalent minima separated by high barriers.

Below T_f, there will be no long range order. This will show up as a lack of magnetic Bragg peaks in the neutron diffraction pattern below T_f. Other signatures of the spin glass phase include a frequency dependence in the ac susceptibility, measured in an oscillating magnetic field. The static susceptibility can be measured by first cooling the sample with an applied magnetic field or with zero applied field. The susceptibility is then measured for increasing temperature. In spin glasses below T_f, different values are measured in the field-cooled and zero field-cooled cases. The heat capacity at low temperatures often shows a T^1 dependence. Measured using some experimental method which can probe the spin dynamics, such as inelastic neutron scattering or muon spin relaxation, the relaxation time shows a sharp increase below T_f.

In general magnetic materials, in the paramagnetic regime at high temperature, the susceptibility, χ, follows a Curie-Weiss law

$$\chi = \frac{C}{T - \theta} \tag{1.9}$$

where C and θ are constants. This follows from mean field theory. In ferromagnets, $\theta \simeq T_C$, the critical temperature for the transition between ferromagnetic and paramagnetic states. In antiferromagnets, θ is negative and $|\theta| \simeq T_N$, where T_N is the Neél temperature, the critical temperature for the transition between antiferromagnetic and paramagnetic states. In frustrated antiferromagnets, however, the 'ordering' temperature is usually found to be much lower than the

Curie-Weiss constant. $1/\chi$ should be linear with respect to temperature. Since the mean field theory from which the Curie-Weiss law is derived neglects correlations between spins, deviations from linearity occur as the correlation length rises with decreasing temperature towards the critical temperature. Deviations can set in at temperatures much greater than the critical temperature. In frustrated magnets, the correlation length does not increase at such high temperatures, and the inverse susceptibility remains linear to much lower temperature, even well below the Curie-Weiss temperature.

Schiffer and Daruka [33] examined the susceptibility of a selection of different frustrated magnets. They proposed a model in which there are two different populations of spins. There are clusters of antiferromagnetically correlated spins and also a population of 'orphan spins', not included in clusters, which are only weakly correlated with their neighbours. They proposed a fit to the susceptibility data using two Curie-Weiss laws. They fit the experimental inverse susceptibility using the function

$$\chi^{-1}(T) = \left[\frac{C_1}{T+\theta_1} + \frac{C_2}{T+\theta_2}\right]^{-1} . \tag{1.10}$$

This was found to describe well the experimental susceptibility for all the materials considered.

One family of materials which are often given as a physical realisation of the kagomé Heisenberg antiferromagnet are the jarosites. These have the general formula $AFe_3(SO_4)_2(OH)_6$, where A^+ is a univalent cation e.g. Na^+, K^+, Rb^+, Ag^+, NH_4^+ or H_3O^+. Cr^{3+} can be substituted for the Fe^{3+}. Figure 1.5 shows the crystal structure of potassium jarosite. Fig. 1.6 shows a layer of FeO_6 octahedra within the structure. This shows that the Fe^{3+} ions sit on the sites of a kagomé lattice. Neighbouring Fe^{3+} ions interact via an antiferromagnetic exchange interaction. Between layers, the exchange pathway is long so interlayer interactions

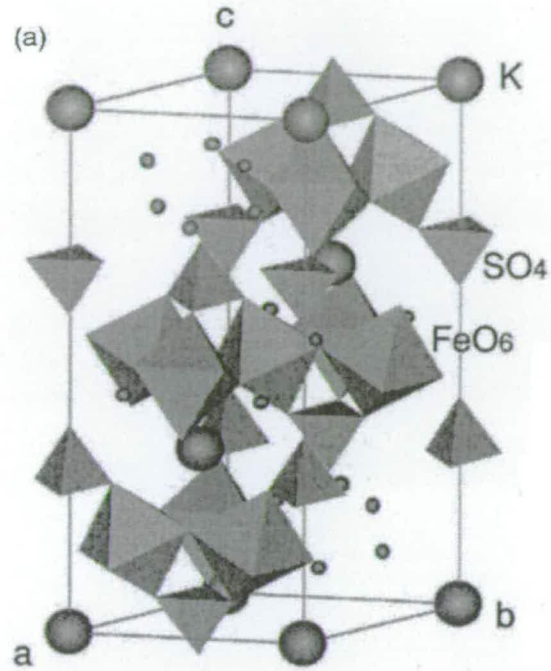

Figure 1.5: Crystal structure of $KFe_3(SO_4)_2(OH)_6$.

are weak. Thus this system can be describe by a two dimensional system consisting of spins located on the sites of a kagomé lattice. The Fe^{3+} ions have a high value of spin angular momentum, $S = 5/2$. It is therefore reasonable to describe the system using a Heisenberg model in which the spins are represented as classical vectors which can point in any direction (formally corresponding to $S = \infty$). Another material which was said to contain a kagomé lattice is $SrGa_{12-x}Cr_xO_2$ (SCGO). However, this does not correspond exactly with the model studied by theorists because it contains an extra triangular layer between the kagomé layers.

The magnetic properties of the jarosites have been extensively studied experimentally because of the high degree of frustration which leads to unusual behaviour. All the jarosites show a transition at temperature T_C of the order of 50K to a state with long range order. The transition can be identified as a cusp in the susceptibility as a function of temperature. The magnetic structure adopted by the spins in the ordered phase can be determined by neutron diffraction. Below

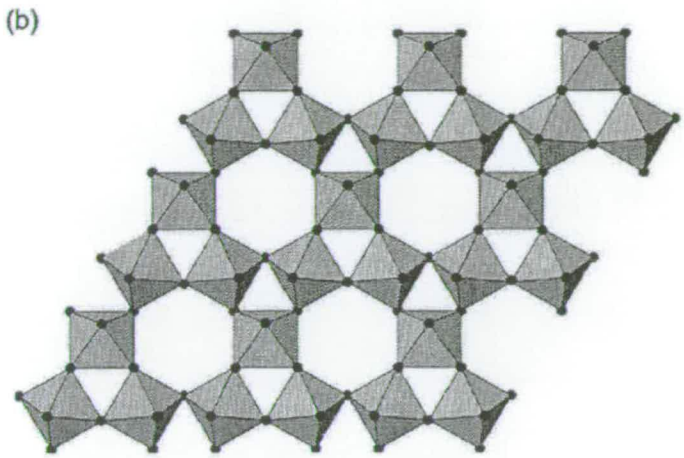

Figure 1.6: Layer of FeO_6 octahedra.

the transition temperature, Bragg peaks occur due to both scattering for the nuclei and to magnetic scattering. Above T_C the system is no longer exhibits long range order. By comparing the diffraction peaks above and below T_C, the magnetic Bragg peaks can be identified. The diffraction studies reveal that the structure of the spins in the long range ordered state is of the $\boldsymbol{q} = 0$ form (Fig. 1.7(a)) in which the spins have adopted their compromise 120° orientations. This is rather surprising given that many theoretical and simulation studies conclude that another compromise structure, the $\sqrt{3} \times \sqrt{3}$ (Fig. 1.7(b)) is more stable than the $\boldsymbol{q} = 0$ structure.

The hydronium ($A^+ = H_3O^+$) or deuteronium ($A^+ = D_3O^+$) appears to be an exception [34–38]. Magnetic susceptibility measurements show a transition at a temperature $T_f \simeq 15$K. Below this temperature, the system enters a spin-glass like state. Neutron diffraction confirms the absence of long range order. The evidence that this is a spin-glass state is as follows. Below T_f, there is a divergence between the field-cooled and the zero-field-cooled dc susceptibility. Measurements of the ac susceptibility showed a decrease in T_f as frequency is increased. This behaviour is typical of a spin glass. The behaviour of the heat capacity is

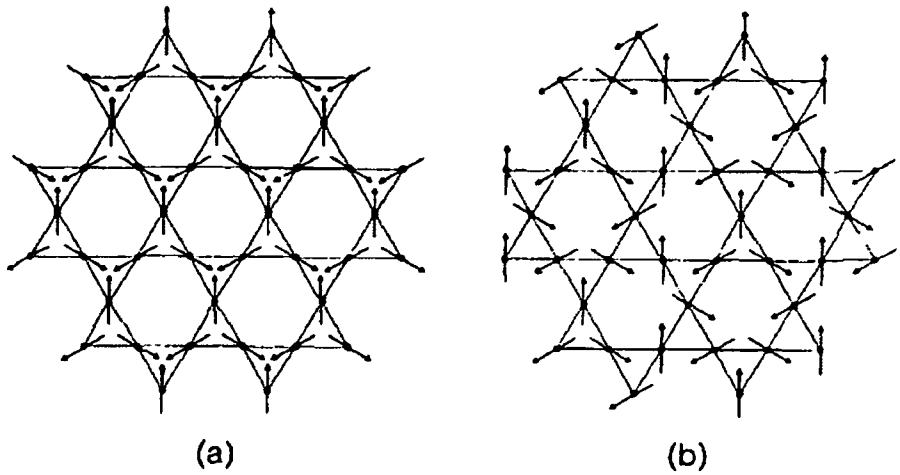

Figure 1.7: Compromise 120° ground state configurations of the kagomé antiferromagnet: (a) $\boldsymbol{q} = 0$ (b) $\sqrt{3} \times \sqrt{3}$.

less conventional. In a conventional spin glass, the heat capacity has a T^1 dependence on temperature as $T \to 0$. In hydronium jarosite, the heat capacity goes as T^2. This is more typical of a conventional two-dimensional long range ordered state. The same behaviour was also found in SCGO.

The fact that the hydronium jarosite freezes into a spin-glass state whereas all the other jarosites show long range order is a little puzzling. There are no obvious structural differences between the two cases. The only difference is in the coverage of the magnetic lattice. The jarosites are rather difficult to prepare in pure form. Fe^{3+} ions can be lost from the structure, leaving vacancies. The coverage of the magnetic lattice is typically around 89%. The coverage is usually higher (~97%) for hydronium jarosite. Wills *et al.* [35, 36] suggested that this might account for the difference in behaviour. In order to test this hypothesis, they prepared hydronium jarosite doped with non-magnetic aluminium in which the coverage of the magnetic lattice is 89%. In this material, spin glass behaviour disappeared and was replaced by a transition to a long range ordered state at 25.5K,

similar to the other jarosites. No divergence was observed between field-cooled and zero-field cooled dc susceptibility.

The simple model of isotropic Heisenberg spins on a kagomé lattice may not apply exactly to the jarosites. It was shown by Mermin and Wagner [5] that the Heisenberg model on a one or two dimensional lattice cannot show long range order at any non-zero temperature (although it does not rule out the possibility of long range order at $T = 0$). Examples of perturbations from the standard Heisenberg model include anisotropies, interactions ranging beyond nearest neighbours, interlayer interactions, or the site dilution mentioned above. In chapter 5, we investigate the possibility of bond dilution. This is motivated by the suggestion that in hydronium jarosite, a proton may migrate from the interlayer hydronium ion onto one of the OH^- ions that bridge between neighbouring Fe^{3+} ions [30]. This will weaken the exchange interaction between the Fe^{3+} ions. We consider the extreme case that the exchange is zero; the bond is effectively 'broken'.

1.3 Coarse grained models of biological membrane proteins

In Chapter 6, we explore the phase diagram for a two dimensional system of triangular molecules. This could serve as a very crude model for proteins in a biological membrane. It may seem too simplistic a model, but as we shall see this kind of coarse grained model has been successful in the past in the study of the phase behaviour of proteins. Some of motivation for this study is discussed below.

Integral membrane proteins are proteins which are found in the phospholipid bilayers which constitute a biological membrane. These proteins perform a variety of functions. They can serve as selective channels allowing molecules of

a specific species to pass in or out of a cell. In order to understand how proteins perform their function, it is necessary to have a detailed knowledge of their structure, not only which atom is connected to which but also how the protein is folded up. The usual way to do this is to produce three dimensional crystals of the protein which can then be analysed using X-ray crystallography. More recently, an alternative approach has been developed [39]. Membrane proteins can be reconstituted into a two dimensional crystal along with lipids. The resultant structure can then be imaged directly using electron microscopy or atomic force microscopy.

There are many proteins which are roughly triangular in shape, or which form trimeric units of three protein molecules (see for example Refs. [40–49]). We highlight some examples of the vast numbers of studies into the aggregation of such proteins. The outer capsid shell of the rotavirus consists of a protein called VP6. The protein molecules form into trimers which then form the basic units for the further aggregation of these proteins [40]. Fig. 1.8 shows a projection density map of a two dimensional crystal of VP6 as determined by cryo-electron microscopy. The trimers pack together in a manner determined by their roughly triangular shape, forming a crystal with two trimers per unit cell and $p6$ symmetry. The prion protein PrP 27-30 also forms trimeric units [45]. In the two dimensional crystal, the trimers pack together onto a triangular lattice (space group $p3$) (Fig. 1.9). In Ref.[43], two dimensional crystals of AmtB, a protein involved in transport of ammonium across cell membranes, have been imaged using atomic force microscopy (Fig. 1.10). The molecular envelope of the protein molecules can be seen, which clearly shows the association of the proteins into trimers. Again, the trimers pack together to form the crystal structure.

Coarse grained models like the one we use in Chapter 6 have in the past been successful in the study of the self-assembly of membrane proteins. Here, we

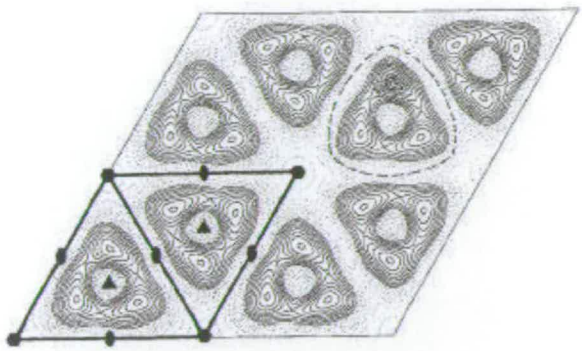

Figure 1.8: Projection density map of a two dimensional crystal of VP6, obtained by electron microscopy [40].

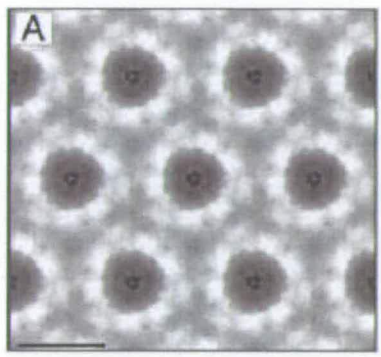

Figure 1.9: Projection map of prion protein PrP 27-30 obtained by electron microscopy [45].

present two examples of this kind of study. In Section 6.1 we will give a more detailed justification of the use of coarse grained models. The first example is the membrane protein bacteriorhodopsin found in certain bacteria. It is known that these proteins self-assemble into a structure known as the 'purple membrane'. The proteins are shaped like 120° sectors of a circle. In the purple membrane the molecules associate into trimeric units, completing the circle. Jagannathan *et al.* [50] performed Monte Carlo simulations in which the protein molecules were modelled as hard circle sectors. With the addition of an attractive interaction between the straight edges of the sectors to mimic specific interactions between parts of the molecules, the particles spontaneously form into trimers. At high density, these trimers then form a crystalline phase with the trimer units forming

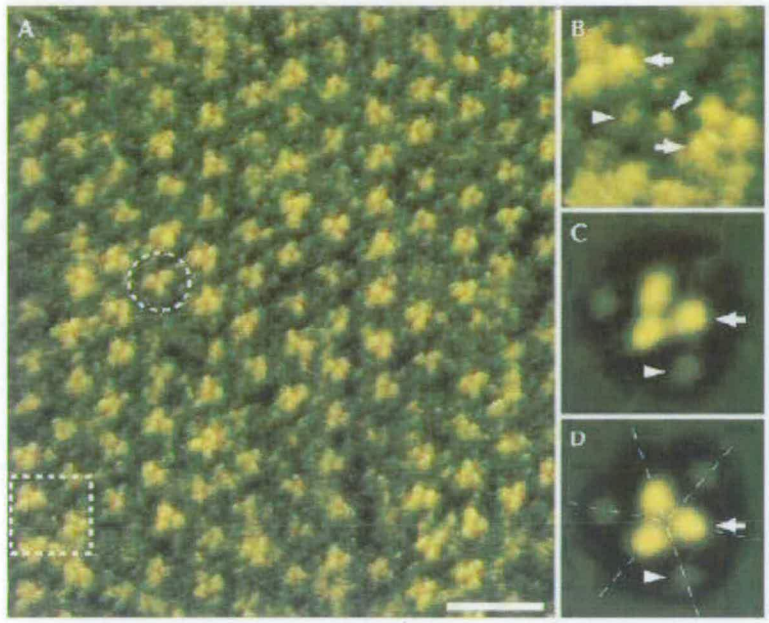

Figure 1.10: Atomic force microscope image of a two dimensional crystal of AmtB [43].

a triangular lattice. The trimer units display no orientational order, in contrast to the real system. It was found that if there is an additional specific interaction between the curved parts of the molecules, this could cause the system to adopt a structure with orientational order. The main features of the bacteriorhodopsin molecule responsible for the formation of the purple membrane structure have thus been identified.

Bates *et al.* [51, 52] carried out a similar study to investigate the phase behaviour of the membrane protein annexin V. These proteins form tightly bound trimers which then become the basic units for the further collective self-assembly. Electron microscopy and atomic force microscopy show there are two possible structures. In one of these, of $p6$ symmetry, there is an rigid honeycomb structure. In a certain proportion of the holes in the structure there is a more loosely bound trimer (Fig. 1.11(a)). The other possible structure is a triangular structure of $p3$ symmetry (Fig. 1.11(b)). The $p6$ structure is more stable at low density. Bates *et al.*

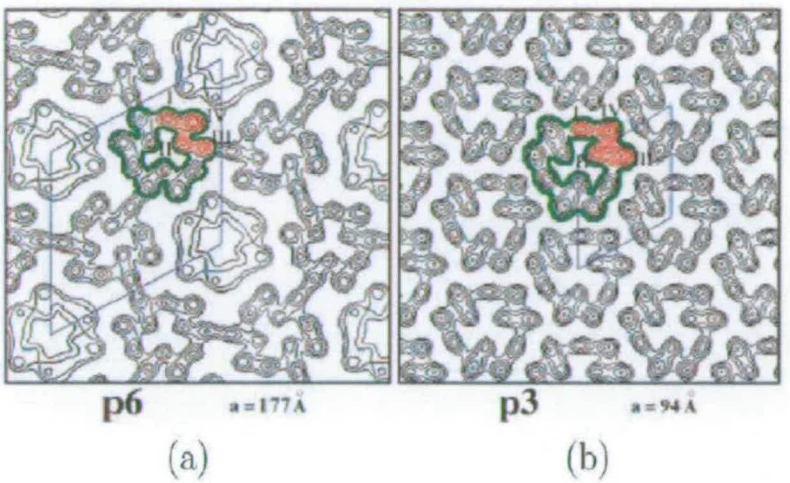

Figure 1.11: Projection maps of annexin V in the $p6$ (a) and $p3$ (b) phases, obtained by electron microscopy [51].

carefully constructed a model to capture the essential features of the annexin V trimers. The trimers were modelled as hard spheres with angle-dependent interactions at specific sites representing specific interactions in the real trimers. Their Monte Carlo simulations showed at low density the honeycomb structure of the $p6$ phase (Fig. 1.12(a)). As density is increased, more loosely bound trimers start to fill up the holes in the honeycomb (Fig. 1.12(b)), exactly as seen in experiment. As density is increased further, eventually all the holes are filled up (Fig. 1.12(c)). The only way to pack the trimers any closer is now to adopt a new structure. The system undergoes a first order phase transition into the p3 phase, which has more efficient packing (Fig. 1.12(d)).

Observing the success of these simulations of very simple models in elucidating the bulk properties of proteins and considering the many membrane proteins which form trimeric units led us to investigate the hard disk trimer system discussed in chapter 6. The hexagonal close packing of the disks observed in our system is not dissimilar to the kinds of structures observed in two dimensional crystals of membrane proteins. As mentioned above, with these kind of models

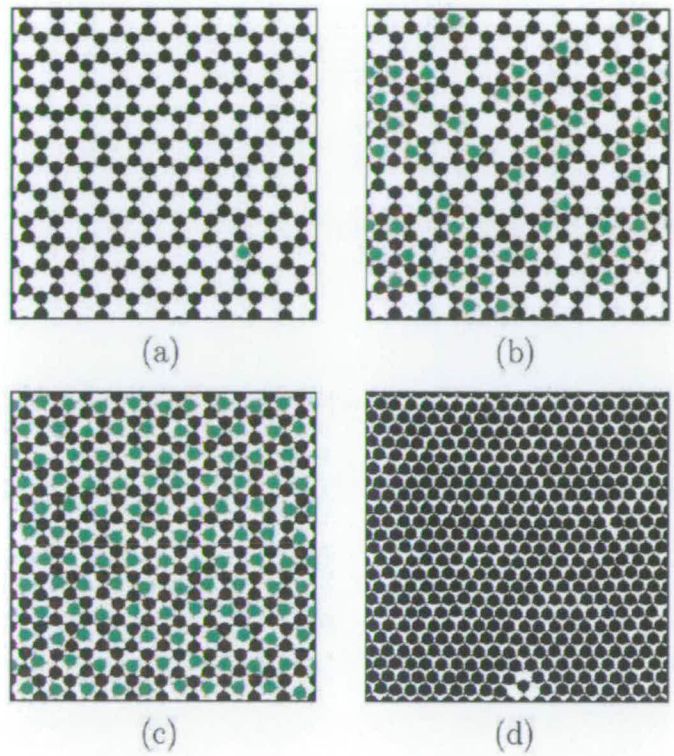

Figure 1.12: Configurations from Monte Carlo simulations of a model of annexin V. (a)-(c) $p6$ phase at increasing density (d) $p3$ phase [51].

we cannot hope to study the detailed mechanisms by which these proteins operate but we are more interested in the bulk phase behaviour. In any case, the function of many proteins is dependent on the formation of some kind of pattern.

1.4 Summary

In this introductory chapter, we have presented a range of different two-dimensional experimental systems. These are the real systems that we hope to gain some insight into by the simulations reported in Chapters 3-6. Each of these studies has required different set of computational techniques to be used. In Chapter 2, we briefly introduce these techniques, and also some general aspects of computer simulation.

CHAPTER 2

Computer simulation

Traditionally, there have been two ways in which condensed matter research has been carried out - by experiment and by theory. The aim of theory is to try to provide some explanation of experimental results. In order to proceed, we need to construct some model of the system under study. Very few cases are exactly solvable analytically. To make progress, many approximations have to be made. The ultimate test of a theory is to compare its predictions with experimental results. However, if there is a discrepancy, it may mean the theory is wrong, or it may mean that the model is not an adequate description of the real system.

With the advent of computers, an alternative mode of research has become possible. Computer simulation plays a role intermediate between theory and experiment. Computer simulations provide essentially 'exact' results for the particular model used, against which theories can be tested. On the other hand, simulations can act as 'computer experiments' which can stimulate further theory. Simulations can also be compared directly with experiment, and can aid in interpreting the experimental results. In this regard, computer simulation is a useful tool because of the link it makes between the microscopic and macroscopic levels of description.

We have performed simulations of the two-dimensional systems introduced in Chapter 1. In this chapter, we introduce the basic simulation techniques used in these studies, and then describe some of the quantities which are measured during the simulations to obtain information about the system. Full coverage of the methods of computer simulation can be found in the textbooks by Allen and Tildesley [53] and Frenkel and Smit [54].

2.1 Fluid systems

2.1.1 General aspects of computer simulation

Interaction potentials

We describe our model of the system of interest by a function which gives the potential energy for a given configuration of the particles in the system. Usually, the assumption is made that the potential is pairwise additive. That is, we calculate the potential energy for each pair of particles, which is expressed as a function of their relative positions (and possibly orientations) and we assume that the total potential is just the sum of these interactions for all pairs of particles.

Perhaps the simplest model of an atom is to regard it as an impenetrable hard sphere. This may be represented by the potential

$$U(r) = \begin{cases} \infty & r \leq \sigma \\ 0 & r > \sigma \end{cases} , \tag{2.1}$$

where r is the distance between the particles and σ is the particle diameter. The hard core interaction which prevents the particles from overlapping provides a good representation of the Pauli repulsion which operates at short distances and

has its origin in the exclusion principle. Another widely used pair potential is the Lennard-Jones potential,

$$U(r) = 4\epsilon \left[\left(\frac{\sigma}{r}\right)^{12} - \left(\frac{\sigma}{r}\right)^{6} \right] , \tag{2.2}$$

where r is the distance between the particles, σ is a distance parameter and ϵ is a parameter giving the depth of the minimum in the potential. At large distances, this has the asymptotic $1/r^6$ dependence of the van der Waals interaction, and the $1/r^{12}$ term approximately describes the hard core repulsion when the particles come close together. This potential provides a good description for argon.

For short range potentials, we can truncate the potential at a certain distance beyond which the interactions are negligible. This means that any two particles further apart than this distance do not need to be considered when calculating the total potential energy, speeding up the simulation. The discontinuity in the potential can cause problems, however. A discontinuous potential means an infinite force (since $\boldsymbol{F} = -\boldsymbol{\nabla} U$), which can lead to numerical instabilities. One way to avoid this is to multiply the potential in the vicinity of the cut-off by a function which brings it smoothly to zero.

Periodic boundary conditions

In a simulation of a finite number of particles, a significant fraction of the particles will be at the edges of the system. The environment of these particles will be very different to the environment of a particle within a bulk system. In order to reduce this problem, periodic boundary conditions are normally employed. We make copies of the system in all directions (Fig. 2.1). When a particle leaves the central simulation cell at one side, its periodic image enters from the other side, thus conserving the number of particles in the central simulation cell.

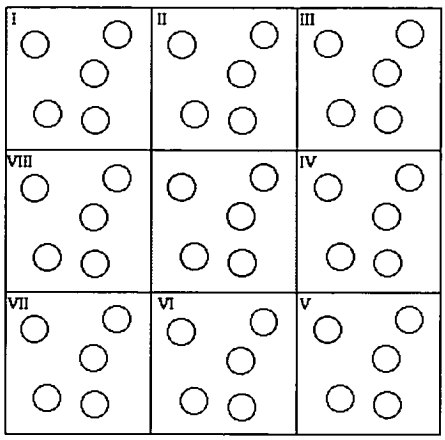

Figure 2.1: Periodic boundary conditions

Technically, every particle interacts with every particle in all cells, but often the minimum image convention is used. When calculating the force on a particle, the only interaction that is considered is that due to only the nearest of the periodic images of a particular particle.

Reduced units

When carrying out a computer simulation it is convenient to define a set of reduced units in terms of the potential parameters of the system under study [53]. For example, for a Lennard-Jones fluid, with the pair potential given by Eq. 2.2, distances can be expressed in terms of the parameter σ, and energies can be expressed in terms of ϵ. We also use the mass of the particles in the system as a fundamental unit (i.e. m=1). From these fundamental definitions, we can obtain other quantities in reduced units. Some reduced units for the Lennard-Jones potential are listed below.

Distance	$r^* = r/\sigma$
Density	$\rho^* = \rho\sigma^3$
Energy	$E^* = E/\epsilon$
Temperature	$T^* = k_B T/\epsilon$
Pressure	$P^* = P\sigma^3/\epsilon$
Time	$t^* = (\epsilon/m\sigma^2)^{1/2}t$

The most important reason for using reduced units is that there are many different states in real units that correspond to the same state in reduced units. The use of reduced units means we do not have to repeat the simulation for each of these states. Another advantage is that values in reduced units will be of order unity, hence we avoid the potential problems of using the very small numbers of atomic systems on a computer. The use of reduced units also simplifies the potential, allowing us to set the parameters of the potential to one. We do not need to choose specific values of these parameters.

2.1.2 *Techniques*

Monte Carlo

We wish to obtain ensemble averages, i.e. average of some quantity A over all the states of the system weighted by the Boltzmann probability of each state,

$$\langle A \rangle = \frac{1}{Z} \sum_i A_i \exp(-\beta E_i) \,, \tag{2.3}$$

where $\beta = 1/k_B T$ and $Z = \sum_i \exp(-\beta E_i)$ is the partition function. The sum is over all accessible states, A_i is the value of A in that state and E_i is the energy of state i. One way to obtain this average might be to sample all possible states and use the values of A_i and E_i for each state. However, in general there will be a vast number of possible states. It is not feasible to attempt to sample all of these states.

Moreover, a great many of these states will have a small Boltzmann weight and so contribute very little to the ensemble average. What we need is some way to sample those states which make the largest contribution to the ensemble average. This is provided by the importance sampling Monte Carlo technique.

The algorithm in the canonical ensemble is as follows:

1. Prepare the system in some initial configuration.
2. Choose a particle at random and give it a random displacement within some prescribed interval.
3. If the trial move results in a decrease in energy, it is accepted unconditionally. If the trial move results in an increase in energy it is accepted with a probability $e^{-\beta\Delta E}$, where ΔE is the difference in energy between the trial configuration and the previous configuration. To implement this in a program, a uniformly distributed random number is generated in the interval 0.0 to 1.0. If it is less than $e^{-\beta\Delta E}$, the move is accepted, otherwise the move is rejected.
4. The process is then repeated with the next randomly selected particle.

Using this scheme, states are sampled with a probability proportional to their Boltzmann weight. The ensemble average can then be calculated as a simple unweighted average over the states visited. The method can be adapted to spin systems by making moves involving flips or small rotations of the spins.

In order to perform Monte Carlo simulations in the isobaric-isothermal ensemble (constant NPT), we introduce trial moves which increase or decrease the volume of the system. We make a change in volume from V' to $V = V' + \Delta V$, where ΔV is a random number between $-\Delta V_{max}$ and $+\Delta V_{max}$. This move is accepted with

a probability

$$\min\left\{1, \exp\left(-\frac{1}{k_B T}\left[U(V') - U(V) + p(V' - V) - k_B T N \ln(V'/V)\right]\right)\right\} . \quad (2.4)$$

In this ensemble the enthalpy is important rather than energy.

Molecular Dynamics

An alternative method of obtaining ensemble averages is molecular dynamics. We follow the actual dynamics of the system by integrating the classical equations of motion in order to follow the particle trajectories in time. The equations of motion will be a set of coupled differential equations which in general can only be solved using numerical methods. This is usually done using finite difference methods. Given knowledge of the particle positions and momenta at some time t, we obtain the positions and momenta a short time later, $t + \Delta t$. A well-known example is the Verlet algorithm:

$$\boldsymbol{r}(t + \Delta t) = 2\boldsymbol{r}(t) - \boldsymbol{r}(t - \Delta t) + \boldsymbol{a}(t)\Delta t^2 \quad (2.5)$$

The velocities are not needed in the calculation of the trajectory, but they can be estimated by

$$\boldsymbol{v}(t) = \frac{\boldsymbol{r}(t + \Delta t) - \boldsymbol{r}(t - \Delta t)}{2\Delta t} . \quad (2.6)$$

We proceed as follows: we have the positions and momenta of the particles in the system at time t. The force on each particle due to all the others is then calculated via the pair potential, from which we get the accelerations from Newton's Second Law, $\boldsymbol{F} = m\boldsymbol{a}$. The positions and momenta can then be updated to time $t + \Delta t$ using Eqs. (2.5) and (2.6).

The velocities are not handled very satisfactorily by the Verlet algorithm. The errors in the positions are of order Δt^4, whereas the errors in the velocities using

Eq. (2.6) are of order Δt^2. An alternative algorithm, the 'velocity Verlet', has update equations for both the positions and velocities:

$$\boldsymbol{r}(t+\Delta t) = \boldsymbol{r}(t) + \boldsymbol{v}(t)\Delta t + \frac{1}{2}\boldsymbol{a}(t)\Delta t^2 \tag{2.7}$$

$$\boldsymbol{v}(t+\Delta t) = \boldsymbol{v}(t) + \frac{1}{2}\Delta t\left[\boldsymbol{a}(t) + \boldsymbol{a}(t+\Delta t)\right] . \tag{2.8}$$

The algorithm is implemented as follows. The positions are updated according to Eq. (2.7). The velocities are then updated to half-timestep:

$$\boldsymbol{v}(t+\frac{1}{2}\Delta t) = \boldsymbol{v}(t) + \frac{1}{2}\boldsymbol{a}(t)\Delta t . \tag{2.9}$$

The forces and accelerations at time $t + \Delta t$ are then calculated using the newly calculated positions $\boldsymbol{r}(t + \Delta t)$. Finally, the update of the velocities can be completed:

$$\boldsymbol{v}(t+\Delta t) = \boldsymbol{v}(t+\frac{1}{2}\Delta t) + \frac{1}{2}\Delta t\boldsymbol{a}(t+\Delta t) . \tag{2.10}$$

Since energy is conserved by the Newtonian equations of motion, the molecular dynamics method simulates a microcanonical (constant NVE) ensemble. Note also that the total momentum is conserved. The conservation of energy and momentum serves as a useful test of the program.

Various methods exist to perform molecular dynamics in a constant temperature ensemble. The most extreme is to rescale the velocities of all particles at each time step to ensure they correspond with the equipartition theorem. A system at constant temperature is considered to be coupled to a heat bath. In the Anderson thermostat, every so often a particle is chosen at random and its velocity is reassigned from the Maxwell-Boltzmann distribution. This corresponds to the collision of the molecule with an imaginary heat bath particle. The Nosé-Hoover method is an 'extended Lagrangian' method in which an additional degree of

freedom representing the heat bath is added to the equations of motion. An alternative is to use the Brownian Dynamics technique described in the next section.

Brownian Dynamics

If we wish to simulate a colloidal suspension, in which there are relatively large particles surrounded by very many much smaller solvent particles, there is a separation of timescales. The motion of the solvent molecules will be on a very much shorter timescale than the motion of the colloidal particles. If we explicitly try to simulate the solvent molecules, we will need a short timestep to deal with the solvent motion but long runs will be needed to be able to observe the motion of the colloidal particles. We are not usually interested in the dynamics of the solvent molecules themselves. In Brownian dynamics, we replace an explicit description of the solvent with a random force, representing the forces from the solvent molecules which give rise to Brownian motion, and a drag force.

Brownian dynamics is based on the Langevin equation rather than the Newtonian equations of motion. This can be integrated using a finite difference algorithm in the same way as in molecular dynamics. The Langevin equation is

$$m_i \ddot{\boldsymbol{r}}_i(t) = -\gamma \dot{\boldsymbol{r}}(t) + \boldsymbol{F}_i(t) + \boldsymbol{f}(t), \tag{2.11}$$

where $r_i(t)$ is the position of particle i at time t. The first term on the right hand side represents the friction force, which is proportional to velocity with friction coefficient γ. $\boldsymbol{F}_i(t)$ is the usual conservative force derived from the pair potential, exerted on the particle by the surrounding particles, and $\boldsymbol{f}(t)$ is the random force. It is assumed that the random force averages to zero,

$$\langle \boldsymbol{f}(t) \rangle = 0\,, \tag{2.12}$$

and has a Gaussian distribution with variance given by

$$\langle f_{i\alpha}(t) f_{i\alpha}(0) \rangle = 2mk_B T\gamma\delta(t) \,, \tag{2.13}$$

where $f_{i\alpha}(t)$ is the x, y or z component of the force on particle i. The random force is related to the friction coefficient, since the drag force on a particle is also due to random collisions it experiences as it moves through the fluid.

2.1.3 Measurable quantities

In order to probe what is happening in a simulation, we make 'measurements' of certain quantities. What we can observe are functions of the configuration of the system at a particular step in the simulation. We are usually interested in ensemble averages of the measured quantity rather than the instantaneous values. As mentioned before, in Monte Carlo this is a simple average over all the states visited and in molecular dynamics, this would be an average over different time origins. Throughout this thesis, the ensemble average of a quantity is signified by placing the quantity in triangular brackets.

Structure

The structure of a fluid is often characterised by a quantity called the radial distribution function. We first introduce the n-particle reduced distribution, $\rho_n(\boldsymbol{r}_1, \ldots, \boldsymbol{r}_n)$, which is the probability density for finding any set of n particles at the given positions. For an ideal gas,

$$\rho_2(\boldsymbol{r}_1, \boldsymbol{r}_2) = \rho^2(1 - N^{-1}) \simeq \rho^2 \,, \tag{2.14}$$

where N is the number of particles. The last equality assumes that the quantity N^{-1} is negligible for systems with large N. We can thus quantify the deviation

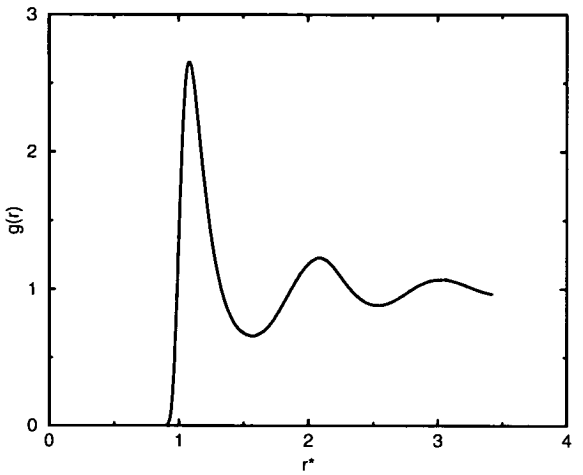

Figure 2.2: Radial distribution function for a Lennard-Jones fluid at density $\rho^* = 0.8$ and temperature $T^* = 1$.

of the structure from the random ideal gas structure using the function

$$g(\boldsymbol{r}_1, \boldsymbol{r}_2) = \frac{\rho_2(\boldsymbol{r}_1, \boldsymbol{r}_2)}{\rho^2} \,. \tag{2.15}$$

In an isotropic fluid, this is a function only of the separation of the two particles, $r = |\boldsymbol{r}_2 - \boldsymbol{r}_1|$. In this case, $g(r)$ is called the 'radial distribution function'. The radial distribution function measures the probability of finding a pair of particles a distance r apart, relative to the probability in a random (ideal gas) structure. A typical $g(r)$ for a liquid is shown in Fig. 2.2. The co-ordination shells around a given particle give rise to the peaks. $g(r)$ eventually decays to 1 as $r \to \infty$ as correlations between particle positions die away. The liquid has short range order.

We next introduce the static structure factor [55] which can also be measured in X-ray or neutron scattering experiments, so it provides a link between experiment and simulation. First we define the 'local particle density',

$$\rho(\boldsymbol{r}) = \sum_{i=1}^{N} \delta(\boldsymbol{r} - \boldsymbol{r}_i) \,, \tag{2.16}$$

where $\boldsymbol{r}_i$ is the position of particle i. Its spatial Fourier components are

$$\rho_{\boldsymbol{q}} = \int \exp(-i\boldsymbol{q}\cdot\boldsymbol{r})\rho(\boldsymbol{r})d\boldsymbol{r} \tag{2.17}$$

$$= \sum_{i=1}^{N} \exp(-i\boldsymbol{q}\cdot\boldsymbol{r}_i)\ . \tag{2.18}$$

The structure factor is defined as an autocorrelation function of the Fourier components:

$$S(\boldsymbol{q}) = \langle \rho_{\boldsymbol{q}}\rho_{-\boldsymbol{q}} \rangle\ . \tag{2.19}$$

It can be shown that the structure factor is related to the Fourier transform of the radial distribution function, $g(r)$:

$$S(q) = 1 + \rho \int [g(\boldsymbol{r}) - 1]\, e^{-i\boldsymbol{q}\cdot\boldsymbol{r}} d\boldsymbol{r}\ , \tag{2.20}$$

where ρ is the average density. Thus, the both radial distribution function and the structure factor provide information about the structure.

Time correlation functions

Time correlation functions are useful probes of the dynamics of the system, i.e. the time dependent properties. The time correlation function between two time-dependent quantities $A(t)$ and $B(t)$ is defined as

$$C_{AB}(t) = \langle A(t)B(0) \rangle\ , \tag{2.21}$$

and the autocorrelation function is

$$C_{AA}(t) = \langle A(t)A(0) \rangle\ . \tag{2.22}$$

To see what kind of information a time correlation function provides, let us examine the limits of the autocorrelation function. At $t = 0$, $C_{AA}(t) = \langle A(0)A(0) \rangle =$

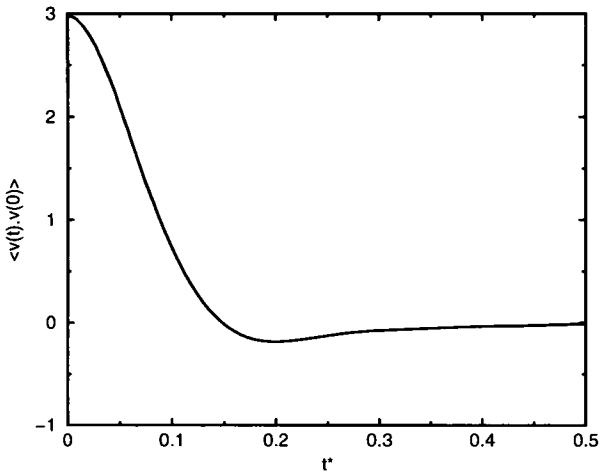

Figure 2.3: Velocity autocorrelation for a Lennard-Jones fluid at density $\rho^* = 0.8$ and temperature $T^* = 1$.

$\langle A^2 \rangle$. As $t \rightarrow \infty$, the system eventually 'forgets' what was happening at $t = 0$, and $A(t)$ becomes uncorrelated with $A(0)$. Therefore $\langle A(t)A(0) \rangle \rightarrow \langle A(t) \rangle \langle A(0) \rangle$. Since most of the quantities we consider average to zero, their autocorrelation functions decay from $\langle A^2 \rangle$ to zero as correlations die away.

If the decay is assumed to be exponential, $\frac{C_{AA}(t)}{C_{AA}(0)} = \exp(-t/\tau)$, then τ can be found by

$$\tau = \int_0^\infty \frac{C_{AA}(t)}{C_{AA}(0)} dt \tag{2.23}$$

Thus the integral of a correlation function gives a measure of the correlation time.

Figure 2.3 shows a typical velocity autocorrelation function, $\langle v(t) \cdot v(0) \rangle$ in a high density liquid. This is usually averaged over particles. At short times, there is a negative portion in the curve. This is attributed to the particles colliding with their surrounding co-ordination shells and reversing their velocities. Eventually particle velocities become decorrelated with their initial values and the velocity autocorrelation function decays to zero.

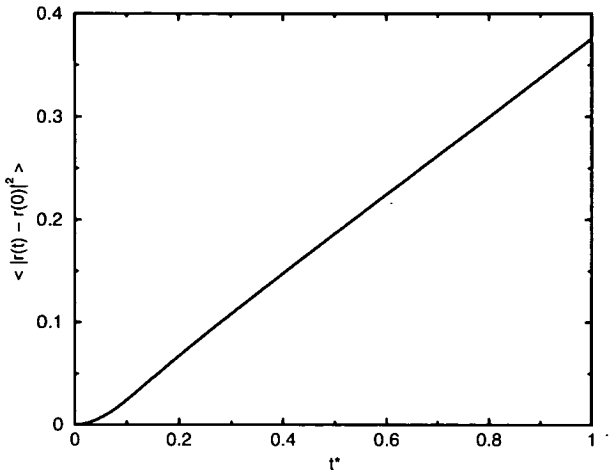

Figure 2.4: Mean square displacement for a Lennard-Jones fluid at density $\rho^* = 0.8$ and temperature $T^* = 1$.

Diffusion

The diffusion of particles can be measured using the mean square displacement,

$$\Delta R^2(t) = \left\langle |\boldsymbol{r}_i(t) - \boldsymbol{r}_i(0)|^2 \right\rangle , \tag{2.24}$$

where $\boldsymbol{r}_i(t)$ is the position of particle i at time t. This is usually averaged over particles as well as taking the ensemble average in order to obtain better statistics. A typical graph of mean square displacement versus time is plotted in Fig. 2.4. At short times, the particles have not yet collided with any of their neighbours. The particles move with constant velocity and therefore $\Delta R^2 \propto t^2$. This is the inertial or ballistic regime. At longer times, we enter the diffusive regime. A given particle has made many collisions with neighbouring particles and its progress through the system slows down. The long time behaviour is given by the Einstein relation,

$$\Delta R^2(t) = 2dDt \tag{2.25}$$

in d dimensions. Thus the diffusion coefficient, D can be obtained from the gradient of the asymptotic linear portion of the curve.

The diffusion coefficient is also related to the velocity autocorrelation function,

$$D = \frac{1}{d}\int_0^\infty \langle \boldsymbol{v}(t)\cdot\boldsymbol{v}(0)\rangle \,. \tag{2.26}$$

We can also measure a rotational diffusion coefficient in an analogous way from the angular velocity autocorrelation function:

$$D_R = \frac{1}{3}\int_0^\infty \langle \boldsymbol{\omega}(t)\cdot\boldsymbol{\omega}(0)\rangle \,, \tag{2.27}$$

where ω is the angular velocity.

Heat capacity

The canonical heat capacity (at constant volume), $C_V = \left(\frac{\partial E}{\partial T}\right)_V$ is related to fluctuations in the energy. In a simulation at constant temperature, the heat capacity can be calculated by

$$C_V = \frac{\langle E^2\rangle - \langle E\rangle^2}{k_B T^2} \,. \tag{2.28}$$

Instantaneous temperature

A measure of the instantaneous temperature is provided by the 'kinetic temperature'. This is based on the equipartition theorem which states that each degree of freedom which appears as a quadratic term in the energy contributes $\frac{1}{2}k_BT$ to the average. Thus, in a three-dimensional system, the average kinetic energy at equilibrium is $3k_BT$ (three translational and three rotational degrees of freedom). We therefore define an instantaneous kinetic temperature by

$$T = \frac{1}{3Nk_B}\sum_i m_i v_i^2 \tag{2.29}$$

We can also define a separate translational and rotational temperature. It is useful to check that energy is correctly partitioned between translational and rotational degrees of freedom.

Of course, velocities are not available in Monte Carlo simulations. An alternative measure of the instantaneous temperature is the configurational temperature based only on the positions (or orientations) of the particles in the system. The translational configurational temperature can be found from [56]

$$k_B T_{trans} = \frac{\sum_{i=1}^{N} F_i^2}{-\sum_{i=1}^{N} \sum_{j \neq i}^{N} \nabla_{\boldsymbol{r}_{ij}} \cdot \boldsymbol{F}_{ij}} , \tag{2.30}$$

where F_i is the total force acting on particle i, F_{ij} is the contribution to the force on particle i due to particle j and r_{ij} is the distance between particles i and j. The rotational configurational temperature can be found from [57]

$$k_B T_{rot} = -\frac{\langle \tau_i^2 \rangle}{\langle \nabla_{\Omega_i} \tau_i \rangle} = \frac{\langle (\nabla_{\Omega_i} \phi)^2 \rangle}{\left\langle \nabla_{\Omega_i}^2 \phi \right\rangle} . \tag{2.31}$$

Here τ_i is the torque on particle i, ϕ is the pair potential, ∇_{Ω_i} is the angular gradient operator, and $\nabla_{\Omega_i}^2$ is the angular Laplacian.

2.2 Spin systems

2.2.1 Simulation techniques

Spin Dynamics

The static thermodynamic properties of many different models of magnetism have been studied extensively using Monte Carlo simulations. Spin dynamics

has received much less attention. Spin dynamics simulations consist of the integration of the equations of motion for spins on the sites of a lattice. We can derive a semi-classical equation of motion for the Heisenberg model as follows.

The Heisenberg Hamiltonian is

$$\mathcal{H} = -J \sum_{[ij]} \hat{\boldsymbol{S}}_i \cdot \hat{\boldsymbol{S}}_j. \tag{2.32}$$

$\hat{\boldsymbol{S}}_i$ is a unit vector pointing in the direction of the spin angular momentum on site i. The sum is over all pairs of spins which are nearest neighbours on the lattice. J is the exchange energy. In quantum mechanics, the rate of change of an observable, O is given by

$$\frac{\partial O}{\partial t} = \frac{i}{\hbar} [\mathcal{H}, O] \tag{2.33}$$

Using Eqs. 2.32 and 2.33, we get

$$\frac{\partial \hat{\boldsymbol{S}}_i}{\partial t} = \frac{i}{\hbar} \left[-J \sum_j \hat{\boldsymbol{S}}_i \cdot \hat{\boldsymbol{S}}_j, \hat{\boldsymbol{S}}_i \right] \tag{2.34}$$

$$= -\frac{iJ}{\hbar} \sum_j \left[\hat{\boldsymbol{S}}_i \cdot \hat{\boldsymbol{S}}_j, \hat{\boldsymbol{S}}_i \right] , \tag{2.35}$$

where the sum is over the nearest neighbours of spin i. Expanding out the commutator,

$$\left[\hat{\boldsymbol{S}}_i \cdot \hat{\boldsymbol{S}}_j, \hat{\boldsymbol{S}}_i \right] = [S_{ix}S_{jx} + S_{iy}S_{jy} + S_{iz}S_{jz}, S_i] \tag{2.36}$$

$$\begin{aligned} = {} & [S_{ix}S_{jx}, S_{ix}] + [S_{iy}S_{jy}, S_{ix}] + [S_{iz}S_{jz}, S_{ix}] + \\ & [S_{ix}S_{jx}, S_{iy}] + [S_{iy}S_{jy}, S_{iy}] + [S_{iz}S_{jz}, S_{iy}] + \\ & [S_{ix}S_{jx}, S_{iz}] + [S_{iy}S_{jy}, S_{iz}] + [S_{iz}S_{jz}, S_{iz}] \end{aligned} \tag{2.37}$$

Each of these terms can be evaluated using the relation $[AB, C] = [A, C]B + A[B, C]$, and then using the usual commutation relations for angular momentum:

$$[S_x, S_y] = i\hbar S_z \tag{2.38}$$

$$[S_y, S_z] = i\hbar S_x \tag{2.39}$$

$$[S_z, S_x] = i\hbar S_y \tag{2.40}$$

We arrive at

$$\begin{aligned} \left[\hat{\boldsymbol{S}}_i \cdot \hat{\boldsymbol{S}}_j, \hat{\boldsymbol{S}}_i\right] &= i\hbar(S_{iy}S_{jz} - S_{iz}S_{jy}) + i\hbar(S_{iz}S_{jx} - S_{ix}S_{jz}) && (2.41)\\ &\quad + i\hbar(S_{ix}S_{jy} - S_{iy}S_{jx}) && (2.42)\\ &= i\hbar\hat{\boldsymbol{S}}_i \times \hat{\boldsymbol{S}}_j && (2.43) \end{aligned}$$

Finally, substituting Eq. 2.43 into Eq. 2.35, the equation of motion for spin i is

$$\frac{d\hat{\boldsymbol{S}}_i}{dt} = J\hat{\boldsymbol{S}}_i \times \sum_j \hat{\boldsymbol{S}}_j \,, \tag{2.44}$$

We proceed to integrate these equations of motion by a finite difference algorithm in the same manner as in molecular dynamics [58–61]. Commonly used algorithms include a predictor-corrector algorithm or an algorithm based on Suzuki-Trotter decomposition of exponential operators. A commonly used predictor-corrector is the explicit Adams-Bashforth four step predictor followed by the implicit Adams-Moulton three step corrector. This provides a solution to the differential equation $\dot{y}(t) = f(y(t))$.

$$y(t+\Delta t) = y(t) + \frac{1}{24}\Delta t[55f(y(t)) - 59f(y(t-\Delta t)) + 37f(y(t-2\Delta t)) - 9f(y(t-3\Delta t))], \tag{2.45}$$

followed by the implicit Adams-Moulton three step corrector

$$y(t+\Delta t) = y(t) + \frac{1}{24}\Delta t[9f(y(t+\Delta t)) + 19f(y(t)) - 5f(y(t-\Delta t)) + f(y(t-2\Delta t))], \tag{2.46}$$

where we feed in the result for $y(t+\Delta t)$ from the predictor step.

The equations of motion (Eq. 2.44) conserve energy and magnetisation, $\sum_i \hat{\boldsymbol{S}}_i$. In order to perform a simulation at constant temperature, initial configurations for the dynamics runs can be provided by a Monte Carlo simulation at a prescribed temperature. A canonical ensemble average can then be obtained by averaging over the trajectories generated.

2.2.2 *Measurable quantities*

In magnetic systems, we define the magnetisation as the sum of all the dipole moments

$$\boldsymbol{M} = \sum_i \boldsymbol{\mu}_i \tag{2.47}$$

The susceptibility is defined as $\chi = \left(\frac{\partial M}{\partial H}\right)_{H=0}$, where H is the magnetic field. This related to the fluctuations in the magnetisation by

$$\chi = \frac{\langle M^2 \rangle - \langle M \rangle^2}{k_B T} \tag{2.48}$$

We next introduce the dynamic structure factor in the context of spin systems although it can also be measured for fluid systems. This quantity makes an important link between simulation and experiment as it can be obtained from inelastic neutron scattering experiments. The intermediate scattering function is defined by

$$F(\boldsymbol{q}, t) = \langle \boldsymbol{M}(\boldsymbol{q}, t) \cdot \boldsymbol{M}(\boldsymbol{q}, 0) \rangle \,, \tag{2.49}$$

where $\boldsymbol{M}(\boldsymbol{q}, t)$ is a Fourier component of the magnetisation,

$$\boldsymbol{M}(\boldsymbol{q}, t) = \sum_{j=1}^{N} \hat{\boldsymbol{S}}_j(t) e^{-i\boldsymbol{q}\cdot\boldsymbol{r}_j} \tag{2.50}$$

The temporal Fourier transform of $F(\boldsymbol{q}, t)$ yields the dynamic structure factor

$$S(\boldsymbol{q}, \omega) = \int_{-\infty}^{\infty} F(\boldsymbol{q}, t) e^{-i\omega t} dt \, . \tag{2.51}$$

CHAPTER 3

Structure and dynamics of a quasi-two-dimensional dipolar fluid

3.1 Introduction

In this chapter, we study the structure and dynamics of the dipolar fluid using molecular dynamics simulations. This model is most closely relevant to ferrofluids. In experiments on ferrofluids, thin films are often used, especially when the aim is to image the structure. We thus study a quasi-two-dimensional system where the centres of mass of the particles are confined to a plane, but the dipoles are able to rotate in three dimensions.

The energy of two dipoles is minimised when they align 'nose-to-tail', and this leads, for high dipole moment, to the formation of chain-like aggregates. This aggregation has a profound effect on the dynamics. In particular, our results show a separation of timescales between the fast motion of particles within chains, and the slow motion of the chains as a whole.

Before describing more recent work on quasi-two-dimensional dipolar fluids, we shall discuss some of the issues which have been considered in the literature for the three dimensional case.

The structure of dipolar spheres in three dimensions has been surveyed in many studies [12–14]. Camp and Patey [14] performed Monte Carlo simulations of a system of dipolar hard spheres and observed the structures formed at different densities along an isotherm. At the lowest densities, the structure consists of isolated chains and rings. As the density is increased, there is a network of interconnected chains. At a higher density still, aggregation breaks down, and the structure appears as that of a 'normal' liquid.

Camp and Patey also computed the static structure factor, $S(q)$. One finding which will be relevant to the present work was that at lower density, where chaining occurs, the structure factor displays a power-law scaling at low q. The low wavevector (long wavelength) region corresponds to correlations over distances greater than one particle diameter, and therefore this is the region in which chaining would make its presence felt. The structure factor was found to scale as $S(q) \sim q^{-D}$ with $D = 1$. This is the scaling expected for rod-like molecules, as we will show later.

Wei and Patey [62] showed evidence from their molecular dynamics simulations that in three dimensions dipolar soft spheres can form a ferromagnetic liquid state at high densities near the freezing transition. They measured the first and second rank orientational order parameters, $\langle P_1 \rangle$ and $\langle P_2 \rangle$ which are usually used in the study of liquid crystals to identify ferroelectric nematic states. In a ferromagnetic state with a net magnetisation and dipoles preferentially aligned along a director, both $\langle P_1 \rangle$ and $\langle P_2 \rangle$ would be expected to be non-zero. Wei and Patey found that as a function of density, the order parameters displayed large jumps at densities of $\rho^* \simeq 0.65$ and $\rho^* \simeq 0.87$. This they assigned to phase transitions

between the isotropic fluid and ferromagnetic fluid and between the ferromagnetic fluid and ferromagnetic solid state. Monte Carlo simulations by Weis and Levesque [12, 13, 63] also confirmed the presence of a ferromagnetic liquid state.

A long-standing question is whether the dipolar fluid exhibits a liquid-vapour phase transition in the absence of any additional attractive interactions. Although the works cited below are concerned with the three dimensional case, the question is also important in the two dimensional case. The issue was first raised by de Gennes and Pincus [10], who noted that the angle-averaged dipole-dipole interaction gives an attractive interaction which has a $1/r^6$ dependence on distance, like the van der Waals interaction. On this basis, they conjectured that the phase diagram should be similar to that for the Lennard-Jones potential, which does display liquid-vapour coexistence. Early theoretical work appeared to confirm this, as did a simulation study by Ng *et al.* [64]. However, they simulated a very small system of only 32 particles. Later simulations showed no evidence of a liquid-vapour transition. Caillol [65] performed Monte Carlo simulations along the isotherms $T^* = 0.22$ and $T^* = 0.18$ in the isobaric-isothermal (constant NPT) ensemble and also using the Gibbs ensemble method. These two isotherms are below the critical temperature estimated by Ng *et al.* [64]. If this were indeed the correct critical temperature, we would expect to see phase coexistence at some point along isotherms at lower temperature. For various pressures along each isotherm, the probability distribution for values of density was calculated. At first, in simulations with $N = 100$ or 256 particles, it seemed that there may be two peaks in this distribution, which would indicate phase coexistence. However, with $N = 512$ particles, the curves showed only one peak at all pressures. The results of the Gibbs ensemble simulations also showed no phase coexistence. Weis and Levesque [12, 13] carried out a Monte Carlo study in the canonical (constant NVT) of the phase behaviour of a system of dipolar

hard spheres over a wide range of densities and reduced temperatures T^* between 0.08 and 0.25 in the fluid region of the phase diagram. Their simulations failed to show any evidence of the system dividing into a low density and high density region, i.e. no liquid-vapour coexistence was observed.

It appears that additional attractive interactions are necessary to recover the liquid-vapour transition. van Leeuwen and Smit [66] added a dispersive (van der Waals) $1/r^6$ term to the dipolar soft sphere potential. They used Gibbs ensemble Monte Carlo simulations to investigate the phase behaviour of a system whose particles interact via the following pair potential:

$$U(\boldsymbol{r}_{ij}, \boldsymbol{\mu}_i, \boldsymbol{\mu}_j) = 4\epsilon \left[\left(\frac{\sigma}{r_{ij}} \right)^{12} - \lambda \left(\frac{\sigma}{r_{ij}} \right)^{6} \right] + \frac{\boldsymbol{\mu}_i \cdot \boldsymbol{\mu}_j}{r_{ij}^3} - \frac{3(\boldsymbol{\mu}_i \cdot \boldsymbol{r}_{ij})(\boldsymbol{\mu}_j \cdot \boldsymbol{r}_{ij})}{r^5} \quad (3.1)$$

When $\lambda = 0$, this is just the dipolar soft sphere model. When $\lambda = 1$, it becomes the Stockmayer potential. The liquid-vapour coexistence curve was obtained for values of λ in the range 0.3-1. No phase coexistence was observed for $\lambda < 0.3$. Instead, in the region where the coexistence is expected, chaining occurred. For $\lambda > 0.3$, the critical temperature and pressure decrease with decreasing λ. Extrapolation to $\lambda = 0$ shows that if there is a liquid-vapour transition, the critical temperature must be much lower than previously predicted.

Contrary to all this, Camp *et al.* [15] performed three independent sets of simulations which appear to suggest that there is at least one and possibly two fluid-fluid phase transitions. They obtained the equation of state from simulations in the NPT ensemble along the isotherm $T^* = 0.1322$. There appears to be three distinct branches in the equation of state. It may that one of the branches represents metastable states. A metastable state is a state in which the system is trapped, even though it is not the most thermodynamically stable state (i.e. it is not the state of lowest free energy). The system may be trapped in a local free

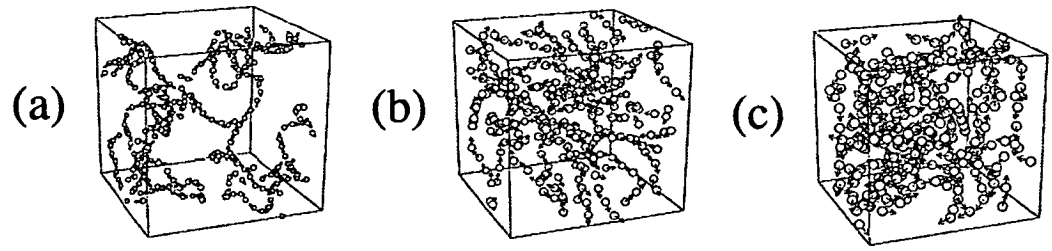

Figure 3.1: Snapshots of the three phases observed by Camp *et al.* [15] (a) low density phase (b) intermediate density phase (c) high density phase.

energy minimum, surrounded by high free energy barriers, making the conversion from the metastable state to the true thermodynamically stable state an extremely slow process. Snapshots of the structure in the three branches are shown in Fig. 3.1. In the low density phase, the particles are clearly aggregated into chains. In the intermediate density phase, chains are still discernible, forming a network structure. In the high density phase, the structure is more like that of a 'normal' fluid. Grand canonical Monte Carlo simulations also indicated the existence of three different isotropic fluid phases. Finally, the Helmholtz free energy along several isotherms was calculated by thermodynamic integration. At the lowest temperatures studied, the free energy showed three weak minima as a function of density. The densities at which these minima occur is consistent with the densities at which the three phases identified earlier appear. Above about $T^* = 0.15$, the free energy was found to be a monotonic function of the density, showing that the distinction between the phases disappears above this temperature. This suggests a critical temperature of $T^* = 0.15 - 0.16$. The isotherms studied by Caillol would thus be supercritical, which may be the reason why no liquid-vapour coexistence was observed in that case.

The phase transition in the dipolar fluid must be of a different nature to the traditional liquid-vapour phase transition. In a 'normal' liquid-vapour transition, there is a vapour phase with high energy and high entropy and a liquid phase

with low energy but low entropy. It is these large differences in energy and entropy which drive the transition. In the dipolar fluid, however, there is chaining at both low and high density, meaning that the energy and entropy are low in both cases. Hence, there must be some other driving force for a phase transition in dipolar fluids. Tlusty and Safran [6, 67] have proposed a topological transition in which the low density phase has a high concentration of end defects and the high density phase has a high concentration of 'Y' defects, creating an interconnected network of chains. A similar kind of transition may also be seen in other network-forming systems [68, 69] e.g. wormlike micelles, gels, microemulsions. Thus, dipolar fluids provide simple model system which can act as a paradigm for our understanding of a large range of other systems.

More recently, attention has turned to the simulation of the quasi-two-dimensional dipolar fluid. In this case, the particles' centres of mass are confined to a plane, but their dipole moments are free to rotate in three dimensions. This corresponds to the experimental situation of having a thin film of ferrofluid, which is often used in imaging. The thickness of the film is often comparable to the particle diameter and this can be thought of as a two-dimensional system.

As in the three dimensional case, it is unknown whether the quasi-two-dimensional dipolar fluid exhibits a liquid-vapour phase transition. No evidence has as yet been reported. Also, ferromagnetic liquid state which is observed in three dimensions does not occur in two dimensions.

The quasi-two-dimensional dipolar fluid was studied by Weis using Monte Carlo simulations [16]. It was confirmed that chaining occurs in the quasi-two-dimensional case as it does in three dimensions. It was also shown that the dipole moments have a strong tendency to lie within the plane because they are lined up nose-to-tail along the chains. The variation of structure with density was surveyed. A more detailed study of the structural and conformational properties

was carried out by Weis, Tavares and Telo da Gama [17, 18]. They used a distance criterion to identify the aggregates and classified them as chains, rings or defect clusters.

There is a vast literature on dynamics of weakly polar fluids. For reviews, see Refs. [70], [71]. There have been far fewer studies on the dynamics of strongly polar fluids in the regime where chaining occurs. Murashov, Camp, and Patey performed both molecular dynamics and Brownian Dynamics simulations of a three-dimensional strongly polar system in order to study the dielectric spectrum (or, strictly, the magnetic susceptibility spectrum in the case of magnetic dipoles) [19]. This is related to the Fourier transform of the bulk magnetisation time autocorrelation function. They found that the spectrum exhibits a low frequency band and a high frequency band. The high frequency peak became very weak at high density, where the particles show little tendency to form chains. The high frequency peak is thus due to the presence of chaining, and was attributed to oscillations of individual dipole moments within the chains, while the low frequency band was attributed to the rotation of whole chains. This is an example of the separation of timescales mentioned earlier, and reflects the behaviour observed by Butter *et al.* [23] in their measurements of magnetic susceptibility spectra in real ferrofluids.

Murashov *et al.* [19] made an interesting comparison between their molecular dynamics and Brownian Dynamics results. Brownian Dynamics might be expected to be a more realistic model for colloidal systems such as ferrofluids because the effect of solvent is included in the form of the stochastic forces. Murashov *et al.*, however, found their results were essentially the same using either technique. In the present work, we employ molecular dynamics simulations in the constant NVE ensemble. This is the natural ensemble for molecular dynamics, since

the Newtonian equations of motion conserve energy. Schemes to perform simulations at constant temperature do well with calculating static thermodynamic properties, but inevitably cause perturbation to the particle dynamics. Since it is the dynamics we are most interested in, we use ordinary molecular dynamics in the NVE ensemble.

3.2 Computational details

Molecular dynamics simulations were performed on a quasi-two-dimensional system of soft spheres with a central point dipole. The potential is the dipole-dipole potential plus a short-range repulsive potential,

$$u(r) = u_{SS}(r) + \frac{\boldsymbol{\mu}_1 \cdot \boldsymbol{\mu}_2}{r^3} - \frac{3(\boldsymbol{\mu}_1 \cdot \boldsymbol{r})(\boldsymbol{\mu}_2 \cdot \boldsymbol{r})}{r^5}\,, \tag{3.2}$$

where $\boldsymbol{r}$ is the interparticle separation vector and $\boldsymbol{\mu}_1$ and $\boldsymbol{\mu}_2$ are the dipole moments of particles 1 and 2, respectively. u_{SS} is a short-range repulsive interaction, taken to be the repulsive part of a Lennard Jones potential,

$$u_{SS}(r) = 4\epsilon \left(\frac{\sigma}{r}\right)^{12}\,. \tag{3.3}$$

ϵ is an energy parameter and σ is the particle 'diameter'.

The particles are confined to a plane but their dipole moments are free to rotate in three dimensions. Periodic boundary conditions were applied with a square box of width L. The potential was truncated by multiplying between $0.9 \times L/2$ and $L/2$ by a switching function due to Andrea *et al.* [72] which brings the potential smoothly to zero.

Long range potentials such as the Coulomb interaction or the dipole-dipole interaction present a problem in computer simulation. In the case of the Coulomb

interaction or the dipole-dipole interaction, for example, the range of the interaction extends well beyond half the box length and each particle will interact with all periodic images of every particle. One simple way to deal with this might be just to cut off the potential at some distance r_{cutoff}, setting it to zero beyond this distance. This can lead to problems. In the solid phase, for example, spherical truncation of a long range potential can lead to a distortion of the lattice. By arranging to be separated by a distance of r_{cutoff} or greater, a pair of particles can lower their energy. We therefore see a distortion of the lattice in which particles tend to move towards the edge of a sphere of radius r_{cutoff} around a given particle. The system can find a configuration with lower energy than the theoretical ground state. It is more usual to handle long range forces using Ewald summation or reaction field methods.

At low density, in the fluid phase, the problems should not be so severe, and we cite Ref. [73] to justify our use of truncated potentials. This study considered the effect of truncating the potential at different ranges in a two-line system of dipolar spheres and concluded that a cutoff length of 5σ is reasonable. Our cutoff range of $L/2$ is much longer than this, even at the highest density studied. At a density of $\rho^* = 0.5$, $L/2 = 21.9\sigma$.

Reduced units are defined in terms of the energy (ϵ) and distance (σ) parameters in the potential as follows: surface density $\rho^* = N\sigma^2/A$; temperature $T^* = kT/\epsilon$; dipole moment $\mu^* = (\mu^2/\epsilon\sigma^3)^{1/2}$; time $t^* = (\epsilon/m\sigma^2)^{1/2}t$ and moment of inertia $I^* = I/m\sigma^2$.

$N = 961$ particles, with $m = 1$ and $I^* = 0.1$ were used throughout. I^* was chosen as the value of the moment of inertia in reduced units for a sphere of uniform density. $I = 2/5mr^2$ for a sphere of radius r and mass m. Given that

$I^* = I/m\sigma^2$, we obtain for a sphere of radius $\sigma/2$,

$$I^* = \frac{2/5m(\sigma/2)^2}{m\sigma^2} = \frac{1}{10} \tag{3.4}$$

Simulations were performed in the NVE ensemble. Equilibration was performed in the NVT ensemble at $T^* = 1.0$. This latter ensemble was achieved by simple translational and rotational velocity scaling. Typical runs were of $\mathcal{O}(10^5)$ timesteps after equilibration, with a timestep $\delta t^* = 0.0025$. This was chosen to ensure conservation of energy. The equations of motion were integrated using the velocity Verlet algorithm for translations and a leapfrog algorithm for rotations. Dipole orientations were represented using quaternions.

3.3 Structure

Figure 3.2 shows the variation of the structure with density at the highest dipole moment studied ($\mu^* = 2.75$). The particles self-assemble into chain-like aggregates or closed rings. This is caused by the strong dipole-dipole interactions which align neighbouring dipoles in a nose-to-tail configuration. At a density $\rho^* = 0.05$, the structure consists mainly of rings with a few isolated chains. A ring is the ground state structure for an aggregate containing four or more particles. At higher density, the structure consists mostly of chains, with a few rings. This is because the aggregates are closer together on average and there will be more collisions between them, leading to the breakup of rings. At the highest density, $\rho^* = 0.5$, we see a structure with different areas containing 'bundles' of parallel chain segments. The dipole moments of particles in neighbouring chains are either parallel or antiparallel. Figure 3.3 shows the variation of the structure with dipole moment at a fixed density of $\rho^* = 0.2$. Below $\mu^* = 2.0$ there is little positional or orientational ordering. At $\mu^* = 2.0$, we see the onset of ordering,

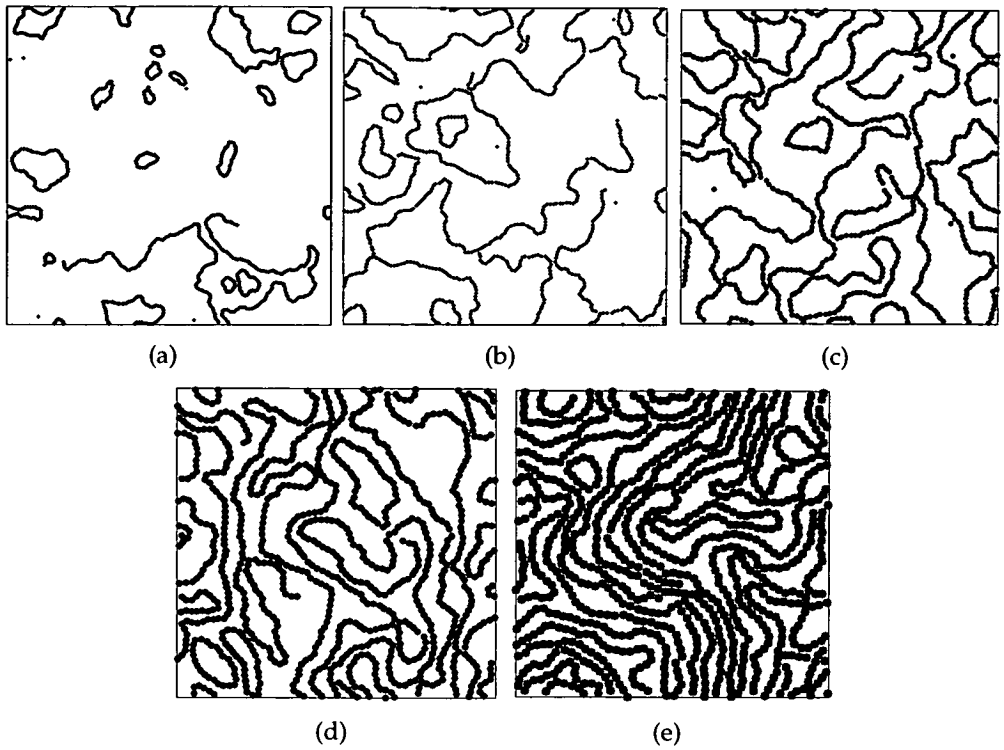

Figure 3.2: Snapshots showing the equilibrium structure at dipole moment $\mu^* = 2.75$ and different densities: (a) $\rho^* = 0.05$; (b) $\rho^* = 0.1$; (c) $\rho^* = 0.2$; (d) $\rho^* = 0.3$ and (e) $\rho^* = 0.5$.

with the particles beginning to form very loose chain-like structures. At a dipole moment of $\mu^* = 2.5$, most particles are now in chains or rings, although there are still a few free particles. At $\mu^* = 2.75$, there are almost no free particles. For all the densities considered $\mu^* = 2.0$ marks the boundary between the non-aggregated and aggregated regimes. This observation is consistent with the results from some of the structural and the dynamical functions presented below.

The structure was characterised using the radial distribution function, $g(r)$. These are shown in Fig. 3.4. At low dipole moment, the dipole-dipole interaction has little effect on the structure; the radial distribution function appears typical of a normal fluid. Peaks which appear with increasing density at 1.3σ and 2.6σ correspond to the first and second co-ordination shells. Above a dipole moment of $\mu^* = 2$, the structure is very different. The radial distribution function displays

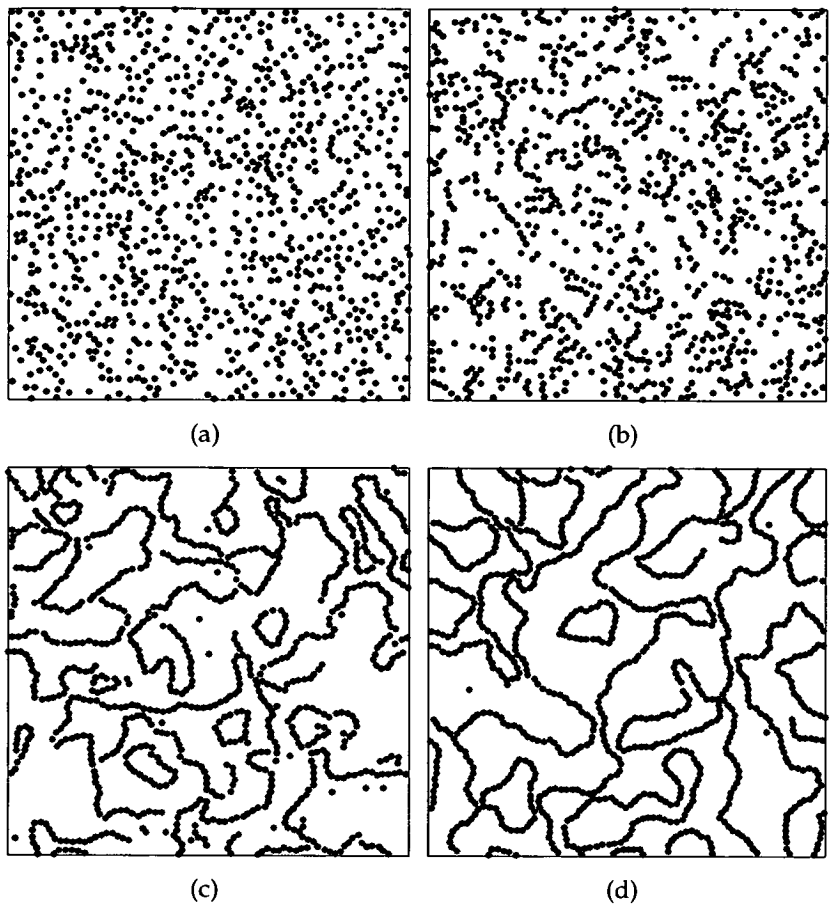

Figure 3.3: Snapshots showing the equilibrium structure at density $\rho^* = 0.2$ for different values of dipole moment: (a) $\mu^* = 1.5$, (b) $\mu^* = 2.0$, (c) $\mu^* = 2.5$, (d) $\mu^* = 2.75$.

a long series of sharp peaks at distances close to integer multiples of σ. This is due to the chaining which occurs in this regime. Neighbouring particles within chains will be roughly one particle diameter apart.

Peak positions in $g(r)$ shift to lower distances as the dipole moment increases because of the stronger interparticle interactions. In order to account for the positions of the first peak in $g(r)$, we give the position of the minimum in the potential for a pair of particles. We consider the case where the dipoles are aligned 'nose-to-tail' as they are within chains, i.e., the dipoles point along their separation vector. In that case, $\boldsymbol{\mu}_1 \cdot \boldsymbol{\mu}_2 = \mu^2$ and $\boldsymbol{\mu}_1 \cdot \boldsymbol{r} = \boldsymbol{\mu}_2 \cdot \boldsymbol{r} = \mu r$. With the soft sphere

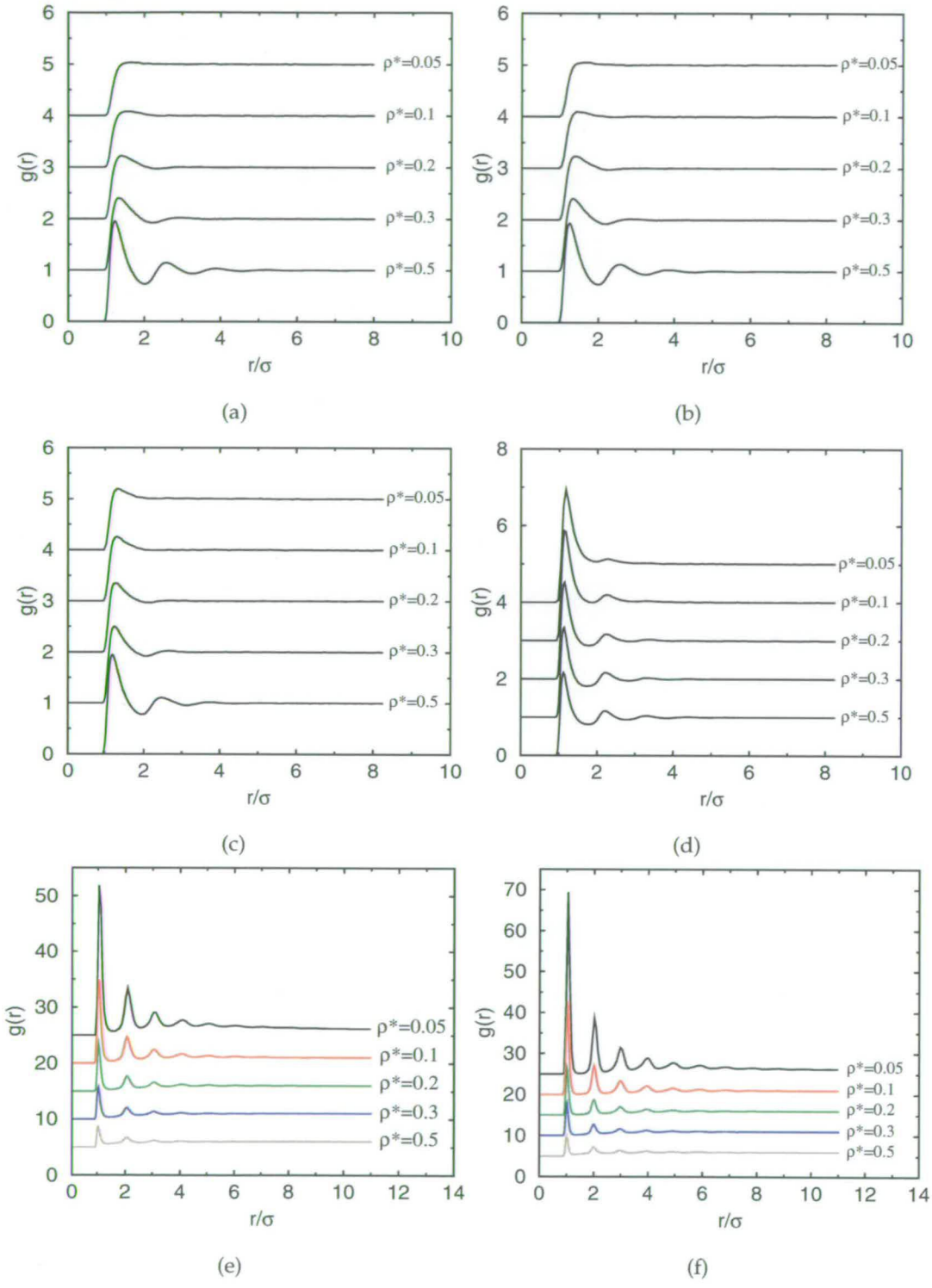

Figure 3.4: Radial distribution function at different densities, with (a) $\mu^* = 0.5$, (b) $\mu^* = 1.0$, (c) $\mu^* = 1.5$, (d) $\mu^* = 2.0$, (e) $\mu^* = 2.5$, (f) $\mu^* = 2.75$. In each graph, successive curves are displaced by one unit along the ordinate.

potential given in Eq. (3.3), the position of the minimum is given by

$$r_0 = 2^{\frac{1}{3}}\mu^{*-\frac{2}{9}}\sigma \tag{3.5}$$

The value of the potential at that point is

$$u(r_0) = -\frac{3}{4}\mu^{*\frac{8}{3}}\epsilon \tag{3.6}$$

For $\mu^* = 0.5$, we obtain $r_0 = 1.47\sigma$ and for $\mu^* = 2.75$, we obtain $r_0 = 1.01\sigma$. These values roughly match the positions of the first peak in $g(r)$.

The structure can be further analysed by examining the static structure factor, $S(q)$. This was calculated from the Fourier Transform of $h(r) = g(r) - 1$,

$$S(q) = 1 + \int h(r)\exp(-i\boldsymbol{q}\cdot\boldsymbol{r})d\boldsymbol{r}\ , \tag{3.7}$$

where q is the wavevector.

Figure 3.5 shows the structure factor for various densities and for dipole moments $\mu^* = 0.5$ and $\mu^* = 2.75$. The peaks in $S(q)$ in the region $q\sigma > 4.0 \simeq 10^{0.6}$ correspond to correlations between nearest neighbours. The peaks correspond to waves with wavelengths fitting into the nearest neighbour spacing. At high dipole moment where particles in chains are roughly a distance of σ apart, this means that integer$\times\lambda = \sigma$. Therefore, there are peaks at $q = (2\pi/\lambda) = 2\pi, 4\pi, 6\pi$ (i.e. $q\sigma \simeq 10^{0.8}, 10^{1.1}, 10^{1.3}$). These peaks shift to higher wavevector with increasing dipole moment. In real space this corresponds to the decreasing separation between neighbouring particles.

The most striking feature in the structure factor for high dipole moment is the power law scaling for $q\sigma < 5.0 \simeq 10^{0.7}$. A function $S(q) \sim q^{-D}$ was fit to the data in this region, yielding $D = 1.02 \pm 0.01$. A scaling of $S(q) \sim q^{-1}$ is expected

for rod-shaped objects, as we now show (see also Refs. [74, 75]). For particles arranged along a line, the number of particles within a radius r of a given particle scales as $n(r) \sim r^1$. The radial distribution function, $h(r) = g(r) - 1$, is proportional to the number of particles at a distance r, i.e. it is proportional to the number of particles in a shell of radius r ($dn(r)$) divided by the volume of the shell. In two dimensions the 'volume' of the shell is $2\pi r dr$, so $h(r)$ scales as

$$h(r) \sim \frac{1}{2\pi r}\frac{dn(r)}{dr} \tag{3.8}$$

$$\sim \frac{1}{2\pi r}. \tag{3.9}$$

The structure factor is then

$$S(q) \sim \int h(r) e^{-i\boldsymbol{q}\cdot\boldsymbol{r}} d\boldsymbol{r} \tag{3.10}$$

$$\sim 2\pi \int r dr \int d\theta e^{-iqr\cos\theta} h(r) \tag{3.11}$$

$$\sim \int dr \int d\theta e^{-iqr\cos\theta}. \tag{3.12}$$

Making the substitution $x = qr$,

$$S(q) \sim \frac{1}{q}\int dx \int d\theta e^{-ix\cos\theta}. \tag{3.13}$$

The integrals are independent of q, so we treat them as a constant, giving finally,

$$S(q) \sim \frac{1}{q}. \tag{3.14}$$

Thus the power law scaling in the structure factor is due to the fact that the system is composed of chains. This scaling was also observed in a Monte Carlo study of the three-dimensional dipolar fluid [14]. The scaling only emerges for dipole moments $\mu^* > 2.0$. This is consistent with the boundary between associating and non-associating regimes identified earlier on the basis of the snap-

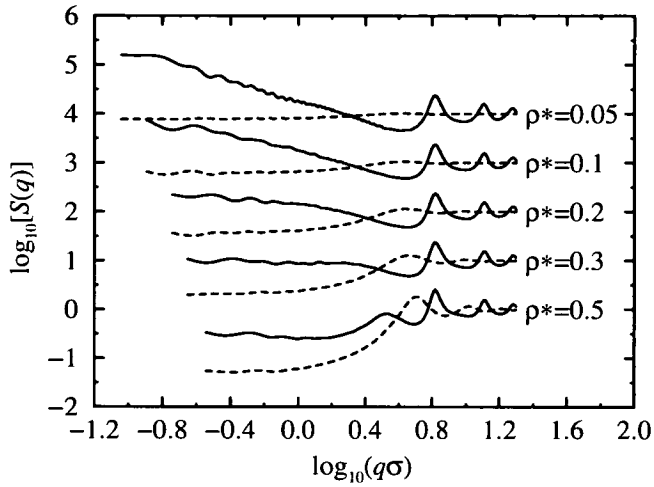

Figure 3.5: Static structure factor for dipole moments $\mu^* = 0.5$ (dotted line) and $\mu^* = 2.75$ (solid line) at various densities. Successive curves are displaced by one unit along the ordinate.

shots. There is an interesting 'pre-peak' in the structure factor for the case where $\rho^* = 0.5$ and $\mu^* = 2.75$ at $q\sigma \simeq 3.4 = 10^{0.54}$, corresponding to a distance in real-space of $2\pi/q \simeq 1.8\sigma$. This gives the typical separation between the parallel or antiparallel chain segments which can be seen in Fig. 3.2.

3.4 Single-particle translational motion

The presence of chaining should be expected to have a substantial effect on the motion of particles in the system. The single-particle translational motion was explored by measuring the velocity autocorrelation function. The velocity autocorrelation function is defined as

$$C_v(t) = \left\langle \frac{1}{N} \sum_{i=1}^{N} \boldsymbol{v}_i(t) \cdot \boldsymbol{v}_i(0) \right\rangle , \tag{3.15}$$

where $\boldsymbol{v}_i(t)$ is the velocity of particle i at time t. The triangular brackets denote an average over different time origins. This should be equivalent to the ensemble average, assuming ergodicity. We also average over particles.

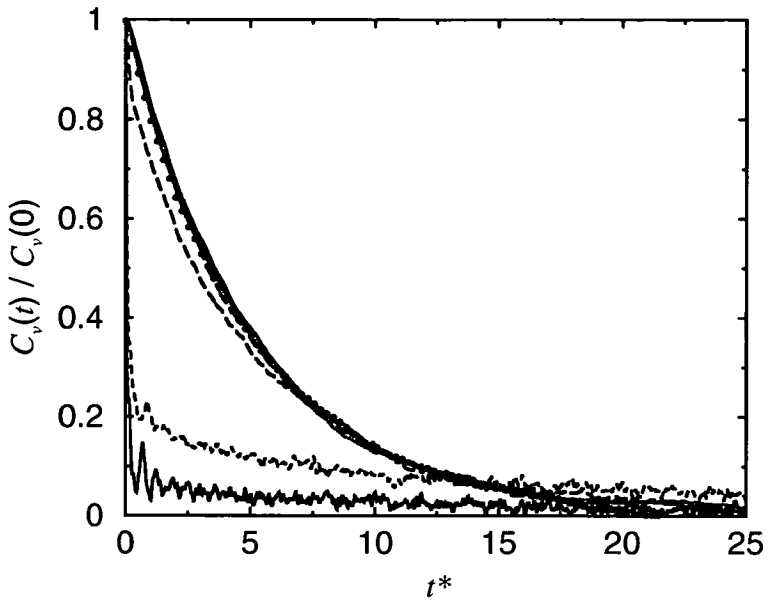

Figure 3.6: Velocity autocorrelation function at density $\rho^* = 0.05$ with various dipole moments (from bottom to top): $\mu^* = 2.75$ (solid line); $\mu^* = 2.5$ (dashed line); $\mu^* = 2$ (long-dashed line); $\mu^* = 1.5$ (dotted line); $\mu^* = 1$ (dot-dashed line); $\mu^* = 0.5$ (solid line); $\mu^* = 0$ (dotted line).

Figure 3.6 shows the velocity autocorrelation function at a density $\rho^* = 0.05$ for different values of the dipole moment. At low dipole moment, the function decays monotonically to zero. This behaviour is typical of simple fluids at low density. Above a dipole moment of $\mu^* = 2$, we see oscillations superimposed on the decay. We interpret this as a sign of chaining. A particular particle within a chain will oscillate around its 'equilibrium' position between its two neighbours. The particle will also have a 'drift' velocity due to the motion of the chain as a whole. Over time, the motion of the chains in the system will become uncorrelated with their initial motion, hence the drift velocities of the individual particles will become uncorrelated with their initial values. It is this that leads to the main decay of the velocity autocorrelation function. Superimposed on that will be oscillations due to the motion of the particles between their neighbours. Thus, we see motions on two different timescales: the fast oscillatory motion of individual particles within chains and the slow motion of the chains as a whole.

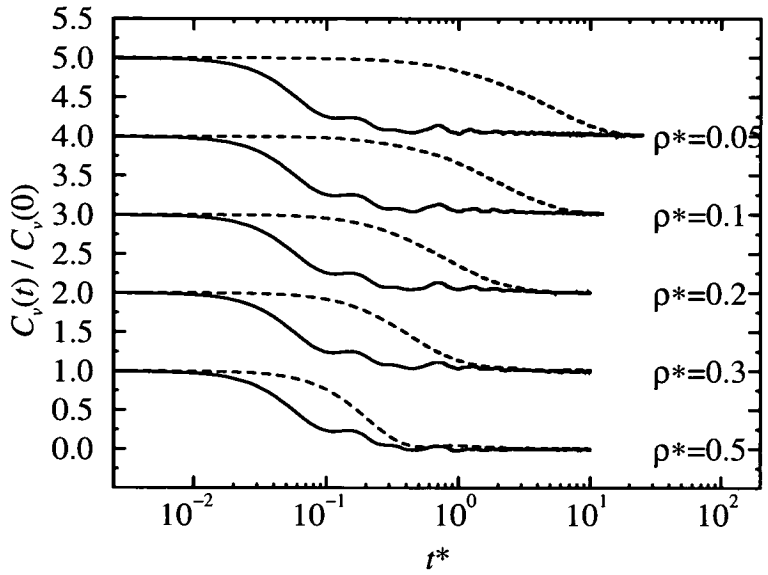

Figure 3.7: Velocity autocorrelation function for dipole moments $\mu^* = 0.5$ (dotted line) and $\mu^* = 2.75$ (solid line) at various densities. Successive curves are displaced by one unit along the ordinate.

To investigate single-particle translational motion further, we measured the diffusion coefficient. This can be found by two methods. Firstly, it can be obtained from the integral of the velocity autocorrelation function via the Green-Kubo relationship,

$$D = \frac{1}{2}\int_0^\infty C_v(t)dt \,. \tag{3.16}$$

Secondly, it can be obtained from the gradient of the asymptotic linear part of the mean square displacement, $\langle \Delta R^2 \rangle$, as a function of time using the Einstein relation,

$$\left\langle \Delta R^2 \right\rangle = \left\langle |\boldsymbol{r}_i(t) - \boldsymbol{r}_i(0)|^2 \right\rangle = 4Dt \tag{3.17}$$

in two dimensions, where $\boldsymbol{r}_i(t)$ is the displacement of particle i.

It is well established that in simple fluids, the velocity autocorrelation decays as $t^{-d/2}$ at long times, where d is the number of spatial dimensions, rather than exponentially [55]. These so-called long time tails were first discovered by Alder and Wainwright in their molecular dynamics simulation of the hard sphere

fluid [76], and have since been seen in a range of other systems (see for example Ref. [77]). Their discovery came as a surprise since the theories of time predicted a faster exponential decay. Alder and Wainwright attributed the long time tail to hydrodynamic effects [76]. When a particle in a fluid moves, it will compress the fluid in front and leave a gap behind. Surrounding particles will flow from in front of the particle to behind, creating a vortex. Hydrodynamic theories, which treat the fluid over larger length scales and longer timescales, may be more successful. Ernst *et al.* [78] showed that starting from the Navier-Stokes equations, it was indeed possible to derive the asymptotic $t^{-d/2}$ behaviour.

It can be seen from Eq. (3.16) that in two dimensions, when the long-time tail is present in the velocity autocorrelation function, it causes the diffusion coefficient to become divergent, and hence the diffusion coefficient does not really exist. The mean square displacement in our system is plotted in Fig. 3.8. It can be seen that the mean square displacement attains an apparent linear dependence on time at long times. The system therefore appears to exhibit diffusive behaviour, at least on the timescales accessible in our simulations. At the very lowest densities, the case is not so clear, but we can look at longer times if we consider an unaveraged curve from a single time origin. Despite being rather noisy, this seems to show that the linear time dependence is also eventually attained here. What might account for an absence of the long time tail? The presence of chaining might inhibit the formation of the hydrodynamic back-flow, postponing the hydrodynamic long time tail. The long time tail might then make its presence felt over timescales much longer than have been simulated here. Another effect of chaining are the long-lived damped oscillations in the velocity autocorrelation function described above. These oscillations could obscure the long time tail, meaning that very long runs would be necessary to observe the tail.

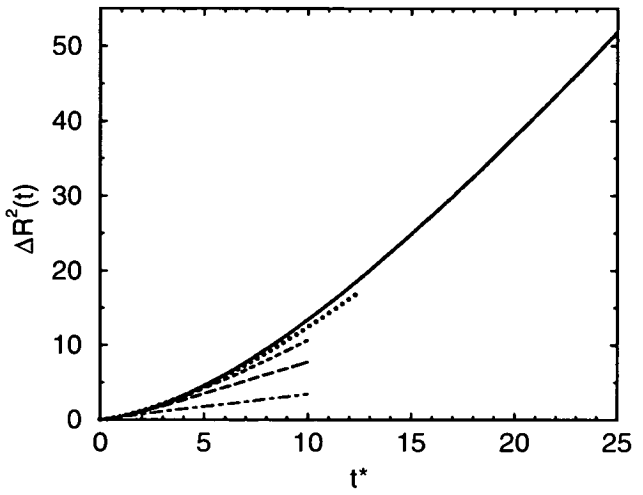

Figure 3.8: Mean square displacement as a function of time for different densities with $\mu^* = 2.75$: $\rho^* = 0.05$ (solid line); $\rho^* = 0.1$ (dotted line); $\rho^* = 0.2$ (dashed line); $\rho^* = 0.3$ (long-dashed line); $\rho^* = 0.5$ (dot-dashed line).

It would seem, then, that what is necessary is to perform the simulations to longer times. However, this is not an easy task. In examining the tail of a correlation function at very long times, we are measuring a very small quantity. There will thus be a very small signal-to-noise ratio. Another problem is that, because of the periodic boundary conditions, a disturbance such as a sound wave can make its way across the simulation cell and re-enter from the other side. The time it takes for the sound wave to propagate across the simulation cell thus sets an upper limit on the time to which we calculate dynamical properties accurately. In addition to long timescales, this means larger system sizes would be required in order to increase the time in which the sound wave will reappear.

We note that there are other systems in which the long time tail has been found to be absent in certain regimes of density. Hurley and Harrowell performed molecular dynamics simulations of a two-dimensional system of soft disks, and found diffusive behaviour at very high density ($\rho^* > 0.9$) [79]. It was suggested that this is because at this high density, the motion of a particle may cause an elastic response in the surrounding particles, hindering the formation of the convective

back-flow patterns. Another case is the core-softened fluid studied by Camp [80]. Diffusive behaviour is observed at densities $\rho^* > 0.25$. This coincides with the density at which the particles start to aggregate. This seems to suggest that in this system, as in our dipolar fluid system, the aggregation of particles hinders the hydrodynamic back-flow which leads to the long time tails.

It is not our purpose here to investigate the issue of long time tails in the dipolar fluid. We are merely interested in obtaining some sort of indication of the mobility of the particles. We therefore assume that we can extract a diffusion constant from the apparent linear portion of the mean square displacement curves.

The reduced diffusion coefficients, $D^* = D\sqrt{m/\epsilon\sigma^2}$, are plotted as a function of density for different dipole moments in Fig. 3.9. In calculating the mean square displacement, particles were allowed to diffuse out of the simulation cell. The diffusion coefficient decreases with density. This is to be expected because the particles are on average closer together and so will experience more collisions, impeding their motion. The variation with dipole moment is more interesting. For $\mu^* \leq 2.0$, the dependence on dipole moment is minor. For higher dipole moments, however, the diffusion coefficient is very much diminished. This is because the particles are now trapped in chains, which restricts their motion. The boundary $\mu^* = 2.0$ between associated and non-associated regimes is consistent with the boundary identified earlier on the basis of the snapshots and in the structure factor and velocity autocorrelation function.

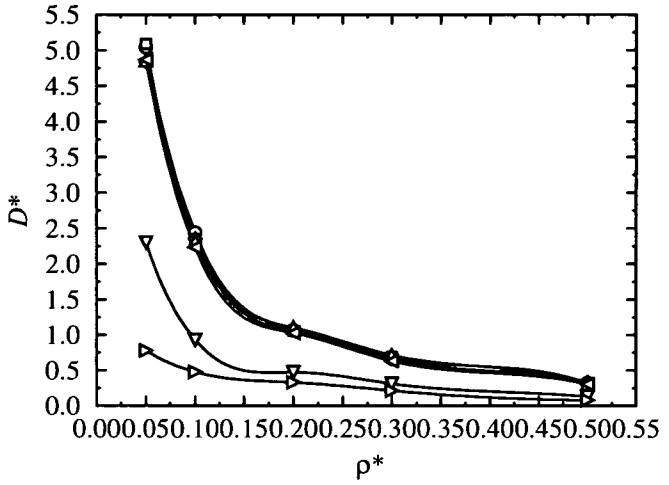

Figure 3.9: Diffusion coefficient versus density for dipole moments $\mu^* = 0.5$ (circles), $\mu^* = 1.0$ (squares), $\mu^* = 1.5$ (diamonds), $\mu^* = 2.0$ (left triangles), $\mu^* = 2.5$ (down triangles) and $\mu^* = 2.75$ (right triangles).

3.5 Single-particle rotational dynamics

The effect of chaining upon the rotational dynamics was investigated by measuring the dipole moment autocorrelation function,

$$C_\mu(t) = \left\langle \frac{1}{N\mu^2} \sum_{i=1}^{N} \boldsymbol{\mu}_i(t) \cdot \boldsymbol{\mu}_i(0) \right\rangle , \tag{3.18}$$

where $\boldsymbol{\mu}_i(t)$ is the dipole moment on particle i at time t. This has been normalised by dividing by μ^2, so that $C_\mu(0) = 1$. The x, y, or z components are given by

$$C_\mu^\alpha(t) = \left\langle \frac{1}{N\mu^2} \sum_{i=1}^{N} \mu_i^\alpha(t)\mu_i^\alpha(0) \right\rangle , \tag{3.19}$$

where α is x, y, or z and $\mu_i^\alpha(t)$ is the α component of the dipole moment on particle i at time t. $C_\mu^z(t)$ will provide information about out-of-plane rotations, while $C_\mu^{xy} = C_\mu^x + C_\mu^y$ will provide information about in-plane rotations. Fig. 3.10 shows for each density the in-plane and out-of-plane correlation functions for dipole moments $\mu^* = 0.5$ and $\mu^* = 2.75$. Firstly, we note that for the low dipole moment ($\mu^* = 0.5$), the initial values $C_\mu^{xy}(0) = 0.67$ and $C_\mu^z(0) = 0.33$ show that there is

no tendency for the dipoles to lie either within the plane or out of the plane. In contrast, the values at high dipole moment ($\mu^* = 2.75$) are $C_\mu^{xy}(0) = 0.966$ and $C_\mu^z(0) = 0.034$, showing that the dipoles are strongly constrained to lie within the plane. This is because the particles adopt their nose-to-tail configurations within the chains.

At the low dipole moment, there is dip to negative values in both $C_\mu^z(t)$ and $C_\mu^{xy}(t)$, before they decay away to zero. This is due to the free rotation of the dipoles. After a certain amount of time a dipole will have rotated so that it points in the opposite direction, hence the negative portion in the correlation function. The correlations die away before we can see another period of the rotation. At low dipole moment, it is expected that the frequency of the rotation should be close to the free-rotor limit, $\omega_0^* = \sqrt{T^*/I^*} \approx 3.16$; this is confirmed below. The free-rotor limit is derived as follows. There are two rotational degrees of freedom for the dipole moment vectors. The equipartition theorem states that each degree of freedom contributes $1/2kT$ to the ensemble averaged rotational kinetic energy, i.e.,

$$I_1\omega_1^2 + I_2\omega_2^2 \equiv I\omega^2 = kT \tag{3.20}$$

$$\Rightarrow \omega = \sqrt{\frac{kT}{I}}\,. \tag{3.21}$$

At high dipole moment, $C_\mu^{xy}(t)$ shows a very slow decay with a high frequency oscillation, whereas $C_\mu^z(t)$ shows a damped oscillation about zero. This is a result of the oscillations of dipoles about their equilibrium nose-to-tail orientations within chains. The slow decay of $C_\mu^{xy}(t)$ shows that the motion of the chains as a whole is slow. As is the case with the velocity autocorrelation function, we again see two different timescales due to motion of individual particles and collective motion of the chains.

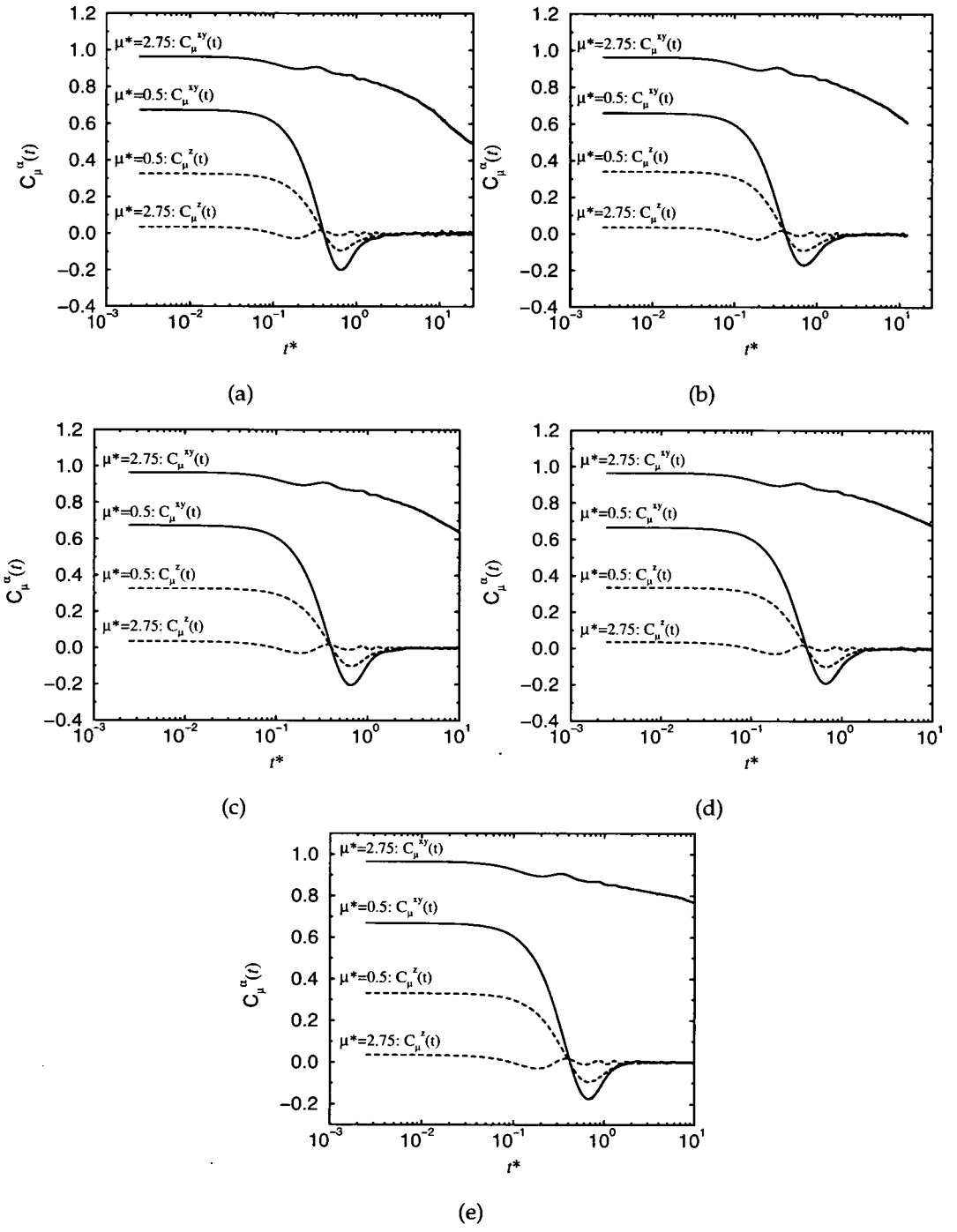

Figure 3.10: In-plane ($C_\mu^{xy}(t)$) and out-of-plane ($C_\mu^z(t)$) single-dipole autocorrelation functions for dipole moments $\mu^* = 0.5$ and $\mu^* = 2.75$ and at density (a) $\rho^* = 0.05$ (b) $\rho^* = 0.1$ (c) $\rho^* = 0.2$ (d) $\rho^* = 0.3$ (e) $\rho^* = 0.5$.

In order to obtain the oscillation frequency, the spectrum is calculated by taking the Fourier transform of the single-dipole autocorrelation function,

$$\chi_\mu^z(\omega) = \frac{1}{2\pi C_\mu^z(0)} \int_{-\infty}^{\infty} C_\mu^z(t) \exp(-i\omega t) dt \,. \tag{3.22}$$

Because C_μ^{xy} decays so slowly, it was not possible to obtain accurate Fourier transforms of this function. The xy function decays on a timescale comparable to the entire 100000 timesteps length of the simulation, but it would only be possible to obtain quantities from one time origin, i.e., no averaging could be done. The truncation of the function at shorter time can create spurious low frequency features in the Fourier transform. Therefore, a windowing function was applied to the correlation functions prior to taking the Fourier Transform. The Blackman window function was used:

$$B(t) = 0.42 + 0.5\cos(\pi t/t_{max}) + 0.08\cos(2\pi t/t_{max}) \tag{3.23}$$

where t_{max} is the time to which the correlation function was computed. Figure 3.11 compares $\chi_\mu^{xy}(\omega)$ and $\chi_\mu^z(\omega)$ for a dipole moment of $\mu^* = 2.75$ and density of $\rho^* = 0.5$. Although the low frequency end of the xy spectrum will be unreliable, the interesting features corresponding to the oscillations in the correlation functions will appear at high frequency. It can be seen that in both the xy and z cases, there is a clear high frequency peak at a reduced angular frequency of about $\omega_0^* = 14.3$. However, we will concentrate on the z component in what follows because it is easier to obtain an accurate Fourier transform. Figure 3.12 compares the spectra for different values of the dipole moment at each density. The peak frequency increases with increasing dipole moment as a result of the stronger interaction between particles. The peak frequencies have been

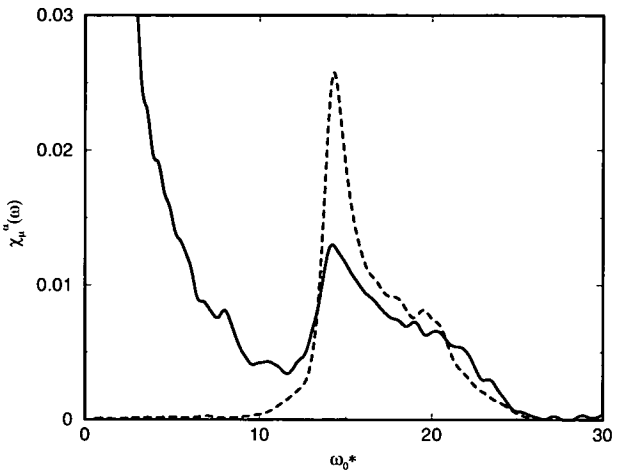

Figure 3.11: Fourier Transform of single-dipole autocorrelation at a density of $\rho^* = 0.5$ and dipole moment $\mu^* = 2.75$. Solid line: in-plane function, $\chi_\mu^{xy}(\omega)$, Dotted line: out-of-plane function, $\chi_\mu^z(\omega)$.

estimated by fitting a Lorentzian function in the vicinity of the peaks:

$$L(x) = a\left[\frac{1}{1+(\omega+\omega_0)^2\tau^2} + \frac{1}{1+(\omega-\omega_0)^2\tau^2}\right] \tag{3.24}$$

The values of ω_0^* are given in Table 3.1, and plotted in Fig. 3.13 as a function of dipole moment. The frequency is largely independent of density, indicating that interchain interactions are weak. It might have been expected that interchain interactions would be more important at higher density, where the average chain separation is smaller. At the dipole moment of $\mu^* = 0.5$, the frequency is close to the free-rotor limit $\omega_0^* = \sqrt{T^*/I^*} \simeq 3.16$. In the associated regime $\mu^* > 2.0$, a shoulder emerges in $\chi_\mu^z(\omega)$ on the high frequency side of the main peak. This can be attributed to a coupling between the oscillation of particles within chains and the collective motion of those chains as a whole.

Following Murashov *et al.* [19], we now present a simple theory for the rotational motion of the dipoles. Since interchain interactions are weak, we consider the motion of a single dipole in an infinitely long chain. The chain is assumed to lie along the x-axis, and we consider oscillations of the dipole in the xy-plane.

		D^*						ω_0^*		
		From	From					From	From	Eq.
μ^*	ρ^*	$\langle \Delta R^2 \rangle$	$C_v(t)$	D_R^*	$C_\mu^z(0)$	$C_M^{xy}(0)$	$C_M^z(0)$	$C_\mu^z(t)$	$C_\Omega(t)$	3.29
0.0	0.05	5.3665(5)								
	0.1	2.5995(1)								
	0.2	1.2658(1)								
	0.3	0.76670(6)								
	0.5	0.4005(2)								
0.5	0.05	5.0245(7)	5.1		0.33	0.67	0.32	3.6		1.9
	0.1	2.5660(1)	2.3		0.34	0.67	0.33	3.5		1.9
	0.2	1.16939(5)	1.1		0.33	0.71	0.30	3.6		1.9
	0.3	0.7767(1)	0.69		0.34	0.72	0.30	3.5		1.9
	0.5	0.34884(7)	0.29		0.33	0.74	0.26	3.5		1.9
1	0.05	4.9263(4)	4.8		0.33	0.68	0.30	3.6		4.9
	0.1	2.3549(3)	2.4		0.33	0.71	0.27	3.6		4.9
	0.2	1.2671(1)	1.1		0.33	0.83	0.21	3.7		4.9
	0.3	0.7873(1)	0.66		0.32	0.97	0.21	3.8		4.9
	0.5	0.37256(5)	0.34		0.31	1.3	0.17	4.2		4.9
1.5	0.05	5.0490(3)	4.9	67	0.33	0.71	0.26	3.7		8.4
	0.1	2.5057(3)	2.3	28	0.32	0.85	0.22	3.9		8.4
	0.2	1.30367(8)	1.1	14	0.30	1.1	0.13	4.2		8.4
	0.3	0.86287(6)	0.71	6.5	0.28	1.4	0.14	4.5		8.4
	0.5	0.36543(5)	0.31	2.6	0.23	2.1	0.082	5.2		8.4
2	0.05	4.791(9)	4.9	29	0.29	0.95	0.20	4.0		12.4
	0.1	2.3659(3)	2.2	11	0.25	1.4	0.17	4.7		12.4
	0.2	1.1561(1)	1.0	3.5	0.20	2.2	0.10	5.5	6.4	12.4
	0.3	0.8605(4)	0.63	1.7	0.17	2.3	0.067	6.4	7.7	12.4
	0.5	0.35307(9)	0.30	0.70	0.13	2.8	0.049	7.6	8.3	12.4
2.5	0.05	4.090(4)	2.3	9.0	0.082	6.7	0.055	10.3	12.2	16.6
	0.1	1.1661(2)	0.93	2.4	0.068	11	0.043	12.4	12.2	16.6
	0.2	0.58647(9)	0.47	0.65	0.057	8.5	0.034	12.7	12.3	16.6
	0.3	0.34714(4)	0.31	0.37	0.057	2.2	0.028	12.5	12.4	16.6
	0.5	0.13754(3)	0.13	0.17	0.052	3.3	0.022	12.7	12.4	16.6
2.75	0.05	1.3862(8)	0.78	0.95	0.035	11	0.023	14.0	14.2	18.9
	0.1	0.6392(3)	0.48	0.42	0.036	15	0.021	14.3	14.3	18.9
	0.2	0.18736(6)	0.33	0.17	0.035	111	0.023	14.6	14.3	18.9
	0.3	0.2666(1)	0.21	0.11	0.035	250	0.019	14.6	14.3	18.9
	0.5	0.03158(9)	0.079	0.095	0.034	280	0.016	14.3	14.5	18.9

Table 3.1: Dynamical and transport properties of the quasi-two-dimensional dipolar fluid: Translational diffusion coefficient, D^*, obtained from radial distribution or velocity autocorrelation function as explained in the text; rotational diffusion coefficient, obtained from angular velocity autocorrelation function; initial values of z component of single dipole autocorrelation function and xy and z components of bulk magnetisation autocorrelation function; oscillation frequencies obtained from Fourier transform of $C_m u^z(t)$ and $C_\Omega(t)$ or from the mean field theory leading to Eq. 3.29.

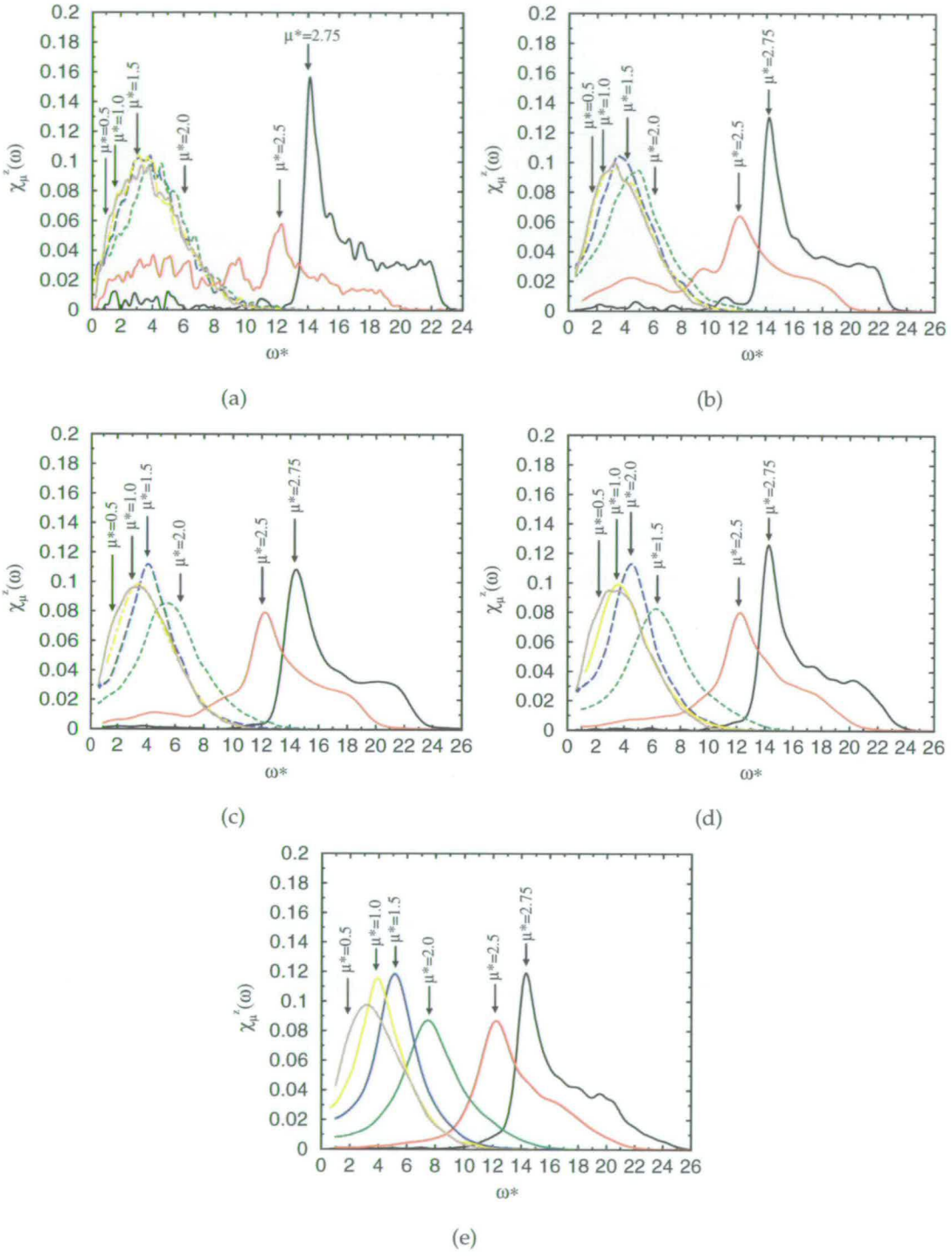

Figure 3.12: Fourier transforms of the z component of the single-dipole autocorrelation function for different dipole moments at density (a) $\rho^* = 0.05$ (b) $\rho^* = 0.1$ (c) $\rho^* = 0.2$ (d) $\rho^* = 0.3$ (e) $\rho^* = 0.5$.

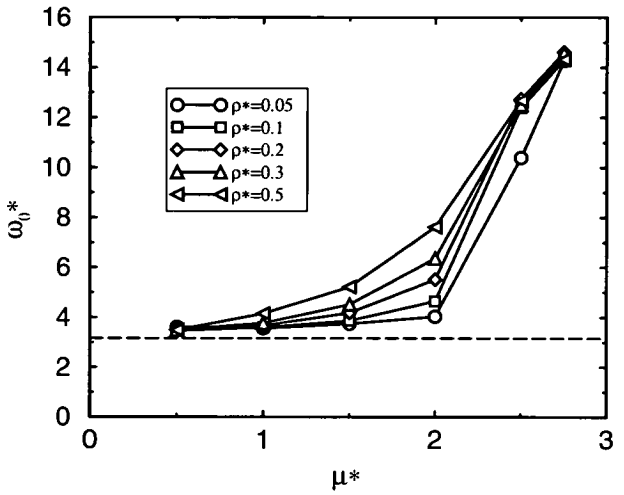

Figure 3.13: Position of peaks in spectra of single-dipole autocorrelation functions, plotted as a function of dipole moment for various densities: $\rho^* = 0.05$ (circles); $\rho^* = 0.1$ (squares); $\rho^* = 0.2$ (diamonds); $\rho^* = 0.3$ (up triangles) and $\rho^* = 0.5$ (left triangles). The dotted line is plotted at $\omega_0^* = \sqrt{10}$ and represents the free-rotor limit.

Neighbours along the chain are separated by r_0, the position of the minimum in the potential, as given by Eq. (3.5). The tagged dipole is given, in terms of the angle (γ) it makes with the chain, by $\boldsymbol{\mu} = \mu[\cos\gamma(t), \sin\gamma(t), 0)]$. The other dipoles are constrained to point along the chain in the nose-to-tail configuration. The torque on the tagged dipole due to all the others is given by

$$2\sum_{n=1}^{\infty}\left[\frac{2\mu^2\sin\gamma}{(nr_0)^3}\right] = -\frac{4\mu^2\zeta(3)}{r_0^3}\sin\gamma \tag{3.25}$$

where $\zeta \simeq 1.202$ is the Riemann zeta function. At high dipole moment, the amplitude of the oscillations will be small. In this limit $\sin\gamma \approx \gamma$. The equation of motion is then $\ddot{\gamma} = -\omega_0^2\gamma$, where

$$\omega_0 = \sqrt{\frac{4\mu^2\zeta(3)}{Ir_0^3}} \tag{3.26}$$

The solution of the equation of motion is

$$\gamma(t) = \gamma(0)\cos\omega_0 t + \frac{\dot{\gamma}(0)}{\omega_0}\sin\omega_0 t\,. \tag{3.27}$$

Thus, for the orientational autocorrelation function we have,

$$\langle \boldsymbol{\mu}(t)\cdot\boldsymbol{\mu}(0)\rangle \propto 1 - \left\langle\gamma^2\right\rangle + \left\langle\gamma^2\right\rangle\cos\omega_0 t\,. \tag{3.28}$$

Combining Eq. (3.26) with Eq. (3.5) gives for the angular frequency of the oscillation,

$$\omega_0^* = \sqrt{\frac{2(\mu^*)^{8/3}\zeta(3)}{I^*}} \tag{3.29}$$

It is assumed that there is no friction, but even in the presence of friction, a peak should appear in the Fourier transform at a position given by Eq. (3.29). Table 3.1 compares the frequency calculated from the present theory with those obtained from the peak position of the Fourier transform of $C_\mu^\alpha(t)$. In the aggregated high dipole moment regime, where the theory is relevant, the frequencies are overestimated by about 30%. This is because this rather crude model assumes that the chains are completely straight rigid objects, and it does not take into account the fluctuations in the shape of the chains. In a twisted chain of finite length, the average field experienced by a particular dipole will be reduced relative to this ideal case. Thus, the frequency of the oscillation will be reduced.

Another function which can give information about the rotational dynamics is the angular velocity autocorrelation function, defined by

$$C_\Omega(t) = \left\langle \sum_{i=1}^{N} \boldsymbol{\Omega}_i(t)\cdot\boldsymbol{\Omega}_i(0)\right\rangle\,, \tag{3.30}$$

where $\boldsymbol{\Omega}_i(t)$ is the angular velocity of particle i. It is expected that this function should exhibit similar behaviour to the single dipole autocorrelation function. It

can be seen in Fig. 3.14 that this is indeed the case. These have been normalised by divided by the initial value, which in all cases was $C_\Omega(0) = 20$. This comes from the equipartition theorem. There are two rotational degrees of freedom, and therefore, according to equipartition, $\left\langle \frac{1}{2} I\Omega^2 \right\rangle = kT$. The initial value of the autocorrelation function is then $C_\Omega(0) = \langle \mathbf{\Omega}(0) \cdot \mathbf{\Omega}(0) \rangle = \langle \Omega^2 \rangle = 2kT/I = 20$. At high dipole moment, there is again a high frequency oscillation and at low dipole moment, a damped oscillation. The frequencies were obtained from the Fourier transform as in case of the single dipole autocorrelation function. These are shown in Table 3.1. The Fourier transforms exhibit the same behaviour as for the single-dipole autocorrelation function, including the high frequency shoulder which develops at high dipole moment (Fig. 3.15). The peak frequencies obtained from the two functions are roughly the same.

A rotational diffusion coefficient can be calculated from $C_\Omega(t)$ using a Green-Kubo relation,

$$D_R = \frac{1}{2} \int_0^\infty C_\Omega(t) dt \,. \tag{3.31}$$

Rotational diffusion is entirely analogous to translational diffusion but instead of considering the positions of the particles, we consider their orientations. The rotational diffusion coefficients are given in Table 3.1. D_R decreases with increasing dipole moment, again because the particles are confined within chains and constrained to point in their nose-to-tail configuration. D_R decreases with increasing density due to increasingly restricted rotation of the chains.

3.6 Collective rotational motion

The problems with obtaining the Fourier transforms of the autocorrelation functions are even more severe in the case of collective rotational motion. Therefore, as before we will mostly concentrate on the z component of the magnetisation

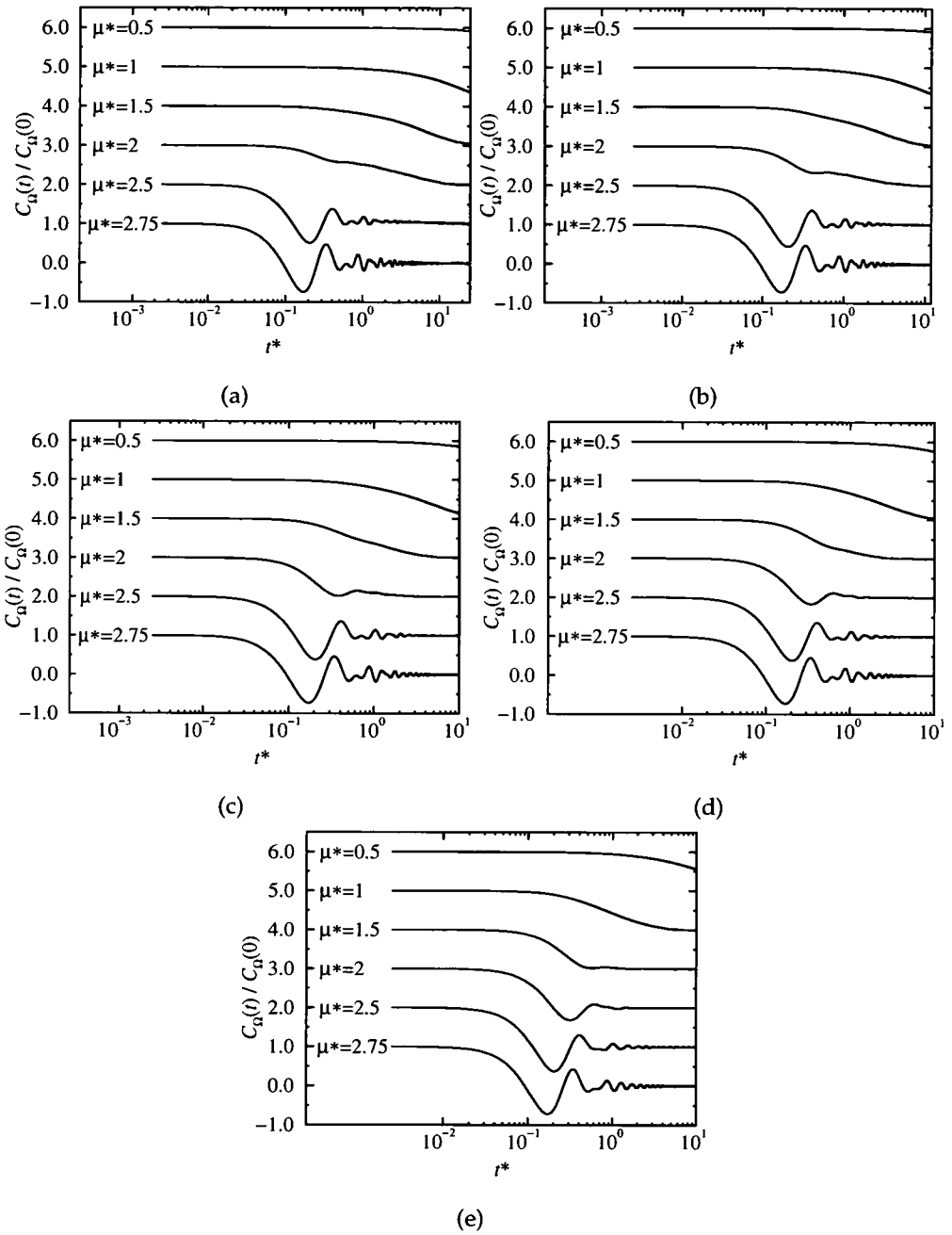

Figure 3.14: Angular velocity autocorrelation functions for different values of dipole moment and at density (a) $\rho^* = 0.05$ (b) $\rho^* = 0.1$ (c) $\rho^* = 0.2$ (d) $\rho^* = 0.3$ (e) $\rho^* = 0.5$. Successive curves are displaced by one unit along the ordinate.

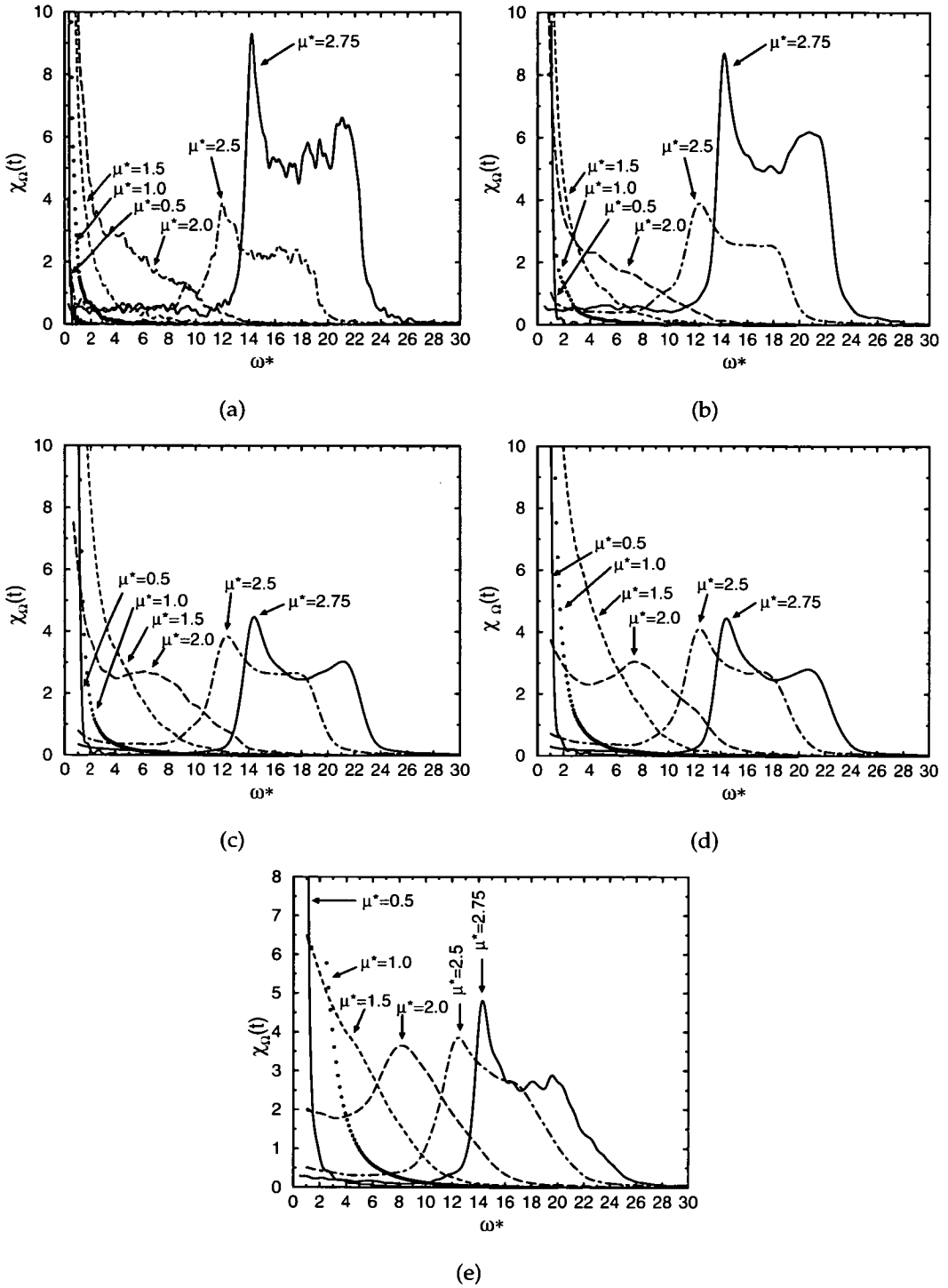

Figure 3.15: Fourier transforms of the angular velocity autocorrelation function for different dipole moments at density (a) $\rho^* = 0.05$ (b) $\rho^* = 0.1$ (c) $\rho^* = 0.2$ (d) $\rho^* = 0.3$ (e) $\rho^* = 0.5$.

autocorrelation function. The bulk magnetisation is defined as the vector sum of the dipole moments,

$$\boldsymbol{M}(t) = \sum_{i=1}^{N} \boldsymbol{\mu}_i(t) \tag{3.32}$$

The autocorrelation function for its α component is given by

$$C_M^{\alpha}(t) = \frac{1}{N\mu^2} \langle M_{\alpha}(t) M_{\alpha}(0) \rangle \tag{3.33}$$

The in-plane autocorrelation function, $C_M^{xy}(t) = [C_M^x(t) + C_M^y(t)]$ exhibits an extremely long decay time, orders of magnitude longer than the length of the simulation. In some cases, it hardly varied at all over the entire run. Nevertheless, we can extract some information from the $t = 0$ values, $C_M^{xy}(0)$. The in-plane susceptibility is proportional to $\left\langle M_x^2 + M_y^2 \right\rangle$. The values of $C_M^{xy}(0)$ are presented in Table 3.1. These show that the in-plane susceptibility increases dramatically above $\mu^* = 2.0$. This is due to the presence of chains.

The bulk magnetisation autocorrelation function for $\rho^* = 0.5$, with $\mu^* = 0.5$ and $\mu^* = 2.75$ is shown as an example in Fig. 3.16. The bulk magnetisation autocorrelation function is plotted in Fig. 3.16 for different dipole moments at each density. This exhibits the same kind of features as $C_{\mu}^{\alpha}(t)$. In particular, at high dipole moment there is a high frequency oscillation. The frequency is higher than in the case of $C_{\mu}^{\alpha}(t)$. To obtain an estimate of the frequency, a function of the form $C_M^z(t) \propto \exp(t/\tau) \cos \omega_0 t$ was fitted to the data in the region $0 < t^* < 10$. This yields $\omega_0^* \simeq 25$ and $\tau^* \simeq 3$ for $\mu^* = 2.75$, and $\omega_0^* \simeq 5$ and $\tau^* \simeq 0.5$ for $\mu^* = 0.5$. The initial value of $C_M^z(0)$ provides a measure of the out-of-plane susceptibility. These are shown in Table 3.1. The values decrease sharply above $\mu^* = 2.0$. This reflects the increasing planarity as dipoles line up in their nose-to-tail configurations within the chains. It would then difficult to align the dipoles along a field perpendicular to the plane. If we recall that $\chi = \frac{\partial M}{\partial H}$, this then means that the susceptibility will be small.

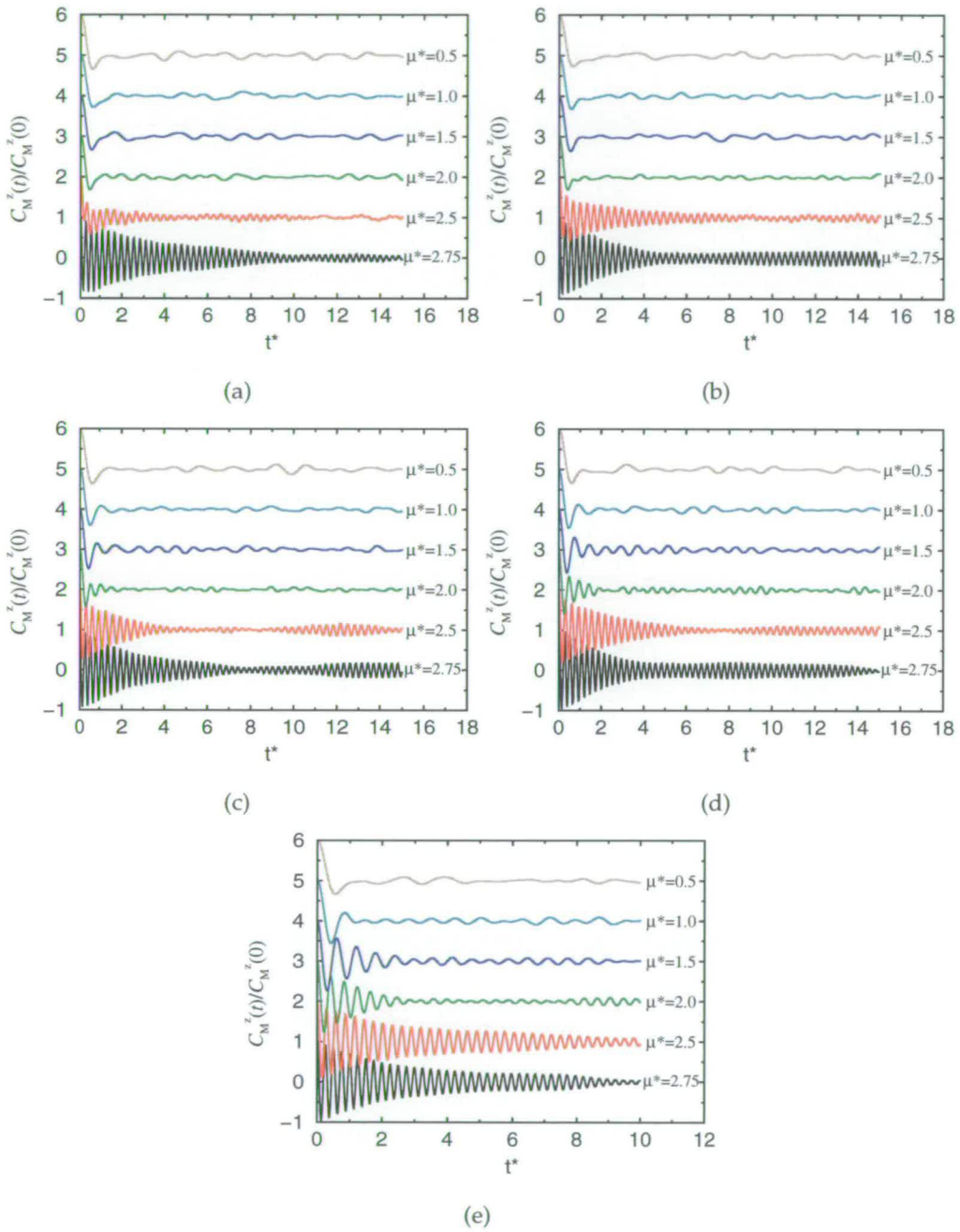

Figure 3.16: Autocorrelation function of the z component of the bulk magnetisation for different dipole moments at density (a) $\rho^* = 0.05$ (b) $\rho^* = 0.1$ (c) $\rho^* = 0.2$ (d) $\rho^* = 0.3$ (e) $\rho^* = 0.5$. Successive curves are displaced by one unit along the ordinate.

The Fourier transform of $C_M^z(t)$ is reported here normalised by its zero-time value:

$$\chi_M^z(\omega) = \frac{1}{2\pi C_M^z(0)} \int_{-\infty}^{\infty} C_M^z(t) \exp(-i\omega t) dt \tag{3.34}$$

This is plotted in Fig. 3.17. There is a sharp peak which shifts to higher frequency as dipole moment increases. For $\mu^* = 2.5$ and $\mu^* = 2.75$, this peak corresponds to the position of the high frequency shoulder in the single-particle rotational spectrum. This lends weight to the idea that there is some kind of coupling between single-particle motion and collective motions of chains. This coupling also gives rise to the shoulder in the single-particle spectrum.

Further work needs to be carried out to study the collective motions. In particular, it is possible that within the chains there could be excitations analogous to the spin waves in solid magnetic materials (see Chapter 5). This possibility could be investigated by measuring space- and time-dependent correlation functions such as $\langle \boldsymbol{M}(\boldsymbol{q}, t) \cdot \boldsymbol{M}(\boldsymbol{q}, 0) \rangle$, where $\boldsymbol{M}(\boldsymbol{q}, t)$ is a Fourier component of the bulk magnetisation, $\boldsymbol{M}(\boldsymbol{q}, t) = \sum_{j=1}^{N} \boldsymbol{\mu}_j(t) \exp[-i\boldsymbol{q} \cdot \boldsymbol{r}_j(t)]$.

3.7 Conclusions

We have investigated the structure and dynamics of quasi-two-dimensional dipolar fluids by means of molecular dynamics simulation. A major feature of these systems is the self-assembly of particles into chain-like aggregates, caused by the preference of dipoles on neighbouring particles to align in a nose-to-tail fashion. Chains start to appear above a dipole moment $\mu^* = 2$. Below this boundary, the structure appears as that of a 'normal' fluid.

In the structure factor, an important signature of the presence of chains is the power-law scaling at low wavevectors. The exponent was found to be $\alpha = 1.02 \pm 0.01$, consistent with the q^{-1} dependence expected for rod-like objects.

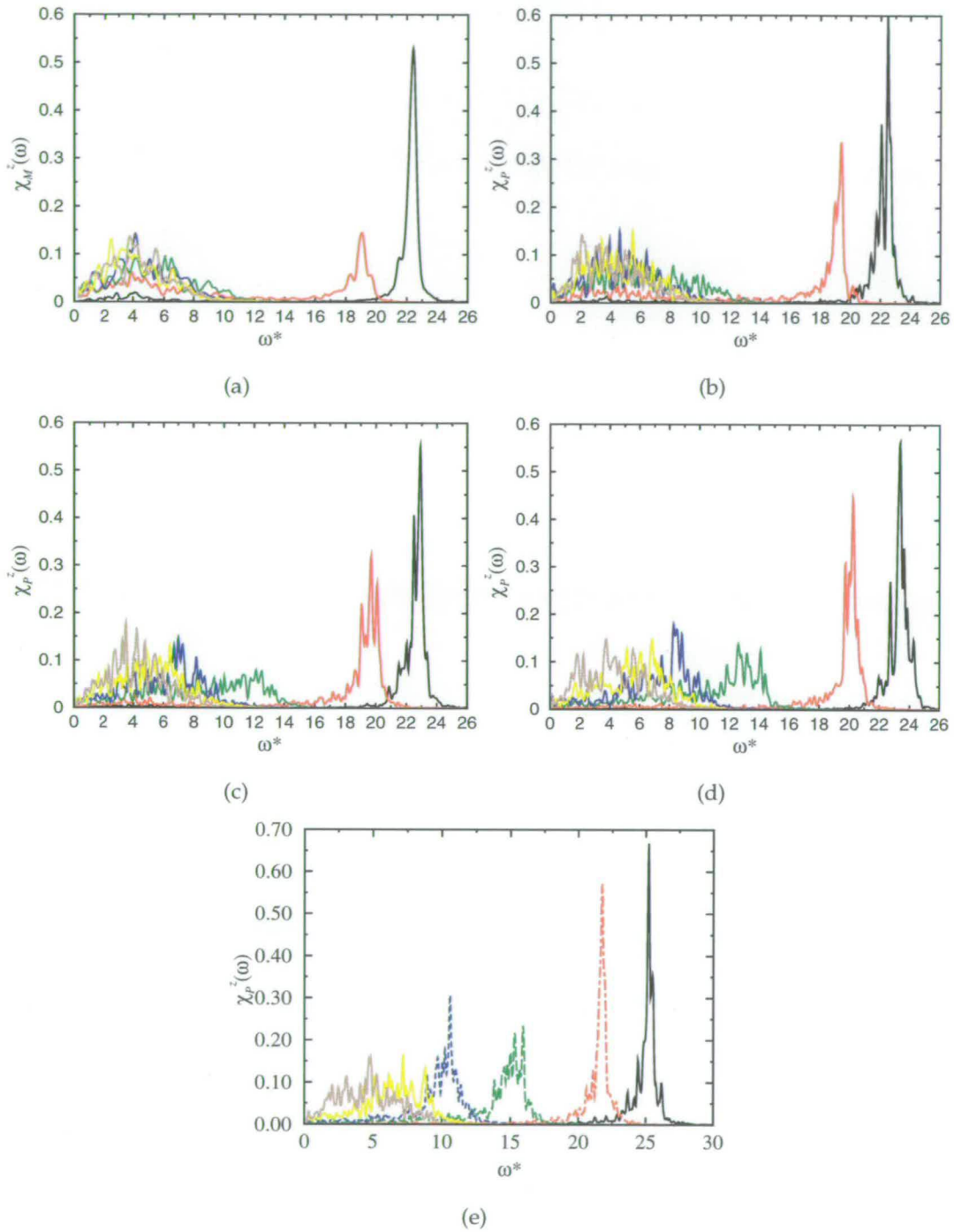

Figure 3.17: Fourier transforms of the z component of the magnetisation autocorrelation function at density (a) $\rho^* = 0.05$ (b) $\rho^* = 0.1$ (c) $\rho^* = 0.2$ (d) $\rho^* = 0.3$ and (e) $\rho^* = 0.5$. For each density, results are shown for dipole moments $\mu^* = 2.75$ (black), $\mu^* = 2.5$ (red), $\mu^* = 2$ (green), $\mu^* = 1.5$ (blue), $\mu^* = 1.0$ (yellow) and $\mu^* = 0.5$ (brown).

In two dimensions, there is a possibility that the velocity autocorrelation function could possess a 'long-time tail', decaying as t^-1, rather than exponentially. This can lead the diffusion coefficient as calculated from the Green-Kubo relation to be divergent. In all our simulations, the mean square displacement does appear to exhibit an asymptotic linear time dependence and we assume it is reasonable to extract diffusion coefficients using the Einstein relation. The diffusion coefficient decreases as density increases, as expected. However, there is a dramatic decrease as the dipole moment is increased above $\mu^* = 2$ at fixed density. This is because particles are trapped in chains, which restricts their motion.

The chaining which occurs at high values of the dipole moment has a profound effect on the dynamics. We see a separation of timescales between the motion of individual particles on the one hand, and the collective motion of these chains as a unit on the other.

The velocity autocorrelation function at high dipole moment displays an oscillation superimposed on the ordinary decay. This is attributed to back-and-forth motion of particles between their neighbours in the chains, while the chains themselves are moving with some 'drift' velocity.

The single-dipole autocorrelation function at high dipole moment exhibits oscillations due to the oscillation of individual dipoles about their equilibrium nose-to-tail configuration within chains. The characteristic frequencies of the oscillatory motion were extracted from the Fourier transform of the single-dipole autocorrelation function or the angular velocity autocorrelation function. The frequencies were found to be largely independent of density in the aggregated regime, indicating that interchain interactions are negligible. At low dipole moment, the frequency approaches the free-rotor limit. A high frequency shoulder develops on the peak in the spectrum, which we attribute to a coupling between single particle and collective motions. The collective dynamics is consistent with

this; the peak in the spectrum of the bulk magnetisation autocorrelation function appears at the same frequency as the shoulder.

CHAPTER 4

Aggregation kinetics of the dipolar fluid

In this chapter, we explore the mechanisms by which the structures in the dipolar fluid observed in Chapter 3 are formed during equilibration. We prepare the system in a 'random' configuration by performing a simulation at high temperature with dipole moment $\mu^* = 0$. Starting from one of these configurations, we 'switch on' the dipoles and monitor the aggregation progress by counting the clusters formed, classified as chains, rings or defect clusters.

We have already discussed the previous experimental and simulation work on dipolar fluids in Chapters 1 and 3. Here we will highlight the work that is most relevant to the study presented in this chapter.

Weis, Tavares and Telo da Gama [17, 18] carried out a detailed Monte Carlo study of the equilibrium structure of the quasi-two-dimensional dipolar fluid in the chaining regime. The aggregates were classified into three types: chains; rings and defect clusters. A distance criterion was used to identify which particles were in the same cluster. The clusters were characterised by their internal energy and the length distribution and conformational properties of the different types

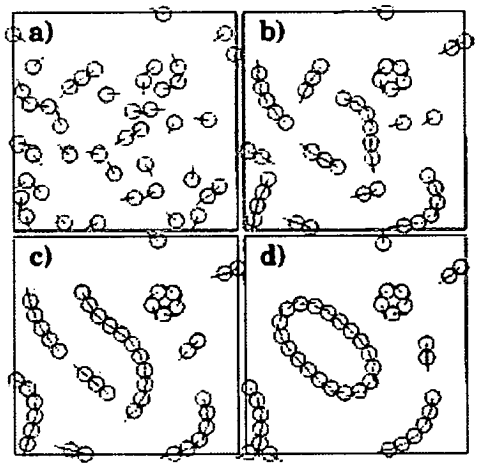

Figure 4.1: Ring formation mechanism proposed by Wen *et al.* [27].

of cluster. The fact that we have a system composed of linear structures in chemical equilibrium, with chains constantly breaking and reforming or exchanging segments suggests an analogy with equilibrium polymers. A comparison was made between the simulation results and various scaling laws from the standard theory of equilibrium polymers. The agreement was found to be favourable. In the work reported in this chapter, we have adopted the same classification of clusters into chains, rings or defect clusters to study the size distribution and conformation of the clusters changes during the aggregation process.

Wen *et al.* [27], as well as observing the aggregation of glass microspheres coated with nickel, also performed complementary molecular dynamics simulations. They proposed a mechanism for the formation of rings. This is illustrated in Fig. 4.1. Particles initially form into short chains (Fig. 4.1(a)). Chains which happen to be in the correct orientation join together to form longer chains (Fig. 4.1(b) and (c)). Side-by-side chains tend to form with their net magnetisation in opposite directions. Rings can form by the joining together of the ends of these neighbouring chains (Fig. 4.1(d)). We find, however, that chains are more likely to form by the joining together of the two ends of the same chain (see below).

Also relevant to the present chapter is the discussion on the existence of a vapour-liquid phase transition. Tlusty and Safran [6, 67] have proposed that there may be a different kind of phase transition which replaces the ordinary liquid-vapour transition. In their work they consider the chains of particles as the basic unit, rather than the individual particles themselves. The chains are free to break, reform and exchange segments. Y-shaped defects can be formed by the addition of one chain onto the side of another. The ends of a chain are also considered to be defects. Using a mean field theory, they demonstrated the possibility of a phase coexistence between a high density phase consisting of a network of chains connected by Y defects and a gas phase of separate chains (rich in end defects). It is found, however, that the concentration of Y defects is always low at equilibrium which might make it seem unlikely that such a phase transition could exist. In this chapter, we report our finding that there is a high transient concentration of defects during the aggregation process. This suggests that it might be possible to observe Tlusty and Safran's transition as a metastable phase transition.

4.1 Simulation details

The aggregation process in the quasi-two-dimensional dipolarfluid was studied via Brownian dynamics simulations using the same potential as in Chapter 3. The simulation needs to be carried out in a constant temperature ensemble. Since we are watching the process as the system comes to equilibrium from some non-equilibrium starting point, the potential energy is likely to decrease. If temperature were not kept constant, the kinetic energy must rise in order to conserve energy and hence aggregation might not occur.

We employ the Brownian dynamics algorithm derived by Jones and Alavi for particles with a preferred axis represented by a body-fixed unit vector (such as a

dipole moment vector) [81]:

$$\boldsymbol{r}_i(t+\Delta t) = \boldsymbol{r}_i(t) + \frac{D_t}{k_B T}\boldsymbol{F}_i(t)\Delta t + \boldsymbol{\zeta}_i^t \tag{4.1}$$

$$\hat{\boldsymbol{\mu}}_i(t+\Delta t) = \hat{\boldsymbol{\mu}}_i(t) + \frac{D_r}{k_B T}\boldsymbol{T}_i(t) \times \hat{\boldsymbol{\mu}}_i(t)\Delta t + \boldsymbol{\zeta}_i^r \times \hat{\boldsymbol{\mu}}_i(t)\ . \tag{4.2}$$

Here, $\boldsymbol{r}_i(t)$ and $\boldsymbol{\mu}_i(t)$ are the position and dipole moment, and $\boldsymbol{F}_i(t)$ and $\boldsymbol{T}_i(t)$ are force and torque on particle i at time t. Note that $\boldsymbol{\mu}_i(t)$ is a unit vector and it must be renormalised at the end of each time step. $\boldsymbol{\zeta}_i^t$ and $\boldsymbol{\zeta}_i^r$ are random vectors chosen from Gaussian distributions with the following moments:

$$\left\langle \boldsymbol{\zeta}_i^t \right\rangle = 0,\ \left\langle \boldsymbol{\zeta}_i^r \right\rangle = 0 \tag{4.3}$$

$$\left\langle \boldsymbol{\zeta}_i^t \cdot \boldsymbol{\zeta}_j^t \right\rangle = 4D_t\Delta t\delta_{ij},\ \left\langle \boldsymbol{\zeta}_i^r \cdot \boldsymbol{\zeta}_j^r \right\rangle = 6D_r\Delta t\delta_{ij}\ . \tag{4.4}$$

This algorithm ignores short-time inertial dynamics. In such schemes, the momentum variables are dropped from the equations of motion. This is reasonable if, as in this case, we are interested in the long-time configurational dynamics [53]. As can be seen from the mean square displacement plots in Chapter 3, the inertial regime last for a time of order 1, whereas the aggregation processes considered in this chapter take place over times orders of magnitude longer.

As in Chapter 3, the following reduced units are defined in terms of the energy (ϵ) and distance (σ) parameters in the potential: temperature $T^* = kT/\epsilon$; density $\rho^* = \rho\sigma^2$; dipole moment $\mu^* = (\mu^2/\epsilon\sigma^3)^{1/2}$; time $t^* = (\epsilon/m\sigma^2)^{1/2}t$; translational diffusion coefficient $D_t^* = (m/\epsilon\sigma^2)^{1/2}$; rotational diffusion coefficient $D_r^* = (m\sigma^2/\epsilon)^{1/2}$.

We use a timestep of $\Delta t^* = 0.01$ and integrate for 10^6 timesteps. All simulations were carried out at temperature $T^* = 1.0$. A system size of $N = 1024$ was

used. The diffusion coefficients were chosen to correspond with a typical real ferrofluid. The diffusion coefficients can be found from the Stokes laws

$$D_t = \frac{kT}{3\pi\eta d} \tag{4.5}$$

and

$$D_r = \frac{kT}{\pi\eta d^3}\,, \tag{4.6}$$

where T is the temperature, η is the viscosity of the solvent and d is the diameter of the particles. Using $T = 298\text{K}$, $d = 10\text{nm}$ and $\eta = 0.89 \times 10^{-3}\text{Pa s}$ (the viscosity of water) yields $D_t = 4.90 \times 10^{-11}\text{m}^2\text{s}^{-1}$ and $D_r = 1.47 \times 10^{6}\text{s}^{-1}$. To convert to reduced units, we use the density of magnetite ($5.046 \times 10^3\text{kg m}^3$) to calculate the mass of the particles. Since in all our simulations, $T^* = kT/\epsilon = 1.0$, we substitute $\epsilon = kT$. We arrive at $D_t^* = 3.9 \times 10^{-3}$ and $D_r^* = 1.2 \times 10^{-2}$. Initial configurations were prepared by simulations of soft spheres (i.e. $\mu = 0$) at $T^* = 10$, providing an essentially random configuration. For each state point, results were averaged over runs started from five different initial soft sphere configurations.

Aggregates were identified using the cluster counting method of Stoddard [82]. Clusters in which all particles are connected to exactly two others were counted as rings. Clusters in which any particle was connected to three or more others we call defect clusters. Otherwise the cluster is considered to be a chain.

In the cluster counting algorithm, it is necessary to have some criterion to decide whether a particular pair of particles are connected. In Refs. [17, 18], two particles were said to be connected if they are within a distance 1.15σ of each other. In Refs. [12, 13], an energy criterion was used. Two particles were said to be connected if their potential energy was lower than $0.7E_0$, where $E_0 = -2\mu^{*2}$ is the dipole-dipole energy for two particles with their dipoles aligned nose-to-tail at 'contact' (i.e. a distance σ apart). It can be argued that the energy criterion

should be more reliable. The energy criterion only counts particles if they are in the nose-to-tail configuration, as they are within chains. The distance criterion might tend to count particles that happen to come close to each other at a particular instant in time. For this reason, we chose to use an energy criterion.

We chose the value of the threshold in the manner of Weis and Levesque [12, 13], by considering the average dipole-dipole interaction energy with the first, second and third neighbours of a given particle. At a density $\rho* = 0.1$ and dipole moment $\mu^* = 2.75$, these were respectively $\overline{E}_1 = -13.3$, $\overline{E}_2 = -9.2$, $\overline{E}_3 = -1.52$. Since the particles are mostly in chains with two neighbours, we need to choose a threshold which will include the two nearest neighbours but exclude the third. The threshold chosen was $0.3E_0$. This is a considerably higher threshold energy than that used by Weis and Levesque, but it was chosen to ensure that particles in a variety of arrangements such as at a defect or at a sharp corner that may occur as a ring fluctuates were counted as being connected. We also performed some test runs using a distance criterion and obtained essentially the same results.

In order to check that the program is correctly sampling from the constant temperature it would be desirable to measure the instantaneous temperature during the course of the simulation. The usual way to do this is to measure the kinetic energy and use the equipartition theorem. However, since the Brownian Dynamics algorithm used in our case does not include inertial motion, the velocities, and hence the kinetic energy is not accessible. We therefore considered the configurational temperature [56, 57] which is based rather on the positions or orientations of the particles.

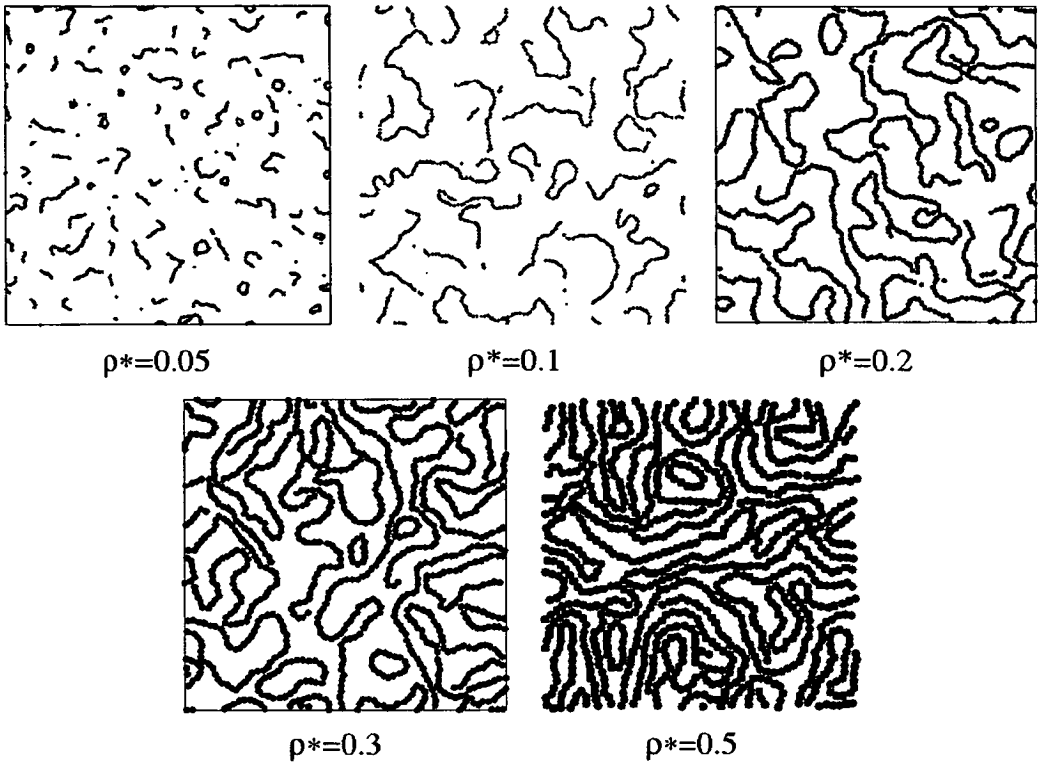

Figure 4.2: Final equilibrium configurations from simulations at the densities shown.

4.2 Results

Snapshots of the final equilibrium state of the system at different densities are shown in Fig. 4.2. These can be seen to be very similar to the structures observed in Chapter 3. This confirms that the two different simulation techniques generate essentially the same equilibrium configurations.

As a verification of the simulations, we measured the translational and orientational configurational temperatures. Fig. 4.2 shows the configurational temperature during the course of a run at density $\rho^* = 0.05$ and dipole moment $\mu^* = 2.75$. Both the translational and rotational temperatures settle rapidly on the expected value of $T^* = 1.0$.

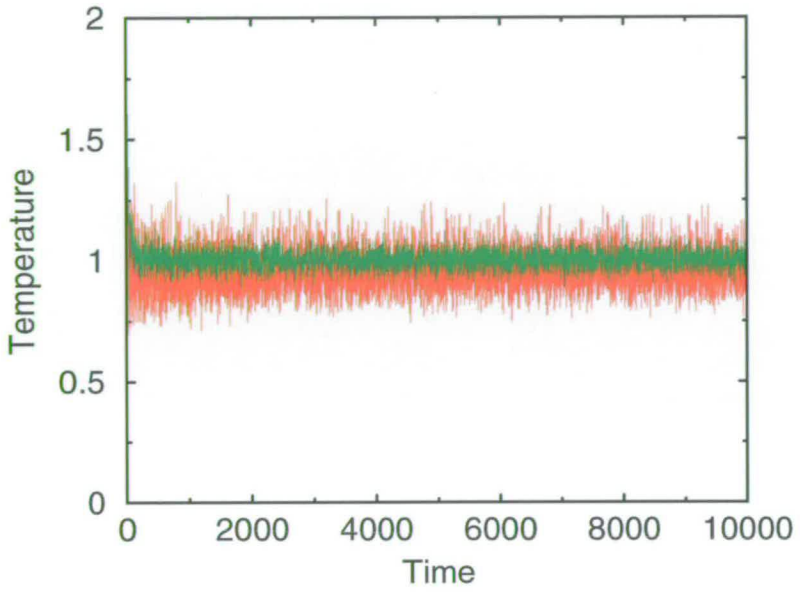

Figure 4.3: Translational (red) and orientational (green) configurational temperature for a run at density $\rho^* = 0.05$ and dipole moment $\mu^* = 2.75$.

In the rest of this section, we take each density in turn and and examine the cluster distributions as a function of time during equilibration. We concentrate on the case of high dipole moment $\mu^* = 2.75$, where at equilibrium, almost all particles are included in chains.

4.2.1 $\rho^* = 0.05$

Fig. 4.4 shows the number of clusters containing a particular number of particles as a function of time. We see that at time zero, virtually all the particles exist as monomers. As time increases, first dimers start to form and later trimers, then 4-mers etc. The number of clusters of a certain size successively rises to a peak and then falls. This points to a mechanism by which dimers form first, which then aggregate to form short chain segments. The segments join together to form longer chains, leading to the eventual decrease in the numbers of clusters with lower numbers of particles.

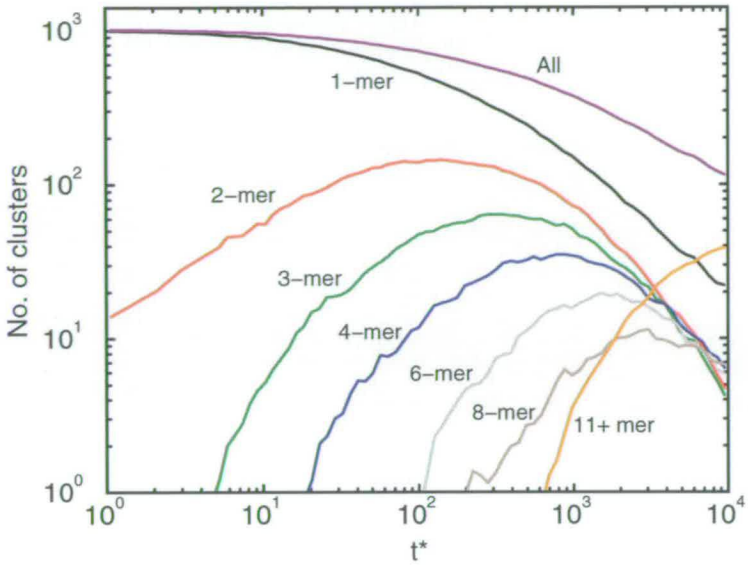

Figure 4.4: Number of clusters of a particular size as a function of time at density $\rho^* = 0.05$. 5, 7, 9 and 10-mers are omitted for clarity.

At this low density, the equilibration process is extremely slow. Even after 10^6 timesteps, the system has not yet come to equilibrium. At this density, the particles are on average far apart, and hence particles come into contact infrequently. The situation is exacerbated by the fact that we are using an integration algorithm which neglects inertial motion. Particles will only move in response to forces from surrounding particles or from the random forces. Presumably, the number of clusters with 11 or more particles will eventually level off.

We can further classify the clusters into chains, rings or defect clusters as mentioned in the introduction. Figure 4.5 shows the total number of each of these types of clusters as a function of time. The number of chains is initially high (monomers are counted as chains of length 1). After a certain amount of time, the number of chains declines and rings begin to form. Rings do not form until a significant number of chains has formed. This suggests that rings are formed from chains.

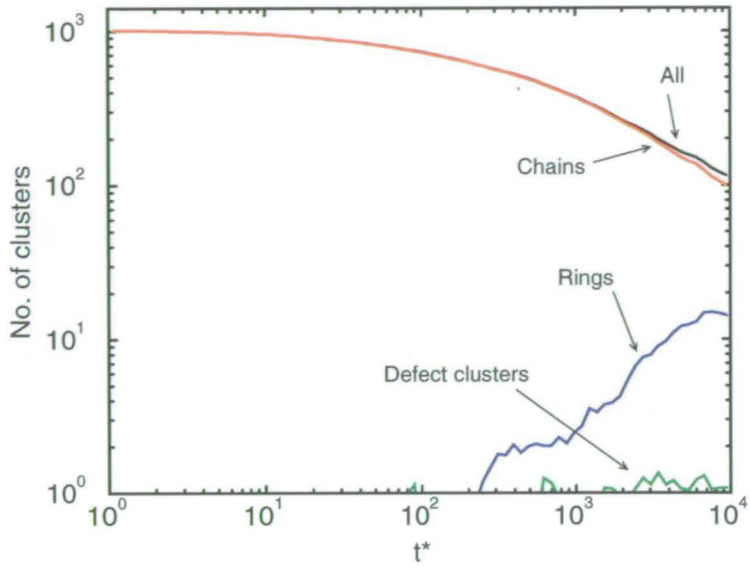

Figure 4.5: Total number of clusters of each type as a function of time at a density of $\rho^* = 0.05$.

The mechanism of ring formation is illustrated in fig. 4.6. First, short chains form from monomers and dimers. These chains come together to form longer chains. The chains fluctuate, and eventually the ends of the chain might come close enough that they snap together. The chain ends will already be in the correct orientation to form the new nose-to-tail interaction in the ring. A different mechanism was proposed by Wen *et al.* [27] on the basis of their Molecular Dynamics simulations. They suggested that when short chains form in the early stages of aggregation, side-by-side chains will tend to form with their net polarisation in opposite directions. The chains must then be in the correct orientation so that their ends can join together to form a ring. However, according to our observations this seems to be a marginal process. It requires two or more chains to come together with very specific mutual orientations.

4.2.2 $\rho^* = 0.1$

Figure 4.7 shows the cluster sizes as a function of time for a density of $\rho^* = 0.1$. As before, the system passes to larger and larger cluster sizes, with each size suc-

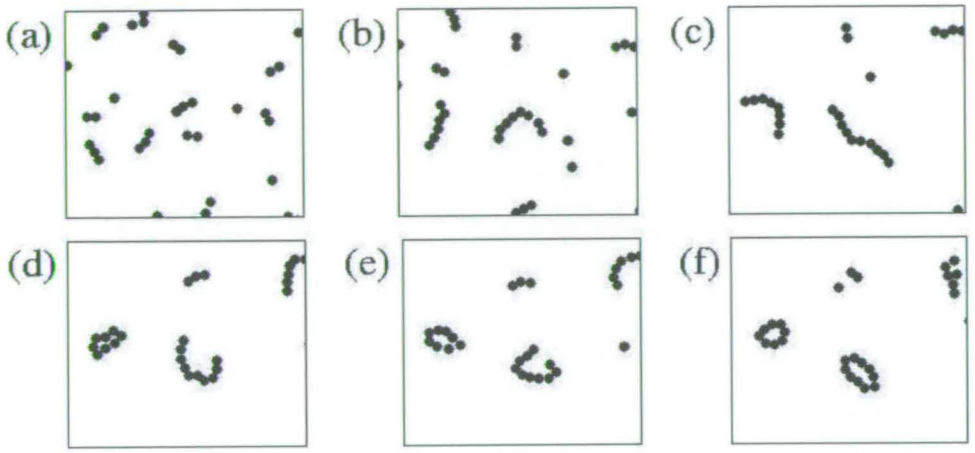

Figure 4.6: Ring formation mechanism. Snapshots from a run at a density $\rho^* = 0.05$.

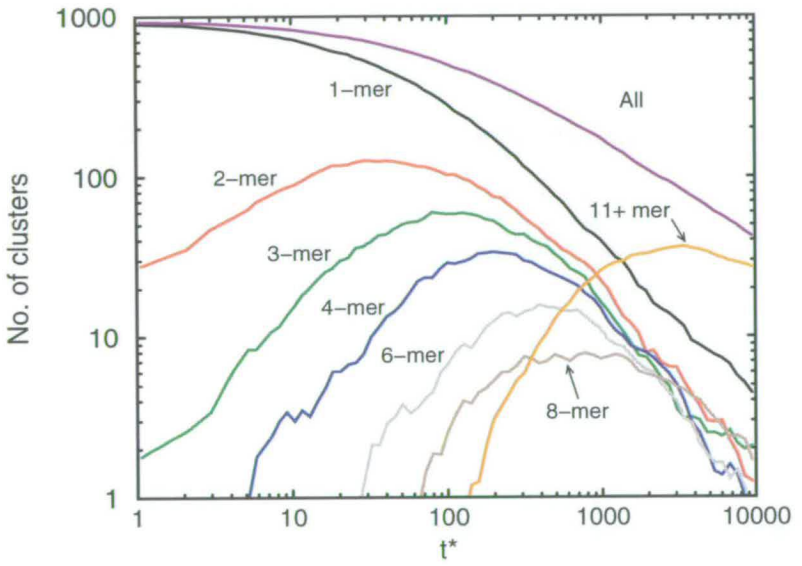

Figure 4.7: Number of clusters of a particular size as a function of time at density $\rho^* = 0.1$. 5, 7, 9 and 10-mers are omitted for clarity.

cessively reaching a peak and declining. The mechanism is again the formation of small chains which join together to form larger chains and rings.

Figure 4.8 breaks down the cluster distribution into the different types. As before, we see the formation of rings only after a significant number of small chains has formed. At this density there are fewer rings, but more defect clusters compared to $\rho^* = 0.05$. This is due to the fact that at this higher density, particles are on

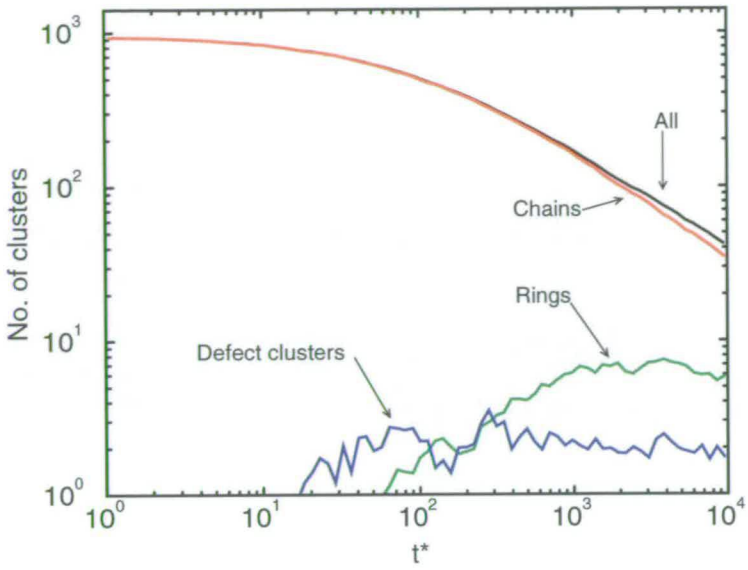

Figure 4.8: Total number of clusters of each type as a function of time at a density of $\rho^* = 0.1$.

average closer together. There will be more collisions between clusters, leading to the break-up of chains and the joining together of chains to form a defect.

4.2.3 $\rho^* = 0.2$

Figure 4.9 shows the number of particles in clusters of a certain size. Again the formation of longer and longer chains is seen. The number of clusters with 11 or more particles levels off as the system reaches equilibrium. Figure 4.10 shows the numbers of different types of clusters. There are less rings and more defect clusters than at lower density. The number of defect clusters increases, reaches a peak and declines again. A process involving the formation of a defect is shown in Fig. 4.11. Two initially separate chains wriggle about and one attaches to the side of the other. At this point, two things could happen. Either the attached chain falls off, or, as in the case of Fig. 4.11, the defect cluster can break in another way at the point of the defect, with a segment exchanged from one chain to the other. When chains form initially in the system, there are many chains

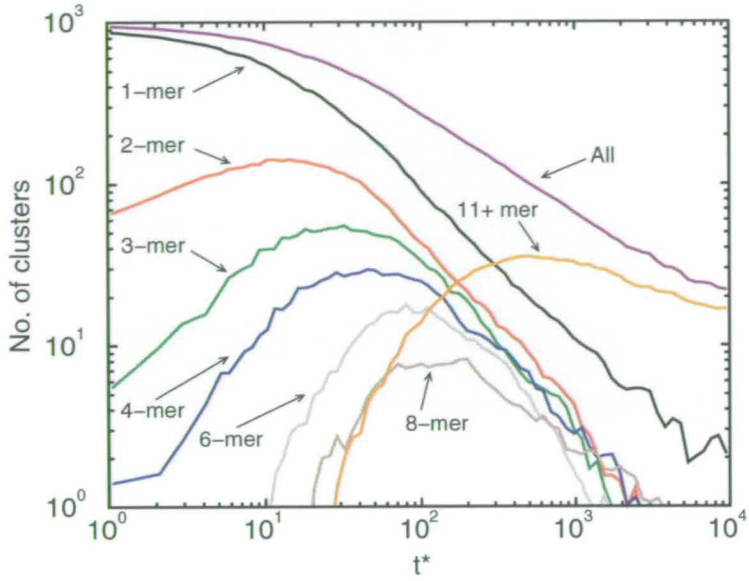

Figure 4.9: Number of clusters of a particular size as a function of time at density $\rho^* = 0.2$. 5, 7, 9 and 10-mers are omitted for clarity.

formed close to each other and so many defects form. By the kind of process described above, chains continually interact and exchange segments. This allows the chains to disentangle, and the number of defects decreases as the system reaches equilibrium.

The question arises whether we could have clusters with more than one defect. Figure 4.12 gives the number of clusters containing at least one defect and the number of defect *particles*, defined as particles with three or more neighbours. The number of defect particles is roughly equal to the number of defect clusters, meaning there is usually only one defect per defect cluster.

4.2.4 $\rho^* = 0.3$

Figure 4.13 shows the same trend of initially small chains forming which join together to form larger aggregates. The processes occur more quickly because the particles are on average closer together at this higher density.

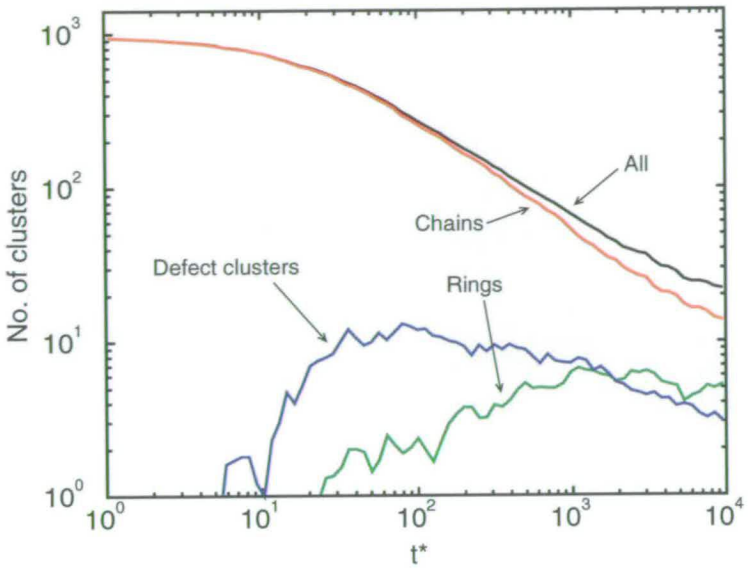

Figure 4.10: Total number of clusters of each type as a function of time at a density of $\rho^* = 0.2$.

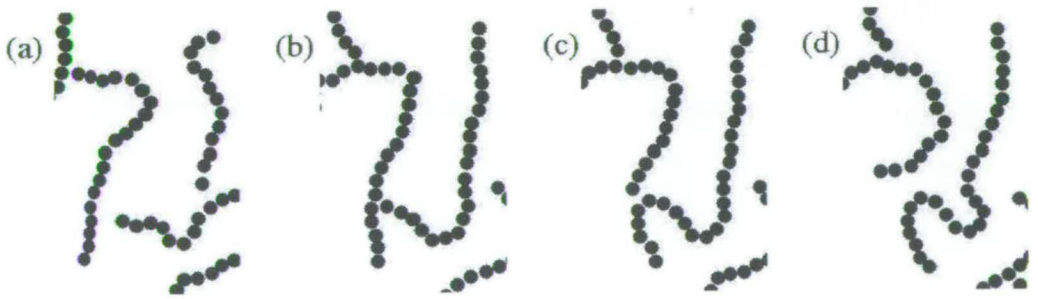

Figure 4.11: Process involving the creation of a defect. Snapshots from a run at $\rho^* = 0.2$.

Already in the 'random' initial configurations, some particles by chance are close together and are counted as dimers by the cluster counting algorithm, hence we see a small population of dimers and trimers at time zero.

Figure 4.14 shows the distribution of cluster types. The numbers of rings and defect clusters are now approximately equal at equilibrium. The rise and fall in the number of defect clusters is again prominent. From Fig. 4.15 we can see that the actual number of defects is much greater than the number of defect clusters,

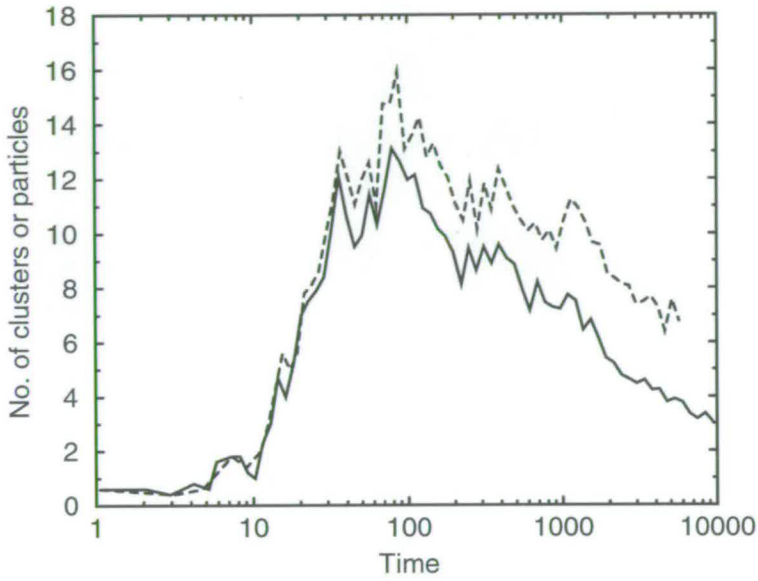

Figure 4.12: Number of defect clusters (solid line) and number of defect particles (dashed line) as a function of time at density $\rho^* = 0.2$.

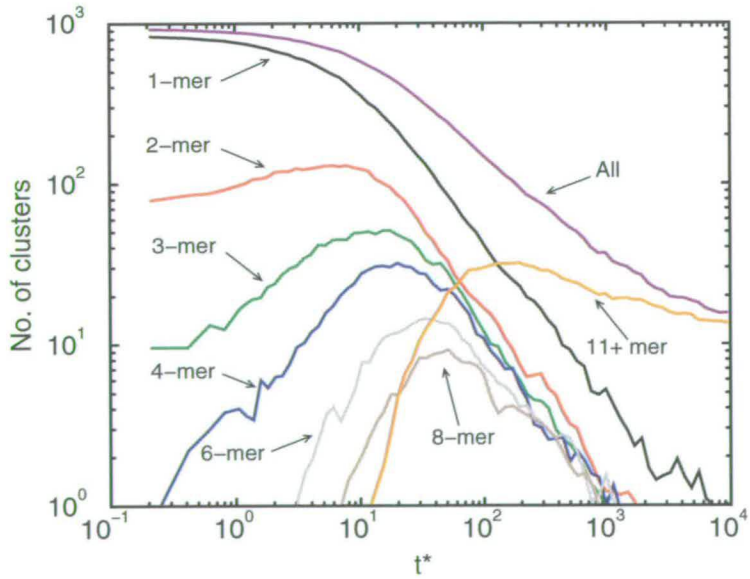

Figure 4.13: Number of clusters of a particular size as a function of time at density $\rho^* = 0.3$. 5, 7, 9 and 10-mers are omitted for clarity.

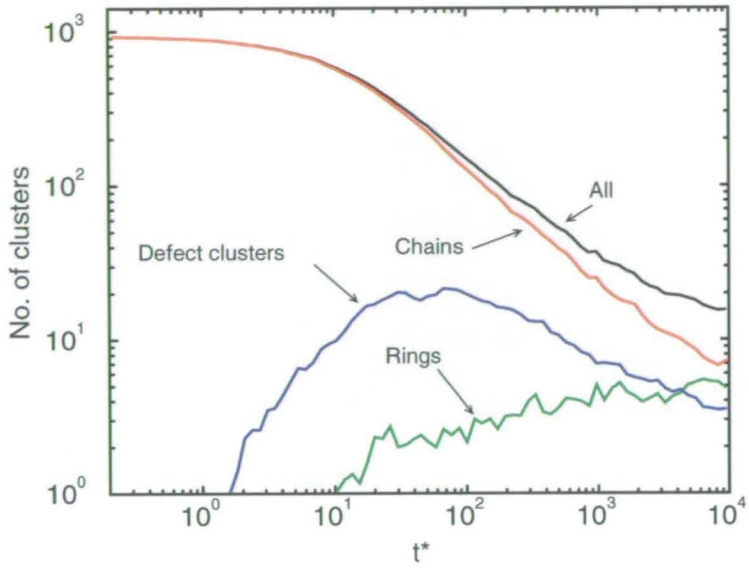

Figure 4.14: Total number of clusters of each type as a function of time at a density of $\rho^* = 0.3$.

i.e. there are many chains with more than one branching point. There is an interconnected network of chains, at least in the intermediate stages of equilibration.

4.2.5 $\rho^* = 0.5$

At this density, equilibration proceeds quickly (Fig. 4.16). The initial aggregation into short chains is very rapid, after which the chains link together to form longer chains. Significant numbers of particles have already, by chance, formed into dimers and trimers at time zero.

Figure 4.17 shows that very few rings are formed at this density. The number of defect clusters increases and reaches a large maximum at intermediate time. The chains have little room for manoeuvre and defects form easily. Figure 4.18 shows that there are many defects per defect cluster. There are many branching points on each chain, giving an interconnected network of chains. The kind of processes outlined above whereby chains exchange segments will occur. This will eventually disentangle the network of chains and we are left with a 'stringy' structure

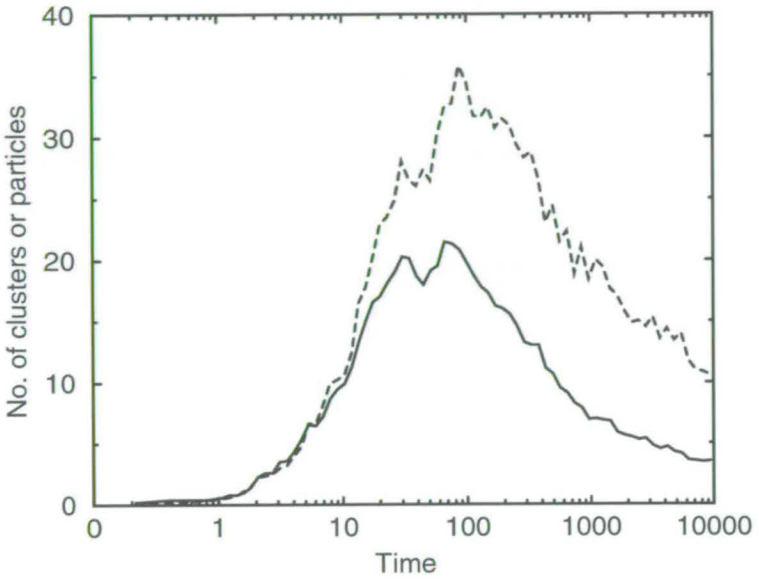

Figure 4.15: Number of defect clusters (solid line) and number of defect particles (dashed line) as a function of time at density $\rho^* = 0.3$.

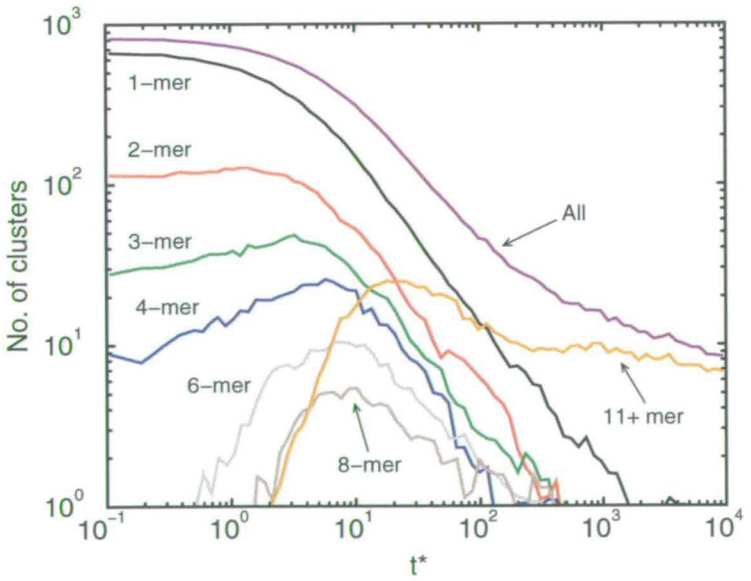

Figure 4.16: Number of clusters of a particular size as a function of time at density $\rho^* = 0.5$. 5, 7, 9 and 10-mers are omitted for clarity.

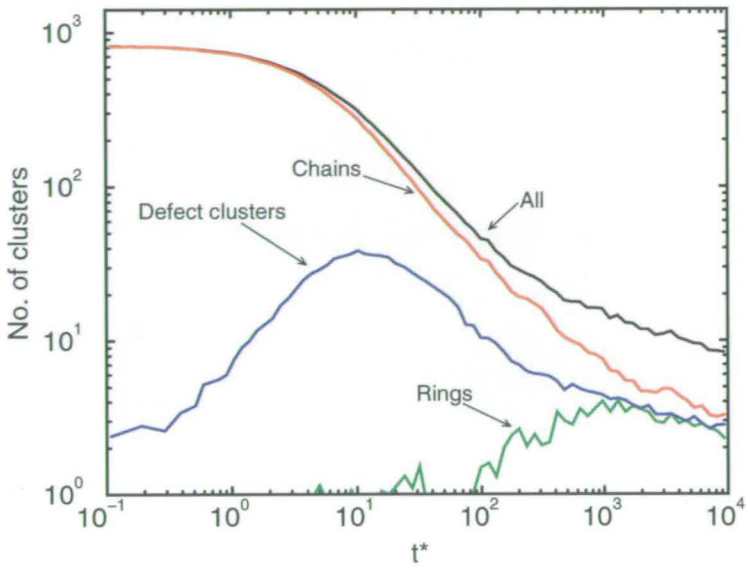

Figure 4.17: Total number of clusters of each type as a function of time at a density of $\rho^* = 0.5$.

with areas of parallel chains (with dipole moments in neighbouring chains pointing parallel or antiparallel), as can be seen from the equilibrium snapshots in Fig. 4.2 and also in Chapter 3. This is reflected in the decline in the number of defect clusters seen in Figs. 4.17 and 4.18.

4.2.6 *Fits using solutions to Smoluchowski coagulation equation*

In our system there is an aggregation process starting from monomers which join to form dimers which can then join with other monomers or previously formed dimers and so on, producing larger and larger aggregates. This kind of process has been studied extensively since 1917, when Smoluchowski studied the kinetics in the context of the coalescence of liquid droplets [83]. If we consider the elementary process of a cluster of size i combining with an cluster of size j to form an cluster of size $i + j$, its rate is given by

$$rate = K_{ij}\rho_i\rho_j \ , \tag{4.7}$$

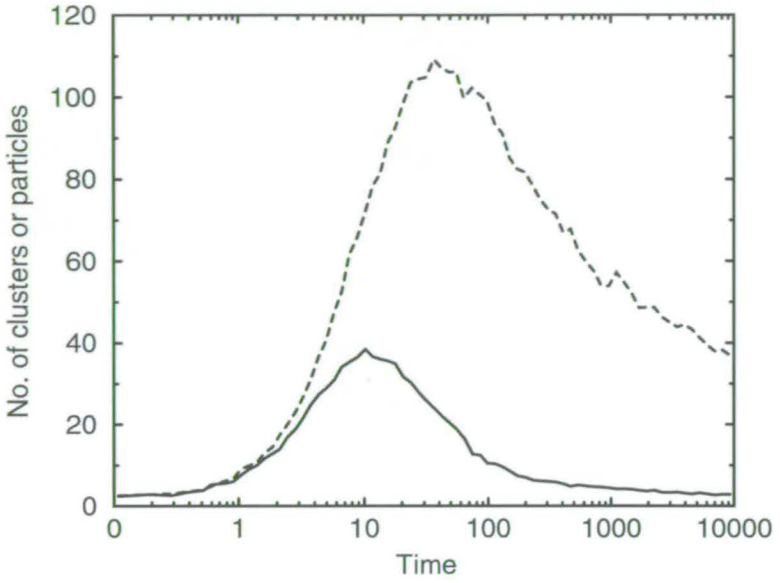

Figure 4.18: Number of defect clusters (solid line) and number of defect particles (dashed line) as a function of time at density $\rho^* = 0.5$.

where K_{ij} is the rate constant, ρ_i is the number of clusters of size i per unit volume and ρ_j is the number of clusters of size j per unit volume. The overall rate of production of clusters of size n is then given by the Smoluchowski coagulation equation:

$$\frac{d\rho_n}{dt} = 1/2 \sum_{i+j=n} K_{ij}\rho_i\rho_j - \rho_n \sum_{i=1}^{\infty} K_{ni}\rho_i \; . \tag{4.8}$$

The first term on the right hand side describes all the combinations of clusters of sizes i and j which form clusters of size n. The second term describes the removal of clusters of size n by combining with clusters of any size. In order to solve this equation for ρ_n, we need some model of how the 'coagulation kernel', K_{ij}, depends on i and j. The case where K_{ij} is a constant K is straightforward [84].

We define $\rho_\infty = \sum_{i=1}^{\infty} \rho_i$ as the total number of clusters per unit volume. Summing Eq. (4.8) over all values of n gives

$$\frac{d\rho_\infty}{dt} = \frac{K}{2} \sum_{n=1}^{\infty} \sum_{i+j=n} \rho_i\rho_j - K\rho_\infty^2 \; . \tag{4.9}$$

Expanding the summation gives

$$\frac{d\rho_\infty}{dt} = \frac{K}{2}\rho_\infty^2 - K\rho_\infty^2 \tag{4.10}$$

$$= -\frac{K}{2}\rho_\infty^2 \,. \tag{4.11}$$

The solution is

$$\rho_\infty = \frac{\rho_0}{1+\frac{1}{2}K\rho_0 t} \,, \tag{4.12}$$

where $\rho_0 = \rho_\infty(0)$ is the number of monomers per unit volume at time zero. For $n = 1$, Eq. (4.8) becomes

$$\frac{d\rho_1}{dt} = -K\rho_1\rho_\infty \,, \tag{4.13}$$

the solution of which is

$$\rho_1 = \frac{\rho_0}{(1+\frac{1}{2}K\rho_0 t)^2} \tag{4.14}$$

For $n = 2$, we obtain

$$\rho_2 = \frac{\rho_0(\frac{1}{2}K\rho_0 t)}{(1+\frac{1}{2}K\rho_0 t)^3} \,, \tag{4.15}$$

and the general case is

$$\rho_n = \frac{\rho_0(\frac{1}{2}K\rho_0 t)^{n-1}}{(1+\frac{1}{2}K\rho_0 t)^{n+1}} \,. \tag{4.16}$$

Fits were made to the data for the number of clusters, with K as an adjustable parameter. The fit parameters obtained are shown in Table 4.1. The results are shown in Fig. 4.19. The Smoluchowski theory gives a qualitatively correct representation of the data. Peak positions are roughly correct but the fitted curve deviates from the data at short times and long times. The rate constants increase with increasing density. This is because the particles are on average closer together, and so the aggregation process will be quicker. Although Eqs. (4.12) and (4.14)–(4.16) are derived with the assumption that the coagulation kernel is constant, we have performed a separate fit for each cluster size. The fact that the value of k determined from the fit decreases as the size of the cluster increases

	K^*				
	$\rho^* = 0.05$	$\rho^* = 0.05$	$\rho^* = 0.05$	$\rho^* = 0.05$	$\rho^* = 0.05$
1-mers	0.072(4)	0.105(4)	0.170(4)	0.27(1)	0.63(4)
2-mers	0.068(4)	0.111(4)	0.183(4)	0.33(1)	0.79(4)
3-mers	0.060(4)	0.094(4)	0.168(5)	0.29(1)	0.85(5)
4-mers	0.043(2)	0.078(3)	0.171(5)	0.273(7)	0.76(4)
5-mers	0.040(2)	0.079(4)	0.180(5)	0.269(8)	0.72(3)
6-mers	0.035(2)	0.066(3)	0.147(4)	0.264(7)	0.76(4)
7-mers	0.028(2)	0.060(3)	0.136(3)	0.257(8)	0.77(4)
8-mers	0.028(2)	0.057(3)	0.146(5)	0.254(8)	0.85(5)
9-mers	0.031(3)	0.061(3)	0.128(6)	0.242(9)	0.79(4)
10-mers	0.024(2)	0.041(3)	0.124(6)	0.217(9)	0.83(4)
All	0.049(3)	0.085(4)	0.157(4)	0.250(8)	0.57(3)

Table 4.1: Values of K as determined by fits using Eqs. (4.12) and (4.14)–(4.16).

shows that this assumption may not be correct. The decrease may be due to the fact that in order for a chain to grow, other chains must usually add onto one of the ends, which becomes less likely for longer chains. Another assumption of the Smoluchowski model is that the clusters can grow by the addition of monomers or other clusters, but do not break apart once formed. This may be a reasonable assumption at the early stages of the aggregation process, but clearly at longer times, much more complicated processes are occurring, as has been shown above. Thus the simple Smoluchowski model used here does not provide a good description of the aggregation process at long times. This is particularly the case at the highest densities, where the defect concentration is high, and, for example, events can occur exchanging chain segments (see Fig. 4.11).

4.3 Phase transition

We now consider the possibility of observing the phase transition proposed by Tlusty and Safran [6] between a low density phase with a high concentration of end defects and a high density phase with a high concentration of Y or X defects, forming a interconnected network structure. We would be most likely to observe the transition, then, under conditions where at low density phase there

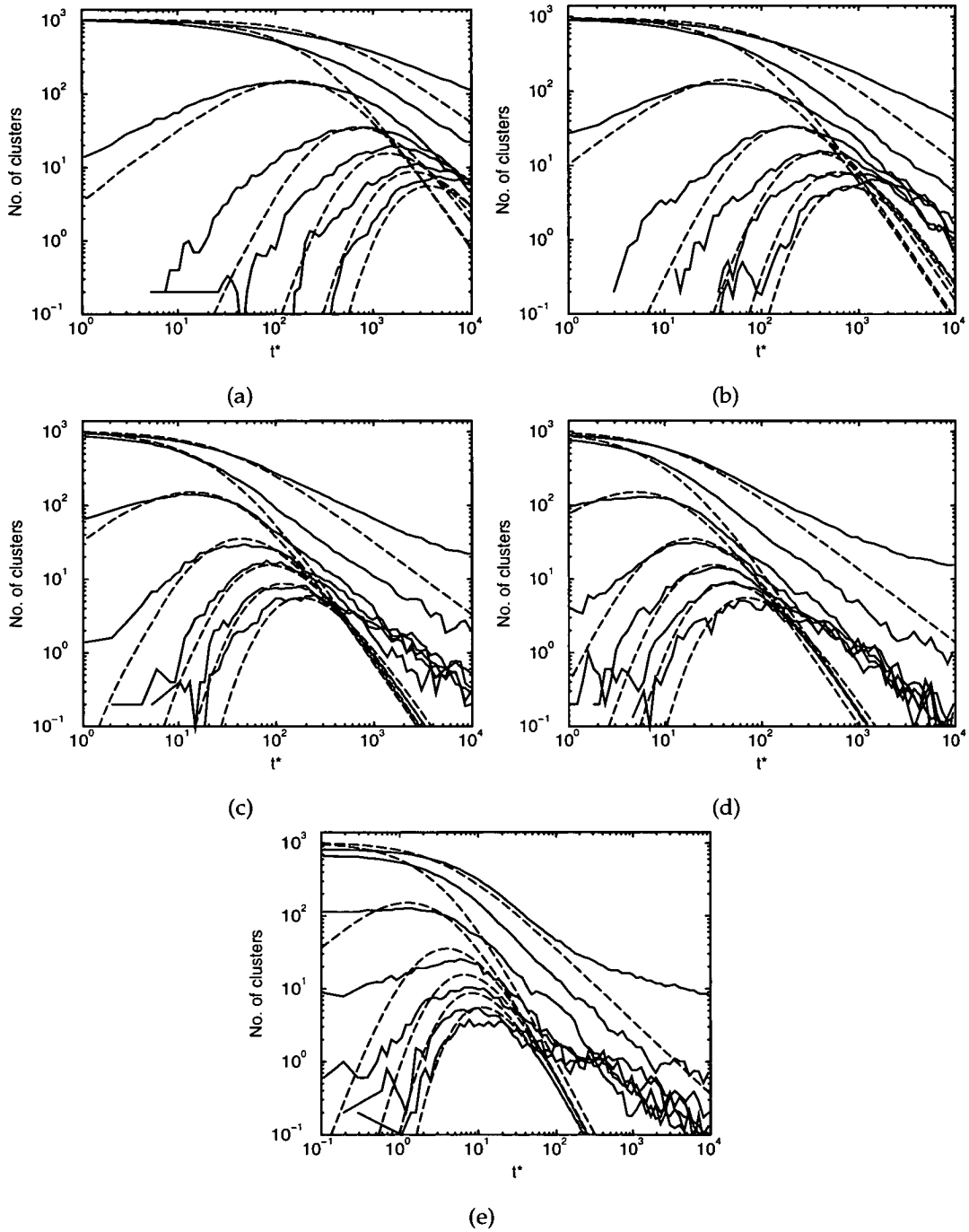

Figure 4.19: Numbers of clusters of a certain size per unit area as a function of time at density (a) $\rho^* = 0.05$, (b) $\rho^* = 0.1$, (c) $\rho^* = 0.2$, (d) $\rho^* = 0.3$, (e) $\rho^* = 0.5$, along with fits using solutions to Smoluchowski equation. From top to bottom on each graph: total, 1-mers, 2-mers, 4-mers, 6-mers, 8-mers, 10-mers.

		$\rho^* = 0.1$				$\rho^* = 0.5$			
μ^*	t^*	$x_0(t)$	$x_1(t)$	$x_2(t)$	$x_3(t)$	$x_0(t)$	$x_1(t)$	$x_2(t)$	$x_3(t)$
2	∞	0.65	0.27	0.06	< 0.01	0.14	0.38	0.42	0.05
2.25	∞	0.29	0.34	0.30	< 0.01	0.05	0.26	0.62	0.07
2.5	∞	0.05	0.15	0.73	< 0.01	0.01	0.10	0.84	0.06
2.75	∞	0.02	0.06	0.83	< 0.01	< 0.01	0.02	0.94	0.04
2.75	80	0.55	0.39	0.19	< 0.01	0.02	0.13	0.75	0.10
2.5	80	0.41	0.39	0.12	< 0.01	0.03	0.20	0.66	0.10

Table 4.2: Fraction of particles, $x_n(t)$, having n neighbours at time t^* (equilibrium labelled as $t^* = \infty$).

is a high concentration of end defects but low concentration of Y/X defects and at high density there is a high concentration of Y/X defects but a low concentration of end defects. Additionally, since the chains are the basic units in Tlusty and Safran's theory, we also require that particles are mostly in clusters, i.e. that there is a low concentration of free monomers. We demonstrate below that these conditions are best met at high dipole moment, at a time of $t^* \sim 10^2$ where there is a transient peak in the number of Y and X defects.

We now use the densities $\rho^* = 0.1$ and $\rho^* = 0.5$ to exemplify the low and high density phases implicated in the phase transition of Tlusty and Safran. Table 4.2 lists the fraction of particles, x_n with n neighbours at equilibrium ($t^* = \infty$) and at an intermediate time during the aggregation process. The trends can be seen more clearly in Figs. 4.20 and 4.21, where the x_n are plotted as a function of time during the aggregation process for the two densities.

Let us consider first the case at equilibrium. We require that there is a high concentration of Y defects in the high density phase but the concentration of Y defects (x_3) is always low at equilibrium because the Y defect is energetically unfavourable. Even at the highest density studied here, $\rho^* = 0.5$, the equilibrium structure consists of parallel chains with little cross-branching. If we go to lower dipole moment (or equivalently higher temperature), the Boltzmann weight for a state with Y defects may be higher because of the lower energy cost of defect.

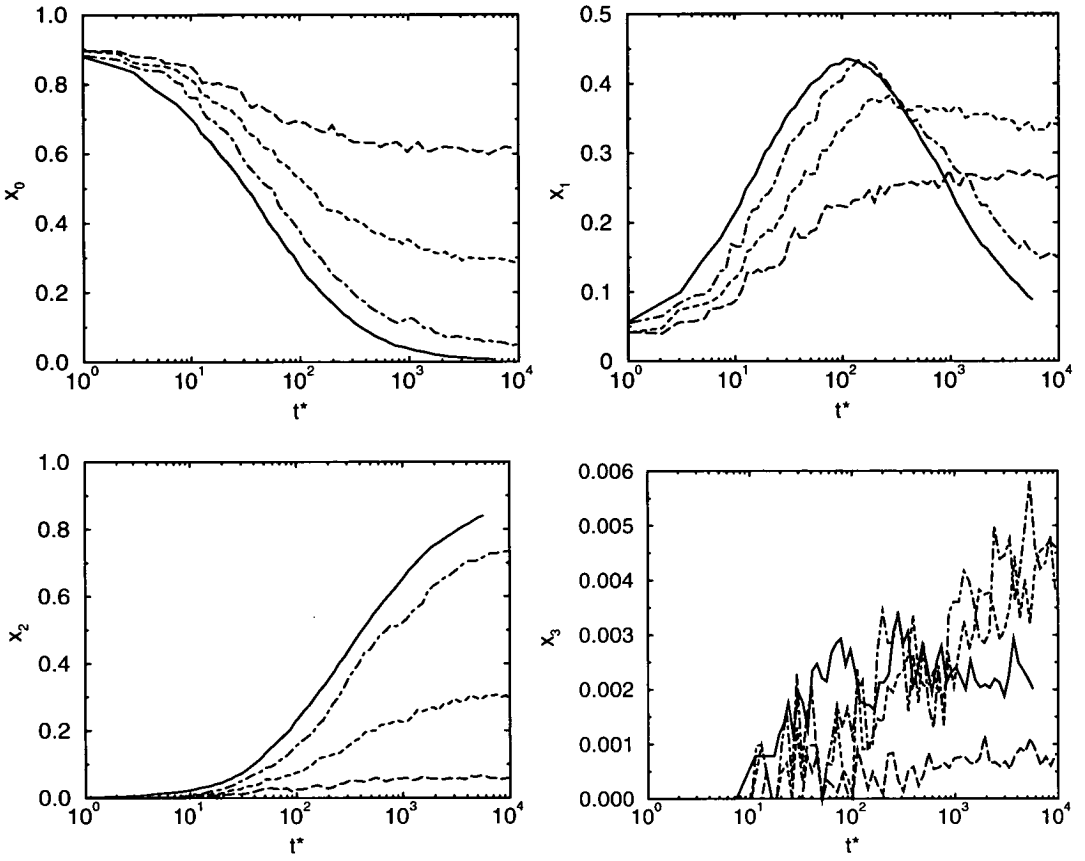

Figure 4.20: Fraction of particles, x_n, having n neighbours as a function of time at density $\rho^* = 0.1$ and different dipole moments: $\mu^* = 2.75$ (solid lines); $\mu^* = 2.5$ (dot-dashed line); $\mu^* = 2.25$ (dashed line); $\mu^* = 2$ (long dashed line).

(Alternatively, at higher temperature, states with higher energy are relatively more probable). It can be seen from Table 4.2 and Fig. 4.21 that at high density the equilibrium value of x_3 does indeed increase with decreasing dipole moment. However, the number of free monomers also increases as the dipole-dipole interactions become weaker with respect to the thermal energy.

As has been noted earlier, at high dipole moment and high density, there is a large transient concentration of Y defects. It can clearly be seen from Fig. 4.21 that the peak value of x_3 at $\mu^* = 2.75$ is higher than the equilibrium value at any dipole moment. Similarly, at low density, it can be seen from Fig. 4.20 that the peak end defect concentration (x_1) at $\mu^* = 2.75$ is higher than the equilibrium

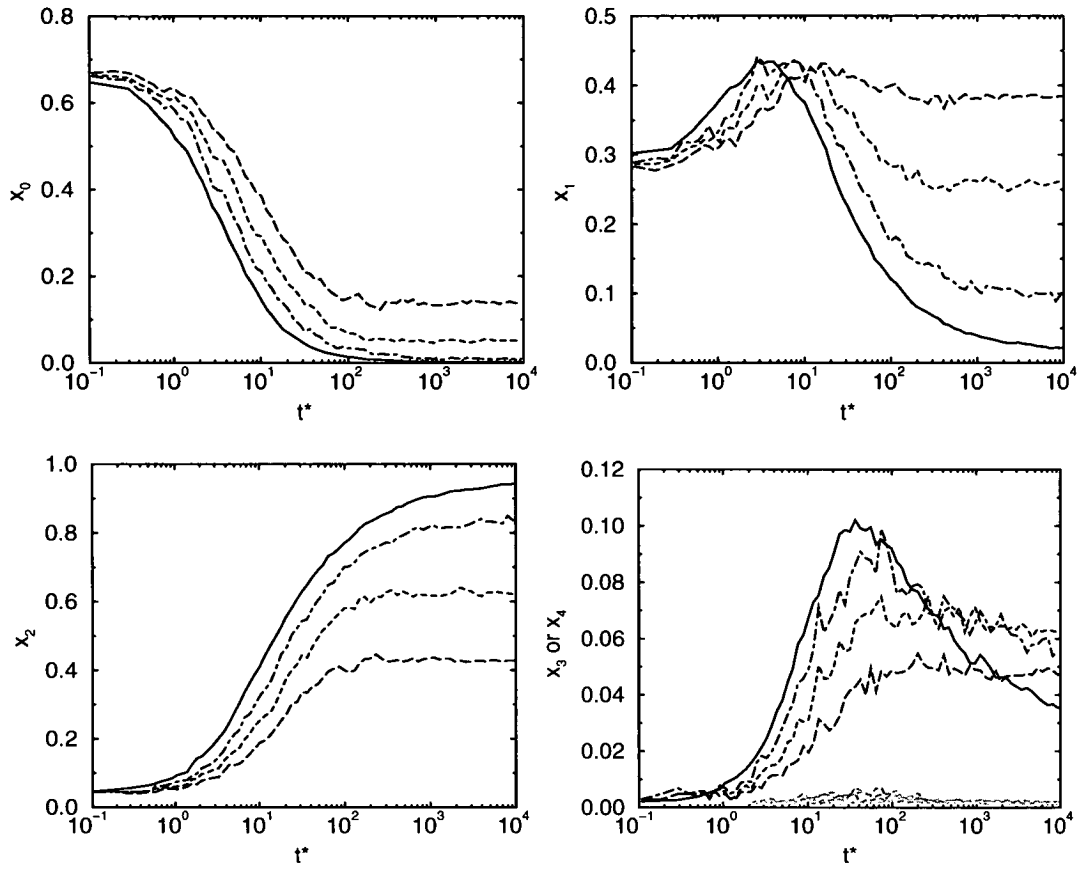

Figure 4.21: Fraction of particles, x_n, having n neighbours as a function of time at density $\rho^* = 0.5$ and different dipole moments: $\mu^* = 2.75$ (solid lines); $\mu^* = 2.5$ (dot-dashed line); $\mu^* = 2.25$ (dashed line); $\mu^* = 2$ (long dashed line). The fraction of particles with four neighbours, x_4, is shown in grey.

value at any dipole moment. The conditions that the end defect concentration is high in the low density phase and the Y defect concentration is high in the high density phase are thus better met at a time of $t^* \sim 10^2$ with high dipole moment than at equilibrium with a lower dipole moment. What is not so ideal is that at the time $t^* \sim 10^2$, there are still many free monomers which have not yet been included in any aggregates. However, comparison of the values of $x_0(t^* = 80)$ for high dipole moment and $x_0(t^* = \infty)$ for low dipole moment shows that the transient high dipole case is at least competitive with the equilibrium low dipole case in terms of the number of free monomers.

The observation that the conditions for the Tlusty-Safran transition are best met at high dipole moment at intermediate times during aggregation leads us to suggest that it might be possible to see the Tlusty-Safran transition as a metastable phase transition if the system could somehow be trapped in the transient network state. Experimentally, this could be achieved by creating some sort of short-range force between the particles, e.g. a depletion force induced by adding a polymer to the system, or by some sort of chemical reaction. In this way, the transient network might be stabilised long enough for phase separation to occur.

4.4 Conclusions

The aggregation of dipolar particles to form chains and rings has been studied by Brownian dynamics simulation. At all densities, short chains quickly form from neighbours which happen to be close in the initial configuration. These chains can then join together to form longer chains. This kind of process is continually repeated, and we see the number of particles in clusters of increasing size successively rise to a peak and then decline. The equilibration process occurs faster at higher density because the particles are on average closer together. Under assumptions about the coagulation kernel, solutions to the Smoluchowski equation can be obtained. In our case, we fit the solutions obtained for constant coagulation kernel [85] to our data for the numbers of clusters of different sizes. Better fits were obtained at higher density than at lower density.

As well as chains, closed rings and defect clusters are formed. The most prevalent mechanism of ring formation seems to be the joining together of the two ends of the same chain. This is different to the mechanism proposed by Wen *et al.* [27], whereby two or more neighbouring chains join together. Rings are most common at low density. Defect clusters become more common at higher density. At the higher densities, once some short chains have been created, a

highly branched network of chains is formed. This network disentangles by processes which swap segments at the point of the defect, and by the time we reach equilibrium, only the occasional defect remains.

We have discussed the possible relevance of our results to the phase transition proposed by Tlusty and Safran [6]. They predict a phase coexistence between a high density branched network and low density gas of chains, which would replace the ordinary liquid-gas phase transition. For this scenario to be realised, we require that the structure at high density has a high concentration of junction (Y and X) defects but a low concentration of end defects and that the structure at low density has a high concentration of ends but low concentration of junctions. The problem is that few junction defects are ever seen at equilibrium, making the Tlusty-Safran transition seem unlikely. The best case at equilibrium is obtained at lower dipole moment, where the energy cost of a junction defect is not so high. However, we have shown that, at high density, the peak transient concentration of junction defects during aggregation is greater than the equilibrium concentration at any dipole moment. At low density, the peak transient concentration of end defects is greater than the equilibrium concentration at any dipole moment. This raises the possibility that Tlusty and Safran's transition may be observed as a metastable phase transition.

Finally, our results may have a technological application. There are many applications where it may be desirable to have a networked material, e.g. in making electrical circuits, or as scaffolds for strong materials. It may be possible to make such a network using dipolar particles. If the particles also have a short range attraction or some chemical reaction occurs which causes them to stick irreversibly when they come into contact, the network might form and then stick together and we have formed the stable network we desired.

CHAPTER 5

Spin dynamics of the kagomé antiferromagnet

5.1 Introduction

In this chapter, we study the effect of bond dilution on the spin dynamics of antiferromagnetically coupled spins on a kagomé lattice. There have been few simulation studies of the spin dynamics in geometrically frustrated antiferromagnets. Keren [86, 87] has performed spin dynamics simulations of classical Heisenberg spins on a kagomé lattice. Moessner and Chalker [88] performed numerical simulations of spin dynamics on the pyrochlore lattice (a three dimensional analogue of the kagomé lattice) to support their analytical conclusions. Also for the pyrochlore lattice, Reimers [89] performed Monte Carlo simulations and looked at the 'dynamics' over Monte Carlo 'time'.

Keren [86] investigated the stability of long range order against excitation in the kagomé lattice. The system was prepared in the $\sqrt{3} \times \sqrt{3}$ (Fig. 1.7(a)) or $\boldsymbol{q} = 0$ (Fig. 1.7(b)) long range ordered states and one spin was rotated out of the plane. Next, the whole system was given an excitation with a certain energy from the ground state structures and the correlation function $\langle \boldsymbol{S}(t) \cdot \boldsymbol{S}(0) \rangle$ was measured, averaged over all the spins in the system. The $\boldsymbol{q} = 0$ state was found to be more

stable against small excitations than the $\sqrt{3}\times\sqrt{3}$ state. Correlations in time decay quickly in the $\sqrt{3} \times \sqrt{3}$ state. The 'spectral density' was calculated as a Fourier transform of the single spin correlation function:

$$j(\omega) = 2\int_0^\infty \langle \boldsymbol{S}(t) \cdot \boldsymbol{S}(0)\rangle \cos\omega t dt \,. \tag{5.1}$$

Keren compared $j(\omega)$ for the kagomé lattice and also the square lattice, which is an unfrustrated lattice with the same co-ordination number. In the square case, as the temperature decreases, the value of $j(0)$ increases and the spectral density is spread over a narrower range in frequency. This is characteristic of a paramagnetic phase. At low temperature, the correlation length reaches the size of the simulation box, and the system is effectively ordered (but note that in the thermodynamic limit, isotropic Heisenberg spins in two-dimensions cannot display long range order). Here, $j(\omega)$ consists of a narrow peak at $\omega > 0$ and $j(0)$ decreases. In the kagomé case, as temperature decreases the spectral density narrows, j(0) increases continuously. This shows that there is no phase transition above $T = 0$.

In Ref. [87], Keren considered the effect of non-magnetic impurities, which in simulations is equivalent to leaving vacancies on the lattice. The single spin correlation function $\langle \boldsymbol{S}(t) \cdot \boldsymbol{S}(0)\rangle$ was measured. With increasing dilution, the asymptotic value increases from zero. This is due to the fact that as spins are removed from the system, some spins may become isolated with no neighbouring spins. These spins will therefore not move and will remain correlated with themselves for all time. It is was found that the initial relaxation of the correlation function is independent of vacancy concentration, however. This is true even for concentrations below the percolation threshold, where we can no longer trace a path across the whole system. This is further evidence that the dynamics consists not of collective motions of whole system, but local motions of small groups of

spins. The correlation time was found from the time integral of the single spin correlation function:

$$\tau = \int_0^\infty \langle \boldsymbol{S}(t) \cdot \boldsymbol{S}(0) \rangle \, dt \tag{5.2}$$

τ is found to be monotonically increasing at $T \to 0$. Given that the order parameter corresponding to the $\sqrt{3} \times \sqrt{3}$ state increases below $T = 0.01J$ [90], we might expect the correlation time to decrease as the system becomes more ordered. This suggests again that the excitations in the kagomé lattice consist of local motions. The low temperature dependence of the correlation function was found to be consistent with $\tau \propto T^{-1}$. This corresponds with theories of critical dynamics for a critical temperature $T = 0$, for which $\tau \propto T^{-\nu z}$, with $\nu = 1/2$ and $z = 2$.

Because of the frustration, a system of spins on a kagomé lattice cannot find a unique ground state. The ground state is highly degenerate. A compromise can be reached by placing neighbouring spins at 120° to one another. Harris *et al.* [91] performed a linear spin wave analysis for classical Heisenberg spins on the kagomé lattice for excitations from the $\boldsymbol{q} = 0$ and $\sqrt{3} \times \sqrt{3}$ states. It was found for both these structures, the dispersion relation includes a dispersionless zero-energy mode. These 'zero modes' are identified with particular local motions of spins around the hexagons in the lattice. Chalker *et al.* [92] and Reimers and Berlinsky [90] discuss an 'order-by-disorder' mechanism whereby thermal fluctuations can select a subset of the ground state manifold at finite temperature. It is states in which the spins are coplanar that are selected (not necessarily in the plane of the kagomé layer). Two such planar states are the $\boldsymbol{q} = 0$ and $\sqrt{3} \times \sqrt{3}$. Chalker *et al.* attribute the selection of planar states to the fact that planar states have more zero modes than any non-planar state [92].

Reimers and Berlinsky in their Monte Carlo simulations measured order parameters $m_{\sqrt{3}}$ and m_0 corresponding to the $\sqrt{3} \times \sqrt{3}$ state and the $\boldsymbol{q} = 0$ state, re-

spectively [90]. $m_{\sqrt{3}}$ was found to rise considerably below $T = 0.01J$. They also established that the $\sqrt{3} \times \sqrt{3}$ state is more stable than the $\boldsymbol{q} = 0$ state by performing warming runs from both of these states. The results indicated that the $\boldsymbol{q} = 0$ state is out of equilibrium. Chalker *et al.* [92] also found from an analysis of their Monte Carlo simulations that the $\sqrt{3} \times \sqrt{3}$ state is the one formed. Harris *et al.* [91] also considered the effect of further neighbour interactions. They found that when $J_2 > J_3$, where J_2 and J_3 are the exchange constants for second and third neighbour interactions, $\boldsymbol{q} = 0$ is the more stable, whereas for $J_2 < J_3$, $\sqrt{3} \times \sqrt{3}$ is more stable.

In this chapter, we perform spin dynamics simulations for the highly frustrated kagomé antiferromagnet. We are particularly interested in the effects of bond dilution which should relieve some of the frustration. As mentioned in Chapter 1, this is motivated by the suggestion that in hydronium (H_3O^+) jarosite, a proton might migrate onto one of the OH^- ions bridging between the magnetic Fe^{3+} ions, weakening the exchange interaction. We investigate the static thermodynamic properties and the single-spin correlation function. We also investigate the collective dynamics by measuring the dynamic structure factor. This function makes an important link with experiment since it can be measured by inelastic neutron scattering.

5.2 Method

The dynamics of a system of antiferromagnetically coupled Heisenberg spins on the sites of a kagomé lattice was studied using the spin dynamics technique. The kagomé lattice is shown in Fig. 5.1. The simulation cell was parallelogram shaped with size $La \times La$ spins, where a is the nearest neighbour distance. In the jarosites, the nearest neighbour distance is $a = 3.4$Å. A system of size $40a \times 40a$ was simulated. The kagomé lattice was generated by creating a triangular lattice

and removing every second site in every second row. We simulated lattices with different fractions, x, of bonds broken. In the bond-diluted cases, five different realisations of bonds broken in the lattice were generated, and the results were averaged over five distinct runs.

The exchange interaction is described by the Heisenberg Hamiltonian

$$\mathcal{H} = \tilde{J} \sum_{i<j} \hat{\boldsymbol{S}}_i \cdot \hat{\boldsymbol{S}}_j \ , \tag{5.3}$$

where $\tilde{J} = JS(S+1)\hbar^2$, $\hat{\boldsymbol{S}}_i$ and $\hat{\boldsymbol{S}}_j$ are unit vectors in the direction of the spin angular momentum at site i and j, and the sum is over all nearest neighbour pairs of spins on the lattice. The equations of motion for this system (see Chapter 2) are given by

$$\frac{d\hat{\boldsymbol{S}}_i}{dt} = +J\sqrt{S(S+1)}\hbar \hat{\boldsymbol{S}}_i \wedge \sum_j \hat{\boldsymbol{S}}_j \ , \tag{5.4}$$

where the sum is over nearest neighbours of site i. Note that these equations of motion conserve both magnetisation and energy. They were integrated using an explicit Adams-Bashforth predictor, followed by an implicit fourth order Adams-Moulton corrector step. (The Runge-Kutta fourth order algorithm was used for the first three time steps [93]).

We define the reduced temperature $T^* = kT/\tilde{J}$ and time $t^* = J\sqrt{S(S+1)}\hbar t$, with the effective exchange coefficient, $\tilde{J}$ as the fundamental unit of energy.

For each realisation of the lattice, 1000 dynamics trajectories were sampled for periods up to 10^4 time steps, with a timestep of $\Delta t^* = 0.01$. The initial configurations were drawn from a Monte Carlo simulation at intervals of 200 Monte Carlo cycles, after an initial 10000 Monte Carlo cycles for equilibration. Since the dynamics are initiated from configurations drawn from the Boltzmann distribution, canonical averages can be estimated by averaging over the different dynamics runs.

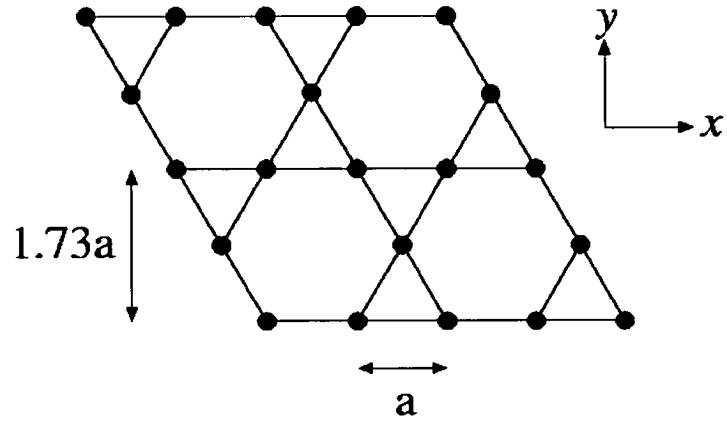

Figure 5.1: Kagomé lattice

Monte Carlo simulations can be used to obtain static thermodynamic properties such as the energy, heat capacity and susceptibility. The heat capacity is measured using the usual fluctuation formula:

$$C_H = \frac{\langle \mathcal{H}^2 \rangle - \langle \mathcal{H} \rangle^2}{k_B T^2} . \tag{5.5}$$

In reduced units, the heat capacity per spin is given by

$$\frac{C_H}{N k_B} = \frac{\langle \mathcal{H}^2 \rangle - \langle \mathcal{H} \rangle^2}{N (k_B T)^2} . \tag{5.6}$$

Since $\langle m \rangle = 0$ in a two dimensional antiferromagnet in the thermodynamic limit, where $m = \sqrt{M_x^2 + M_y^2 + M_z^2}$ is the magnitude of the magnetisation per spin, we replace the usual fluctuation formula for the susceptibility per spin with

$$\chi = \frac{\langle m^2 \rangle}{N k_B T} \tag{5.7}$$

Dynamical quantities were measured in the spin dynamics simulations. The single-spin correlation function is defined as

$$C(t) = \frac{1}{N} \sum_i \left\langle \hat{\boldsymbol{S}}_i(t) \cdot \hat{\boldsymbol{S}}_i(0) \right\rangle \tag{5.8}$$

Collective dynamics can be studied using the intermediate scattering function

$$S(\boldsymbol{q},t) = \frac{1}{N}\left\langle \boldsymbol{M}(\boldsymbol{q},t)\cdot\boldsymbol{M}(\boldsymbol{q},0)\right\rangle \ , \tag{5.9}$$

where

$$\boldsymbol{M}(\boldsymbol{q},t) = \sum_j \hat{\boldsymbol{S}}_j(t)e^{-i\boldsymbol{q}\cdot\boldsymbol{r}} \tag{5.10}$$

is a spatial Fourier component of the magnetisation. An important quantity is the dynamic structure factor, which is the temporal Fourier transform of the intermediate scattering function. It is accessible experimentally from inelastic neutron scattering. The dynamic structure factor is given by

$$S(\boldsymbol{q},\omega) = \int_{-\infty}^{+\infty} S(\boldsymbol{q},t)e^{-i\omega t}dt \ . \tag{5.11}$$

A Gaussian windowing function is applied to $S(\boldsymbol{q},t)$ before taking the temporal Fourier transform (as used in, e.g., Refs. [60, 94]). $S(\boldsymbol{q},t)$ is multiplied by

$$\exp\left[-\frac{(t\Delta\omega)^2}{2}\right] \ . \tag{5.12}$$

$\Delta\omega$ is given by

$$\Delta\omega = 1.2\frac{\pi}{t_{\text{cutoff}}} \ , \tag{5.13}$$

where t_{cutoff} is the time to which the equations of motion are integrated. The windowing function severely reduces the size of the discontinuity in $S(\boldsymbol{q},t)$ at the cutoff time, and thereby reduces the spurious features which can appear in the Fourier transform due to the truncation.

The primitive lattice vectors of the simulation cell (not the lattice) are $\boldsymbol{a}_1 = L(1,0)$ and $\boldsymbol{a}_2 = L(-\frac{1}{2},\frac{\sqrt{3}}{2})$. The corresponding reciprocal lattice vectors can be determined from the relations $\boldsymbol{b}_i\cdot\boldsymbol{a}_j = 2\pi\delta_{ij}$ between the reciprocal lattice vectors, $\boldsymbol{b}_i$,

and the direct lattice vectors, $\boldsymbol{a}_j$ [95]. This gives

$$\boldsymbol{b}_1 = \frac{2\pi}{L}(1, \frac{1}{\sqrt{3}}) \tag{5.14}$$

and

$$\boldsymbol{b}_2 = \frac{2\pi}{L}(0, \frac{2}{\sqrt{3}}) \,. \tag{5.15}$$

Therefore, the wavevectors which are commensurate with the periodic boundary conditions are given by linear combinations of $\boldsymbol{b}_1$ and $\boldsymbol{b}_2$. We consider wavevectors along the x and y directions. To be commensurate with the periodic boundary conditions these must be

$$\boldsymbol{q}_1 = m_1(2\boldsymbol{b}_1 - \boldsymbol{b}_2) = \frac{2\pi n_1}{L}(2, 0) \tag{5.16}$$

and

$$\boldsymbol{q}_2 = m_2\boldsymbol{b}_2 = \frac{2\pi n_2}{L}(0, \frac{2}{\sqrt{3}}) \,, \tag{5.17}$$

where n_1 and n_2 are integers. The wavevectors must also fit with the underlying kagomé lattice. Allowed wavevectors must correspond to waves with wavelength equal to an integer times the spacing between lines of spins in the lattice. In the x direction, this means that

$$\lambda = ma, \tag{5.18}$$

where a is the spacing between points in the lattice. So we have,

$$|\boldsymbol{q}_1| = \frac{4\pi n_1}{L} = \frac{2\pi}{ma} \tag{5.19}$$

Hence, n_1 must be equal to $L/2ma$. In our system, we have $L = 40a$, so the allowed values of n_1 are 1,2,4,5,10,20. In the y direction, the spacing of the lattice

planes is $\sqrt{3}$, so the allowed wavelengths are

$$\lambda = m\sqrt{3}a \, . \tag{5.20}$$

Thus,

$$|\boldsymbol{q}_2| = \frac{4\pi n_1}{\sqrt{3}L} = \frac{2\pi}{\sqrt{3}ma} \, . \tag{5.21}$$

We again find n_2 must be equal to $L/2ma$, and the allowed values of n_2 for $L = 40a$ are $n_2 = 1, 2, 4, 5, 10, 20$.

5.3 Thermodynamic quantities

Before exploring the dynamics, let us first consider the static thermodynamic quantities obtained from Monte Carlo simulations. Figs. 5.2- 5.4 show the energy, heat capacity and susceptibility, respectively, against temperature for systems with varying bond fractions, x. As the temperature is increased, random thermal motion increases, and the energy (Fig. 5.2) tends to zero for all bond fractions. In the fully bonded case ($x = 1$), the energy tends to -1.0 at $T = 0$. This is the energy per spin of the compromise ground state configuration in which neighbouring spins are oriented at 120° to each other. As the bond fraction decreases, the breaking of bonds in the lattice relieves the frustration in some of the triangular plaquettes, allowing some pairs of spins to attain an antiparallel alignment. This accounts for the initial decrease in energy at a given temperature. As more bonds are broken, however, fewer pairs of spins are interacting and the energy eventually rises towards zero.

The heat capacity is shown in Fig. 5.3. The data is subject to rather large statistical errors at low temperature. Nevertheless, it can be seen that the data is consistent with the exact theoretical low temperature limit of $C/Nk = 11/12$ [92].

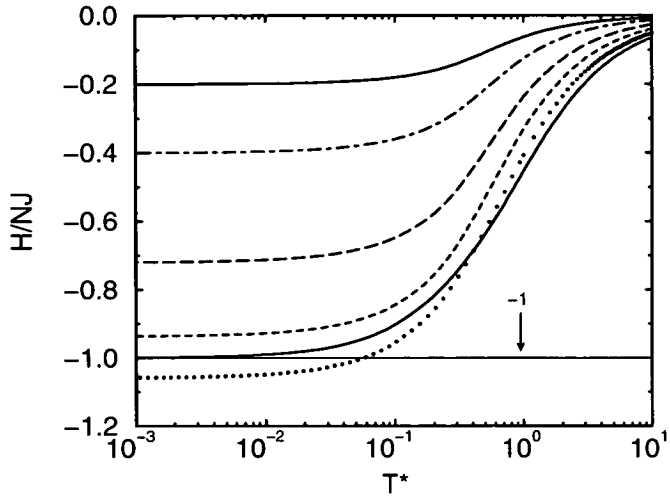

Figure 5.2: Energy as a function of temperature for systems with different bond fractions, x: $x = 1.0$ (solid line); $x = 0.8$ (dotted line); $x = 0.6$ (dashed line); $x = 0.4$ (long-dashed line); $x = 0.2$ (dot-dashed line); $x = 1.0$ (solid line).

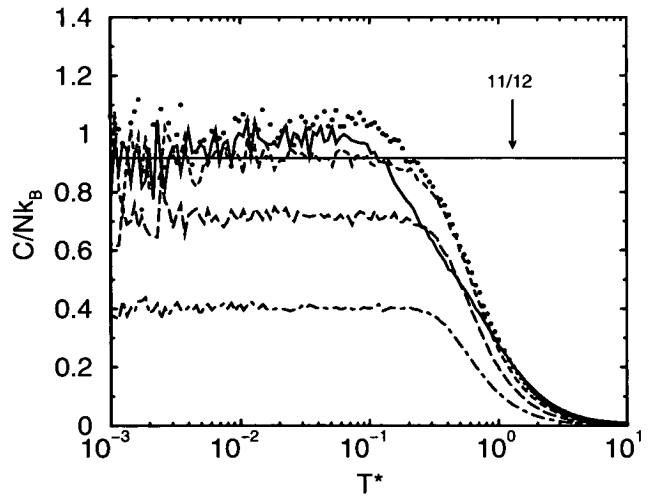

Figure 5.3: Heat capacity as a function of temperature for systems with different bond fractions, x: $x = 1.0$ (solid line); $x = 0.8$ (dotted line); $x = 0.6$ (dashed line); $x = 0.4$ (long-dashed line); $x = 0.2$ (dot-dashed line).

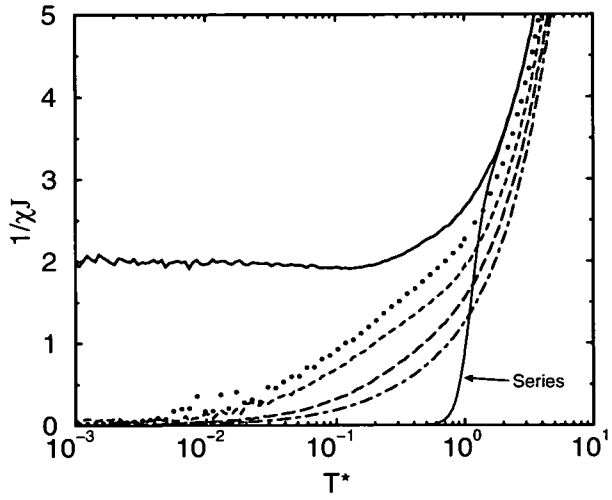

Figure 5.4: Inverse susceptibility as a function of temperature for systems with different bond fractions, x: $x = 1.0$ (solid line); $x = 0.8$ (dotted line); $x = 0.6$ (dashed line); $x = 0.4$ (long-dashed line); $x = 0.2$ (dot-dashed line).

The susceptibility is shown in Fig. 5.4. The high-temperature series expansion of Harris *et al.* [91] gives a good description of the data in the fully bonded case for $T^* > 1.0$. An interesting question is whether the kagomé antiferromagnet exhibits a phase transition at $T = 0$. It is known that a two-dimensional system of Heisenberg spins cannot show long range order at finite temperature [5], but this says nothing about $T = 0$. In frustrated systems long range order may not even be possible at $T = 0$ because of the large ground-state degeneracy. For a critical point at $T = 0$, we would still expect a divergence in the susceptibility in the limit $T \rightarrow 0$. In previous work there is no consensus about this issue. Reimers and Berlinsky [90] performed a finite size scaling analysis using Monte Carlo simulations and concluded that their data was consistent with a $T = 0$ critical point. Harris *et al.* on the other hand speculate that an exact theoretical result for the inverse susceptibility would not show the downturn towards zero at low temperature [91]. Our data appears to suggest that there is no phase transition in the fully bonded case ($x = 1.0$); $1/\chi$ tends to $2J^{-1}$ rather than $0J^{-1}$ (i.e. there is no divergence).

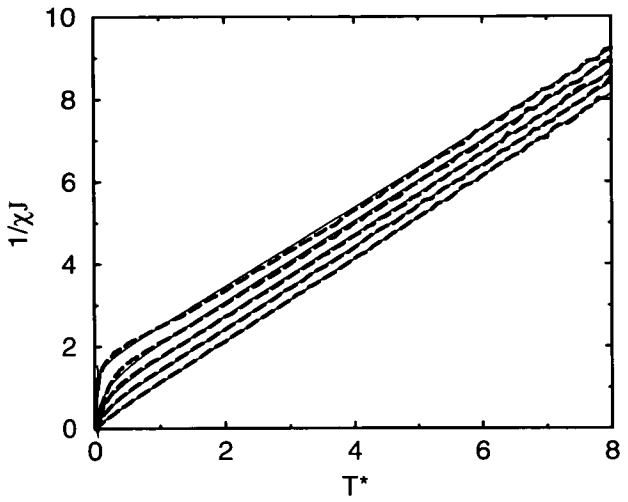

Figure 5.5: Inverse susceptibility from Monte Carlo simulation (dashed lines) and fits using Eq. 5.22 (solid lines). From top to bottom: $x = 0.9$; $x = 0.7$; $x = 0.5$; $x = 0.3$; $x = 0.1$.

Following Schiffer and Daruka [33], we fit our susceptibility data using two Curie-Weiss terms:

$$\chi^{-1} = [C_1/(T + \Theta_1) + C_2/(T + \Theta_2)]^{-1} \ . \tag{5.22}$$

This is based on the assumption that there exist two different populations of spins - clusters of antiferromagnetically correlated spins and 'orphan' spins almost uncorrelated with their neighbours. The first term represents the spins in clusters and the second term represents the orphan spins. The fit parameters are shown in Table 5.1 and the resulting fits are compared with the Monte Carlo data in Fig. 5.5. A good fit is obtained, for both the asymptotic high temperature linear dependence and the downturn in the curve at low temperature. Schiffer and Daruka's proposal is thus plausible in our system. The downturn in χ^{-1} then would be due to the relatively high susceptibility of the orphans spins at low temperatures compared to the spins in correlated clusters. Table 5.1 shows that the orphan spins have a 'transition' at temperature $\Theta_2 \simeq 0$.

Table 5.1: Fits to Monte Carlo susceptibility data using Eq. 5.22 for different values of bond fraction, x.

x	C_1	Θ_1	C_2	Θ_2
0.1	0.36(3)	0.39(5)	0.64(3)	-0.002(2)
0.2	0.62(1)	0.50(2)	0.39(1)	-0.003(1)
0.3	0.765(8)	0.62(2)	0.242(8)	-0.0028(9)
0.4	0.820(5)	0.80(1)	0.191(5)	-0.0025(8)
0.5	0.891(4)	0.95(2)	0.126(4)	-0.0030(7)
0.6	0.962(2)	1.11(2)	0.064(3)	-0.0002(5)
0.7	0.947(3)	1.35(2)	0.0085(3)	-0.0024(9)
0.8	0.992(2)	1.45(1)	0.042(2)	-0.0005(5)
0.9	1.032(2)	1.64(2)	0.0122(6)	-0.0012(2)

5.4 Single spin dynamics

We now turn to the dynamics as studied by spin dynamics simulations. The single-spin correlation function at various temperatures is shown in Fig. 5.6. In the fully bonded lattice ($x = 1$), these functions decay to zero as expected. In the bond diluted cases the asymptotic value is non-zero and increases as the bond fraction, x, decreases. This is due to the possibility that in a realisation of the lattice, a particular spin may have had all of its bonds to neighbouring spins broken; this isolated spin will then remain correlated with itself for all time.

The correlation functions mostly show a featureless decay, apart from a small feature which is most prominent at higher temperature. If conventional spin waves involving the whole system were present, we would expect to see some oscillatory behaviour in the correlation function. The fact that no such feature is present suggests that the main excitations in the system must instead consist of local motions of small groups of spins. Keren [86, 87] identifies these excitations with the localised 'zero modes' discussed by theorists [91]. We present further evidence for this below.

In the bond diluted case, the breaking of bonds means that the excitations which occur can only involve localised motions of small groups of spins. The fact that

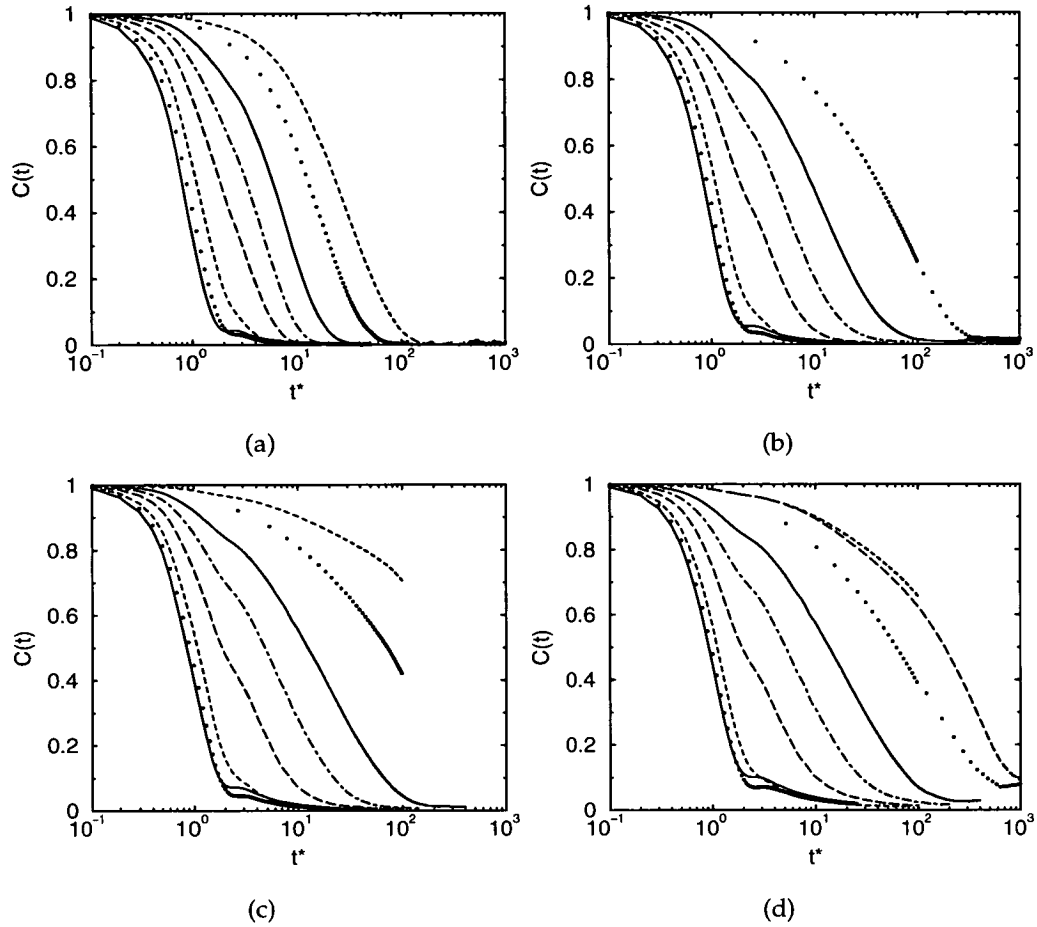

Figure 5.6: Single spin autocorrelation functions at different bond fractions and temperatures. (a) $x = 1.0$ (b) $x = 0.9$ (c) $x = 0.8$ (d) $x = 0.7$. From left to right for each bond fraction $T^* = 2$, $T^* = 1$, $T^* = 0.5$, $T^* = 0.2$, $T^* = 0.1$, $T^* = 0.05$, $T^* = 0.02$, $T^* = 0.01$.

the initial relaxation is independent of the bond fraction indicates that the same kind of dynamics is occurring, and hence the excitations involved must be local even in the fully bonded lattice. Keren studied the effect of site dilution and came to the same conclusion [87].

A single-spin correlation time can be found using

$$\tau = \int_0^\infty C(t)dt \,. \tag{5.23}$$

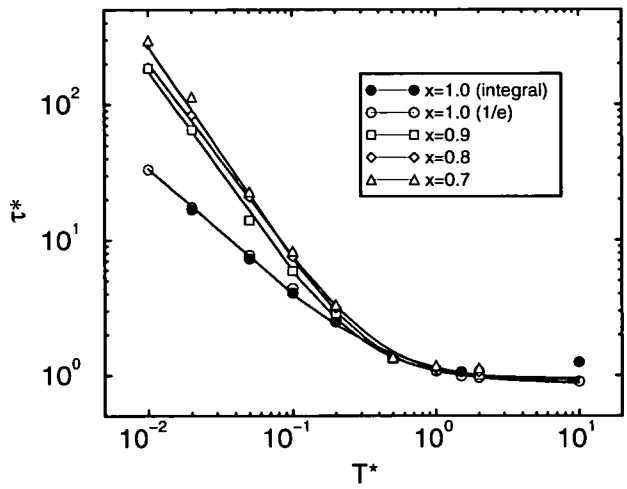

Figure 5.7: Correlation times from the single spin autocorrelation function: $x = 1.0$ (circles); $x = 0.9$ (squares); $x = 0.8$ (diamonds); $x = 0.7$ (triangles). Obtained from time for correlation function to fall to $1/e$ (open symbols) or from integral of correlation function (filled symbols). The solid lines are fits using $\tau(T) = \tau(\infty) + AT^{-\alpha}$

In the strongly bond diluted cases, the correlation functions die away over a much longer time scale than that accessed in the simulation and therefore equation 5.23 could not be used. In these cases, the correlation time was taken to be the time it took for the correlation function to fall to $1/e$ of its initial value. In those cases in which both methods could be used, the correlation times obtained are consistent. The correlation times for different bond fractions are plotted as a function of temperature in Fig. 5.7. In general, the correlation time decreases as temperature increases due to the increased thermal motion. According to theories of critical dynamics [96], the correlation time scales as $T^{-\nu z}$ if there is a critical point at $T = 0$, with the critical exponents $\nu = 1/2$ and $z = 2$. A function of the form $\tau(T) = \tau(\infty) + AT^{-\nu z}$ was fitted to the correlation time data. The resulting fit parameters are given in Table 5.2. For $x = 1$, the value $\nu z = 1.023 \pm 0.042$ is consistent with the expected scaling of T^{-1}.

Table 5.2: Fits to temperature dependence of correlation time using the function $\tau(T) = \tau(\infty) + AT^{-\alpha}$.

x	$\tau(\infty)$	A	α
0.7	0.887(94)	0.218(42)	1.485(54)
0.8	0.927(38)	0.151(14)	1.625(26)
0.9	0.952(53)	0.139(19)	1.551(38)
1.0	0.848(55)	0.296(46)	1.023(42)

5.5 Collective dynamics

The collective dynamics were studied by means of the dynamic structure factor. This function is important because it can also be measured in experiment by inelastic neutron scattering. In Figs. 5.9 and 5.10 we show the dynamic structure factor at $T^* = 0.1$ for wavevectors in two different directions in reciprocal space. This corresponds to a typical experimental temperature; given that in the jarosites the exchange constant, $\tilde{J}$ is of the order of 250 K, it corresponds to a real temperature of about 25 K. We also performed a few test cases for wavevectors in other directions and found no significant differences in the dynamic structure factor, comparing wavevectors with the same magnitude. For $x = 1$, there is one peak in the spectrum, in a certain range of wavevectors, at a reduced angular frequency $\omega^* = \omega/\left(J\sqrt{S(S+1)}\hbar\right) \simeq 1.5$. At lower bond fractions, peaks appear in the spectrum at $\omega^* \simeq 1.5, 2.3, 3.1$. For the fully bonded lattice, we determined the peak frequency by fitting two Lorentzians to the dynamic structure factor. The peak frequency versus wavevector – the dispersion relation – is plotted in Fig. 5.8. We include wavevectors in both the $\boldsymbol{q}_1$ and $\boldsymbol{q}_2$ directions. The solid line is the dispersion relation obtained by Harris *et al.* [91] using linear spin wave theory, which is applicable at temperatures close to zero. For our case this is given by $\omega^* = 2\,|\sin(|\boldsymbol{q}|a)|$. The theory and our data correspond qualitatively with each other, but our data is consistently lower than the theory. The discrepancy is due to the fact that we have rather broad features in the spectra and thus it is difficult to obtain an accurate fit. Also, the linear spin wave theory is constructed to

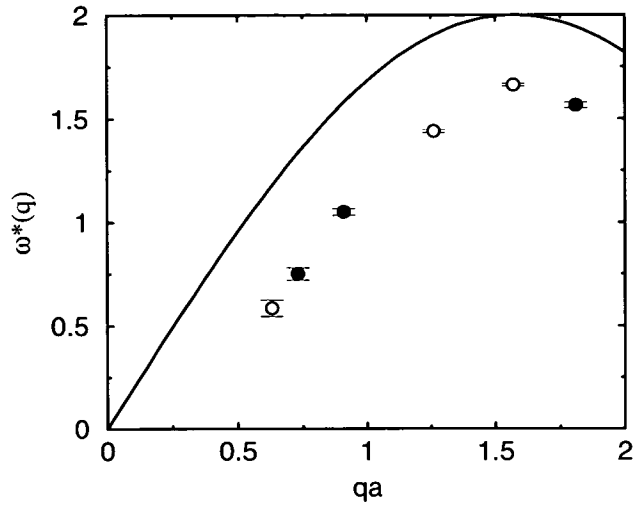

Figure 5.8: Dispersion relation for $x = 1$. Wavevectors in the q_1 direction (open symbols) and in the q_2 direction (closed symbols), dispersion relation from linear spin wave theory (solid line).

deal with low-lying excitations from the ground state and hence is appropriate to much lower temperatures than we have simulated here. There is a general trend that the peak in the dynamic structure factor decreases as temperature increases (see, for example, [60]). The fact that our peak frequencies are lower than the dispersion relation derived in the limit $T \rightarrow 0$ is consistent with this.

With increasing bond dilution, peaks emerge at $\omega^* \simeq 2.3, 3.1$. The position of these peaks are independent of wavevector, i.e. they are dispersionless. Dispersionless modes are often due to localised motions. It is true that the dynamics in the fully bonded case is also local but these new peaks appear due to the relief of frustration as bonds in the lattice are broken. Groups of spins will now be able to attain antiparallel alignment which will then undergo motions characteristic of unfrustrated antiferromagnets.

We note that some inelastic neutron scattering experiments have been carried out on the K^+ and D_3O^+ jarosites [97]. The dynamic structure factor for K^+ jarosite at

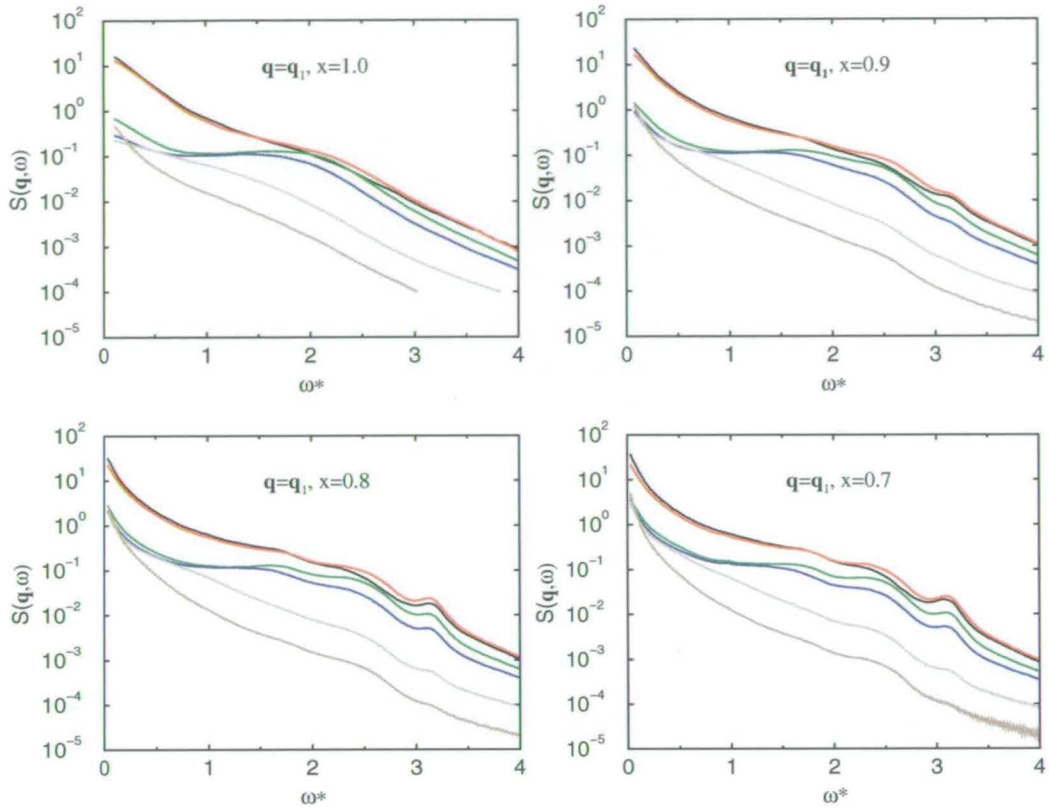

Figure 5.9: Dynamic structure factors for different bond dilutions and wavevectors in the $\boldsymbol{q}_1$ direction: (from top to bottom) (2π,0) (black); (π,0) (red); ($\pi/2$,0) (green); ($2\pi/5$,0) (blue); ($\pi/5$,0) (grey); ($\pi/10$,0) (brown).

a wavevector 1.75 $\text{Å}^{-}1$ showed peaks at approximately 7 meV, 16meV and a possible peak at ~24meV. In order to make a comparison, we convert our data into real units by noting that the typical nearest neighbour spacing in the jarosites is ~3.4 Åand the exchange constant is $\tilde{J} \simeq 250$ K. Our closest wavevector is (2π,0) which corresponds to 1.85 Å. The position of the three peaks in real units for the bond diluted cases is ~11.6 meV, ~17.8 meV and ~24.0 meV, in rough accord with experiment. However, in K^+ jarosite, there are perturbations to the Hamiltonian, such as single-ion anisotropy, and the D_3O^+ jarosite is perhaps a better case for comparison with our simulation results. The experimental analysis has not yet been completed, but the indications seem to be that these kind of peaks

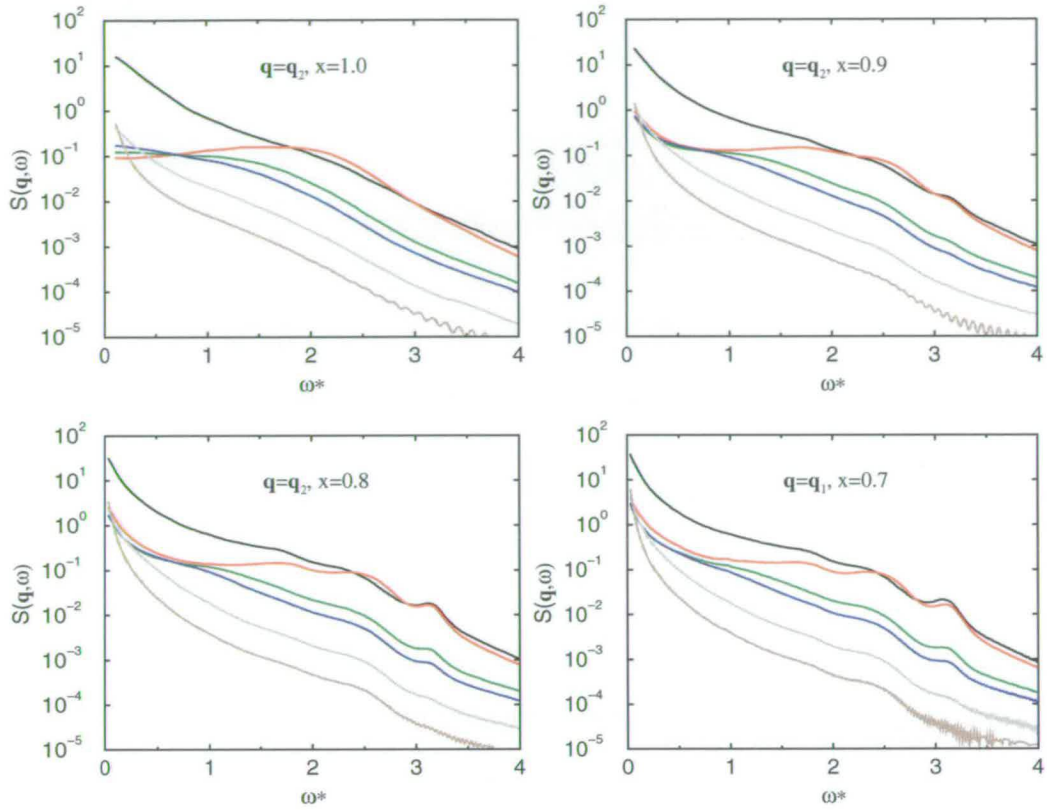

Figure 5.10: Dynamic structure factors for different bond dilutions and wavevectors in the q_1 direction: (from top to bottom) $(0,2\pi/\sqrt{3})$ (black); $(0,\pi/\sqrt{3})$ (red); $(0,\pi/2\sqrt{3})$ (green); $(0,2\pi/5\sqrt{3})$ (blue); $(0,\pi/5\sqrt{3})$ (grey); $(0,\pi/10\sqrt{3})$ (brown)

do not appear in the dynamic structure factor, although only a rather narrow range of energies can be measured experimentally at low enough wavevector.

5.6 Conclusions

We have carried out spin dynamics simulations of antiferromagnetically coupled Heisenberg spins on a kagomé lattice. The equations of motion were integrated using starting configurations sampled from canonical Monte Carlo simulations. We have investigated the effect of bond dilution on the thermodynamics and dynamics of the system.

Static thermodynamic properties were measured using Monte Carlo simulations. Upon increasing bond dilution the energy at a given temperature initially decreases due to the relief of frustration but eventually increases towards zero as less and less pairs of spins interact. The $T^* = 0$ limit of the heat capacity in the case $x = 1$ was found to be consistent with the theoretical value of $11/12$.

At high temperatures, the susceptibility data corresponded well with Harris *et al.*'s high temperature expansion [91]. The inverse susceptibility, $1/\chi$ in the fully bonded case tends to the value $1/2$ as $T \rightarrow 0$, i.e. the susceptibility does not diverge. This appears to indicate that there is no phase transition at $T = 0$, in contrast to Reimers and Berlinsky's conclusions from their finite size scaling analysis. This is an unresolved question in the literature.

A fit of two Curie-Weiss terms to the susceptibility following Schiffer and Daruka [33] was found to give a good description of the data. This is based on the idea that in a diluted frustrated magnet, there are two populations of spins - small clusters of correlated spins and 'orphan spins' which are almost uncorrelated with their neighbours.

The dynamics was studied using the spin dynamics technique. The most important conclusion is that the main excitations in the system consist of local motions of small groups of spins, rather than conventional spin waves spanning the whole system. The single spin correlation functions show a featureless decay, with no oscillatory behaviour as would be expected if spin waves were present. The fact that the initial decay of the correlation functions is independent of bond fraction is also consistent with the picture of local excitations. The correlation time was extracted from the single spin correlation function either by its integral or by the time for the function to fall to $1/e$. The correlation time rises continuously as $T \rightarrow 0$. A fit to the correlation time, τ as a function of temperature

showed the data is consistent with the scaling relation $\tau \propto T^{-\nu z}$ for a critical point at $T = 0$, with the critical exponents $\nu = 1/2$ and $z = 2$.

The collective dynamics was studied by measuring the dynamic structure factor, $S(\boldsymbol{q}, \omega)$. In the fully bonded lattice, $S(\boldsymbol{q}, \omega)$ exhibits a single broad peak. The dispersion relation shows qualitatively the same features as that obtained by Harris *et al.* [91] from their linear spin wave analysis, although the simulation data consistently gives a lower value than the theory. The discrepancy is probably due to the difficulty in obtaining an accurate estimate of the peak frequencies from the dynamic structure factor and the fact that the spin wave analysis is only designed to deal with low-lying excitations. In the bond diluted cases, further peaks appear in $S(\boldsymbol{q}, \omega)$. These peaks are dispersionless, again suggesting local excitations. These extra peaks arise because of the relief of frustration as bonds are broken. Some neighbouring spins are now able to attain their preferred antiparallel alignment and undergo motions characteristic of unfrustrated antiferromagnets.

In summary, we have studied the spin dynamics on the kagomé lattice. This was motivated by many experimental studies on the jarosites which reveal a range of puzzling behaviour, mostly due to the fact the real experimental systems are not quite as simple as models studied by theorists. There has been a suggestion that in H_3O^+ jarosite, the exchange interaction between two Fe^{3+} ions could be reduced by the migration of a proton onto the oxygen bridging between the ions. This led us to explore the consequences of bond dilution on the spin dynamics. There are some indications that our results may be consistent with inelastic neutron scattering experiments on K^+ and H_3O^+ jarosites, but there is nothing conclusive as yet.

CHAPTER 6

Phase behaviour of a system of amphiphilic trimers

6.1 Introduction

In chapter 1, we introduced the experimental study of two dimensional protein crystals. The structure of membrane proteins can be studied by reconstituting them into lipid bilayers. The resulting two dimensional crystals can be imaged by electron microscopy or atomic force microscopy. Some examples of this kind of study were given in chapter 1, particularly focusing on proteins which are either inherently triangular shaped or which form trimeric units from which the structure is built. These kind of studies motivated our investigation of the phase behaviour of a two dimensional system of hard disk trimers with one attractive disk. This model may seem far too simplistic to deal with complicated protein molecules, but as we discuss below, coarse grained models are very successful in the study of bulk behaviour. Indeed, the kind of close-packed structures we see in our simulations are very reminiscent of the structures of the two dimensional protein crystals.

Coarse grained models have been studied since the early days of computer simulation. In particular the study of the hard sphere system has yielded many insights into the fundamental questions of condensed matter theory. It is a very simple system on which to build theories of the liquid and solid states. The hard sphere system was one of the first models to be studied by computer simulation [98–100]. An example of the kind of insight gained is the fact that hard spheres can exhibit a first order fluid-solid phase transition. This is perhaps surprising because there are no attractive interactions between the particles. The phase transition is entirely entropy driven. Hard particle systems of various shapes have been studied by computer simulation, e.g. dimers [101, 102], pentamers and heptamers [103], rectangles [104] and hard pentagons and heptagons [105]. These systems are of interest in their own right. Despite the simplicity of these hard particle models, they can reproduce many of the features of real systems.

To gain an understanding of the detailed biological function of a particular protein, it is necessary to use a detailed model where all the atoms are taken into account. However, it is the case that the function of some proteins is dependent on their formation of some sort of pattern. In this case, we are interested in the collective phase behaviour of a large number of molecules. It would be prohibitively expensive to simulate every molecule in full atomistic detail and some kind of coarse grained model becomes necessary. The phase behaviour does not anyway depend on the exact details of every interaction between each molecule. In fact, it can be argued that the coarse grained models can give us great insight into which features of a molecule are really important in determining the collective behaviour. For example, in order for a molecule to display liquid crystalline phases, all that is necessary is for the molecules to be roughly rod-shaped [106–108]. This is something we may not have learnt from a fully atomistic simulation of a particular molecule which is known to show liquid crystalline phases.

We presented in Chapter 1 two studies which demonstrate that very simple coarse grained models can provide a reliable description of protein molecules for the purposes of understanding the bulk phase behaviour of a large system of these molecules. In this chapter we report a study of the phase behaviour of a coarse grained model that might provide a description of a trimeric protein. We obtain the phase diagram by Monte Carlo simulation and describe the structures in the different regions of the phase diagram.

6.2 Model and simulation details

We study a two-dimensional system of amphiphilic trimer molecules by Monte Carlo simulation. The model trimer consists of three hard disks fused together in a triangular arrangement, with the disks just touching. One disk on each trimer interacts with the corresponding disk on other trimers via an attractive square well potential with a range of 1.25σ, where σ is the hard disk diameter. This could model specific interactions between parts of the protein molecules. Systems of 120 of these trimers were simulated either in the NPT or NVT ensemble. A typical simulation consisted of a few hundred thousand Monte Carlo cycles. As well as ordinary translational and orientational moves, trial moves were attempted in which the trimers were rotated by multiples of 120°. These moves were attempted on average every fifth time. For NPT simulations in the solid phase, the x and y dimensions of the simulation cell were allowed to vary independently. In the fluid phase, the x and y dimensions were kept equal.

We define dimensionless reduced units in terms of the square well depth, ϵ, and the hard disk diameter, σ, as follows: density $\rho^* = \rho/\sigma^2$; temperature $T^* = kT/\epsilon$; pressure $P^* = P\sigma^2/kT$.

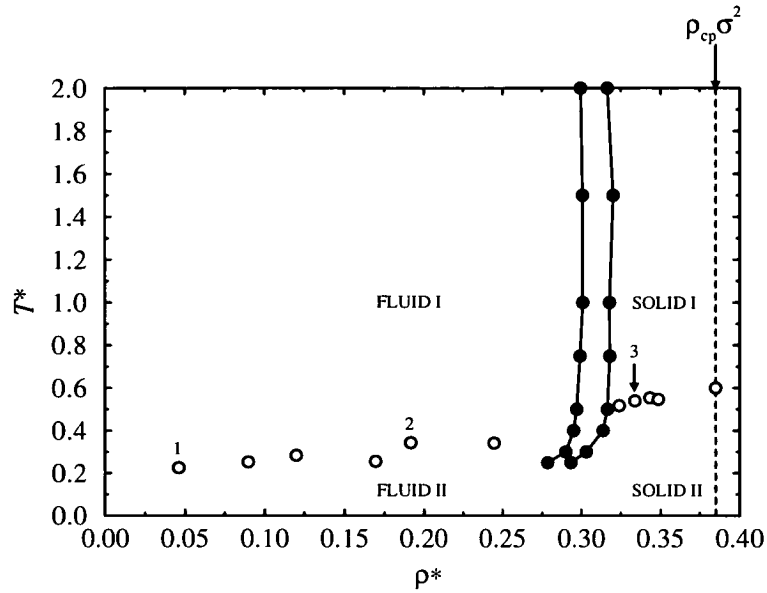

Figure 6.1: Phase diagram in the density-temperature plane. Filled circles mark the fluid-solid coexistence region. Open circles mark the crossover between clustered fluid and normal fluid or orientationally ordered solid and non-orientationally solid. The numbered points are referred to in Figure 6.7.

6.3 Results

The phase diagram in the density-temperature plane is given in Fig. 6.1. Before explaining how the boundaries between phases were determined, we first describe the structures in the four main regions of the phase diagram.

Figure 6.2(a) shows a snapshot of the structure at low density and temperature in the region marked "Fluid II" in the phase diagram. The trimers self-assemble into clusters containing typically three to six trimers, caused by the coming together of the attractive disks. The attractive disks within each cluster are packed closely rather than a more open structure in which the attractive disks are arranged on the circumference of a ring. The close packing of the attractive disks allows more direct contacts between the attractive disks. In the ring structure, each disk interacts only with its two neighbours - particles across the other side

of the ring are outwith the interaction range. Hence, the close packed structure has a lower energy.

The range of the attractive interaction has an important effect on the structure of the fluid. When the range of very short, the disk must come very close together and tight clusters are formed which then only have room to accommodate three or four trimers. At the other extreme, with a long range, rather loose clusters are formed containing more members. If the interaction range, $\lambda > \sqrt{3}$, it is possible for an attractive disk to interact with another trimer even if it approaches from 'behind'. In this case, no aggregation occurs.

We can further characterise the fluid structure by measuring the cluster size distribution. We use the criterion that two trimers are in the same cluster if their attractive disks are within the interaction range of the square well potential. In Fig. 6.3, we show the size distributions for states along the isotherm $T^* = 0.3$. The maximum of the distribution shifts to larger sizes as the density increases. At lower density, entropy has a bigger role to play. This is because the gain in entropy as a particle leaves a cluster is greater. Hence, smaller clusters tend to form at lower density. The maximum shifts towards six as we approach the solid region. The solid phase is built up of motifs containing six trimers.

At higher temperature we enter the region marked 'Fluid I'. The snapshot in Fig. 6.2(e) shows that no aggregation occurs here because entropy becomes more important at higher temperature. The fluid shows the structure of a 'normal' fluid with no translational or orientational ordering.

Figures 6.2(c) and (f) show the structure in the 'Solid I' and 'Solid II' regions of the phase diagram. The individual disks adopt a hexagonally close-packed structure, just as a system of hard disks does in the solid phase. There are different ways of packing the trimers that are consistent with the hexagonal close packing

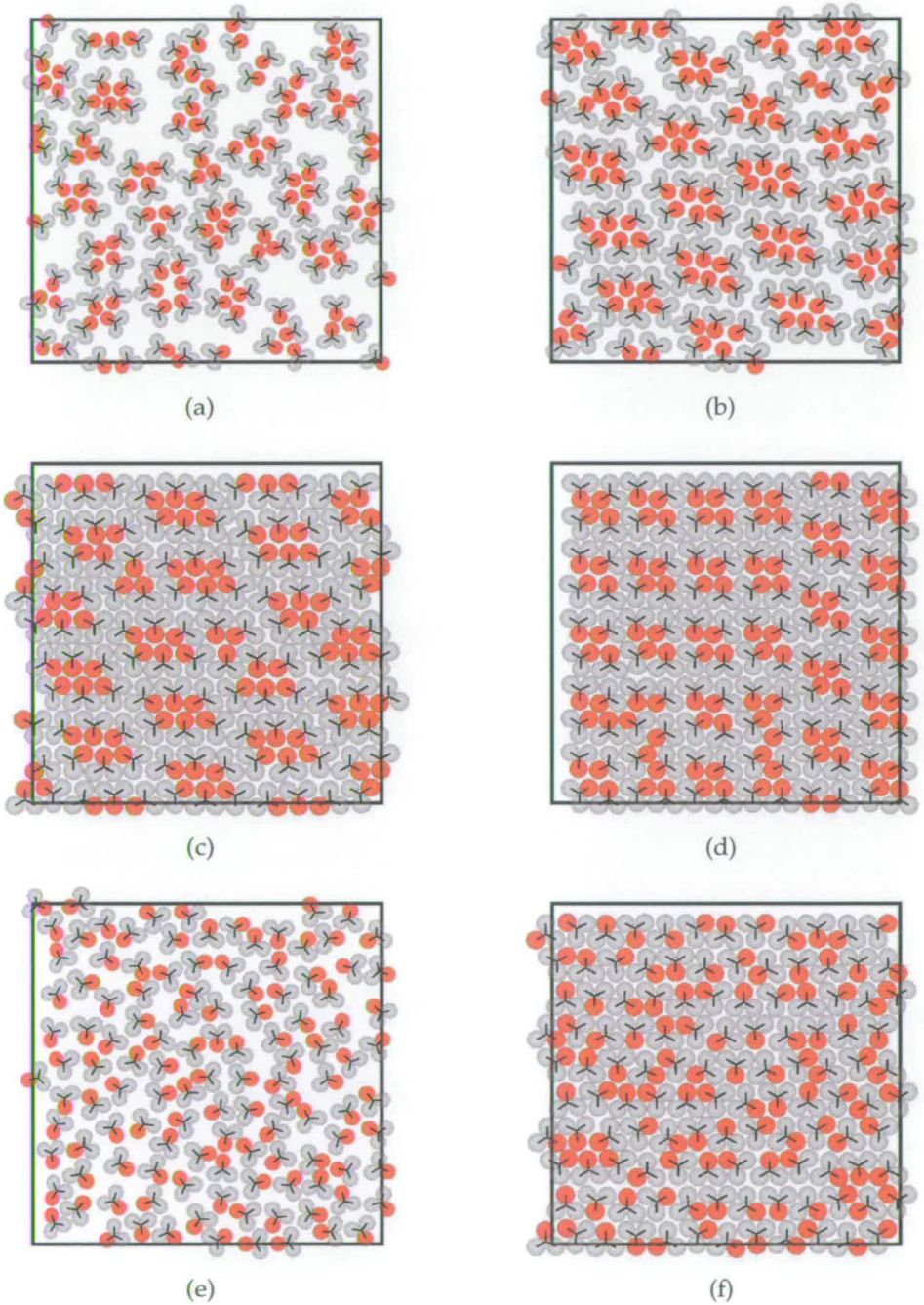

Figure 6.2: Snapshots of configuration from different regions of phase diagram. (a) Fluid II $T^* = 0.25$, $p^* = 0.75$, $\rho^* = 0.222$ (b) Metastable state $T^* = 0.25$, $p^* = 2.85$, $\rho^* = 0.295$ (c) AB solid $T^* = 0.25$, $p^* = 12$, $\rho^* = 0.349$ (d) AA solid $T^* = 0.25$, $p^* = 20$, $\rho^* = 0.356$ (e) Fluid I $T^* = 2$, $p^* = 2.5$, $\rho^* = 0.259$ (f) Solid I $T^* = 2, p^* = 12$, $\rho^* = 0.345$

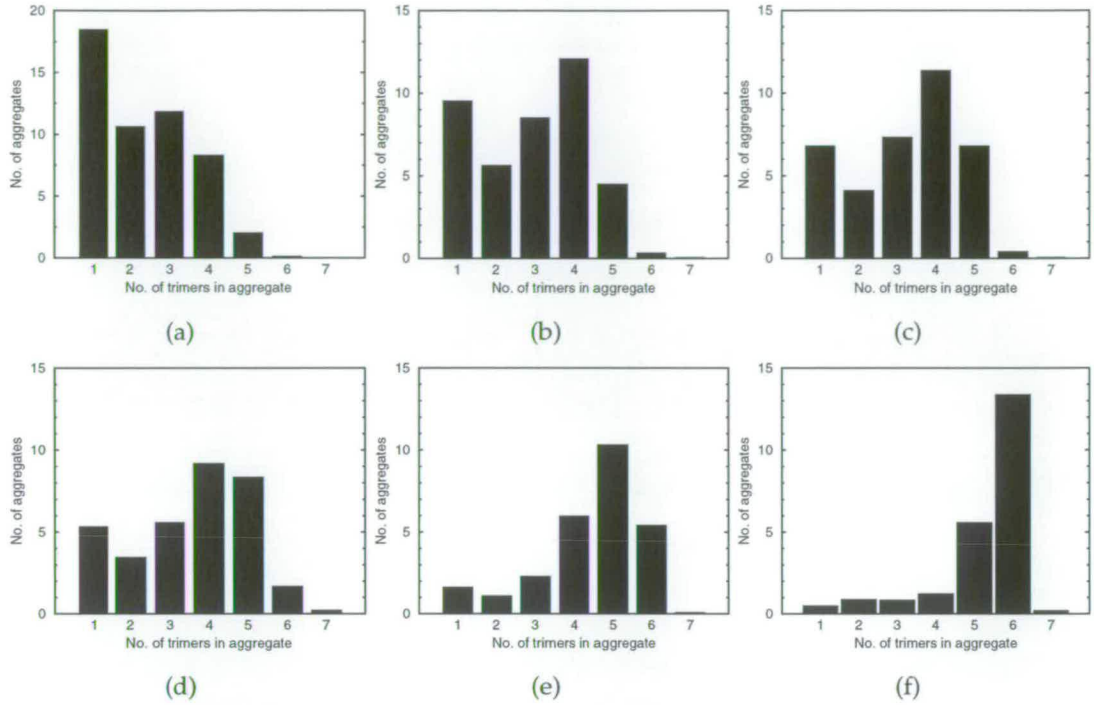

Figure 6.3: Average number of aggregates containing a particular number of particles at points along the isotherm $T^* = 0.3$: (a) $p^* = 0.5$, $\rho^* = 0.188$; (b) $p^* = 1.0$, $\rho^* = 0.228$; (c) $p^* = 1.5$, $\rho^* = 0.252$; (d) $p^* = 2.0$, $\rho^* = 0.264$; (e) $p^* = 2.5$, $\rho^* = 0.277$; (f) $p^* = 6.0$, $\rho^* = 0.329$. (a)-(e) are in the fluid phase, whereas (f) is in the solid phase.

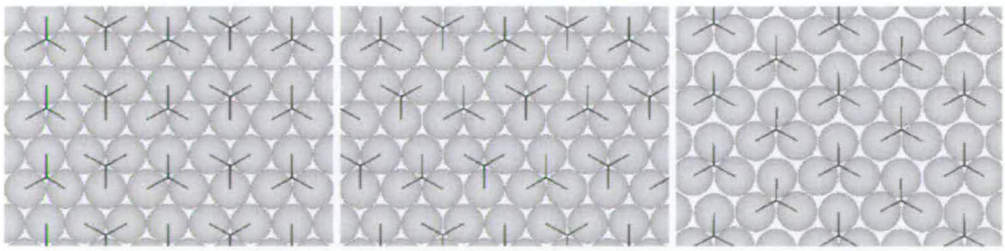

Figure 6.4: Packing structures in the solid phase (a) AA (b) AB (c) C.

of the individual disks (see Fig. 6.4). The structures we call 'AA' and 'AB' are built from rows within which the trimers point alternately 'up' or 'down'. In the 'AA' structure, the rows are all aligned (Fig. 6.4(a)). In the 'AB' structure, alternating rows are shifted along one space (Fig. 6.4(b)). There is another possible packing (structure 'C') with all trimers pointing 'up' (Fig. 6.4(c)).

At low temperature (Solid II), there is also orientational ordering of the trimers. The trimers rotate to allow their attractive disks to interact with the attractive disks on other trimers. In the AA crystal there is a repeating pattern formed from a motif of four interacting trimers (Fig. 6.2(d)). This arrangement allows two of the disks to interact with three neighbours. The energy of this state is then $-5/4\epsilon$ per trimer (assuming there are no defects), since in each unit, two disks interact with three others and two interact with two others, and four trimers participate. In the AB packing it is now possible to form a lower energy structure, built from a motif of six interacting trimers (Fig. 6.2(c)). In this motif, two of the disks interact with four others, two of the disks interact with three others, and two interact with two others, giving an energy of $-3/2\epsilon$ per trimer. We thus assume that the AB structure is the thermodynamically stable state. We shall return to this point later.

In the solid phase, the trimers are packed closely together, and in the Monte Carlo simulations it is not possible for them to move past each other. Therefore, the system will not convert from one packing structure to another during the course of the simulation, even though a different structure may be more thermodynamically stable. We must thus choose which of the structures to simulate. In most of what follows, we have simulated the AB structure.

The same consideration was also important in the hard homonuclear dimer system studied by Wojciechowski et al. [101, 102]. In this system, because of the many ways of arranging the dimers, the close packed structure is highly degenerate. This leads to a large entropy which stabilises a nonperiodic phase. In their Monte Carlo simulations, they employed collective moves of clusters of molecules to allow sampling of all the possible arrangements. In our case, it would be difficult to design such moves because of the need to ensure each molecule contains one attractive disk and two hard disks.

A snapshot of the high temperature, high density solid phase ('Solid I') is shown in Fig. 6.2(f). Here there is still hexagonal packing of the individual disks, but there is no longer any orientational order. This state has a higher entropy than the orientationally ordered Solid II, and thus is favoured at higher temperature.

Having introduced the structures observed in the different regions of the phase diagram, we now detail how the boundaries between the phases were determined. In order to locate the boundary between fluid and solid phases, equations of state $\rho(P)$ along different isotherms were obtained from expansion runs in the NPT ensemble. At each temperature, we performed a series of simulations at successively lower pressure. The final configuration from each simulation was used as the initial configuration for the next pressure and the system was allowed to equilibrate at each pressure before averages were taken. The first simulation of each series was initialised from a configuration in which the trimers are arranged in the AB packing but oriented at random. The orientational order observed in the solid II phase developed spontaneously during equilibration.

We also performed some compression runs, starting from a state in the fluid region and increasing the pressure. These suffer from the problem that as the system enters the solid phase, parts of this system can become stuck in their fluid positions. These defects in the solid state then remained for the rest of compression sequence. We therefore used expansion runs for the purposes of obtaining the phase diagram.

The equations of state obtained from the expansion runs are shown in Fig. 6.5. There are discontinuities in the density as the system changes from solid to fluid. We assume that this signifies a first order phase transition (although we remember the question of the nature of the phase transition in hard disks in two dimensions mentioned in Chapter 1). In the vicinity of the phase transition, there are points marked as crosses in Fig. 6.5 which did not seem to fit on either the fluid

or solid branch of the equation of state. These are metastable partially melted states, as can be seen in Fig. 6.2(b), where part of the system is fluid while another part is still crystalline. These points did not equilibrate even in runs of over 10^6 Monte Carlo cycles.

The boundaries of the fluid-solid coexistence region were found as follows. Fits were made to the equation of state using a virial expansion in the fluid state,

$$P = b_1\rho + b_2\rho^2 + b_3\rho^3 + \dots , \tag{6.1}$$

and a van der Waals equation of state in the solid phase,

$$P = \frac{a}{1 - b\rho} - c\rho^2 . \tag{6.2}$$

The metastable points are ignored in making these fits. We take the metastable points to be points which do not lie on either branch of the equation of state, or points where the configuration can be seen to be partially fluid and partially solid. The coexistence pressure is estimated as halfway between the highest density point identified on the fluid branch and the lowest density point identified on the solid branch. The fits were extrapolated to this pressure to give the coexistence densities. This method can only yield approximate values for the phase boundaries, but our purpose here is to map out the phase diagram of this new system, rather than obtain accurate values for the boundaries.

Figure 6.5(a) shows the extension of the equation of state to lower density. We see an absence of any feature such as the van der Waals loops which would indicate a liquid-vapour phase transition. Long range attractive forces are required to stabilise the liquid phase. The range of attractions is probably not long enough in our system. In a simulation study of a system of hard particles with

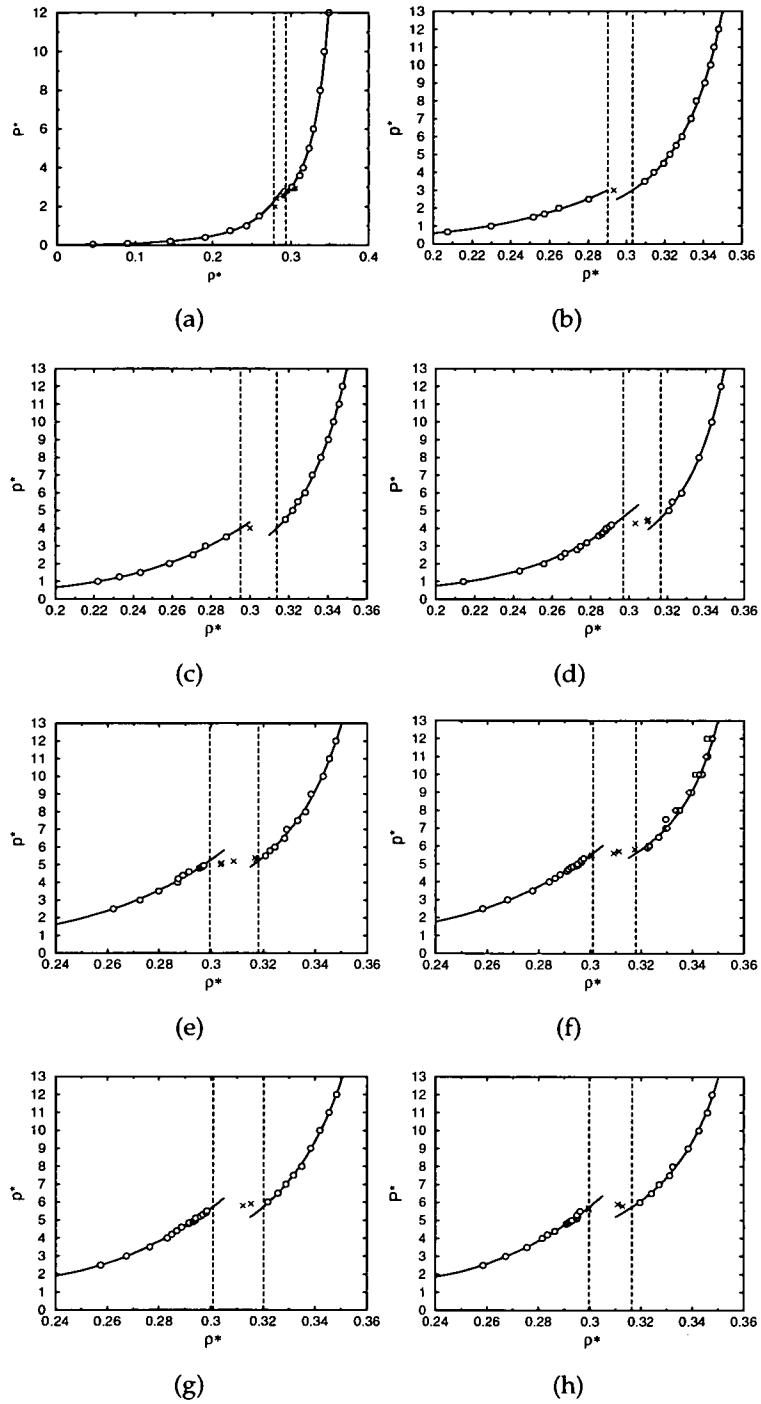

Figure 6.5: Equations of state, $P(\rho)$, along various isotherms: (a) $T^* = 0.25$; (b) $T^* = 0.3$; (c) $T^* = 0.4$; (d) $T^* = 0.5$; (e) $T^* = 0.75$; (f) $T^* = 1.0$; (g) $T^* = 1.5$; (h) $T^* = 2.0$. Circles are points determined from Monte Carlo simulations, crosses mark metastable points. The solid lines are fits to the data as described in the text. The vertical lines mark the coexistence densities. In (f), equations of state are shown for three different packing structures: AB (circles); AA (squares); C (diamonds).

a square well potential [109], it was shown that the liquid-vapour transition becomes metastable when the range of the square well is less than about 1.25σ.

We have also performed expansion runs for the isotherm $T = 1$ starting from the AA and C packing structures. The corresponding equations of state are also plotted in Fig. 6.5 along with the equation of state in the AB solid. For a given pressure, the AB solid is always at higher density than either the AA or C solid. This confirms that the AB structure is at least the most mechanically stable, if not the most thermodynamically stable. It seems unlikely that any entropic effect could stabilise one of the other structures. Further evidence of the thermodynamic stability of the AB structure comes from the fact that it is this structure that forms spontaneously during compression runs starting from a fluid state.

We next consider the crossover from the low temperature associated fluid (Fluid II), and the 'normal' fluid (Fluid I). The boundary between these two states marked on the phase diagram does not represent a sharp phase transition, but rather a crossover between the two regimes. In order to mark out a boundary between the two states, we performed some series of simulations along isobars starting from an equilibrated low density fluid state. We obtained the enthalpy and heat capacity along each isobar. The constant pressure heat capacity, $C_P = \left(\frac{\partial H}{\partial T}\right)_P$, was calculated using the usual fluctuation formula,

$$C_P = \frac{\langle H^2 \rangle - \langle H \rangle^2}{kT^2} , \tag{6.3}$$

where H is the enthalpy. In order to check consistency, the heat capacity was also obtained as the derivative of a Padé approximant fit to the enthalpy as a function of temperature. Padé approximants are given by

$$H = \frac{a_0 + a_1 T + a_2 T^2 + \ldots}{1 + b_1 T + b_2 T^2 + \ldots} . \tag{6.4}$$

We identify the crossover between associated and non-associated regimes with the peak in the heat capacity since we expect a drop in the energy as clustering starts to take place.

The crossover between the orientationally ordered Solid II state and the orientationally disordered Solid I state was marked out in a similar way. In this case, simulations were performed in the canonical (NVT) ensemble at different temperatures along lines of constant density. The constant volume heat capacity, $C_V = \left(\frac{\partial U}{\partial T}\right)_V$, was measured by the fluctuation formula,

$$C_V = \frac{\langle U^2 \rangle - \langle U \rangle^2}{kT^2}, \tag{6.5}$$

or by differentiating Padé approximant fits to the energy as a function of temperature. Again, the crossover was identified with the peak in the heat capacity. We have performed one such set of simulations at the close-packed density, $\rho^*_{CP} = 2\sqrt{3}/3 \simeq 0.3849$. It is impossible to pack hard disks any closer without overlaps. Fig. 6.6 shows the enthalpy and heat capacity at this density, along with the Padé approximant fit. The two methods of obtaining the heat capacity yield consistent results.

Fig. 6.7 shows the heat capacity as a function of temperature along two isobars in the fluid phase and one isochore in the solid phase. The peak height decreases as density increases. This is because at higher density particles are on average closer together, and so some pairs of particles will be within interaction range even in the high temperature unclustered regime. We therefore expect a smaller drop in energy as we enter the clustered regime.

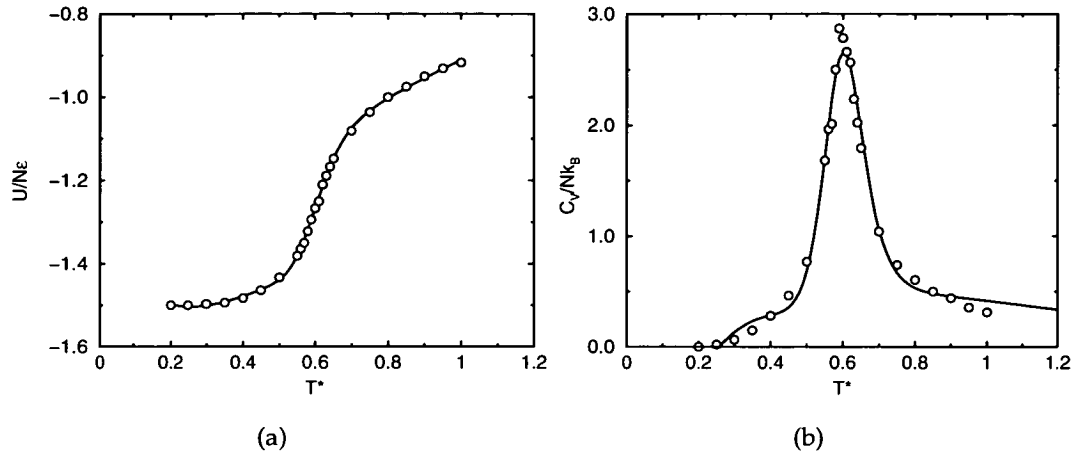

Figure 6.6: Energy (a) and heat capacity (b) as a function of temperature at the close packed density, $\rho^*_{CP} = 2\sqrt{3}/3 \simeq 0.3849$. Circles: data from Monte Carlo simulations (using fluctuation formula for the heat capacity). Solid lines: Padé approximant fit to energy data.

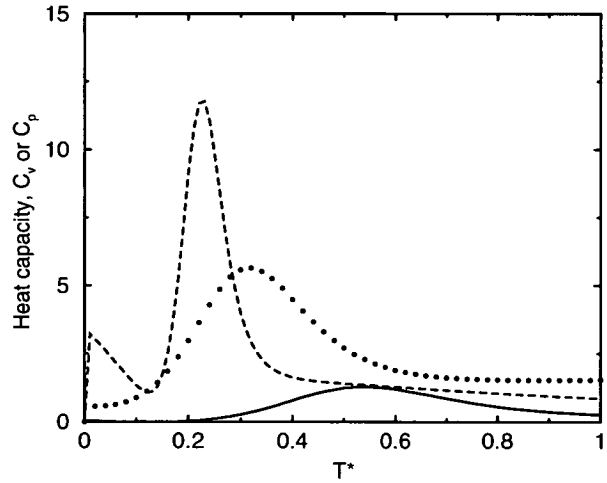

Figure 6.7: Heat capacity as a function of temperature, measured along isobars in the fluid phase with $P^* = 0.01$ ($\rho^* = 0.046$ at the peak position, corresponding to point 1 in Fig. 6.1) (dashed line) and $P^* = 0.2$ ($\rho^* = 0.192$, point 2 in Fig. 6.1) (dotted line), and along a line of constant density in the solid phase with $\rho = 0.334$ (point 3 in Fig. 6.1) (solid line).

6.4 Conclusions

We have explored the phase diagram of a two-dimensional system of hard disk trimers by Monte Carlo simulation. The model consists of three hard disks fused in a triangular arrangement, one of which interacts with the corresponding disk on other trimers via an attractive square well potential. This study was motivated by the kind of structures that have been observed in two-dimensional crystals of proteins.

There are four main regions of the phase diagram. At high temperature and low density, there is a 'normal' fluid phase with no translational or orientational ordering (Fluid I). At low temperature (Fluid II), the attractive disks come together to minimise their energy, causing the formation of clusters of trimers. We counted number of particles in each cluster. The peak in the size distribution moves to larger cluster size as the density increases. The cluster size moves towards six as we approach the fluid-solid coexistence region. The clusters adopt a form with the attractive disks closely packed rather than a more open form with the disks on the circumference of a ring. This arrangement allows more contacts between the attractive disks and hence has a lower energy.

In the solid phase, the individual disks within the trimer units are hexagonally close packed, just as in a system of hard disks. At high temperature (Solid I) there is no additional orientational ordering of the trimers. At low temperature (Solid II) there is an orientational ordering dependent upon the packing of the trimers. We have identified three possible ways of packing the trimers consistent with the hexagonal close packing of the individual disks. With the 'C' packing, the structure is built from motifs of three interacting trimers. With the 'AA' packing, a lower energy structure is possible, built from motifs of four interacting trimers in which two of the disks interact with three others. The 'AB' solid adopts a still lower energy structure, with motifs of six trimers. We assume that the 'AB'

structure is thermodynamically the most stable. This is borne out by the fact that this is the structure which forms spontaneously during compression runs. In the equations of state along an isotherm, the 'AB' solid always has a higher density for a given pressure, showing that the 'AB' packing is at least the most mechanically stable. Free energy calculations would be required to provide a definitive conclusion about which state is thermodynamically stable.

The fluid-solid phase coexistence region was determined by measuring the equation of state, $P(\rho)$ along different isotherms in the NPT ensemble. These showed a discontinuity in density which we take to be an indication of a first order phase transition. We demarcate the crossover between the unclustered Fluid I and the clustered Fluid II by measuring the equation of state along isobars in the NPT ensemble. The crossover was identified with the peak in the heat capacity as a function of temperature. The crossover between the orientationally disordered Solid I and the orientationally ordered Solid II was determined in a similar way, by carry out simulations in the NVT along lines of constant pressure and finding the peak in the heat capacity as a function of temperature. Note that in both cases, we have a crossover between two regimes, rather than a thermodynamic phase transition.

Despite the simplicity of our model, we have seen some interesting behaviour. This type of coarse-grained model, as well as being of intrinsic interest has been shown before to be useful in studying the bulk phase behaviour of membrane proteins. In our simulations we see structures in the solid phase similar to the structures typically observed in two-dimensional crystals of triangularly shaped proteins, and caused by the close packing of the molecules.

CHAPTER 7

Conclusions

This thesis has reported on four separate computer simulation studies on two-dimensional systems.

The first system studied was a quasi-two-dimensional dipolar fluid, consisting of soft spheres with a central point magnetic dipole confined to a plane, but whose dipole moments were able to rotate in three dimensions. This system was studied using Molecular Dynamics simulations. The minimum potential for the dipole-dipole interaction is when the dipoles are aligned in a 'nose-to-tail' fashion. At low density and temperature, this leads to the particles forming into chains and rings. Power law scaling in the structure factor as $q \rightarrow 0$ provides a signature of the chaining. At a temperature of $T^* = 1$, chaining occurs for dipole moments $\mu^* > 2$. This is accompanied by a drastic decrease in the diffusion coefficient. The presence of chaining was found to have a profound effect on dynamics. Auto-correlation functions of various quantities were measured. In the chained regime these reveal processes over two different timescales: the fast oscillatory motions of individual particles within chains and the slow motion of the chains themselves.

We also investigated using Langevin Dynamics simulations the aggregation process in the dipolar fluid from an initially 'random' configuration. An energy criterion was used to identify particles belonging to the same aggregate. The clusters were then classified into chains, rings or defect clusters. At low density, the number of clusters with increasing numbers of particles successively rise to a maximum and then decline again. This suggests a scenario in which monomers quickly form into dimers, then trimers and larger chains are built up from smaller ones. Rings mostly form by the joining together of the two ends of the same chains. At the highest density, there is a large transient concentration of defects which eventually declines. At intermediate times, there is a network of interconnected chains which eventually disentangles by processes such as the exchange of segments between chains.

Spin dynamics simulations were carried out for classical Heisenberg spins on a kagomé lattice coupled antiferromagnetically. In order to produce a canonical distribution, initial configurations for the dynamics are fed in from a Monte Carlo simulation. Canonical ensemble averages can then be obtained by averaging over the different trajectories generated. We investigate the effect of bond dilution on the dynamics. The kagomé lattice is highly frustrated, being composed of triangular plaquettes which place competing constraints on the spins. Our main conclusion is that the dynamics consists of local excitations of small groups of spins rather than involving the whole system. The initial decay of the single spin correlation function is independent of bond fraction, indicating local excitations. The correlation time can be obtained from the integral of the single spin correlation function. This is seen to rise as T^{-1} as $T \rightarrow 0$, consistent with the expected dynamical critical exponents for a critical point at $T = 0$. We observe one peak in the dynamic structure factor for the fully bonded lattice. As bond dilution is increased, further peaks appear. The relief of frustration as bonds are

broken will allow some spins to align fully antiparallel and undergo excitations characteristic of an unfrustrated magnet.

The phase behaviour of a system of trimeric molecules has been explored using Monte Carlo simulations. The model consists of three hard disks fused together in a triangular arrangement, one of which has an attractive square well interaction with the corresponding disk on other trimers. This could provide a very crude model for a protein consisting of three 'domains', one of which might be hydrophilic. Four main regions of the phase diagram were identified. At high temperature and low density there is the 'Fluid I' region. The system behaves as an 'ordinary' fluid. As the temperature lowered, there is a crossover to 'Fluid II'. Here the trimers self-assemble into aggregates containing usually 3–6 trimers. There was no evidence of a vapour-liquid transition. In the solid phase at high density, the trimers pack such that the individual disks are close packed in a triangular arrangement. In the high temperature 'Solid I' phase, the trimers are oriented at random. The structure in the low temperature 'Solid II' phase depends on the packing of the trimers. There are different packings of the trimers which are consistent with the triangular close packing of the individual disks. With the 'AA' packing, neighbouring trimers are oriented so as to create a repeating motif of four interacting hydrophilic disks, minimising the energy. With 'AB', it is possible to form a motif of six disks, which has lower energy. The 'AB' structure is mechanically stable over the 'AA' structure, and we suspect it is also thermodynamically more stable, although free energy calculations would be required to confirm this.

We finish by giving some suggestions of how the work reported in this thesis could be extended. In the case of the dipolar fluid dynamics, more work is required on the collective dynamics. As was mentioned in Section 3.6, measuring functions such as $\langle \boldsymbol{M}(\boldsymbol{q},t) \cdot \boldsymbol{M}(\boldsymbol{q},0) \rangle$, where $\boldsymbol{M}(\boldsymbol{q},t)$ is a Fourier component of

the bulk magnetisation, it may be possible to identify excitations analogous to the spin waves in solid magnetic materials. It would also be interesting to extend the work on both the dynamics and the kinetics of aggregation in the dipolar fluid to the three dimensional case. In three dimensions it becomes essential to use Ewald sums to deal with the long range nature of the potential.

In the work on the trimer system, it would be desirable to determine conclusively which of the possible solid state structures is the thermodynamically stable one. This could be achieved by calculating the free energy via the Frenkel-Ladd method [110]. We could also try to determine the phase diagram more accurately. It might also be interesting to explore the phase behaviour of slightly different models, for example one in which two disks in each trimer have an attractive square well interaction.

Finally, in the case of the spin dynamics on the kagomé lattice, the Hamiltonian could be extended to study the effect of perturbations such as interlayer coupling, next nearest neighbour interactions, Dzyaloshinsky-Moriya interactions, spin anisotropies etc. As was discussed in Chapter 1, a subtle balance between these kind of perturbations may be responsible for some of the puzzling properties of the real experimental systems we are trying to model.

APPENDIX A

Papers published

1. P. D. Duncan and P. J. Camp, "Structure and dynamics in a monolayer of dipolar spheres", J. Chem. Phys. **121**, 11322 (2004)
2. P. J. Camp and P. D. Duncan, "Two-dimensional structure in a generic model of triangular proteins and protein trimers", Phys. Rev. E **73**, 046111 (2006)
3. P. D. Duncan and P. J. Camp, "Aggregation kinetics and the nature of phase separation in two-dimensional dipolar fluids", Phys. Rev. Lett. **97**, 107202 (2006)

These are bound at the end of the thesis.

References

[1] J. M. Kosterlitz and D. J. Thouless. Ordering, metastability and phase transitions in two-dimensional systems. *J. Phys. C: Solid State Phys.*, 6:1181–1203, 1973.

[2] D. R. Nelson and B. I. Halperin. Dislocation-mediated melting in two dimensions. *Phys. Rev. B*, 19:2457–2484, 1978.

[3] A. P. Young. Melting and the vector Coulomb gas in two dimensions. *Phys. Rev. B*, 19:1855–1866, 1979.

[4] K. Binder, S. Sengupta, and P. Nielaba. The liquid-solid transition of hard discs: First-order transition or Kosterlitz-Thouless-Halperin-Nelson-Young scenario? *J. Phys.: Condens. Matter*, 14:2323–2333, 2002.

[5] N. D. Mermin and H. Wagner. Absence of ferromagnetism or antiferromagnetism in one- or two-dimensional isotropic Heisenberg models. *Phys. Rev. Lett.*, 17(22):1133–1136, 1966.

[6] T. Tlusty and S. A. Safran. Defect-induced phase separation in dipolar fluids. *Science*, 290:1328–1331, 2000.

[7] P. I. C. Teixeira, J. M. Tavares, and M. M. Telo da Gama. The effect of dipolar forces on the structure and thermodynamics of classical fluids. *J. Phys.: Condens. Matter*, 12:R411–R434, 2000.

[8] J.-J. Weis. Simulation of quasi-two-dimensional dipolar systems. *J. Phys.: Condens. Matter*, 15:S1471–S1495, 2003.

[9] C. Holm and J.-J. Weis. The structure of ferrofluids: A status report. *Curr. Opin. Colloid Interface Sci.*, 10:133–140, 2005.

[10] P. G. de Gennes and P. A. Pincus. Pair correlations in a ferromagnetic colloid. *Phys. Kondens. Materie*, 11:189–198, 1970.

[11] R. W. Chantrell, A. Bradbury, J. Popplewell, and S. W. Charles. Agglomerate formation in a magnetic fluid. *J. Appl. Phys.*, 53(3):2742–2744, 1982.

[12] J. J. Weis and D. Levesque. Chain formation in low density dipolar hard spheres: A Monte Carlo study. *Phys. Rev. Lett.*, 71(17):2729–2731, 1993.

[13] D. Levesque and J. J. Weis. Orientational and structural order in strongly interacting dipolar hard spheres. *Phys. Rev. E*, 49(6):5131–5140, 1994.

[14] P. J. Camp and G. N. Patey. Structure and scattering in colloidal ferrofluids. *Phys. Rev. E*, 62(4):5403, 2000.

[15] P. J. Camp, J. C. Shelley, and G. N. Patey. Isotropic fluid phases of dipolar hard spheres. *Phys. Rev. Lett.*, 84(1):115–118, 2000.

[16] J. J. Weis. Orientational structure in a monolayer of dipolar hard spheres. *Mol. Phys.*, 100(5):579–594, 2002.

[17] J. J. Weis, J. M. Tavares, and M. M. Telo da Gama. Structural and conformational properties of a quasi-two-dimensional dipolar fluid. *J. Phys.: Condens. Matter*, 14:9171–9186, 2002.

[18] J. M. Tavares, J. J. Weis, and M. M. Telo da Gama. Quasi-two-dimensional dipolar fluid at low densities: Monte Carlo simulations and theory. *Phys. Rev. E*, 65:061201, 2002.

[19] V. V. Murashov, P. J. Camp, and G. N. Patey. Dielectric relaxation of chained ferrofluids. *J. Chem. Phys.*, 116(15):6731–6737, 2002.

[20] L. N. Donselaar, P. M. Frederik, P. Bomans, P. A. Buining, B. M. Humbel, and A. P. Philipse. Visualisation of particle association in magnetic fluids in zero-field. *J. Magn. Magn. Mater.*, 201:58–61, 1999.

[21] V. F. Puntes, K. M. Krishnan, and A. P. Alivisatos. Colloidal nanocrystal shape and size control: The case of cobalt. *Science*, 291:2115–2117, 2001.

[22] K. Butter, A. P. Philipse, and G. J. Vroege. Synthesis and properties of iron ferrofluids. *J. Magn. Magn. Mater.*, 252:1–3, 2002.

[23] K. Butter, P. H. Bomans, P. M. Frederik, G. J. Vroege, and A. P. Philipse. Direct observation of dipolar chains in ferrofluids in zero field using cryogenic electron microscopy. *J. Phys.: Condens. Matter*, 15:S1451–S1470, 2003.

[24] K. Butter, P. H. H. Bomans, P. M. Frederik, and A. P. Philipse. Direct observation of dipolar chains in iron ferrofluids by cryogenic electron microscopy. *Nature Mater.*, 2:88–91, 2003.

[25] M. Klokkenberg, C. Vonk, E. M. Claesson, J. D. Meeldijk, B. H. Erné, and A. P. Philipse. Direct imaging of zero-field dipolar structures in colloidal dispersions of synthetic magnetite. *J. Am. Chem. Soc.*, 126:16706–16707, 2004.

[26] M. Klokkenberg, R. P. A. Dullens, W. K. Kegel, B. H. Erné, and A. P. Philipse. Quantitative real-space analysis of self-assembled structures of magnetic dipolar colloids. *Phys. Rev. Lett.*, 96:037203, 2006.

[27] W. Wen, F. Kun, K. F. Pál, D. W. Zheng, and K. N. Tu. Aggregation kinetics and stability of structures formed by magnetic microspheres. *Phys. Rev. E*, 59(5):R4758–R4761, 1999.

[28] I. S. Jacobs and C. P. Bean. An approach to elongated fine-particle magnets. *Phys. Rev.*, 100(4):1060–1067, 1955.

[29] J. E. Greedan. Geometrically frustrated magnetic materials. *J. Mater. Chem.*, 11:37–53, 2001.

[30] D. G. Nocera, B. M. Bartlett, D. Grohol, D. Papoutsakis, and M. P. Shores. Spin frustration in 2D kagomé lattices: A problem for inorganic synthetic chemistry. *Chem. Eur. J.*, 10:3851–3859, 2004.

[31] A. P. Ramirez. Strongly geometrically frustrated magnets. *Annu. Rev. Matter. Sci.*, 24:453–480, 1994.

[32] K. Binder and A. P. Young. Spin glasses: Experimental facts, theoretical concepts, and open questions. *Rev. Mod. Phys.*, 58(4):801–976, 1986.

[33] P. Schiffer and I. Daruka. Two-population model for anomalous low-temperature magnetism in geometrically frustrated magnets. *Phys. Rev. B*, 56(21):13712–13715, 1997.

[34] A. S. Wills and A. Harrison. Structure and magnetism of hydronium jarosite, a model kagomé antiferromagnet. *J. Chem. Soc., Faraday Trans.*, 92(12):2161–2166, 1996.

[35] A. W. Wills, A. Harrison, S. A. M. Mentink, T. E. Mason, and Z. Tun. Magnetic correlations in deuteronium jarosite, a model $S = 5/2$ kagomé antiferromagnet. *Europhys. Lett.*, 42(3):325–330, 1998.

[36] A. S. Wills, A. Harrison, C. Ritter, and R. I. Smith. Magnetic properties of pure and diamagnetically doped jarosites: Model kagomé antiferromagnets with variable coverage of the magnetic lattice. *Physical Review B*, 61(9):6156–6168, 2000.

[37] G. S. Oakley, D. Visser, J. Frunzke, K. H. Andersen, A. S. Wills, and A. Harrison. A polarised neutron scattering study of the magnetic correlations in the kagomé antiferromagnet $AFe_3(SO_4)_2(OD)_6$ (A=D_3O, K). *Physica B*, 267–268:142–144, 1999.

[38] G. S. Oakley, S. Pouget, A. Harrison, J. Frunzke, and D. Visser. Neutron spin echo study of magnetic fluctuations in the kagomé antiferromagnet $(D_3O)Fe_3(SO_4)_2(OD)_6$. *Physica B*, 267–268:145–148, 1999.

[39] P. J. L. Werten, H.-W. Rémigy, B. L. de Groot, D. Fotiadis, A. Philippsen, H. Strahlberg, H. Grubmüller, and A. Engel. Progress in the analysis of membrane protein structure and function. *FEBS Lett.*, 529:65–72, 2002.

[40] G. G. Hsu, A. R. Bellamy, and M. Yeager. Projection structure of VP6, the rotavirus inner capsid protein, and comparison with bluetongue VP7. *J. Mol. Biol.*, 272:362–368, 1997.

[41] H.-W. Wang, Y.-J. Lu, L.-J. Li, S. Liu, D.-N. Wang, and S. f. Siu. Trimer ring-like structure of ArsA ATPase. *FEBS Lett.*, 469:105–110, 2000.

[42] C.-C. Yin, M. L. Aldema-Ramos, M. I. Borges-Walmsley, R. W. Taylor, A. R. Walmsley, S. B. Levy, and P. A. Bullough. The quaternary molecular architecture of TetA, a secondary tetracyline transporter from *Escherichia coli*. *Mol. Microbiol.*, 38(3):482–492, 2000.

[43] M. J. Conroy, S. J. Jamieson, D. Blakey, T. Kaufmann, A. Engel, D. Fotiadis, M. Merrick, and P. A. Bullough. Electron and atomic force microscopy of the trimeric ammonium transporter AmtB. *EMBO Rep.*, 5(12):1153–1158, 2004.

[44] D. L. Gibbons, M.-C. Vaney, A. Roussel, A. Vigouroux, B. Reilly, J. Lepault, M. Keilian, and F. A. Rey. Conformational change and protein–protein interactions of the fusion protein of Semliki Forest virus. *Nature (London)*, 427:320–325, 2004.

[45] C. Govaerts, H. Wille, H. B. Prusiner, and F. E. Cohen. Evidence for assembly of prions with left-handed β-helices into trimers. *Proc. Natl. Acad. Sci. U.S.A.*, 101(22):8342–8347, 2004.

[46] A. Kitmotto, N. Myronova, P. Basu, and H. Dalton. Characterization and structural analysis of an active particulate methane monooxygenase trimer from *Methylococcus Capsulatus* (Bath). *Biochemistry*, 44:10954–10965, 2005.

[47] P. Zhu, E. Chertova, J. Bess Jr., J. D. Lifson, L. O. Arthur, J. Liu, K. A. Taylor, and K. H. Roux. Electron tomography analysis of envelope glycoprotein trimers on HIV and simian immunodeficiency virus virions. *Proc. Natl. Acad. Sci. U.S.A.*, 100(26):15812–15817, 2003.

[48] I. Schmidt-Krey, K. Murata, T. Hirai, K. Mitsuoka, Y. Cheng, R. Morgenstern, Y. Fujiyoshi, and H. Hebert. The projection structure of the membrane protein microsomal glutathione transferase at 3Å resolution as determined from two-dimensional hexagonal crystals. *J. Mol. Biol.*, 288:243–253, 1999.

[49] O. Lambert, H. Benabdelhak, M. Chami, L. Jouan, E. Nouaille, A. Ducruix, and A. Brisson. Trimeric structure of OprN and OprM efflux proteins from *Pseudomonas Aeruginosa* by 2D electron crystallography. *J. Struct. Biol.*, 150:50–57, 2005.

[50] K. Jagannathan, R. Chang, and A. Yethiraj. A Monte Carlo study of the self-assembly of bacteriorhodopsin. *Biophys. J.*, 83(4):1902–1916, 2002.

[51] M. G. Noro, M. A. Bates, A. Brisson, and D. Frenkel. Modeling the phase behaviour of the membrane binding protein annexin V. *Langmuir*, 18:2988–2992, 2002.

[52] M. A. Bates, N. G. Noro, and D. Frenkel. Computer simulation of the phase behaviour of a model protein: Annexin V. *J. Chem. Phys.*, 116(16):7217–7224, 2002.

[53] M. P. Allen and D. J. Tildesley. *Computer Simulation of Liquids.* Oxford University Press, 1987.

[54] D. Frenkel and B. Smit. *Understanding Molecular Simulation.* Academic Press, London, 2002.

[55] J.-P. Hansen and I. R. McDonald. *Theory of Simple Liquids.* Academic Press, London, 1986.

[56] B. D. Butler, G. Ayton, O. G. Jepps, and D. J. Evans. Configurational temperature: Verification of Monte Carlo simulations. *J. Chem. Phys.*, 109(16):6519–6522, 1998.

[57] A. A. Chialvo, J. M. Simonson, P. T. Cummings, and P. G. Kusalik. On the determination of orientational configurational temperature from computer simulation. *J. Chem. Phys.*, 114(15):6514–6517, 2001.

[58] D. P. Landau, A. Bunker, H. G. Evertz, M. Krech, and S.-H. Tsai. Spin dynamics simulations - a powerful method for the study of critical dynamics. *Prog. Theor. Phys. Suppl.*, 138:423–432, 2000.

[59] D. P. Landau and M. Krech. Spin dynamics simulations of classical ferro- and antiferromagnetic model systems: Comparison with theory and experiment. *J. Phys.: Condens. Matter*, 11:R179–R213, 1999.

[60] H. G. Evertz and D. P. Landau. Critical dynamics in the two-dimensional classical XY model: A spin dynamics study. *Phys. Rev. B*, 54(17):12302–12316, 1996.

[61] D. P. Landau and K. Binder. *A Guide to Monte Carlo Simulations in Statistical Physics*. Cambridge University Press, Cambridge, 2000.

[62] D. Wei and G. N. Patey. Orientational order in simple dipolar liquids: Computer simulation of a ferroelectric nematic phase. *Phys. Rev. Lett.*, 68(13):2043–2045, 1992.

[63] J. J. Weis and D. Levesque. Ferroelectric phases of dipolar hard spheres. *Phys. Rev. E*, 48(3):3728–3740, 1993.

[64] K.-C. Ng, J. P. Valleau, G. M. Torrie, and G. N. Patey. Liquid-vapour coexistence of dipolar hard-spheres. *Mol. Phys.*, 38(3):781–788, 1979.

[65] J.-M. Caillol. Search for the gas-liquid transition of dipolar hard spheres. *J. Chem. Phys.*, 98(12):9835–9849, 1993.

[66] M. E. van Leeuwen and B. Smit. What makes a polar liquid a liquid? *Phys. Rev. Lett.*, 71(24):3991–3994, 1993.

[67] P. A. Pincus. Y's and ends. *Science*, 290:1307–1308, 2000.

[68] J. T. Kindt. Simulation and theory of self-assembled networks: Ends, junctions and loops. *J. Phys. Chem. B*, 106:8223–8232, 2002.

[69] A. Zilman, T. Tlusty, and S. A. Safran. Entropic networks in colloidal, polymeric and amphiphilic systems. *J. Phys.: Condens. Matter*, 15:S57–S64, 2003.

[70] B. Bagchi and A. Chandra. Collective orientational relaxation in dense dipolar liquids. *Adv. Chem. Phys.*, 80:1–126, 1991.

[71] D. Kivelson and P. A. Madden. Theory of dielectric relaxation. *Mol. Phys.*, 30(6):1749–1780, 1975.

[72] T. A. Andrea, W. C. Swope, and H. C. Andersen. The role of long ranged forces in determining the structure and properties of liquid water. *J. Chem. Phys.*, 79(9):4576–4584, 1983.

[73] S. Fazekas, J. Kertész, and D. E. Wolf. Two-dimensional array of magnetic particles: The role of an interaction cutoff. *Phys. Rev. E*, 68:041102, 2003.

[74] P. M. Chaikin and T. C. Lubensky. *Principles of Condensed Matter Physics*. Cambridge University Press, 1995.

[75] T. A. Witten and Pincus P. A. *Structured Fluids*. Oxford University Press, 2004.

[76] B. J. Alder and T. E. Wainwright. Decay of the velocity autocorrelation function. *Phys. Rev. A*, 1(1):18–21, 1970.

[77] R. F. A. Dib, F. Ould-Kaddour, and D. Levesque. Long-time behaviour of the velocity autocorrelation function at low densities and near the critical point of simple fluids. *Phys. Rev. E*, 74:011202, 2006.

[78] M. H. Ernst, E. H. Hauge, and J. M. J. van Leeuwen. Asymptotic time behaviour of correlation functions. *Phys. Rev. Lett.*, 25(18):1254–1256, 1970.

[79] M. M. Hurley and P. Harrowell. Non-gaussian behaviour and the dynamical complexity of particle motion in a dense two-dimensional liquid. *J. Chem. Phys.*, 105(23):10521–10526, 1996.

[80] P. J. Camp. Dynamics in a two-dimensional core-softened fluid. *Phys. Rev. E*, 71(3):031507, 2005.

[81] R. B. Jones and F. N. Alavi. Rotational diffusion of a tracer colloid particle: IV. Brownian dynamics with wall effects. *Physica A*, 187:436–455, 1992.

[82] S. P. Stoddard. Identifying clusters in computer experiments on systems of particles. *J. Comp. Phys.*, 27(2):291–293, 1978.

[83] M. Smoluchowski. *Z. Phys. Chem.*, 92:129, 1917.

[84] S. K. Friedlander. *Smoke, Dust and Haze: Fundamentals of Aerosol Behaviour*. John Wiley and Sons, 1977.

[85] A. A. Rzepiela, J. H. J. van Opheusden, and T. van Vliet. Brownian dynamics simulation of aggregation kinetics of hard spheres with flexible bonds. *J. Colloid Interface Sci.*, 244:43–50, 2001.

[86] A. Keren. Dynamical simulation of spins on kagomé and square lattices. *Phys. Rev. Lett.*, 72(20):3254–3257, 1994.

[87] A. Keren. Simulation of spin dynamics on kagomé and square lattices. *J. Magn. Magn. Mater.*, 140–144:1493–1494, 1995.

[88] R. Moessner and J. T. Chalker. Low-temperature properties of classical geometrically frustrated antiferromagnets. *Phys. Rev. B*, 58(18):12049–12062, 1998.

[89] J. N. Reimers. Absence of long-range order in a three-dimensional geometrically frustrated antiferromagnet. *Phys. Rev. B*, 45(13):7587–7294, 1992.

[90] J. N. Reimers and A. J. Berlinsky. Order by disorder in the classical Heisenberg kagomé antiferromagnet. *Phys. Rev. B*, 48(13):9539–9554, 1993.

[91] A. B. Harris, C. Kallin, and A. J. Berlinsky. Possible Néel orderings of the kagomé antiferromagnet. *Phys. Rev. B*, 45(6):2899–2919, 1992.

[92] J. T. Chalker, P. C. W. Holdsworth, and E. F. Shender. Hidden order in a frustrated system: Properties of the Heisenberg kagomé antiferromagnet. *Phys. Rev. Lett.*, 68(6):855–858, 1992.

[93] R. L. Burden and J. D. Faires. *Numerical Analysis*. Brooks/Cole Publishing Company, 1997.

[94] K. Chen and D. P. Landau. Spin dynamics in the diluted three-dimensional classical Heisenberg antiferromagnet. *J. Appl. Phys.*, 73(10):5645–5647, 1993.

[95] N. W. Ashcroft and N. D. Mermin. *Solid State Physics*. W. B. Saunders Company, 1976.

[96] P. C. Hohenberg and B. I. Halperin. Theory of dynamic critical phenomena. *Rev. Mod. Phys.*, 49:435–479, 1977.

[97] F. C. Coomer and A. Harrison. Personal communication.

[98] N. Metropolis, A. W. Rosenbluth, M. N. Rosenbluth, A. H. Teller, and E. Teller. Equation of state calculations by fast computing machines. *J. Chem. Phys.*, 21:1087–1092, 1953.

[99] W. W. Wood and J. D. Jacobson. Preliminary results from a recalculation of the Monte Carlo equation of state of hard spheres. *J. Chem. Phys.*, 27:1207–1208, 1957.

[100] B. J. Alder and T. E. Wainwright. Phase transition for a hard sphere system. *J. Chem. Phys.*, 27:1208–1209, 1957.

[101] K. W. Wojciechowski, Frenkel D., and A. C. Brańka. Nonperiodic solid phase in a two-dimensional hard-dimer system. *Phys. Rev. Lett.*, 66(24):3168–3171, 1991.

[102] K. W. Wojciechowski. Monte Carlo simulations of highly anisotropic two-dimensional hard dumbell-shaped molecules: Nonperiodic phase between fluid and dense solid. *Phys. Rev. B*, 46(1):26–38, 1992.

[103] K. W. Wojciechowski, K. V. Tretiakov, and M. Kowalik. Elastic properties of dense solid phases of hard cyclic pentamers and heptamers in two dimensions. *Phys. Rev. E*, 67:036121, 2003.

[104] A. Donev, J. Burton, F. H. Stillinger, and S. Torquato. Tetratic order in the phase behaviour of a hard-rectangle system. *Phys. Rev. B*, 73:054109, 2006.

[105] T. Schilling, S. Pronk, B. Mulder, and Frenkel D. Monte Carlo study of hard pentagons. *Phys. Rev. E*, 71:036138, 2005.

[106] J. Vieillard-Baron. Phase transitions of the classical hard-ellipse system. *J. Chem. Phys.*, 56(10):4729–4744, 1972.

[107] D. Frenkel, B. M. Mulder, and J. P. McTague. Phase diagram of a system of hard ellipsoids. *Phys. Rev. Lett.*, 52:287–290, 1984.

[108] A. Stroobants, H. N. W. Lekkerkerker, and Frenkel D. Evidence for smectic order in a fluid of hard parallel spherocylinders. *Phys. Rev. Lett.*, 57:1452–1455, 1986.

[109] D. L. Pagan and J. D. Gunton. Phase behaviour of short-range square-well model. *J. Chem. Phys.*, 122:184515, 2005.

[110] D. Frenkel and A. J. C. Ladd. New Monte Carlo method to compute the free energy of arbitrary solids. Application to the fcc and hcp phases of hard spheres. *J. Chem. Phys.*, 81(7):3188–3193, 1984.

JOURNAL OF CHEMICAL PHYSICS VOLUME 121, NUMBER 22 8 DECEMBER 2004

Structure and dynamics in a monolayer of dipolar spheres

Peter D. Duncan and Philip J. Camp[a)]
School of Chemistry, University of Edinburgh, West Mains Road, Edinburgh EH9 3JJ, United Kingdom

(Received 28 May 2004; accepted 14 September 2004)

The structure and dynamics in a monolayer of dipolar soft spheres have been investigated using molecular dynamics simulations. This is a basic model of colloidal ferrofluid monolayers, and other magnetic liquids in planar geometries, which can exhibit self-assembled chainlike aggregates due to strong dipole-dipole interactions. The effects of such chaining on the structure, single-particle translational and rotational motions, and the collective rotational motions are examined. The signatures of aggregation in the various structural and dynamical functions considered in this study could prove useful in experimental investigations of strongly dipolar materials. © *2004 American Institute of Physics.* [DOI: 10.1063/1.1812744]

I. INTRODUCTION

The structure and phase behavior of strongly interacting dipolar fluids continues to attract attention from workers in various disciplines.[1] The most familiar examples of dipolar fluids are colloidal ferrofluids, consisting of roughly spherical ferromagnetic particles with diameters in the range 10 nm–1 μm dispersed in a simple solvent. The particles are usually coated with a thin layer of nonmagnetic inert material which prevents irreversible aggregation. The net interactions between the particles are mainly dipolar in nature, with the coatings providing only relatively weak short-range dispersion interactions.

These materials are of significant technological utility, because the rheological properties can be "switched" with applied magnetic fields. From a fundamental point of view, however, such materials are of interest because of the structural and dynamical complexity at the "molecular" level. One of the most striking structural characteristics of colloidal ferrofluids (even in the absence of applied magnetic fields) is the self-assembly of particles to form chains, arising from the "nose-to-tail" configuration favored by the dipolar forces. The earliest experimental evidence of clustering in colloidal ferrofluids was obtained from thin films using electron microscopy almost 40 years ago.[2] The experimental study of colloidal ferrofluids has recently been rejuvenated through the use of improved synthetic methods and high-resolution transmission electron microscopy.[3–5] The structural similarities between colloidal ferrofluids and a diverse range of materials, such as living polymers, micelles and microemulsions, and biological actin gels,[6] have recently stimulated significant new theories of defect formation and phase behavior.[7,8]

The nature of clustering in strongly dipolar *bulk* fluids has been studied at great length, both theoretically[9–13] and by computer simulation;[14–16] for a comprehensive review, see Ref. 1. In these studies, the dipolar particles are modeled as either hard or soft spheres carrying a central point dipole. The pair potential is given by

$$u(r)=u_{sr}(r)+\frac{\boldsymbol{\mu}_1\cdot\boldsymbol{\mu}_2}{r^3}-\frac{3(\boldsymbol{\mu}_1\cdot\mathbf{r})(\boldsymbol{\mu}_2\cdot\mathbf{r})}{r^5}, \tag{1}$$

where $u_{sr}(r)$ is a short-range isotropic repulsive potential, and the remaining terms represent the dipole-dipole interaction in which $\boldsymbol{\mu}_i$ is the dipole on particle i, $\mathbf{r}$ is the interparticle separation vector, and $r=|\mathbf{r}|$.

One observation which will be relevant to the present work is that the static structure factor $S(q)$ of strongly dipolar three-dimensional fluids exhibits a characteristic $1/q$ power-law scaling at low wave vectors.[16] This scaling arises from the presence of chainlike clusters with persistence lengths of the order of 10 sphere diameters. In principle, $S(q)$ is accessible to scattering experiments, and hence the $1/q$ scaling provides one experimental fingerprint of chain formation. With regard to the phase behavior of bulk dipolar fluids, we note in passing that the existence of a bulk fluid-fluid phase separation driven entirely by dipolar interactions is still an open question.[7,17,18]

Calculations on two-dimensional dipolar systems are more directly relevant to common experimental situations than are those on bulk systems, because the structural characterization of highly aggregated ferrofluids in experiments is largely carried out on thin films or on monolayers.[3–5] Monolayers of dipolar particles under more complex conditions—such as in static[19] or alternating applied fields[20,21]—look set to provide new avenues for research. The current technological interest in thin-film devices and functional materials supplies an additional motivation.

Recently, Weis and co-workers have used computer simulations and theory to survey and examine a large variety of structures formed by two-dimensional monolayers of strongly interacting dipolar spheres.[22–26] In Ref. 22 the dipole orientations are confined to a two-dimensional plane, whereas in Refs. 23–26 the dipoles are free to rotate in three dimensions. Not surprisingly, chain formation occurs in these quasi-two-dimensional systems, although it seems to persist over a higher concentration range than in three dimensions. This can be rationalized on the basis of an increased entropic penalty associated with clustering in higher dimensions. A diverse range of structures arises from the way in which the

a)Electronic mail: philip.camp@ed.ac.uk

chains "fold-up;" for instance, at high densities where the spheres are almost close-packed, vortical-orientational order appears. The characterization of chainlike clusters at low densities has been achieved by adapting equilibrium theories developed for bulk dipolar fluids.[24,25] In none of the studies cited above has there been any evidence of a fluid-fluid phase separation.

The discussion so far has been focused on the microstructural and thermodynamic properties of strongly dipolar fluids. Although the bulk hydrodynamic properties of magnetic fluids are well known,[27] the microscopic dynamics of strongly interacting dipolar particles appears to represent a rich area for further study. Wen *et al.* have carried out an interesting study of the aggregation kinetics of quasi-two-dimensional dipolar fluids[28] by conducting experiments with nickel-plated glass beads, and carrying out molecular dynamics (MD) computer simulations. They showed that the formation of chainlike clusters consisted of rapid association of small numbers of particles to form short chains, followed by the slow aggregation of these chains to form larger chains, and rings. This suggests that there will likely be at least two characteristic time scales present in the *equilibrium* dynamics, one representative of single-particle motion, and the other due to the collective motions of particles within a chain. This scenario has been demonstrated in MD and Brownian dynamics simulations of highly aggregated three-dimensional dipolar soft spheres.[29] The dielectric (or magnetic susceptibility) spectrum was seen to exhibit a high-frequency feature arising from the oscillations of single-dipole orientations within the chains, and a low-frequency feature arising from the relaxation of large aggregates.

In this work we examine the structure and dynamics of a model quasi-two-dimensional dipolar fluid using MD simulations. We consider a fluid comprising N dipolar soft spheres with mass m and moment of inertia I, confined to a two-dimensional square plane of area $A=L\times L$. The interparticle potential is given by Eq. (1) with the short-range part given by

$$u_{sr}(r)=4\epsilon\left(\frac{\sigma}{r}\right)^{12}, \tag{2}$$

where ϵ is an energy parameter and σ is the sphere "diameter." It is emphasized that the dipoles are three-dimensional, and that they interact via the appropriate three-dimensional potential in Eq. (1). We employ reduced units for various molecular, thermodynamic, and dynamical quantities, defined as follows: density $\rho^*=N\sigma^2/A$; temperature $T^*=k_BT/\epsilon$, where k_B is Boltzmann's constant; dipole moment $\mu^*=\sqrt{\mu^2/\epsilon\sigma^3}$; moment of inertia $I^*=I/m\sigma^2$; and time $t^*=t\sqrt{\epsilon/m\sigma^2}$.

We confirm that at high dipole moments, the low-q behavior of $S(q)$ conforms to the same scaling law observed in three-dimensional dipolar fluids.[16] We investigate the translational and orientational dynamics of the two-dimensional system, paying particular attention to the characteristic properties of various time-correlation functions and their associated spectra. It is hoped that this work will provide useful experimental "fingerprints" for strong association in dipolar fluids.

This paper is organized as follows: In Sec. II we summarize the simulation methods used in this work. In Sec. III A we study the structure of the dipolar fluid, as represented by $S(q)$ and the corresponding radial distribution function $g(r)$. In Sec. III B, we present results for the single-particle diffusion coefficient and the velocity autocorrelation function, and assess the impact of chaining on these quantities. The single-particle rotational motion is studied in Sec. III C using the single-dipole autocorrelation function, and the single-particle angular velocity autocorrelation function. Collective rotational motions as evidenced by the bulk polarization autocorrelation functions are considered briefly in Sec. III D. Section IV concludes the paper.

II. MOLECULAR DYNAMICS COMPUTER SIMULATIONS

In all cases MD simulations were performed in the N-V-E ensemble after equilibration in the N-V-T ensemble at a temperature $T^*=1.0$ (achieved by translational and angular velocity scaling). We have used systems of $N=961$ particles with $m=1$ and $I^*=0.1$ throughout. The dipole orientations were represented using quaternions, and the dipolar interactions were handled using a spherical cutoff at $L/2$; the potential was truncated smoothly between $0.9\times L/2$ and $L/2$ using the switching function due to Andrea *et al.*[30] We justify our choice of a truncated potential (as opposed to calculating full Ewald sums) by reference to a recent study in which a cut-off $r_c>5\sigma$ was found to be sufficient to saturate the three-dimensional dipole-dipole interactions in two-dimensional arrays of particles.[31] For the system size simulated in this work, the cutoff is $r_c=L/2\geqslant 21.92\sigma$, the lower limit corresponding to the highest density ($\rho^*=0.5$) considered. The equations of motion were integrated using a velocity-Verlet algorithm for the translational motion, and a leapfrog algorithm for the rotational motion.[32] Simulations consisted of $O(10^5)$ time steps after equilibration, one time step being $\delta t^*=0.0025$. Periodic boundary conditions were applied. Typical simulation timings on a 1.3 GHz processor were 0.2 s per MD step. We have performed a series of N-V-E-MD simulations corresponding to a temperature $T^*=1.0$, and with various dipole moments ($\mu^*=0$, 0.5, 1, 1.5, 2, 2.5, and 2.75) and densities ($\rho^*=0.05$, 0.1, 0.2, 0.3, and 0.5).

III. RESULTS

A. Structure

Figure 1 shows some snapshots from simulations at the state points ($\mu^*=0.5,\rho^*=0.05$), ($\mu^*=0.5,\rho^*=0.5$), ($\mu^*=2.75,\rho^*=0.05$), and ($\mu^*=2.75,\rho^*=0.5$). With the lowest dipole moment ($\mu^*=0.5$) there is very little positional or orientational order apparent in the snapshots, whereas with the high dipole moment ($\mu^*=2.75$) the system is almost completely aggregated over the entire density range considered in this study ($0.05\leqslant\rho^*\leqslant 0.5$). In the aggregated regime, the particles are very strongly aligned in linear chains and rings, with the dipolar orientations adopting the nose-to-tail conformation. At all densities simulated in this work, the onset of aggregation occurs at $\mu^*>2$. This is illustrated in

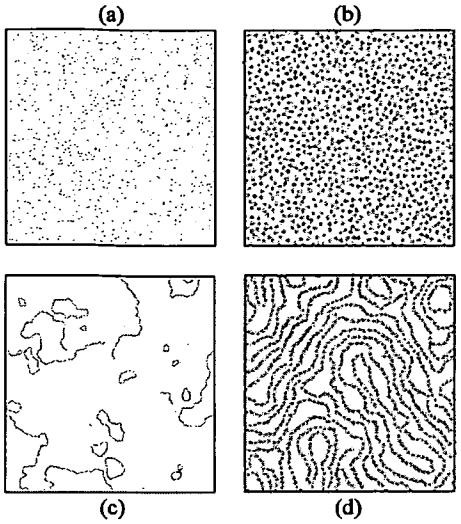

FIG. 1. Snapshots showing the positional and orientational ordering of the particles in systems with dipole moment μ^* and density ρ^*: (a) $\mu^*=0.5$, $\rho^*=0.05$; (b) $\mu^*=0.5$, $\rho^*=0.5$; (c) $\mu^*=2.75$, $\rho^*=0.05$; (d) $\mu^*=2.75$, $\rho^*=0.5$. The particles are represented by gray spheres with diameter σ, and the dipole orientations are shown as black lines of length 0.5σ emanating from the centers of the spheres.

Fig. 2 which shows snapshots from simulations at a fixed density of $\rho^*=0.2$. For dipole moments $\mu^*\leq 2$ the structure is quite uniform, although with $\mu^*=2$ there are a few relatively small and loosely clustered chainlike aggregates. Moving to higher dipole moments, however, results in a dramatic increase in the degree and extent of particle clustering.

In order to characterize the in-plane ordering of the particle centers of mass, the radial distribution function $g(r)$ was calculated in the usual way.[32] Some representative results are shown in Fig. 3 for weakly dipolar ($\mu^*=0.5$) and strongly dipolar ($\mu^*=2.75$) systems. At $\mu^*=0.5$ the structure is absolutely typical of a simple liquid, with peaks

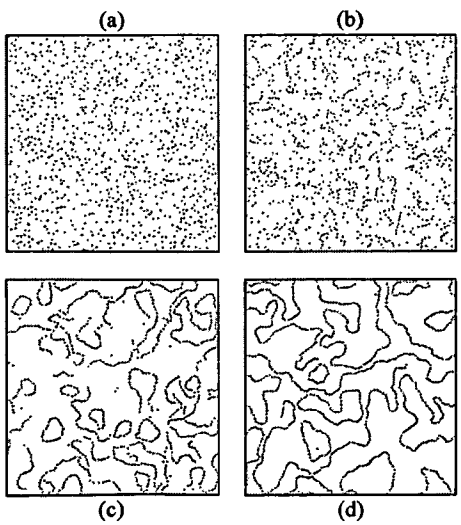

FIG. 2. Snapshots showing the positional and orientational ordering of the particles in systems with density $\rho^*=0.2$ and dipole moment μ^*: (a) $\mu^*=1.5$; (b) $\mu^*=2$; (c) $\mu^*=2.5$; (d) $\mu^*=2.75$. The particles are represented by gray spheres with diameter σ, and the dipole orientations are shown as black lines of length 0.5σ emanating from the centers of the spheres.

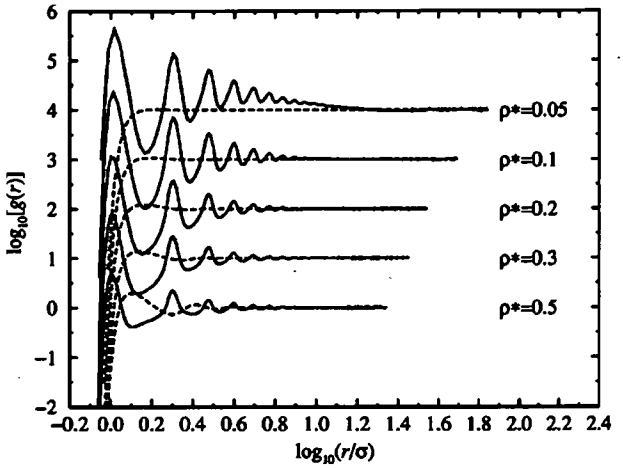

FIG. 3. Logarithms of the radial distribution functions $\log_{10}[g(r)]$ as functions of $\log_{10}(r/\sigma)$ from simulations with $\mu^*=0.5$ (dashed lines) and $\mu^*=2.75$ (solid lines), and at various densities in the range $0.05\leq\rho^*\leq 0.5$. The curves are displaced by one unit along the ordinate for clarity.

emerging at $r\simeq 1.2\sigma$ and $r\simeq 2.6\sigma$ with increasing density. In stark contrast, with the highest dipole moment ($\mu^*=2.75$) and at all densities, $g(r)$ shows pronounced peaks close to integer values of σ. This structure corresponds to chaining of the dipolar particles with the dipoles aligned "nose to tail;" the peaks shift to lower distances as the dipole moment is increased because of the strongly attractive interaction for dipoles in this orientation. To understand the position of the first peak in $g(r)$, we consider the minimum-energy configuration for pairs of dipoles interacting via the potential given by Eqs. (1) and (2). This configuration corresponds to the particles with dipoles parallel and colinear with the interparticle separation vector, i.e., $\boldsymbol{\mu}_1\cdot\boldsymbol{\mu}_2=\mu^2$, $\boldsymbol{\mu}_1\cdot\mathbf{r}=\boldsymbol{\mu}_2\cdot\mathbf{r}=\mu r$. The position and depth of the potential minimum are given by

$$r_0=2^{1/3}(\mu^*)^{-2/9}\sigma \tag{3}$$

and

$$u(r_0)=-\tfrac{3}{4}(\mu^*)^{8/3}\epsilon, \tag{4}$$

respectively. At $\mu^*=0.5$, the potential minimum occurs at $r_0=1.47\sigma$, whereas at $\mu^*=2.75$, $r_0=1.01\sigma$; these rough estimates are in accord with the positions of the first peak in $g(r)$ shown in Fig. 3.

To examine the fluid structure further, we computed the static structure factor $S(q)$ from the Fourier transform of $h(r)=g(r)-1$,[33]

$$S(q)=1+\int h(r)\exp(-i\mathbf{q}\cdot\mathbf{r})d\mathbf{r},$$

$$=1+2\pi\rho\int_0^\infty rJ_0(qr)h(r)dr, \tag{5}$$

where $J_0(z)$ is a Bessel function of the first kind. In Fig. 4 we present $S(q)$ for systems with $\mu^*=0.5$ and $\mu^*=2.75$ at densities in the range $0.05\leq\rho^*\leq 0.5$. In the weakly dipolar case, $S(q)$ looks absolutely typical for a simple fluid, whereas with $\mu^*=2.75$ it shows significant complexity. As

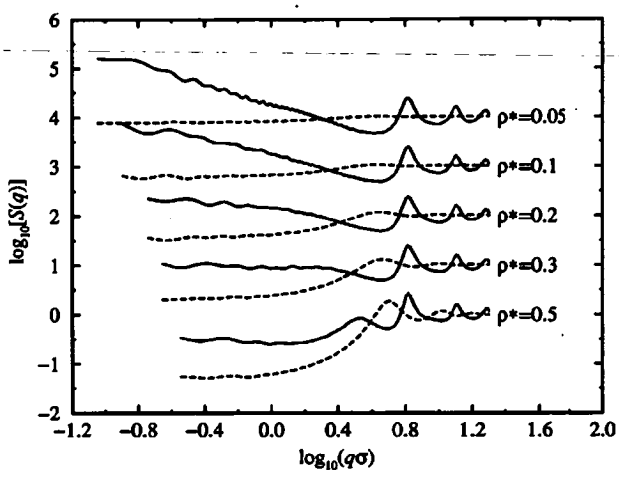

FIG. 4. Logarithms of the static structure factors $\log_{10}[S(q)]$ as functions of $\log_{10}(q\sigma)$ from simulations with $\mu^*=0.5$ (dashed lines) and $\mu^*=2.75$ (solid lines), and at various densities in the range $0.05\leq\rho^*\leq0.5$. The curves are displaced by one unit along the ordinate for clarity.

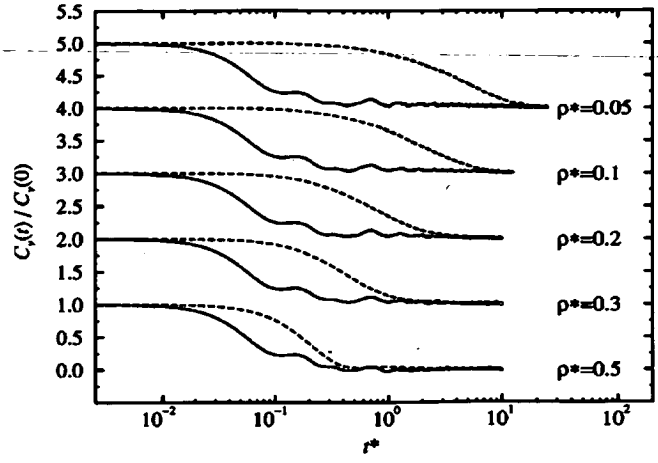

FIG. 5. Normalized velocity autocorrelation functions $C_v(t)/C_v(0)$ for systems with $\mu^*=0.5$ (dashed lines) and $\mu^*=2.75$ (solid lines), and at various densities in the range $0.05\leq\rho^*\leq0.5$. The curves for each density are displaced by one unit along the ordinate for clarity.

the dipole moment is increased, the peaks at $q\sigma>2.5=10^{0.40}$ shift to higher wave vectors, reflecting the decreased separation between near neighbors in the chains. At $\mu^*=2.75$ and $\rho^*=0.05$, $S(q)$ exhibits a power-law dependence on q in the range $q\sigma<4.0=10^{0.60}$; a fit to these results in the range $q\sigma<4.0$ shows that $S(q)\sim q^{-\alpha}$ with $\alpha=1.02\pm0.01$. This is in good agreement with the observed scaling of $S(q)$ for chainlike aggregates in three dimensions ($\alpha=1$),[16] confirming that this is a reliable signal for aggregation in dipolar fluids in both two and three dimensions. In general, this kind of scaling is only apparent with dipole moments $\mu^*>2$, suggesting that this inequality delineates a boundary between "dissociated" and "associated" regimes. This is in accordance with Fig. 2 and the dynamical evidence presented below. $S(q)$ for the most strongly dipolar and dense system ($\mu^*=2.75,\rho^*=0.5$) exhibits an interesting "prepeak" at $q\sigma\simeq3.4=10^{0.54}$, corresponding to a real-space distance of about $2\pi/q\simeq1.8\sigma$; this feature is due to the local parallel ordering of chain segments, as is shown in Fig. 1(d). To summarize, at the highest dipole moments the molecular-scale structure—as characterized by $g(r)$ and $S(q)$—is reminiscent of that observed in three-dimensional dipolar fluids.[16] In both two and three dimensions, the fluid at low densities and temperatures consists of ringlike and chainlike clusters formed from particles in the nose-to-tail configuration, leading to an apparent $1/q$ scaling in the structure factor.

B. Single-particle translational motion

We now turn to the single-particle translational motions in the dipolar fluid. We have calculated the velocity autocorrelation function $C_v(t)$ defined by

$$C_v(t)=\left\langle\frac{1}{N}\sum_{i=1}^{N}\mathbf{v}_i(t)\cdot\mathbf{v}_i(0)\right\rangle, \tag{6}$$

where $\mathbf{v}_i(t)$ is velocity of particle i at time t and the angled brackets denote an average over time origins. Some representative results are shown in Fig. 5 for systems with dipole moments $\mu^*=0.5$ and $\mu^*=2.75$. With a low dipole moment ($\mu^*=0.5$) $C_v(t)$ exhibits a decay typical of simple dilute fluids. At higher dipole moments, however, there is a significant modulation of the curves, and only very small negative portions at the highest densities. We interpret this as being another significant indication of particle chaining. Over short periods of time a tagged particle within a chain can oscillate about its "equilibrium" position between its two nearest neighbors, which might be expected to give rise to oscillatory behavior in $C_v(t)$. The chain as whole is also moving, however, and so any given tagged particle will also have a "drift" velocity which is then modulated by its local motions within the chain. This scenario seems consistent with the results for $\mu^*=2.75$ presented in Fig. 5.

It is well known that in simple two-dimensional fluids, hydrodynamic modes can give rise to a t^{-1} "long-time tail" in $C_v(t)$.[33,34] From the Green-Kubo relation

$$D=\frac{1}{2}\int_0^\infty C_v(t)dt, \tag{7}$$

this long-time tail should lead to a divergent diffusion constant D. Simulation studies of soft-sphere fluids[35] have shown that at high densities ($\rho^*>0.9$) such hydrodynamic effects are absent. In the present case, the highly clustered structures of fluids with high dipole moments might mitigate against the hydrodynamic backflow that gives rise to the long-time tail in $C_v(t)$. Although we cannot categorically rule out the presence of long-time tails, in practice no such features were apparent in $C_v(t)$ within the statistical noise. With this in mind, we have calculated *estimates* of D using Eq. (7), and by computing the mean squared displacement,

$$\Delta R^2(t)=\left\langle\frac{1}{N}\sum_{i=1}^{N}|\mathbf{r}_i(t)-\mathbf{r}_i(0)|^2\right\rangle, \tag{8}$$

where the angled brackets denote an average over time origins. In calculating $\Delta R^2(t)$ we allow the particles to diffuse out of the central simulation cell. As far as we could tell from finite-length simulations, for all of the systems considered in

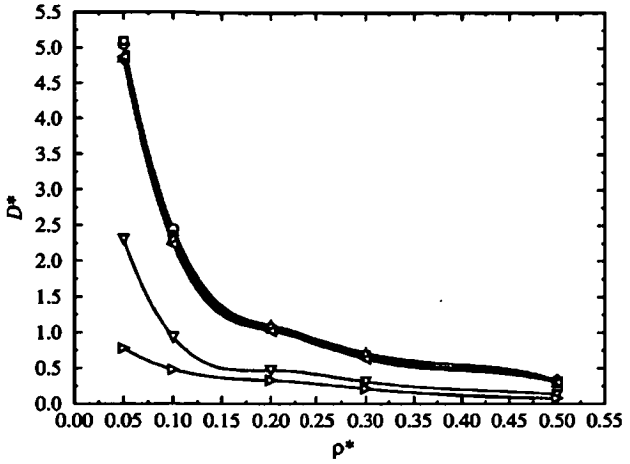

FIG. 6. Reduced diffusion coefficient (see text) as a function of density ρ^* at various dipole moments: $\mu^*=0$ (circles); $\mu^*=0.5$ (squares); $\mu^*=1$ (diamonds); $\mu^*=1.5$ (up triangles); $\mu^*=2$ (left triangles); $\mu^*=2.5$ (down triangles); $\mu^*=2.75$ (right triangles). The solid lines are cubic spline fits to guide the eye. Note that the curves for $0\leqslant\mu^*\leqslant 2$ are almost coincident.

this work $\Delta R^2(t)$ exhibited an approximately linear asymptotic dependence on time. If ΔR^2 exhibits a linear dependence on time at long times, then the diffusion constant D can be defined in two dimensions by the Einstein relation

$$\Delta R^2(t)=4Dt. \tag{9}$$

We found that the values for D obtained from Eqs. (7) and (9) agreed with one another to within 1%. Although it is likely that hydrodynamic effects operate in some of the systems considered in this work, their impact on the measured values of D appears to be small. Nonetheless, the values of D obtained here provide some sort of measure of the single-particle diffusion. In Fig. 6 we plot the reduced diffusion coefficient, $D^*=D\sqrt{m/\epsilon\sigma^2}$, as a function of density for systems with dipole moments in the range $0.5\leqslant\mu^*\leqslant 2.75$. The first thing to note is that the diffusion coefficient decreases with increasing density, as expected. The variation with dipole moment at fixed density is more illuminating. For dipole moments $\mu^*\leqslant 2$, the curves are almost coincident suggesting that the dipolar interactions in this regime have very little effect on the single-particle motion. For dipole moments $\mu^*\geqslant 2.5$, however, the curves are displaced downwards. Essentially the particles become trapped in clusters for long times with the effect of increasing the time scales for single-particle diffusion. The onset of strong association for $\mu^*>2$ evidenced by these dynamical results is consistent with that observed in simulation snapshots and the structural quantities described in Sec. III A. For reference, the values of the diffusion constant are listed in Table I.

C. Single-particle rotational motion

To investigate the impact of chaining upon single-particle rotational motion, we have calculated single-dipole orientation autocorrelation functions defined by

$$C_\mu^\alpha(t)=\left\langle \frac{1}{N\mu^2}\sum_{i=1}^{N}\mu_i^\alpha(t)\mu_i^\alpha(0)\right\rangle, \tag{10}$$

where $\alpha=x$, y, z, and μ_i^α is the component of the dipole vector on particle i along the α axis of the laboratory frame. The function $C_\mu^{xy}(t)=[C_\mu^x(t)+C_\mu^y(t)]$ will therefore characterize the rotational motions of dipoles within the plane of the monolayer, whereas $C_\mu^z(t)$ will reflect out-of-plane motions. In Fig. 7 we compare results for two systems at a density $\rho^*=0.5$ and with dipole moments $\mu^*=0.5$ and $\mu^*=2.75$. With the lower dipole moment ($\mu^*=0.5$) both in-plane and out-of-plane functions show damped oscillatory behavior due to weakly hindered rotations of the dipoles. The quantities $C_\mu^{xy}(0)=0.67$ and $C_\mu^z(0)=0.33$ show that there is no preferred direction of alignment (either in plane or out of plane) for the dipoles at this state point. The weak dipolar forces are therefore insignificant, and so it is anticipated that the reorientational angular frequency in this system will be close to the free-rotor limit, $\omega_0^*=\sqrt{T^*/I^*}=\sqrt{10}$; this is confirmed below. With the higher dipole moment ($\mu^*=2.75$) the in-plane and out-of-plane functions are very different. First, the quantities $C_\mu^{xy}(0)=0.966$ and $C_\mu^z(0)=0.034$ confirm that the dipoles are strongly constrained to lie within the plane. Second, at this admittedly quite extreme dipole moment, $C_\mu^{xy}(t)$ is seen to decay only very slowly but with a small oscillatory modulation. This is clearly a consequence of rapid single-dipole oscillations about the equilibrium nose-to-tail orientations within the chain, while the chain as a whole is rotating only very slowly. The separation between time scales for single-particle and chain rotational motions is analogous to that observed for single-particle and chain translations apparent in the velocity autocorrelation functions discussed in Sec. III B. The out-of-plane function $C_\mu^z(t)$ shows a clear damped oscillation about zero. In Table I we present the values of $C_\mu^z(0)$ for all of the systems considered in this work. $C_\mu^z(0)$ reflects a sharp change in orientational structure that occurs between $\mu^*=2$ and $\mu^*=2.5$. With $\mu^*\leqslant 2$ the values of $C_\mu^z(0)$ are only weakly dependent on density, and for the most part are in close agreement with the value for random dipolar orientations [$C_\mu^z(0)=1/3$]. With $\mu^*=2.5$ and $\mu^*=2.75$ the values of $C_\mu^z(0)$ are very much smaller, reflecting the preferential alignment of dipoles within the plane.

In principle, the time scales for oscillatory orientational motions within the plane and perpendicular to the plane may differ as a result of interchain forces. However, even at the highest density ($\rho^*=0.5$) the mean separation between the chains is significant [see Fig. 1(d)] which suggests that $C_\mu^{xy}(t)$ and $C_\mu^z(t)$ will exhibit similar periods of oscillation. To this end, we have examined the Fourier transforms of $C_\mu^{xy}(t)$ and $C_\mu^z(t)$. Clearly the decay time of $C_\mu^{xy}(t)$ for the system with $\mu^*=2.75$ and $\rho^*=0.5$—as shown in Fig. 7—is very much longer than the duration of the simulation, precluding an accurate calculation of its Fourier transform. Nonetheless, if we use a windowing function, the high-frequency oscillation should still give rise to some sort of peak in the Fourier transform. This extreme truncation will give rise to pathological low-frequency features in the spectrum, but the high-frequency region—where we expect the single-dipole oscillations to manifest themselves—should emerge relatively unscathed. Obviously, calculation of the the Fourier transform of $C_\mu^z(t)$ presents no such problems,

TABLE I. Dynamical properties of the quasi-two-dimensional dipolar fluid: reduced translational diffusion constant $D^*=D\sqrt{m/\epsilon\sigma^2}$; reduced rotational diffusion constant $D_R^*=D_R\sqrt{m\sigma^2/\epsilon}$; single-dipole orientation autocorrelation function at $t=0$, $C_\mu^z(0)$; autocorrelation functions at $t=0$ for the in-plane polarization, $C_P^{xy}(0)$, and the out-of-plane polarization, $C_P^z(0)$; reduced characteristic angular frequencies ω_0^* for single-particle rotational motion estimated from the Fourier transforms of $C_\mu^z(t)$ and $C_\Omega(t)$, and from the approximate theoretical expression in Eq. (15).

							ω_0^*		
μ^*	ρ^*	D^*	D_R^*	$C_\mu^z(0)$	$C_P^{xy}(0)$	$C_P^z(0)$	From $C_\mu^z(t)$	From $C_\Omega(t)$	Eq. (15)
0.5	0.05	5.1		0.33	0.67	0.32	3.6		1.9
	0.1	2.3		0.34	0.67	0.33	3.5		1.9
	0.2	1.1		0.33	0.71	0.30	3.6		1.9
	0.3	0.69		0.34	0.72	0.30	3.5		1.9
	0.5	0.29		0.33	0.74	0.26	3.5		1.9
1	0.05	4.8		0.33	0.68	0.30	3.6		4.9
	0.1	2.4		0.33	0.71	0.27	3.6		4.9
	0.2	1.1		0.33	0.83	0.21	3.7		4.9
	0.3	0.66		0.32	0.97	0.21	3.8		4.9
	0.5	0.34		0.31	1.3	0.17	4.2		4.9
1.5	0.05	4.9	133	0.33	0.71	0.26	3.7		8.4
	0.1	2.3	56	0.32	0.85	0.22	3.9		8.4
	0.2	1.1	27	0.30	1.1	0.16	4.2		8.4
	0.3	0.71	13	0.28	1.4	0.14	4.5		8.4
	0.5	0.31	5.2	0.23	2.1	0.082	5.2		8.4
2	0.05	4.9	58	0.29	0.95	0.20	4.0		12.4
	0.1	2.2	21	0.25	1.4	0.17	4.7		12.4
	0.2	1.0	6.9	0.20	2.2	0.10	5.5	6.4	12.4
	0.3	0.63	3.4	0.17	2.3	0.067	6.4	7.7	12.4
	0.5	0.30	1.4	0.13	2.8	0.049	7.6	8.3	12.4
2.5	0.05	2.3	18	0.082	6.7	0.055	10.3	12.2	16.6
	0.1	0.93	4.8	0.068	11	0.043	12.4	12.2	16.6
	0.2	0.47	1.3	0.057	8.5	0.034	12.7	12.3	16.6
	0.3	0.31	0.74	0.057	2.2	0.028	12.5	12.4	16.6
	0.5	0.13	0.34	0.052	3.3	0.022	12.7	12.4	16.6
2.75	0.05	0.78	1.9	0.035	11	0.023	14.0	14.2	18.9
	0.1	0.48	0.83	0.036	15	0.021	14.3	14.3	18.9
	0.2	0.33	0.34	0.035	111	0.023	14.6	14.3	18.9
	0.3	0.21	0.22	0.035	250	0.019	14.6	14.3	18.9
	0.5	0.079	0.19	0.034	280	0.016	14.3	14.5	18.9

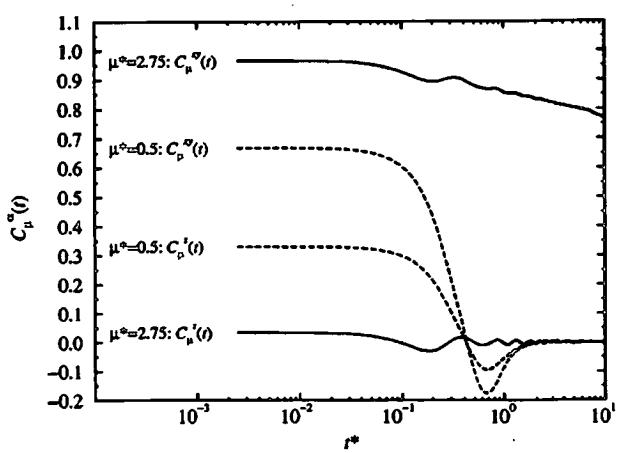

FIG. 7. Single-dipole autocorrelation functions $C_\mu^{xy}(t)=[C_\mu^x(t)+C_\mu^y(t)]$ and $C_\mu^z(t)$ for systems at a density of $\rho^*=0.5$, and with dipole moments $\mu^*=0.5$ (dashed lines) and $\mu^*=2.75$ (solid lines).

but nonetheless we have applied a Blackman windowing function throughout.[32] For the system with $\mu^*=2.75$ and $\rho^*=0.5$ we find peaks in the Fourier transforms of both $C_\mu^{xy}(t)$ and $C_\mu^z(t)$ at a characteristic reduced angular frequency of $\omega_0^*=14.3$. The conclusion is that even at this high density and dipole moment—at which interchain interactions might be significant—the estimates of reorientational time scales extracted from $C_\mu^{xy}(t)$ and $C_\mu^z(t)$ are essentially the same. In the following we therefore concentrate on $C_\mu^z(t)$ since it is easier to calculate Fourier transforms reliably.[36] To assist in comparisons, we present the function

$$\chi_\mu^z(\omega)=\frac{1}{2\pi C_\mu^z(0)}\int_{-\infty}^{\infty}C_\mu^z(t)\exp(-i\omega t)dt, \tag{11}$$

which is simply the Fourier transform of $C_\mu^z(t)$ normalized to unit area. Figure 8 shows $\chi_\mu^z(\omega)$ for systems at a density

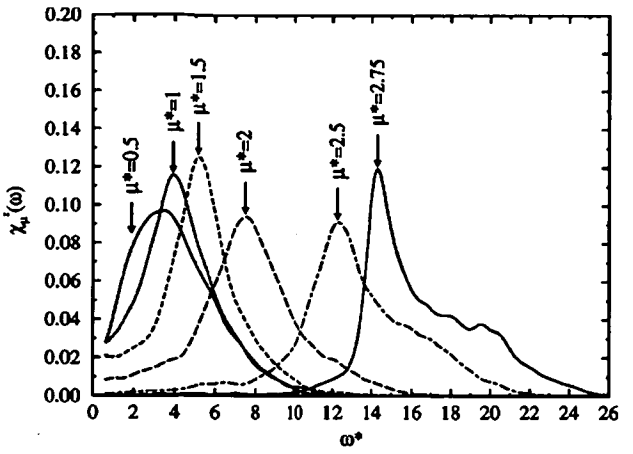

FIG. 8. Normalized Fourier transform of the z component of the single-dipole autocorrelation function $\chi^z_\mu(\omega)$ for systems at a density of $\rho^*=0.5$, and with dipole moments in the range $0.5\leqslant\mu^*\leqslant2.75$.

$\rho^*=0.5$ and dipole moments in the range $0.5\leqslant\mu^*\leqslant2.75$. At the lowest dipole moment ($\mu^*=0.5$) the peak in $\chi^z_\mu(\omega)$ is centered at approximately $\omega_0^*=3.5$, which is close to the free-rotor limit $\omega_0^*=\sqrt{T^*/I^*}\simeq3.16$. The position of this primary peak in $\chi^z_\mu(\omega)$ shifts to higher frequency with increasing dipole moment, reflecting stronger interactions and the presence of chaining which contrive to align dipoles in a "head-to-tail" conformation with their nearest neighbors. It is also clear that with increasing dipole moment a pronounced high-frequency shoulder develops. We speculate that this feature is due to coupling between single-dipole orientational motions and collective rotational motions. We return to this point briefly in Sec. III D, but first we report the positions of the primary peaks in $\chi^z_\mu(\omega)$. We have fitted single Lorentzian functions to the spectra in the vicinity of the peaks to extract estimates of the peak positions; the results are shown in Table I. We note that at the highest dipole moments ($\mu^*=2.5$ and $\mu^*=2.75$) ω_0 is almost independent of density, reflecting the fact that chains are present over the whole density range considered, and that interchain interactions (which would be more significant at higher densities) are actually very weak. Given this observation, we provide simple theoretical estimates of the variation of ω_0 with dipole moment in the high-dipole-moment regime.

In the highly-chained regime it is reasonable to think of the rotational motion of a single dipole in a cluster as being quasiharmonic in that its orientation oscillates about its equilibrium position within the chain. Consider a tagged dipolar sphere as part of a perfectly straight chain oriented along the laboratory x axis in which all of the dipole moments (except the tagged dipole moment) are constrained parallel with the x axis. The equilibrium nearest-neighbor separation is r_0 [Eq. (3)], and for simplicity we consider the motion of the tagged dipole in the xy plane; as shown above, it does not matter in which plane we consider the motion because the effects of interchain interactions are weak. If the tagged dipole is given by $\boldsymbol{\mu}(t)=\mu[\cos\gamma(t),\sin\gamma(t),0]$—where γ is the angle subtended by the dipole moment and the x axis—then the resulting torque due to the rest of the dipoles is oriented along the z axis and has magnitude

$$2\sum_{n=1}^{\infty}\left[-\frac{2\mu^2\sin\gamma}{(nr_0)^3}\right]=-\frac{4\mu^2\zeta(3)}{r_0^3}\sin\gamma, \tag{12}$$

where $\zeta(3)\simeq1.202$ is the Riemann ζ function. For high dipole moments the deviation from perfect alignment will be small, and hence $\sin\gamma\approx\gamma$. In this limit the equation of motion is $\ddot{\gamma}=-\omega_0^2\gamma$ where ω_0 is given by

$$\omega_0=\sqrt{\frac{4\mu^2\zeta(3)}{Ir_0^3}}. \tag{13}$$

The equation of motion yields an oscillatory solution $\gamma(t)=\gamma(0)\cos\omega_0t+(\dot{\gamma}(0)/\omega_0)\sin\omega_0t$. The orientation autocorrelation function in the absence of damping (friction) is therefore proportional to

$$\langle\boldsymbol{\mu}(t)\cdot\boldsymbol{\mu}(0)\rangle\propto1-\langle\gamma^2\rangle+\langle\gamma^2\rangle\cos\omega_0t \tag{14}$$

and even with damping through rotational friction a peak should be apparent in the Fourier transform at an angular frequency given by Eq. (13). In Table I, a comparison is made between the peak positions obtained from simulations, and the result of combining Eqs. (3) and (13) which yields, in reduced units,

$$\omega_0^*=\sqrt{\frac{2(\mu^*)^{8/3}\zeta(3)}{I^*}}. \tag{15}$$

By construction Eq. (15) is consistent with the observation that ω_0^* is roughly independent of density at the highest dipole moments, but it overestimates the simulation results for systems with the highest dipole moments—$\mu^*=2.5$ and $\mu^*=2.75$—by about 30%. It is easy to understand why Eq. (15) yields an overestimate: this approximation is based on a perfectly linear rigid chain, with no account taken of thermal fluctuations in the shape and extent of the chain. These effects will reduce in magnitude the average field experienced by—and hence the "vibrational" frequency of—any given dipole within the chain.

We have measured the single-particle autocorrelation function of the angular velocity $\boldsymbol{\Omega}$ given by

$$C_\Omega(t)=\left\langle\frac{1}{N}\sum_{i=1}^{N}\boldsymbol{\Omega}_i(t)\cdot\boldsymbol{\Omega}_i(0)\right\rangle, \tag{16}$$

and performed a similar analysis to that carried out on $C^\alpha_\mu(t)$ above. As defined, $C_\Omega(0)=2k_BT/I$. Unsurprisingly we find the same general behavior as with $C^\alpha_\mu(t)$, including the shapes and positions of the peaks in the Fourier transforms; for completeness, in Table I we have included estimates of ω_0^* obtained from these peak positions. The estimates of ω_0^* obtained from $C_\Omega(t)$ and $C^z_\mu(t)$ are consistent, as expected. In Fig. 9 we show some examples of $C_\Omega(t)$ from simulations at a density of $\rho^*=0.5$ and dipole moments in the range $0.5\leqslant\mu^*\leqslant2.75$. With low dipole moments ($\mu^*\leqslant1$) the relaxation of this function occurs very slowly, and at long times monotonically, reflecting the lack of strong interparticle interactions. With increasing dipole moment $C_\Omega(t)$ develops oscillations which can be identified with the quasiharmonic motion described above.

From $C_\Omega(t)$ we have calculated the rotational diffusion constant D_R given by[33]

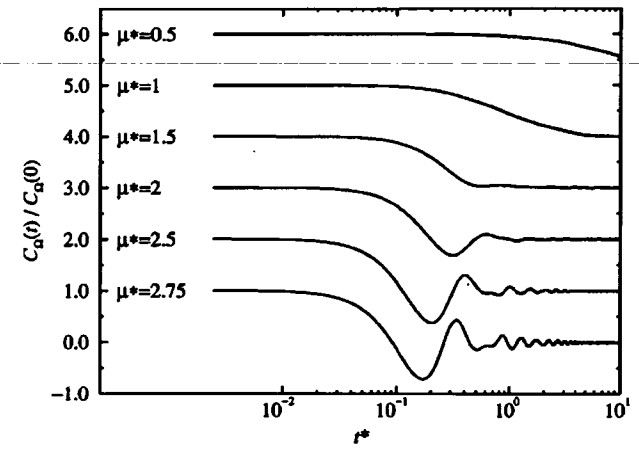

FIG. 9. Normalized angular velocity autocorrelation functions $C_\Omega(t)/C_\Omega(0)$ for systems at $\rho^*=0.5$ with various dipole moments in the range $0.5\leq\mu^*\leq2.75$. The curves for each dipole moment are displaced by one unit along the ordinate for clarity.

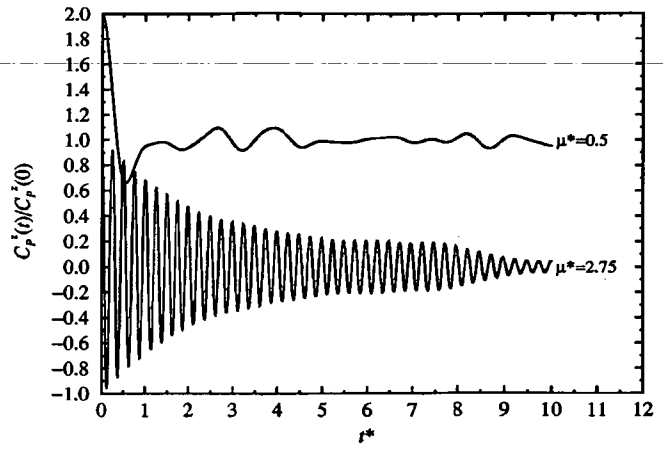

FIG. 10. Normalized autocorrelation function of the z component of the bulk polarization $C_P^z(t)/C_P^z(0)$ for systems at a density $\rho^*=0.5$ and dipole moments $\mu^*=0.5$ (top) and $\mu^*=2.75$ (bottom). The curves are displaced by one unit along the ordinate for clarity.

$$D_R=\tfrac{1}{2}\int_0^\infty C_\Omega(t)dt. \tag{17}$$

Some results are shown in Table I. The calculation of D_R was not possible at low dipole moments and low densities due to the very long decay of $C_\Omega(t)$ (see Fig. 9). For a given dipole moment, D_R decreases with increasing concentration; at high dipole moments this trend probably reflects an increased restriction of chain motions, as well as the quasiharmonic motions of single dipoles. For a given density D_R decreases with increasing dipole moment obviously due to increased aggregation.

D. Collective rotational motion

The problems encountered above with performing the Fourier transforms of single-dipole orientation autocorrelation functions are exacerbated when we turn to the analysis of the collective rotational motion. For exactly the same reasons as noted in Sec. III C, we will concentrate primarily on the autocorrelation function of the z component of the bulk polarization, rather than the x and y components. The bulk polarization is given by

$$\mathbf{P}(t)=\sum_{i=1}^{N}\boldsymbol{\mu}_i(t). \tag{18}$$

We define an autocorrelation function of its α component by

$$C_P^\alpha(t)=\frac{\langle P_\alpha(t)P_\alpha(0)\rangle}{N\mu^2}. \tag{19}$$

The function characterizing the in-plane polarization is $C_P^{xy}(t)=[C_P^x(t)+C_P^y(t)]$. At high dipole moments this function decays extremely slowly, with a decay time orders of magnitude larger than the length of our simulations; in some cases it hardly varies at all over simulation runs of $O(10^5)$ MD time steps. This situation appears analogous to the predicted increase of the Debye relaxation time in three-dimensional dipolar fluids as the dipole moment is increased.[37] A full analysis of $C_P^{xy}(t)$ is impractical, although the values of these functions at $t=0$ provide some measure of the in-plane susceptibility, this being proportional to $\langle P_x^2+P_y^2\rangle$. Values of $C_P^{xy}(0)$ are presented in Table I; these results show that the in-plane susceptibility increases markedly with increasing dipole moment [note that the trivial factor of μ^2 in the susceptibility is canceled in Eq. (19)]. This is due to the presence of long, almost linear segments within the chains which would be easily polarized with the application of an external field.

The autocorrelation function of the z component of the bulk polarization yields more information. For the purposes of illustration, we show $C_P^z(t)/C_P^z(0)$ in Fig. 10 for two systems at a density $\rho^*=0.5$, and with dipole moments $\mu^*=0.5$ and $\mu^*=2.75$. $C_P^z(t)$ exhibits damped oscillatory behavior in both cases, but clearly at high dipole moments the oscillation is of higher frequency and far less damped; crudely fitting a function of the form $C_P^z(t)\propto\exp(-t/\tau)\cos\omega_0 t$ in the range $0\leq t^*\leq10$ yields $\tau\simeq0.5$ and $\omega_0\simeq5$ for $\mu^*=0.5$, and $\tau\simeq3$ and $\omega_0\simeq25$ for $\mu^*=2.75$. The value of $C_P^z(0)$ is proportional to the out-of-plane susceptibility and is shown in Table I. The results show that the out-of-plane susceptibility decreases with increasing dipole moment due to the preferred in-plane orientations of the dipoles.

We now turn to the Fourier transform of $C_P^z(t)$, which for the purposes of comparison is defined as a normalized quantity, i.e.,

$$\chi_P^z(\omega)=\frac{1}{2\pi C_P^z(0)}\int_{-\infty}^{\infty}C_P^z(t)\exp(-i\omega t)dt. \tag{20}$$

Figure 11 shows $\chi_P^z(\omega)$ for systems with density $\rho^*=0.5$ and dipole moments in the range $1.5\leq\mu^*\leq2.75$; results for lower dipole moments are omitted for clarity as they consist of increasingly broad and noisy peaks. As in the case of single-particle rotational motion, the characteristic frequency increases with increasing dipole moment. For the systems with $\mu^*=2.5$ and $\mu^*=2.75$, the peaks in $\chi_P^z(\omega)$ are very sharp and well defined. In both cases, the positions of these peaks coincide with the high-frequency edge of the shoulder

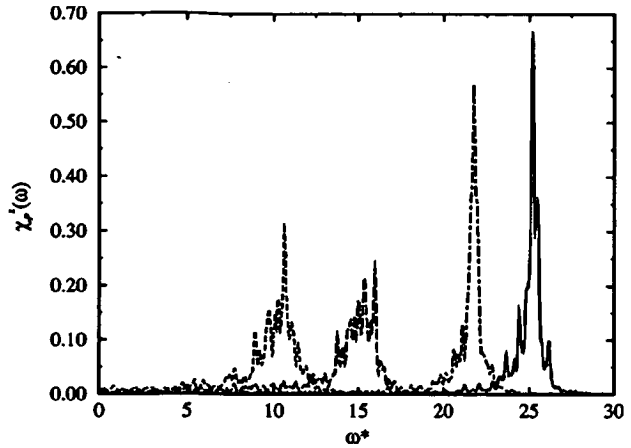

FIG. 11. Normalized Fourier transforms of the z component of the bulk polarization autocorrelation function $\chi_P^z(\omega)$ for systems at a density of $\rho^* = 0.5$, and with dipole moments in the range $1.5 \leqslant \mu^* \leqslant 2.75$. From left to right: $\mu^* = 1.5$ (short-dashed line); $\mu^* = 2$ (long-dashed line); $\mu^* = 2.5$ (dot-dashed line); $\mu^* = 2.75$ (solid line).

in the corresponding single-particle functions, $\chi_\mu^z(\omega)$. We suggest that this is a signal of some sort of coupling between single-particle and collective motions which give rise to the high-frequency shoulder in $\chi_\mu^z(\omega)$.

It is reasonable to suggest that long-range dipolar forces can lead to collective orientational motions within chains over considerable length scales. A full examination of these properties will require the calculation of space- and time-dependent correlation functions,[37] like $\langle \mathbf{P}(\mathbf{q},t)\cdot\mathbf{P}(-\mathbf{q},0)\rangle$, where $\mathbf{P}(\mathbf{q},t) = \sum_{j=1}^{N} \boldsymbol{\mu}_j(t)\exp[-i\mathbf{q}\cdot\mathbf{r}_j(t)]$ is a Fourier component of the bulk polarization. In the case of strongly chained systems at high dipole moments, this could lead to the identification of excitations analogous to spin waves in solid magnetic materials. In Refs. 37 and 38 relationships are derived between the single-particle relaxation time, $\tau_R = 1/2D_R$, associated with the decay of $\langle \boldsymbol{\mu}_i(t)\cdot\boldsymbol{\mu}_i(0)\rangle$, and the Debye relaxation time τ_D associated with the decay of $\langle \mathbf{P}(t)\cdot\mathbf{P}(0)\rangle$. In Ref. 38, for instance, the results are based on a micro-macro theorem stating that if the single-dipole correlation function can be expressed as a sum of decaying exponentials, then so can the bulk polarization correlation function. It is not clear whether such theories can be applied successfully to the very high dipole moment regime where the correlation functions are highly oscillatory; in the current work we have been concerned with oscillation frequencies in the correlation functions, not the decay times. To study the latter, accessing the relevant time scales will require much longer simulations than those conducted here, particularly for the in-plane motions.

IV. CONCLUSIONS

In this work, MD simulations have been used to study a simple model of fluid monolayers comprising spherical dipolar particles. Experimental realizations of these systems include colloidal ferrofluids and other magnetic liquids. The emphasis of this study has been on the effects of strong dipolar interactions on structure, and translational and orientational dynamics; these interactions favor the formation of chainlike aggregates, which profoundly affect the observable properties of the bulk material.

The signature of chaining on the structure factor has been examined, leading to the identification of power-law scaling at low wave vectors, analogous to that observed in simulations of three-dimensional dipolar fluids. This should provide a very clear fingerprint of chainlike aggregates which should be accessible in scattering experiments.

Dramatic effects of aggregation on the diffusion constant and the velocity autocorrelation function have been demonstrated. With weak dipolar interactions these quantities are absolutely typical for a simple two-dimensional "atomic" fluid. At high dipole moments, however, the chainlike aggregates lead to a discrimination between local "intracluster" motions and motions of clusters as integral units. The effect of the coupling between single-particle and collective motions is clearly visible in the velocity autocorrelation function. Unsurprisingly, aggregation is accompanied by a sharp drop in the single-particle diffusion coefficient, reflecting the fact that individual particles are strongly constrained by their nearest neighbors within the chain.

The orientational motion has been examined, and characteristic frequencies have been identified with particular types of motions. The characteristic frequencies for single-particle orientational motion have been determined from the Fourier transforms of the appropriate autocorrelation functions. At low dipole moments, the characteristic rotational frequency is close to the free-rotor limit. At high dipole moments this frequency is dictated by quasiharmonic oscillations of single-dipole orientations about the equilibrium orientations within chains, and hence the frequency increases with increasing dipole moment. In general, the characteristic frequencies are independent of density which implies that the interactions between neighboring chains are weak; moreover, we did not detect any distinction between the time scales for in-plane and out-of-plane rotational motions. A simple analysis of the effective field experienced by a tagged dipolar particle yields estimates of the characteristic frequencies accurate to within about 30% at high dipole moments. The Fourier transforms of the single-dipole orientation autocorrelation functions develop high-frequency shoulders with increasing dipole moment, which we suggest are due to the coupling between single-particle and collective motions. We have made a brief investigation of the collective rotational motions, the results of which are consistent with this hypothesis.

Further work is required, particularly in calculating space- and time-dependent correlation functions, and in making a detailed connection between single-particle and collective orientational motions. In addition, simulations of the aggregation kinetics in strongly polar fluids could shed light on the different time scales observed in recent experiments.[28] This might best be achieved through the application of computational methods devised for the study of energy landscapes.[39] These will be the topics of future studies.

ACKNOWLEDGMENT

P.D.D. is grateful to the Engineering and Physical Sciences Research Council (U.K.) for the provision of a studentship.

[1] P. I. C. Teixeira, J. M. Tavares, and M. M. Telo da Gama, J. Phys.: Condens. Matter **12**, R411 (2000).
[2] P. H. Hess and P. H. Parker, Jr., J. Appl. Polym. Sci. **10**, 1915 (1966).
[3] V. F. Puntes, K. M. Krishnan, and A. P. Alivisatos, Science **291**, 2115 (2001).
[4] K. Butter, P. H. H. Bomans, P. M. Frederik, G. J. Vroege, and A. P. Philipse, Nat. Mater. **2**, 88 (2003).
[5] K. Butter, P. H. Bomans, P. M. Frederik, G. J. Vroege, and A. P. Philipse, J. Phys.: Condens. Matter **15**, S1451 (2003).
[6] A. Zilman, T. Tlusty, and S. A. Safran, J. Phys.: Condens. Matter **15**, S57 (2003).
[7] T. Tlusty and S. A. Safran, Science **290**, 1328 (2000).
[8] P. Pincus, Science **290**, 1307 (2000).
[9] P. G. de Gennes and P. A. Pincus, Phys. Kondens. Mater. **11**, 189 (1970).
[10] P. C. Jordan, Mol. Phys. **25**, 961 (1973).
[11] M. A. Osipov, P. I. C. Teixeira, and M. M. Telo da Gama, Phys. Rev. E **54**, 2597 (1996).
[12] J. M. Tavares, M. M. Telo da Gama, and M. A. Osipov, Phys. Rev. E **56**, R6252 (1997).
[13] J. M. Tavares, J. J. Weis, and M. M. Telo da Gama, Phys. Rev. E **59**, 4388 (1999).
[14] J. J. Weis and D. Levesque, Phys. Rev. Lett. **71**, 2729 (1993).
[15] D. Levesque and J. J. Weis, Phys. Rev. E **49**, 5131 (1994).
[16] P. J. Camp and G. N. Patey, Phys. Rev. E **62**, 5403 (2000).
[17] P. J. Camp, J. C. Shelley, and G. N. Patey, Phys. Rev. Lett. **84**, 115 (2000).
[18] H. Mamiya, I. Nakatani, and T. Furubayashi, Phys. Rev. Lett. **84**, 6106 (2000).
[19] P. J. Camp, Phys. Rev. E **68**, 061506 (2003).
[20] W. D. Ristenpart, I. A. Aksay, and D. A. Saville, Phys. Rev. Lett. **90**, 128303 (2003).
[21] I. Varga, F. Kun, and K. F. Pál, Phys. Rev. E **69**, 030501 (2004).
[22] J.-J. Weis, Mol. Phys. **93**, 361 (1998).
[23] J. J. Weis, Mol. Phys. **100**, 579 (2002).
[24] J. J. Weis, J. M. Tavares, and M. M. Telo da Gama, J. Phys.: Condens. Matter **14**, 9171 (2002).
[25] J. M. Tavares, J. J. Weis, and M. M. Telo da Gama, Phys. Rev. E **65**, 061201 (2002).
[26] J. J. Weis, J. Phys.: Condens. Matter **15**, S1471 (2003).
[27] R. E. Rosensweig, *Ferrohydrodynamics* (Dover, New York, 1998).
[28] W. Wen, F. Kun, K. F. Pál, D. W. Zheng, and K. N. Tu, Phys. Rev. E **59**, R4758 (1999).
[29] V. V. Murashov, P. J. Camp, and G. N. Patey, J. Chem. Phys. **116**, 6731 (2002).
[30] T. A. Andrea, W. C. Swope, and H. C. Andersen, J. Chem. Phys. **79**, 4576 (1983).
[31] S. Fazekas, J. Kertész, and D. E. Wolf, Phys. Rev. E **68**, 041102 (2003).
[32] M. P. Allen and D. J. Tildesley, *Computer Simulation of Liquids* (Clarendon, Oxford, 1987).
[33] J.-P. Hansen and I. R. McDonald, *Theory of Simple Liquids* (Academic, London, 1986).
[34] B. J. Alder and T. E. Wainwright, Phys. Rev. A **1**, 18 (1970).
[35] M. M. Hurley and P. Harrowell, J. Chem. Phys. **105**, 10521 (1996).
[36] Of course, we could have obviated all of these problems by carrying out a longer MD simulation. To estimate the simulation time required, we fitted a single exponential function to the "tail" of $C_{\mu}^{xy}(t)$ for $\mu^*=2.75$ and $\rho^*=0.5$ in the region $t^*>3$. The decay constant was of the order of 0.01, which means that $C_{\mu}^{xy}(t)$ will have decayed to 1% of its initial value after a reduced time of about 500. To ensure good statistics one might need to perform a simulation at least 20 times longer in duration, which equates to a simulation consisting of 4×10^6 time steps. Unfortunately this is an order of magnitude longer than we can simulate with the current computational resources at our disposal.
[37] B. Bagchi and A. Chandra, Adv. Chem. Phys. **80**, 1 (1991).
[38] D. Kivelson and P. A. Madden, Mol. Phys. **30**, 1749 (1975).
[39] D. J. Wales, *Energy Landscapes: Applications to Clusters, Biomolecules and Glasses* (Cambridge University Press, Cambridge, 2004).

Two-dimensional structure in a generic model of triangular proteins and protein trimers

Philip J. Camp* and Peter D. Duncan
School of Chemistry, University of Edinburgh, West Mains Road, Edinburgh EH9 3JJ, United Kingdom
(Received 30 December 2005; published 10 April 2006)

Motivated by the diversity and complexity of two-dimensional (2D) crystals formed by triangular proteins and protein trimers, we have investigated the structures and phase behavior of hard-disk trimers. In order to mimic specific binding interactions, each trimer possesses an "attractive" disk which can interact with similar disks on other trimers *via* an attractive square-well potential. At low density and low temperature, the fluid phase mainly consists of tetramers, pentamers, or hexamers. Hexamers provide the structural motif for a high-density, low-temperature periodic solid phase, but we also identify a metastable periodic structure based on a tetramer motif. At high density there is a transition between orientationally ordered and disordered solid phases. The connections between simulated structures and those of 2D protein crystals—as seen in electron microscopy—are briefly discussed.

DOI: 10.1103/PhysRevE.73.046111 PACS number(s): 64.60.−i, 64.70.Dv, 05.10.Ln

I. INTRODUCTION

Two-dimensional (2D) materials present some fascinating challenges to condensed-matter theory, with even the most simple 2D systems harboring surprises. One of the most famous problems involves the precise description of melting in 2D solids made up of hard, disklike particles with short-range repulsive interactions [1–4]. Specifically, does the fluid undergo a weak first-order transition to the solid, or is there an intermediate hexatic phase linked by two continuous phase transitions? Related avenues of research concern the existence of exotic phases in systems made up of more complex particles, such as (non)periodic solids of hard-disk dimers [5,6], pentamers and hexamers [7], tetratic phases of hard squares [8] and hard rectangles [9], and orientationally ordered solids of hard pentagons and heptagons [10]. The effects of additional interactions on the phase behavior and dynamics of 2D systems are also of interest, as evidenced by recent studies on dipolar potentials in the context of magnetic colloids [11]. Such models provide an ideal testing ground for condensed-matter theories, and in some cases challenge our most fundamental understanding of the properties of matter.

Despite their simplicity, 2D models can provide reliable descriptions of some real, and rather complex, experimental situations. For example, in a number of recent studies, 2D models have been employed to help interpret and understand the clustering and crystallization of proteins at interfaces. The conformations and interactions of proteins are central to biological activity, and ideally one would like to investigate these properties *in vivo*. Unfortunately, structural information is most commonly obtained from x-ray diffraction studies on crystals. There is a class of proteins, however, that can be studied under conditions resembling those *in vivo*. Membrane proteins constitute a large class of molecules found within the lipid bilayers that constitute cell walls. They fulfill a variety of roles, such as controlling the selective transport of ions and molecules across cell membranes, or providing binding sites for other molecules onto the membrane. The structures of membrane proteins can be studied by deposition onto a surface, alongside lipids, to form either low surface coverage or 2D crystals; the hydrophobic lipids help to mimic the interior of the membrane. Electron microscopy or atomic-force microscopy can then be used to image directly the clustering and packing of proteins at the solid-air interface [12]. In many cases, the ordering of proteins can be rationalized on the basis of their gross shapes (the way in which those shapes would "tile the plane") and the presence of specific binding interactions between domains on different molecules. For example, the surface structure of bacteriorhodopsin (a transmembrane protein) is comprised of a close-packed array of trimers, each made up of monomers that resemble 120° sectors of a circle. Monte Carlo (MC) simulations of hard sectors—with an additional attractive square-well potential to mimic specific binding interactions—yield insight on the self-assembly and subsequent crystallization processes [13]. In another application, the ordering in 2D crystals of annexin V—another "triangular" membrane protein—was reproduced in simulations of a hard-disk model decorated with an appropriate orientation-dependent potential to mimic the locations of the specific binding sites on the protein [14,15]. Experimentally observed honeycomb and triangular structures were captured by the molecular model. These examples show that the basic physics of large scale structural order in 2D protein crystals can be studied with simple models, and without resorting to atomistically detailed—and hence very expensive—computer simulations.

There are a large number of proteins which are either inherently triangular in shape, or otherwise form trimeric structures [16–22]. For example, rotavirus inner capsid protein V6 forms trimers resembling equilateral triangles, which pack in 2D crystals (space group $p6$) [16]. Specific fragments of prion proteins found *in vivo* form trimeric units that crystallize into a 2D structure (space group $p3$) [21]. Finally, we highlight an example in which a membrane fusion protein (from the Semliki forest virus) is seen to form pentagons of trimers, with the center of the pentagon raised slightly out of the plane [20]. Some semblance of local fivefold coordina-

*Email address: philip.camp@ed.ac.uk

tion can also been seen in TetA—a roughly triangular transporter protein—at moderate surface coverages [18].

Motivated by the diversity of 2D crystal structures exhibited by trimeric protein units, and also by the observation of fivefold coordination [20], we have investigated the structure and phase behavior of model trimeric molecules made up of hard disks. In order to mimic specific binding interactions, such as those that might give rise to local fivefold coordination, we focus on an equilateral triangle of three hard disks at contact, in which one disk can interact with the corresponding disks on other molecules *via* a short-range attractive square-well potential. As we will show below, this raises the possibility of generating orientational order within simple close-packed structures, and also offers the opportunity of forming clusters at low surface coverages. Using MC simulations, we map out the phase diagram of the model system, and characterize the structures of the low-density clustered fluid and high-density solids which are formed at low temperature. The remainder of the article is organized as follows. In Sec. II we describe the molecular model, and summarize the simulation methods. The results are presented in Sec. III, and Sec. IV concludes the paper.

II. MODEL AND METHODS

The molecular model consists of three hard disks, each of diameter σ, fused at mutual contact to form an equilateral triangle. Two of the disks on each molecule are purely repulsive, and interact with all other disks in the system through the potential

$$u(r) = \begin{cases} \infty, & r < \sigma, \\ 0, & r \geqslant \sigma, \end{cases} \tag{1}$$

where r is the separation between the centers of two disks. The third disk on each molecule carries a central attractive interaction site; these "attractive" disks interact with each other *via* the potential

$$u(r) = \begin{cases} \infty, & r < \sigma, \\ -\epsilon, & \sigma \leqslant r < \lambda\sigma, \\ 0, & r \geqslant \lambda\sigma, \end{cases} \tag{2}$$

where $\lambda > 1$ controls the range of the attraction. This potential crudely mimics an effective attraction between vertices of the molecular triangles, which might arise through specific interactions (e.g., hydrogen bonding, disulfide bridges, effective solvophobic interactions).

The parameter λ will clearly have a crucial role to play in the thermodynamics of the system. If $\lambda \gg 1$ then one should anticipate a conventional phase diagram containing a vapor-liquid transition, and a fluid-solid transition. The orientation of a trimer can be defined by a vector $\mathbf{n}$ joining the geometrical center of the trimer with the center of the attractive disk. It is unlikely that there would be any periodic orientational ordering of $\mathbf{n}$ in the solid phase; if two trimers can interact favorably irrespective of the mutual orientation, then on entropy grounds the orientations will be disordered. In the opposite extreme, $\lambda \gtrsim 1$, the molecules will feel the orientation dependence of the net trimer-trimer potential, and ultimately we might expect the vapor-liquid transition to disappear from the equilibrium phase diagram. Indeed, in a pure square-well hard-sphere fluid, condensation becomes metastable with respect to freezing when $\lambda < 1.25$ [23]. In the present case, an interaction range $\lambda < \sqrt{3}$ guarantees that attractive sites must face each other directly in order to interact; when $\lambda > \sqrt{3}$ it is possible for an attractive disk to be within interaction range of a trimer even if it approaches from "behind." With these comments in mind, we have chosen to study a system with $\lambda = 1.25$. The ratio of $\lambda\sigma$ to the (angle-averaged) diameter of the trimer is smaller than that in a pure square-well hard-sphere system with the same value of λ, and assuming some sort of correspondence between two- and three-dimensional systems, we do not anticipate there being a vapor-liquid transition in the equilibrium phase diagram. On the other hand, because the trimers have to attain quite specific mutual orientations in order to interact favorably (since $\lambda < \sqrt{3}$), we should expect to see some sort of nontrivial structure in fluid and solid phases at low temperatures.

Systems of $N = 120$ trimers were studied using MC simulations either in the isothermal-isobaric (NpT) ensemble or the canonical (NAT) ensemble [24]. The simulation cell was rectangular with dimensions L_x and L_y, and area $A = L_x L_y$. Each MC cycle consisted of one translational trial move and one rotational trial move for each of N randomly selected molecules. Displacement parameters were adjusted to give $\sim 50\%$ acceptance rates. To help equilibrate dense phases, we included trial moves in which a randomly selected trimer was rotated by $\pm 120°$. In NpT simulations of solid phases, L_x and L_y were varied independently; in NpT simulations of fluid phases, the simulation cell was constrained to be square. For most thermodynamic state points typical equilibration runs consisted of $\sim 10^5$ MC cycles, but some points (close to phase transitions) required $\sim 10^6$ MC cycles. Production runs were typically $\sim 10^5$ MC cycles. We define the following dimensionless units in terms of the square-well depth, ϵ, and the hard-disk diameter, σ: number density $\rho^* = N\sigma^2/A$; temperature $T^* = k_B T/\epsilon$; pressure $p^* = p\sigma^2/k_B T$.

III. RESULTS

The phase diagram of the model trimers in the density-temperature (ρ^*-T^*) plane is sketched in Fig. 1. Before detailing the determination of the phase boundaries, the characteristics of the different phases will be described. There are four distinct regions in the phase diagram. At low density and high temperature, a normal fluid phase is in evidence (fluid I). A typical simulation configuration is shown in Fig. 2(a). There is neither translational nor long-range orientational order in the system.

At high density and high temperature, the stable solid phase (solid I) possesses an orientationally disordered structure (in the sense that $\mathbf{n}$ is disordered) with the trimers close-packed to form alternating rows displaced by $\sigma/2$. Figure 2(b) shows both the lack of orientational order, and the registry between alternating rows. Notice the black bonds showing how the disks are connected within the trimers; we call this an "*AB*" structure to denote the alternating alignment of the rows. The close-packed rows resemble those formed by

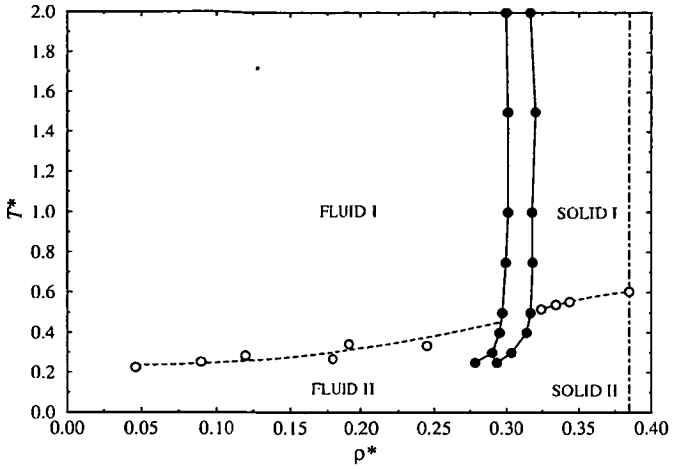

FIG. 1. Phase diagram of the model trimer system in the density-temperature (ρ^*-T^*) plane: (solid points and solid lines) approximate fluid-solid phase boundaries, assumed to be first order; (open points and dashed lines) boundaries between high-temperature unclustered states and low-temperature clustered states, as evidenced by maxima in the heat capacity along isobars; (dot-dashed line) close-packed density, $\rho^*_{cp}=2/3\sqrt{3}\simeq 0.3849$.

VP6 [16], although the registry between the rows is different. At the end of this section, we will briefly discuss the possibility of solids with other close-packed structures.

At low temperature and low density we find a highly associated fluid (fluid II), in which the attractive disks aggregate to form distinct clusters. A typical configuration is shown in Fig. 2(c), which exhibits a broad distribution of

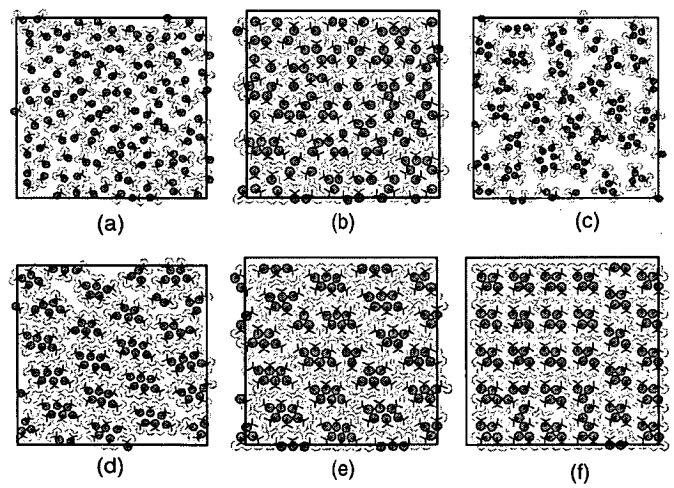

FIG. 2. (Color online) Configuration snapshots from NpT simulations: (a) normal fluid phase (fluid I) at $T^*=2$, $p^*=2.5$, $\rho^*=0.259$; (b) orientationally disordered AB solid phase (solid I) at $T^*=2$, $p^*=12$, $\rho^*=0.345$; (c) clustered fluid phase (fluid II) at $T^*=0.25$, $p^*=0.75$, $\rho^*=0.222$; (d) metastable state at $T^*=0.25$, $p^*=2.6$, $\rho^*=0.290$; (e) orientationally ordered AB solid phase (solid II) at $T^*=0.25$, $p^*=12$, $\rho^*=0.349$; (f) metastable orientationally ordered AA solid at $T^*=0.25$, $p^*=20$, $\rho^*=0.356$. In each case the attractive disks are colored dark gray (red online), the repulsive disks are colored light gray, and all disks are drawn with diameter 1σ.

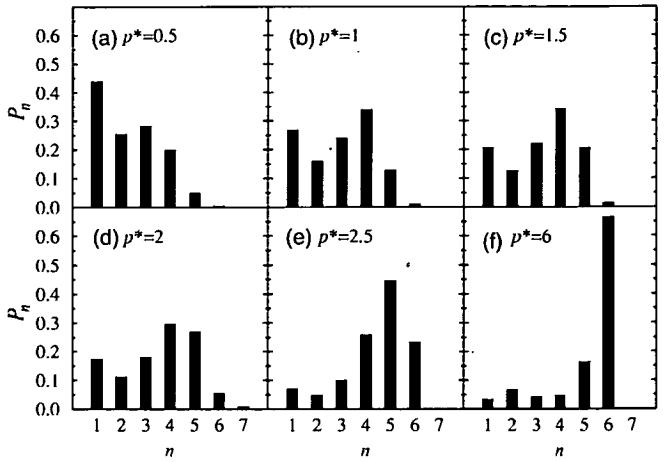

FIG. 3. Cluster distributions for systems along the isotherm $T^*=0.3$: (a) $p^*=0.5$, $\rho^*=0.188$; (b) $p^*=1$, $\rho^*=0.230$; (c) $p^*=1.5$, $\rho^*=0.252$; (d) $p^*=2$, $\rho^*=0.265$; (e) $p^*=2.5$, $\rho^*=0.280$; (f) $p^*=6$, $\rho^*=0.329$. In (a)–(e) the system is fluid, whilst in (f) the system is solid (II).

cluster sizes. To identify clusters, we employ the obvious criterion that two trimers with attractive disks within interaction range belong to the same cluster. With this definition in mind, Fig. 2(c) shows that, in general, the attractive disks within the clusters form close-packed motifs, rather than loose arrangements of disks on the circumference of a ring. For clusters of three trimers there is no distinction, whereas for four or more trimers the close-packed arrangement is more favorable; in a ring, each disk would have two nearest neighbors, whereas close-packed motifs can accommodate more than two direct contacts. In Fig. 3 we show the probability distribution function of clusters containing n molecules, at different pressures along an isotherm with $T^*=0.3$. As the pressure and density increase, the distributions show peaks at progressively higher values of n. At the highest fluid-density shown—$\rho^*=0.280$, Fig. 3(e)—the most probable cluster size is $n=5$. We had hoped that these clusters would adopt a pentagonal structure, but instead the attractive disks form "Olympic rings" motifs, such as those shown in Fig. 2(c). The maximum disk-disk separation in a perfect pentagon of disks at contact is $\sqrt{2(1-\cos 108°)}\sigma \simeq 1.62\sigma$, which is longer than the range of the potential studied in this work. Hence, to minimize the energy, the cluster will contract to form a close-packed structure. Perhaps pentagonal clusters would be formed in a system with $1.62\leqslant\lambda\leqslant\sqrt{3}$? (The upper limit means that there can be no other disks between two interacting attractive disks.) We did some test runs in the fluid phase with $\lambda=1.7$, but no pentagonal clusters were observed. If anything, fewer distinct clusters were in evidence as compared to $\lambda=1.25$, presumably because it is less crucial that the trimers attain a specific mutual orientation in order to interact.

Upon compression of the low-temperature fluid we often encountered metastable structures, such as that shown in Fig. 2(d). This clearly shows a predominance of $n=6$ clusters, with the attractive disks close packed to form a parallelogram motif, but the clusters are not yet fully packed into a solid structure. This process is completed upon further com-

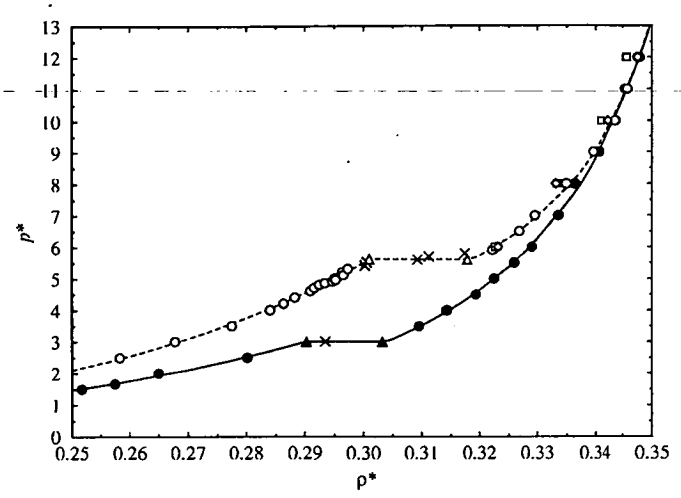

FIG. 4. Equations of state along isotherms with $T^*=0.3$ (solid symbols, solid lines), and $T^*=1$ (open symbols, dashed lines): (circles) state points from NpT simulations of AB solid phase; (squares) state points from NpT simulations of AA solid phase ($T^*=1$ only); (diamonds) state points from NpT simulations of $p3$ solid phase shown in Fig. 6 ($T^*=1$ only); (crosses) putative metastable state points; (triangles) approximate coexistence densities; (lines) fits to the fluid and solid branches (see text). The statistical errors in the NpT simulation points are smaller than the symbols.

pression, to form a $p2$ periodic solid (solid II), a defective example of which is shown in Fig. 2(e). In simulations of the high-density solid II phase, the initial configuration consisted of the appropriate AB structure, but with $\mathbf{n}$ for each molecule chosen randomly from the three molecular arms; the orientational structure shown in Fig. 2(e) develops spontaneously. The cluster distribution for such a solid at temperature $T^*=0.3$ and density $\rho^*=0.329$ is shown in Fig. 3(f). The primary peak is at $n=6$, but the presence of defects—such as those shown in Fig. 2(e)—gives rise to smaller "clusters" of attractive disks.

The fluid-solid phase boundaries were located by monitoring the equation of state $p(\rho)$ along selected isotherms in NpT simulations. For each isotherm, two sets of simulations were performed: a compression branch, starting from a low-density fluid configuration; and an expansion branch, starting from the perfect solid structure corresponding to that found in the compression branch at high pressure. Portions of two representative examples ($T^*=0.3$ and $T^*=1$) are shown in Fig. 4. Of course, the fluid equations of state extend to much lower densities, but these exhibit entirely conventional behavior and hence are not shown; in particular, there is no sign of a "van der Waals" loop which would indicate a vapor-liquid phase transition. The main features of interest are the apparent discontinuities in the density at what are assumed to be first-order phase transitions (we will not open up the can of worms associated with the precise nature of two-dimensional melting and freezing [1–4]). In Fig. 4 we indicate distinct fluid and solid branches in the equations of state, a number of putative metastable states (as discussed above), and approximate tie-lines connecting the fluid and solid coexistence densities, obtained as follows. The fluid branch was fitted with a virial expansion containing terms up to ρ^5, i.e., $p/k_BT=\rho+\Sigma_{n=2}^{5}B_n\rho^n$, while the solid branch was found to be fitted rather well by a simple van der Waals equation [25] of the form $p/kT=a\rho/(1-b\rho)-c\rho^2$, which contains a free-volume term arising from repulsive interactions, and a mean-field term arising from the attractions. The coexistence densities were then estimated by extrapolating the fitted branches of the equation of state to a pressure half way between those in the highest-density stable fluid and the lowest-density stable solid; the metastable states were identified as those that did not fit onto either branch and/or for which the simulation configuration was clearly neither pure solid nor pure fluid, e.g., Fig. 2(d). Obviously this approach provides only very rough locations for the phase boundaries shown in Fig. 1, but some general trends are nonetheless apparent. At very low temperatures, the coexistence densities decrease as the system is cooled, and the transition appears to be getting weaker. At high temperatures ($T^*\geqslant 1$) the fluid coexistence density ($\rho^*\simeq 0.30$) is very similar to the density at which the pure hard-disk fluid undergoes its transition, either to a hexatic or a solid (disk density $\rho^*=0.899$ [4], "trimer" density $\rho^*=0.300$). The apparent trimer solid coexistence density ($\rho^*\simeq 0.32$) is significantly larger than the melting density of hard disks (disk density $\rho^*\simeq 0.914$ [4], trimer density $\rho^*\simeq 0.305$).

The final piece of the equilibrium phase diagram concerns the crossover from high-temperature orientationally disordered states to low-temperature states that possess structural motifs arising from the clustering of the attractive disks. To delineate the boundary between these two regimes, we calculated the heat capacity appropriate to the statistical mechanical ensemble being sampled. In general we used NpT simulations to measure $C_p=(\partial H/\partial T)_p$—where $H=U+pA$ is the enthalpy (minus the kinetic contribution)—as a function of temperature along an isobar. Since clustering must be accompanied by a drop in the configurational energy, and enthalpy, a peak in C_p would seem to be an obvious signal of a crossover from unclustered to clustered states. In simulations we evaluated the usual fluctuation formula, $C_p=[\langle H^2\rangle-\langle H\rangle^2]/k_BT^2$, and, as a check, differentiated an $[n,n]$ Padé approximant fitted to the enthalpy as a function of T;

$$H=\frac{a_0+a_1T+a_2T^2+\cdots+a_nT^n}{1+b_1T+b_2T^2+\cdots+b_nT^n}. \tag{3}$$

These two approaches yielded consistent results, and the peak in C_p was easy to locate accurately. In general the peak height is less pronounced at high densities, mainly due to the fact that even in the high-temperature phase there must be some attractive disks within interaction range due to the confinement. Thus, the most difficult situation obtains at close packing of the trimers, $\rho_{cp}^*=2/3\sqrt{3}$. In this case we studied a perfect close-packed AB solid, and carried out NAT MC simulations with $\pm 120°$ rotations only. We show results for the configurational energy, U, and the excess constant-area heat capacity, $C_A=(\partial U/\partial T)_A$, in Fig. 5. A [5,5] Padé fit provides a reliable description of the energy, and the corresponding results for C_A are consistent with those obtained *via* the fluctuation formula.

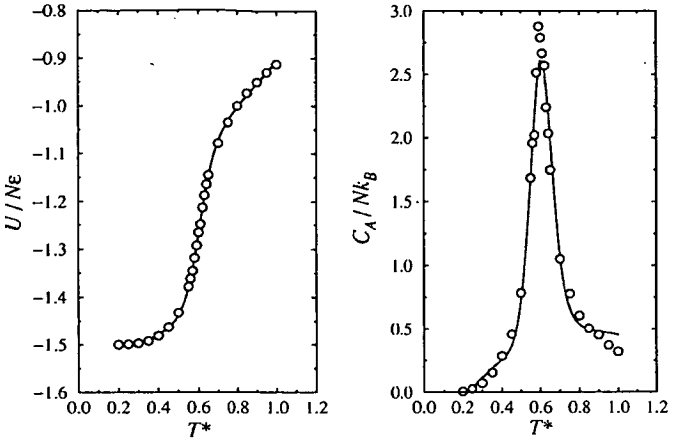

FIG. 5. Configurational energy U (left) and excess heat capacity C_A (right) as functions of reduced temperature T^* at the close-packed density $\rho^*=2/3\sqrt{3}\simeq 0.3849$: (circles) simulation results; (lines) results derived from a Padé [5,5] fit (see text).

In Fig. 1 we show the positions of the maxima in C_p—and C_A at $\rho^*_{cp}=2/3\sqrt{3}$—along with separate cubic fits to the points in the fluid and solid regions of the phase diagram. It appears that the two branches would meet up somewhere in the fluid-solid coexistence region. We stress that the boundaries indicated do not represent thermodynamic phase transitions; rather, they separate different regimes of trimer association.

Finally, we briefly consider the possibility of the trimer system adopting other solid structures, such as the $p2$ AA structure shown in Fig. 2(f), in which the close-packed (horizontal) rows are matched with the neighboring rows. In this case, the low-temperature, orientationally ordered solid exhibits rhombic cluster-motifs containing only four attractive disks. Out of those four disks, two are interacting with two other disks, and two are interacting with three other disks. Hence, the minimum configurational energy for an AA solid is $-\frac{5}{4}\epsilon$ per trimer. In the AB structure, there are six attractive disks per parallelogram motif, of which two have two neighbors, two have three neighbors, and two have four neighbors, giving a minimum energy of $-\frac{3}{2}\epsilon$ per trimer. Hence, on energetic grounds, we should expect the AB structure to be thermodynamically favored. Even at high temperature, the AA structure appears to be less stable with respect to the AB structure. As an example, in Fig. 4, we show an AA solid branch of the equation of state at $T^*=1$, alongside the AB solid branch. For a given pressure, the AB solid has the higher density which makes this state at least mechanically stable with respect to AA. Indeed, we only ever observed the fluid spontaneously freezing into an AB structure. Although we have not performed free-energy calculations, it would be very surprising if an entropic effect could compensate for the relative energetic and mechanical stability of the AB phase with respect to the AA phase.

Another possible close-packed structure is illustrated in Fig. 6(a), without any indication of the attractive disks. This structure resembles that adopted by 2D crystals of TetA [18], although we never saw this packing structure emerge spontaneously from our simulations. As far as our model is concerned, the absence of this structure at low temperature is easy to understand. In Figs. 6(b) and 6(c) we illustrate mirror images of the most obvious periodic arrangement of the attractive disks (space group $p3$). The energy per trimer is only -1ϵ, and so this is not competitive with the AB structure that is seen to emerge spontaneously in our simulations. In Fig. 4 we include some equation-of-state data for the $p3$ structure at $T^*=1$, which show that this structure is marginally less mechanically stable than the AB structure. Nonetheless, free-energy calculations would be of interest, particularly at high temperatures where entropy is everything.

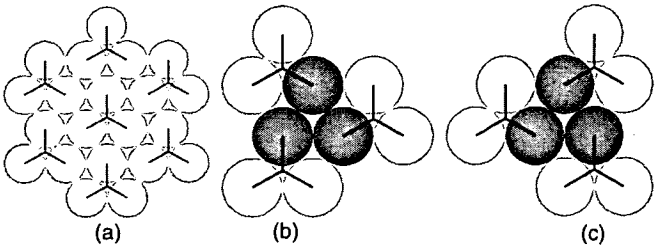

FIG. 6. (Color online) Illustrations of an alternative close-packed structure: (a) without an assignment of attractive disks; (b) and (c) mirror images of a possible structural motif for a periodic arrangement of attractive disks. The attractive disks are colored dark gray (red online), the repulsive disks are colored light gray, and all disks are drawn with diameter 1σ.

IV. DISCUSSION

In this article we have described the structure and phase behavior of a generic model of trimeric molecules, largely motivated by recent experimental 2D microscopy studies of clustering and crystallization in triangular proteins and protein trimers. The molecular model consists of a triangle of hard disks, with one of the disks participating in attractive square-well interactions with similar disks on other trimers. The range of the square-well potential, $\lambda\sigma$, was 1.25 times the disk diameter. This system crudely mimics the general shape and specific interactions of a wide range of proteins. The model system exhibits fluid and solid phases which, at low temperatures, possess interesting structural motifs arising from the clustering of the "attractive" disks.

In the fluid, a distribution of clusters is in evidence, including tetramers, pentamers, and hexamers (of trimers). In the pentamers and hexamers, the attractive disks close-pack to form Olympic rings and parallelogram shapes, respectively. We had hoped to find more open pentagonal clusters of trimers, such as those reported in Ref. [20]. To investigate the formation of such clusters further, it might be interesting to study a system of hard isosceles triangles with the unique angle equal to 72°, and a short-range attraction operating between the corresponding vertices.

In the low-temperature solid, the basic structural motif consists of clusters of six molecules, with the attractive disks close-packed to form a parallelogram. A metastable solid possessing a motif made up of four molecules was also identified. The fundamental difference between the two situations is the registry between neighboring close-packed rows of tri-

mers (*AB* versus *AA*). Even at high temperatures, the orientationally disordered *AB* solid is at least mechanically stable with respect to the *AA* solid. We identified a third structure based on hexagonal close packing, but this structure is not competitive either, at least in terms of energy. It would be worth performing free-energy calculations to study these issues further.

Finally, it is worth commenting that a diverse range of 2D structures can be generated from very simple molecular models. Fully atomistic calculations of 2D protein structures are expensive, and, it could be argued, yield little insight on the fundamental physics behind clustering and crystallization. As has been shown in a variety of cases, including the present study, the process of developing and studying simple models of complex systems can yield some surprising results.

ACKNOWLEDGMENTS

P.D.D. gratefully acknowledges the Engineering and Physical Sciences Research Council (UK).

[1] J. M. Kosterlitz and D. J. Thouless, J. Phys. C **6**, 1181 (1973).
[2] D. R. Nelson and B. I. Halperin, Phys. Rev. B **19**, 2457 (1979).
[3] A. P. Young, Phys. Rev. B **19**, 1855 (1979).
[4] K. Binder, S. Sengupta, and P. Nielaba, J. Phys.: Condens. Matter **14**, 2323 (2002).
[5] K. W. Wojciechowski, D. Frenkel, and A. C. Branka, Phys. Rev. Lett. **66**, 3168 (1991).
[6] K. W. Wojciechowski, Phys. Rev. B **46**, 26 (1992).
[7] K. W. Wojciechowski, K. V. Tretiakov, and M. Kowalik, Phys. Rev. E **67**, 036121 (2003).
[8] K. W. Wojciechowski and D. Frenkel, J. Comput. Methods Sci. Eng. **10**, 235 (2004).
[9] A. Donev, J. Burton, F. H. Stillinger, and S. Torquato, Phys. Rev. B **73**, 054109 (2006).
[10] T. Schilling, S. Pronk, B. Mulder, and D. Frenkel, Phys. Rev. E **71**, 036138 (2005).
[11] J. J. Weis, J. Phys.: Condens. Matter **15**, S1471 (2003).
[12] P. J. L. Werten, H.-W. Remigy, B. L. de Groot, D. Fotiadis, A. Philippsen, H. Strahlberg, H. Grubmüller, and A. Engel, FEBS Lett. **529**, 65 (2002).
[13] K. Jagannathan, R. Chang, and A. Yethiraj, Biophys. J. **83**, 1902 (2002).
[14] M. A. Bates, M. G. Noro, and D. Frenkel, J. Chem. Phys. **116**, 7217 (2002).
[15] M. G. Noro, M. A. Bates, A. Brisson, and D. Frenkel, Langmuir **18**, 2988 (2002).
[16] G. G. Hsu, A. R. Bellamy, and M. Yeager, J. Mol. Biol. **272**, 362 (1997).
[17] H.-W. Wang, Y.-J. Lu, L.-J. Li, S. Liu, D.-N. Wang, and S.-F. Siu, FEBS Lett. **469**, 105 (2000).
[18] C.-C. Yin, M. L. Aldema-Ramos, M. I. Borges-Walmsley, R. W. Taylor, A. R. Walmsley, S. B. Levy, and P. A. Bullough, Mol. Microbiol. **38**, 482 (2000).
[19] M. J. Conroy, S. J. Jamieson, D. Blakey, T. Kaufmann, A. Engel, D. Fotiadis, M. Merrick, and P. A. Bullough, EMBO Rep. **5**, 1153 (2004).
[20] D. L. Gibbons, M.-C. Vaney, A. Roussel, A. Vigouroux, B. Reilly, J. Lepault, M. Kielian, and F. A. Rey, Nature (London) **427**, 320 (2004).
[21] C. Govaerts, H. Wille, H. B. Prusiner, and F. E. Cohen, Proc. Natl. Acad. Sci. U.S.A. **101**, 8342 (2004).
[22] A. Kitmotto, N. Myronova, P. Basu, and H. Dalton, Biochemistry **44**, 10954 (2005).
[23] D. L. Pagan and J. D. Gunton, J. Chem. Phys. **122**, 184515 (2005).
[24] M. P. Allen and D. J. Tildesley, *Computer Simulation of Liquids* (Clarendon Press, Oxford, 1987).
[25] A. Daanoun, C. F. Tejero, and M. Baus, Phys. Rev. E **50**, 2913 (1994).

Aggregation Kinetics and the Nature of Phase Separation in Two-Dimensional Dipolar Fluids

Peter D. Duncan and Philip J. Camp*

School of Chemistry, University of Edinburgh, West Mains Road, Edinburgh EH9 3JJ, United Kingdom

(Received 8 March 2006; published 6 September 2006)

The kinetics of aggregation in a monolayer of dipolar particles are studied using stochastic dynamics computer simulations. Transient concentrations of end defects (at low density) and Y-shaped defects (at high density) clearly exceed those at equilibrium. Although very large dipole moments are expected to disfavor such defects at equilibrium, it is found that the transient defect concentrations increase with increasing dipole moment. The results suggest that the conditions for defect-driven condensation—as proposed by Tlusty and Safran [T. Tlusty and S. A. Safran, Science **290**, 1328 (2000)]—could be met by kinetic trapping, giving rise to a metastable phase transition between isotropic fluid phases.

DOI: 10.1103/PhysRevLett.97.107202 PACS numbers: 75.50.Mm, 82.20.Wt, 82.70.Dd

The structure, phase behavior, and dynamics of strongly interacting, dipolar fluids present considerable challenges to soft-matter physics. The most common realization of a dipolar fluid is a ferromagnetic colloidal suspension, or ferrofluid. In the ideal case, this consists of spherical, homogeneously magnetized monodisperse particles with diameters ~ 10 nm, sterically stabilized and immersed in a nonpolar solvent. The resulting colloidal interactions are caricatured by the widely studied dipolar hard sphere fluid. Despite almost four decades of intensive experimental, theoretical, and simulation study [1,2], at least one outstanding question remains to be answered definitively: are point dipolar interactions alone sufficient to drive vapor-liquid phase separation? On the one hand, the Boltzmann-weighted, angle average of the dipole-dipole potential gives (to leading order) an isotropic, attractive pair potential that varies like $-1/r^6$, where r is the interparticle separation; this is expected to produce conventional condensation behavior [3]. On the other hand, simulations show that conventional condensation is preempted by strong aggregation, driven at low temperatures by the energetically favorable "nose-to-tail" conformation [4]. If phase separation occurs in 3D, then it is of a rather unusual nature; simulations suggest that the low-density phase mainly consists of chainlike aggregates, while the high-density phase resembles a network of interconnected segments [5]. One possible scenario involves a defect-mediated phase transition [6] in which the chains' defects are the singly connected particles at the chain ends ("end defects"), while the network's defects predominantly consist of particles with three near neighbors in a Y-shaped conformation ("Y defects").

Recently, 2D dipolar fluids (with 3D magnetostatics) have received attention due to the possibility of directly imaging aggregation in thin films using cryogenic transmission electron microscopy [7–9]. The equilibrium structure [10,11] and dynamics [12] of 2D dipolar fluids have been studied in detail using computer simulations. At low density and low temperature (or large dipole moment), the dominant structural motifs are isolated chains and rings, while the high-density structure consists of a labyrinthine network of long chains (forming a "disordered lamellar" structure). There has never been any suggestion of a vapor-liquid phase transition in the 2D system, although end and Y defects *are* observed at equilibrium when the density and dipole moment are not too large; very large dipole moments disfavor Y defects because they are not ground-state conformations, while the excluded volume of Y defects means that the disordered lamellar structure is favored at very high densities. Note, however, that a transition between isolated and system-spanning clusters at low density has recently been characterized [13].

This Letter reports the first simulation study of the aggregation process in monolayers of strongly dipolar particles. Starting from equilibrated configurations of nonpolar particles, cluster formation is monitored after the dipoles are "switched on". The main findings are that high transient concentrations of end and Y defects are observed in aggregating systems with large dipole moments, and that these transient concentrations are always higher than the equilibrium values seen with smaller dipole moments. This suggests that the necessary conditions for defect-driven dipolar condensation might best be met by kinetically trapping transient, highly defective configurations. The results yield new insights on the properties of two-dimensional dipolar fluids, and, significantly, suggest a new strategy for realizing defect-driven condensations in the laboratory.

The system is modeled as a monolayer of monodisperse dipolar soft spheres. The interparticle potential is given by

$$u(\boldsymbol{r}, \boldsymbol{\mu}_1, \boldsymbol{\mu}_2) = 4\epsilon\left(\frac{\sigma}{r}\right)^{12} + \frac{\boldsymbol{\mu}_1 \cdot \boldsymbol{\mu}_2}{r^3} - \frac{3(\boldsymbol{\mu}_1 \cdot \boldsymbol{r})(\boldsymbol{\mu}_2 \cdot \boldsymbol{r})}{r^5}, \tag{1}$$

where ϵ is an energy parameter, σ is the sphere diameter, $\boldsymbol{\mu}_i$ is the dipole vector on particle i, $\boldsymbol{r}$ is the interparticle separation vector, and $r = |\boldsymbol{r}|$. To maintain a constant temperature in a physically relevant way, stochastic dynamics (as opposed to molecular dynamics) simulations

were performed according to the integrated Langevin equations [14]

$$\boldsymbol{r}_i(t+\delta t) = \boldsymbol{r}_i(t) + \frac{D_0^t}{k_B T}\boldsymbol{F}_i \delta t + \delta \boldsymbol{W}_i^t, \quad (2)$$

$$\hat{\boldsymbol{\mu}}_i(t+\delta t) = \hat{\boldsymbol{\mu}}_i(t) + \frac{D_0^r}{k_B T}\boldsymbol{T}_i \wedge \hat{\boldsymbol{\mu}}_i(t)\delta t + \delta \boldsymbol{W}_i^r \wedge \hat{\boldsymbol{\mu}}_i(t), \quad (3)$$

where $\boldsymbol{F}_i$ ($\boldsymbol{T}_i$) is the net force (torque) acting on dipole i at time t, $\hat{\boldsymbol{\mu}}_i = \boldsymbol{\mu}_i/\mu$ is a unit dipole orientation vector (renormalized after each time step), δt is the integration time step, and D_0^t (D_0^r) is the translational (rotational) diffusion constant at infinite dilution. The components of the 2D vector $\delta \boldsymbol{W}_i^t$ and the 3D vector $\delta \boldsymbol{W}_i^r$ were generated independently from Gaussian distributions subject to the conditions $\langle \delta \boldsymbol{W}_i^t \rangle = \langle \delta \boldsymbol{W}_i^r \rangle = 0$, $\langle \delta \boldsymbol{W}_i^t \cdot \delta \boldsymbol{W}_j^t \rangle = 4D_0^t \delta t \delta_{ij}$, and $\langle \delta \boldsymbol{W}_i^r \cdot \delta \boldsymbol{W}_j^r \rangle = 6D_0^r \delta t \delta_{ij}$. In this scheme the short-time inertial dynamics are suppressed, but this is appropriate because with large dipole moments, single-particle motions occur on time scales (in reduced units) of order 1 [12], while the collective motions of interest here are orders of magnitude slower.

In all simulations, the integration time step was $\delta t^* = 0.01$, where the reduced time is $t^* = t/\tau$ and $\tau = \sqrt{m\sigma^2/\epsilon}$. Results are presented for $N = 1024$ particles in an $L \times L$ simulation cell (with periodic boundary conditions) at densities $0.1 \leq \rho^* = N\sigma^2/L^2 \leq 0.5$, and with dipole moments $2 \leq \mu^* = \sqrt{\mu^2/\epsilon\sigma^3} \leq 2.75$; the temperature $T^* = k_B T/\epsilon = 1$ throughout. Characteristic diffusion constants were estimated from the (stick) Stokes-Einstein laws yielding $D_0^t = k_B T/3\pi\eta\sigma \simeq 4 \times 10^{-11}\ \mathrm{m^2\,s^{-1}}$ and $D_0^r = k_B T/\pi\eta\sigma \simeq 1 \times 10^6\ \mathrm{s^{-1}}$ for spherical particles with $\sigma = 10$ nm in a solvent of viscosity $\eta = 10^{-3}$ Pa s at temperature $T = 300$ K; the dimensionless quantities $D_0^t\tau/\sigma^2 = 0.004$ and $D_0^r\tau = 0.01$ were obtained using the mass of a 10 nm sphere with mass density $\sim 8000\ \mathrm{kg\,m^{-3}}$ (typical for iron or cobalt) and energy parameter $\epsilon = k_B T$. Self-assembly was initiated from configurations equilibrated with $\mu^* = 0$. For each density studied, five independent runs with different initial configurations were conducted and the results for each density were averaged, although the separate runs produced essentially identical results. The configurational temperatures associated with the positions and orientations of the particles were measured independently [15,16]. In each case the instantaneous configurational temperatures fluctuated about $T^* = 1$, with rms deviations of about 0.1, throughout the self-assembly process.

Figures 1(a) and 1(b) shows representative results for the different types of clusters that form in fluids with large dipole moments ($\mu^* = 2.75$), and at low and high densities ($\rho^* = 0.1$ and $\rho^* = 0.5$). Two neighboring particles are considered to belong to the same cluster if $u(\boldsymbol{r}, \boldsymbol{\mu}_1, \boldsymbol{\mu}_2) \leq -0.6\mu^{*2}$ [17]. Clusters were classified as either chains

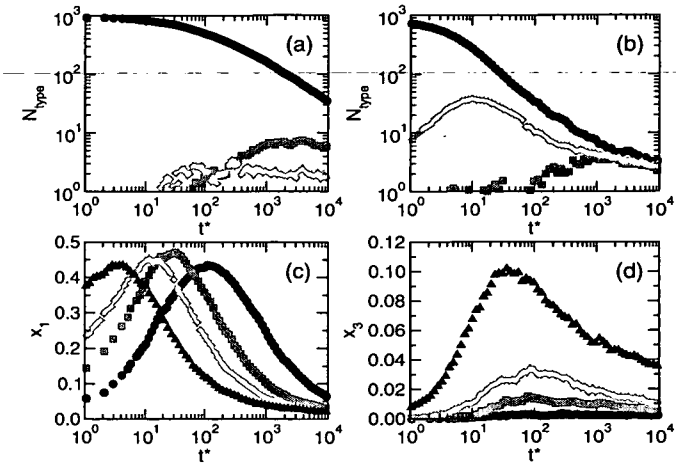

FIG. 1 (color online). Cluster properties in systems with $\mu^* = 2.75$: numbers of clusters at (a) $\rho^* = 0.1$ and (b) $\rho^* = 0.5$, classified as chains (black circles), rings (red squares), and X/Y defect clusters (green diamonds); (c) fraction of particles with one near neighbor and (d) fraction of particles with three near neighbors in fluids at densities $\rho^* = 0.1$ (black circles), $\rho^* = 0.2$ (red squares), $\rho^* = 0.3$ (green diamonds), and $\rho^* = 0.5$ (blue triangles).

(including monomers), rings, or "X/Y defect clusters" containing at least one particle with three (Y) or four (X) neighbors (particles with five or more neighbors were not observed). At low density ($\rho^* = 0.1$) the most common cluster is chainlike, followed by rings and then X/Y defect clusters. Chains are also favored at high density ($\rho^* = 0.5$), but X/Y defect clusters outnumber rings, and show a strong peak at $t^* \sim 10$; at equilibrium, the numbers of chains, rings, and X/Y defect clusters become comparable (and very small as the system undergoes almost complete aggregation). "Equilibrium" fluid structures at both densities are shown in Figs. 2(a) and 2(b). These two densities represent distinct regimes of aggregation behavior and will be considered separately.

Figure 3 shows the fractions of particles with n nearest neighbors, x_n, at time t during the aggregation processes at density $\rho^* = 0.1$ and with dipole moments $\mu^* = 2$, 2.25, 2.5, and 2.75. The monomer fraction—x_0—indicates that complete clustering is only established at equilibrium with $\mu^* \geq 2.5$. With $\mu^* \leq 2.25$, x_1 (signaling end defects) increases to a finite equilibrium value. With larger dipole moments ($\mu^* \geq 2.5$) x_1 shows strong maxima at $t^* \sim 10^2$; note that these maxima exceed all of the equilibrium values seen at smaller dipole moments ($\mu^* \leq 2.25$). The equilibrium values of x_2 indicate that extensive chaining (beyond dimers) occurs only when $\mu^* \geq 2.5$. At this low density, x_3 (signaling Y defects) is insignificant at all dipole moments; particles with four neighbors (X defects, not shown) are essentially absent. The lack of defect clusters suggests that aggregation proceeds by the sequential addition of particles or other small chains to the ends of existing chains, some of which fold up to form rings.

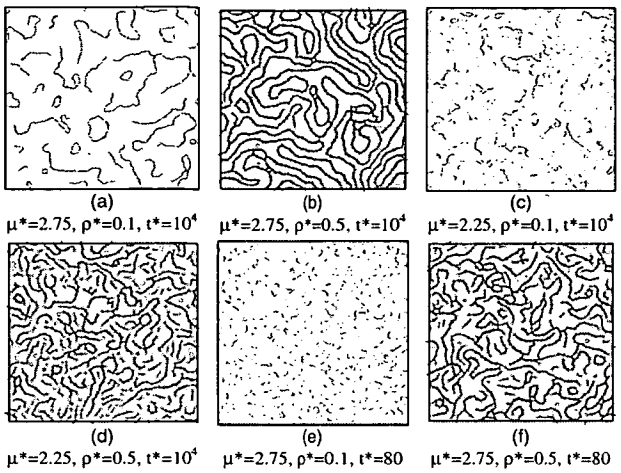

FIG. 2. Instantaneous configurations at various densities, dipole moments, and times. The black lines between particles denote "bonds" identified using the energy criterion.

Results for x_n at a high density of $\rho^* = 0.5$ are shown in Fig. 4. The equilibrium values of x_0 and x_2 show that the degree of chaining at equilibrium increases with increasing dipole moment, for obvious reasons. x_1 exhibits maxima at $t^* \sim 10$, while the equilibrium values decrease with increasing dipole moment, reflecting the energetic penalty of "dangling bonds". The behavior of x_3 depends sensitively on the dipole moment. With $\mu^* \leq 2.25$, x_3 increases from zero and plateaus at a value in the region of 0.05. At high density, even nonpolar particles are likely to have several near neighbors, some of which by chance may be oriented in such a way that when the dipoles are switched on, they cluster around a single particle to produce a Y defect. With small dipole moments, the energetic penalty of this configuration is not so severe, and the defect may

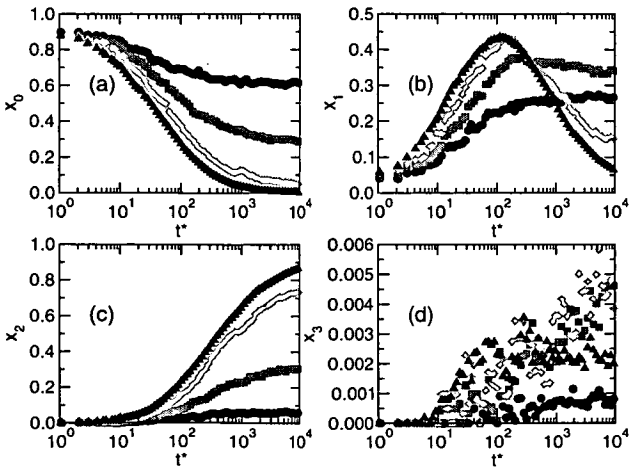

FIG. 3 (color online). Fractions of particles, x_n, with n neighbors during the aggregation process at density $\rho^* = 0.1$ and with dipole moments $\mu^* = 2$ (black circles), $\mu^* = 2.25$ (red squares), $\mu^* = 2.5$ (green diamonds), and $\mu^* = 2.75$ (blue triangles): (a) x_0; (b) x_1; (c) x_2; (d) x_3.

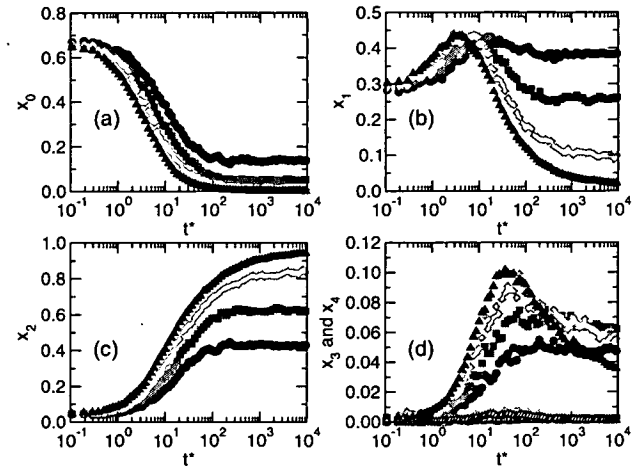

FIG. 4 (color online). Fractions of particles, x_n, with n neighbors during aggregation processes at density $\rho^* = 0.5$ and dipole moments $\mu^* = 2$ (black circles), $\mu^* = 2.25$ (red squares), $\mu^* = 2.5$ (green diamonds), and $\mu^* = 2.75$ (blue triangles): (a) x_0; (b) x_1; (c) x_2; (d) x_3 (filled symbols) and x_4 (open symbols).

persist at equilibrium. With larger dipole moments ($\mu^* \geq 2.5$), however, x_3 shows strong maxima at $t^* \sim 60$, and then tails off to values less than 0.05; significantly, the maxima are approximately two-thirds larger than the equilibrium values seen with smaller dipole moments. X defects (signaled by x_4) are at least an order of magnitude less numerous than Y defects, and are hence insignificant. These results suggest that larger dipole moments promote the initial formation of Y defects (as described above), but that since the associated Boltzmann weight of this configuration is not optimal, the Y defects "anneal out" to form the disordered lamellar phase as the fluid approaches equilibrium.

Defect-driven condensation involves a low-density phase rich in end defects, and a high-density phase rich in Y defects. It is therefore instructive to consider the equilibrium values of x_1, x_2, and x_3 at low density ($\rho^* = 0.1$) and high density ($\rho^* = 0.5$), as shown in Table I. With small dipole moments ($\mu^* \leq 2.25$), the end-defect concentrations at $\rho^* = 0.1$ are significant (~0.3), while the Y-defect concentrations at $\rho^* = 0.5$ are relatively small

TABLE I. Equilibrium ($t^* = \infty$) and transient values of x_1, x_2, and x_3 at densities of $\rho^* = 0.1$ and $\rho^* = 0.5$, and at various dipole moments.

		$\rho^* = 0.1$			$\rho^* = 0.5$		
μ^*	t^*	x_1	x_2	x_3	x_1	x_2	x_3
2	∞	0.29	0.08	<0.01	0.40	0.41	0.05
2.25	∞	0.32	0.32	<0.01	0.28	0.60	0.06
2.5	∞	<0.15	>0.73	<0.01	<0.10	>0.85	<0.04
2.75	∞	<0.06	>0.87	<0.01	<0.02	>0.94	<0.02
2.5	100	0.40	0.16	<0.01	0.17	0.71	0.09
2.75	80	0.43	0.19	<0.01	0.14	0.74	0.10

(~0.05). With larger dipole moments ($\mu^* \geq 2.5$) the equilibrium end-defect and Y-defect concentrations become negligible. (With these large dipole moments, the approach to equilibrium is extremely slow, hence the inequality signs in Table I). This provides an explanation of why an equilibrium defect-driven condensation has not been observed in 2D dipolar fluids: at all dipole moments (or temperatures) there are insufficient concentrations of end defects and Y defects in the low-density and high-density states, respectively.

Transient defect concentrations with $\mu^* = 2.5$ and $\mu^* = 2.75$ are also reported in Table I. In each case times are selected roughly halfway in between the positions of the peaks in x_1 at low density [Fig. 3(b)] and x_3 at high density [Fig. 4(d)]. The key point is that the transient end-defect concentration (at low density) and Y-defect concentration (at high density) are simultaneously greater than the equilibrium values with smaller dipole moments. In addition, the transient end-defect concentrations in the high-density fluid are much smaller with $\mu^* \geq 2.5$ than are the equilibrium concentrations with $\mu^* \leq 2.25$. These findings can be made more tangible by looking at simulation snapshots. Figures 2(c) and 2(d) shows equilibrium structures with $\mu^* = 2.25$, and $\rho^* = 0.1$ and $\rho^* = 0.5$; these are to be compared with the *transient* configurations at the same densities, but with $\mu^* = 2.75$ [Figs. 2(e) and 2(f)].

Thus far, only two densities have been considered, but in Figs. 1(c) and 1(d) are shown x_1 and x_3 for fluids with dipole moment $\mu^* = 2.75$, and at a selection of densities in the range $0.1 \leq \rho^* \leq 0.5$. x_1 peaks earlier and x_3 shows stronger maxima as the density is increased, due to the particles being in closer proximity when the dipoles are first switched on. It is clear that the extremes of this density range correspond to quite distinct regimes of aggregation behavior.

In summary, at low density aggregation proceeds through the formation of chains, some of which go on to form rings; above a critical dipole moment (in the range $\mu_c^* = 2.25$–2.5) transient concentrations of end defects exceed the equilibrium values observed with smaller dipole moments. At high density, increasing the dipole moment leads to a reduction (enhancement) of the equilibrium (transient) Y-defect concentration. When $\mu^* > \mu_c^*$, there is a time window in which the concentrations of end defects in the low-density fluid ($\rho^* \sim 0.1$) and Y defects in the high-density fluid ($\rho^* \sim 0.5$) are simultaneously close to their maximal values. Such defects are precisely those implicated in the defect-driven condensation of dipolar fluids [6]. It might therefore be possible to access a metastable phase separation, even in thin films where no equilibrium transition is expected, through kinetic stabilization of end defects (characterizing the low-density phase) and Y defects (characterizing the high-density phase). For instance, in ferrofluids a rapid temperature quench could freeze the carrier solvent and trap transient defects. Alternatively, the addition of a strong short-range isotropic attraction (e.g., chemically, or with added polymer to induce depletion forces) might stabilize defects. In this scenario, the long-range dipolar interactions drive the initial formation of small clusters with end and Y defects, while the short-range isotropic attractions preclude subsequent reorganization into the equilibrium structures. The relative ease with which 2D dipolar systems can be imaged directly may offer the best hope yet of realizing such a transition in the laboratory.

We thank Gren Patey, Sam Safran, Paulo Teixeira, and Tsvi Tlusty for correspondence, and the School of Chemistry at the University of Edinburgh for support to P. D. D.

*Electronic address: philip.camp@ed.ac.uk

[1] P. I. C. Teixeira, J. M. Tavares, and M. M. Telo da Gama, J. Phys. Condens. Matter **12**, R411 (2000).
[2] C. Holm and J.-J. Weis, Curr. Opin. Colloid Interface Sci. **10**, 133 (2005).
[3] P. G. de Gennes and P. A. Pincus, Phys. Kondens. Mater. **11**, 189 (1970).
[4] J. J. Weis and D. Levesque, Phys. Rev. Lett. **71**, 2729 (1993).
[5] P. J. Camp, J. C. Shelley, and G. N. Patey, Phys. Rev. Lett. **84**, 115 (2000).
[6] T. Tlusty and S. A. Safran, Science **290**, 1328 (2000).
[7] V. F. Puntes, K. M. Krishnan, and A. P. Alivisatos, Science **291**, 2115 (2001).
[8] K. Butter, P. H. H. Bomans, P. M. Frederik, G. J. Vroege, and A. P. Philipse, Nat. Mater. **2**, 88 (2003).
[9] M. Klokkenburg, R. P. A. Dullens, W. K. Kegel, B. H. Erné, and A. P. Philipse, Phys. Rev. Lett. **96**, 037203 (2006).
[10] J. M. Tavares, J. J. Weis, and M. M. Telo da Gama, Phys. Rev. E **65**, 061201 (2002).
[11] J.-J. Weis, J. Phys. Condens. Matter **15**, S1471 (2003).
[12] P. D. Duncan and P. J. Camp, J. Chem. Phys. **121**, 11 322 (2004).
[13] J. M. Tavares, J. J. Weis, and M. M. Telo da Gama, Phys. Rev. E **73**, 041507 (2006).
[14] R. B. Jones and F. N. Alavi, Physica A (Amsterdam) **187**, 436 (1992).
[15] O. G. Jepps, G. Ayton, and D. J. Evans, Phys. Rev. E **62**, 4757 (2000).
[16] A. A. Chialvo, J. M. Simonson, P. T. Cummings, and P. G. Kusalik, J. Chem. Phys. **114**, 6514 (2001).
[17] This energy cutoff captures likely conformations for neighboring dipoles, either in chains or in defect environments, and was determined on the basis of energy calculations for a number of different minimum-energy conformations. Cluster assignments were validated by direct inspection of the simulation configurations.